Beam Energy Scan dependence of elliptic and triangular flow of identified hadrons in the STAR experiment and the EPOS model

Maria Stefaniak

DOCTORAT MATIERE BRETAGNE MOLECULES LOIRE ET MATERIAUX

IMT Atlantique
Bretagne-Pays de la Loire
École Mines-Télécom

THÈSE DE DOCTORAT DE / DOCTORAL THESIS

L'ÉCOLE NATIONALE SUPÉRIEURE
MINES-TÉLÉCOM ATLANTIQUE BRETAGNE
PAYS-DE-LA-LOIRE - IMT ATLANTIQUE

ÉCOLE DOCTORALE N° 596
Matière, Molécules, Matériaux
Spécialité : *Physique Théorique*

ET/AND

WARSAW UNIVERSITY OF TECHNOLOGY
FACULTY OF PHYSICS

Par
Maria STEFANIAK

Beam Energy Scan dependance of elliptic and triangular flow of identified hadrons in the STAR experiment and the EPOS model

Étude de la dépendance en énergie des flux elliptique et triangulaire pour les particules identifiées dans le Beam Energy Scan avec l'expérience STAR et le générateur d'événements EPOS

Thèse présentée et soutenue à Varsovie, le 26.10.2021
Unité de recherche : Subatech-IMT Atlantique, Warsaw University of Technology
Thèse N° : 2021IMTA0255

Composition du Jury :

Rapporteurs avant soutenance :	Barbara ERAZMUS	University of Nantes
	Krzysztof PIASECKI	University of Warsaw
	Beatrice RAMSTEIN	Institut de Physique Nucléaire d'Orsay
Président :	Gabriel WLAZŁOWSKI	Warsaw University of Technology
Examinateurs :	Hubert HANSEN	Institut de Physique Nucléaire de Lyon
	Agata FRONCZAK	Warsaw University of Technology
Dir. de thèse :	Klaus WERNER	University of Nantes and Subatech
Co-dir. de thèse :	Hanna ZBROSZCZYK	Warsaw University of Technology

ABSTRACT

Beam Energy Scan dependance of elliptic and triangular flow of identified hadrons in the STAR experiment and the EPOS model

Studying the properties of the collective expansion of matter created in heavy-ion collisions provides a unique tool to understand better the nonperturbative aspect of QCD. Input from both the theoretical and the experimental side is needed. Hydrodynamic calculations predict anisotropies in particle production, as a consequence of asymmetries in the initial state of the system's evolution. Measurements of the systematics (energy-, system- dependence) of these anisotropies allow one not only to validate theoretical ideas, but also to determine the unknown elements, like plasma properties (EoS), themalization processes. The broadening of our knowledge in this topics is the main goal of the thesis. The experimental methods were used to provide the insight into the investigation of the anisotropies in expansion of the particles and antiparticles, while with the theoretical approach was used for the EoS studies.

Two-particle flow correlations are a powerful tool in studies of the expansion of the matter. They express the relation between the directions of the produced particles. The nonuniform distribution of final-state momenta is a consequence of the initial-stage anisotropy in the collision's geometry. It is transformed via pressure gradients into an asymmetric flow, providing finally a strong correlation of the direction of the particles' motion with the collision's participant plane. The shape of the expansion is described in terms of a Fourier decomposition. Each harmonic corresponds to the subsequent shape of expanding matter: second harmonic (v_2) is the elliptic flow, and third one (v_3) the triangular one. v_2 originates primarily from the eccentricity (ϵ_2) of the overlap collision. On the other hand, all odd coefficients are not sensitive to the ϵ, and the fluctuations and viscous effects dominate the measured signal. It is also less contaminated with the particle correlations not related with flow (non-flow). Possible, detailed investigation about all these ingredients makes the performed studies of both harmonics a comprehensive source of information about various aspects of the matter's initial-state properties.

Multiple interesting observations based on protons' and antiprotons' production are

used as probes of studies of QCD phase diagram. One of the intriguing measurements showed the increasing elliptic flow difference between p and $\bar{p}$ with a decrease of the collision energy. There are several theoretical explanations of the observation. However, none of them has been proven. The STAR data were used to verify several scenarios and improve the experimental reference for theoretical studies. The similar trend of the differences between p and $\bar{p}$ is also observed for the triangular flow, which is mostly driven by fluctuations. Moreover, the $n_q(KE_T)$ scaling gave a piece of information about protons and antiprotons' possible different origins.

On the other hand, the created matter is expected to behave like a viscous fluid, and its expansion can be based on the hydrodynamical equations. Transitions between different states of matter and thermodynamical relations characterizing it are included in the Equation of State (EoS). It cannot be derived directly from first principles or measured by an experiment. Studies of the EoS are crucial in understanding the dynamics of the matter in different regions of the phase diagram of nuclear matter. It is not apparent that experimentally measurable observables could give a piece of information about EoS or its changes. Introducing the possibility of different EoS choices while developing the EPOS model gave a unique possibility for such studies. The family of EoS proposed by the BEST Collaboration was implemented. The Critical Point position and the strength of criticality variation were changed, and the effects on the final observables such as particle yield, transverse momentum spectra, flow, or moments of the net-proton distributions were studied.

The thesis consists of Chapter 1, where we present the concise review of the significant high energy physics aspects necessary for this thesis. The review of anisotropies in the expansion of the matter, flow harmonics and two particles cumulants is in Chapter 2. In Chapter 3, the STAR experiment at RHIC is described. The data selection and evaluation of systematic uncertainties are discussed in Chapter 4. The Chapter 5 is devoted to the experimental results. In subsequent Chapter 6, we included the EPOS event generator description and implemented developments (introduction of new EoS). The studies of the implemented EoS into the EPOS and comparison with the STAR results are presented in Chapter 7. Finally, we summarise the performed studies and provide the outlook for the impact on the future research in Chapter 7.2.5.

There are three Appendices consists of short summary of the my engagement into the iTPC software development Appendix 9, activities conducted in the frame of RIVET project Appendix 10, and list of useful thermodynamic equations in Appendix 8.

This thesis includes the unique combination of both experimental and theoretical approaches to exploring the properties and dynamics of the matter.

ACKNOWLEDGEMENT

The research presented in this thesis would never be completed without the help and support of numerous people. Here, I would like to take the opportunity to express my gratitude and acknowledge the support I have received.

First of all, I would like to thank my supervisors, prof. Hanna Zbroszczyk and prof. Klaus Werner. This journey was quite challenging, but you always supported me and helped with even tiny issues. I really appreciate the freedom you gave me, trusting that I will do my best without daily supervision. Although maybe sometimes I needed some "push", I had to become independent and responsible. Studying in the frame of *BGF Co-tutelle* was an excellent adventure but also a tough challenge for my personal life. I always knew that I could count on both of you! The Covid-19 pandemic started the avalanche of complications, but you helped me even more than I could ever expect. Furthermore, both of you are excellent experts in the field. I have learned a lot, and I promise that I will never forget all the discussions and inspiring meetings!

Prof. Hanna, you have taken care of me for already 8 years! You became my guide and role model as a woman and scientist. I highly admire all our informal discussions related to personal life, career, or just everyday situations. I know I can trust you and count on you; I can share my troubles with you as a friend.

Secondly, I would like to thank Niseem Magdy, the fantastic mentor and guide of my experimental research. You have spent hundreds of hours, just as a volunteer, to help me with my analysis. You really believed in me, and without you, there would be nothing except maybe a few pages of this thesis. You taught me how to stand for my rights and defend my opinions. The discussions with you and Prof. Roy Lacey are the most motivating ones I have ever had. The meetings with the group at Stony Brook University opened a new chapter of my science fascination. They gave me a new perspective on my work as a researcher. I would like to thank Doctor Zhangbu Xu, whose support allowed me to come to BNL and collaborate with Niseem, the SBU, and BNL groups.

I want to thank the Heavy-Ion Relativistic Group, Prof. Jan Pluta, Prof. Adam Kisiel, Prof. Kasia Grebieszkow, Dr Małgosia Janik, Dr Łukasz Graczykowski, Dr Georgy Kornakov, Paweł Szymański, Diana Pawłowska (our participation in lots of conferences were

great adventures!). Our weekly meetings were very productive and educative! But mostly, I would like to thank Prof. Daniel Kikoła, who has never been my official supervisor. Still, he always finds time for discussion with me. I really appreciate all the feedback you gave me (also the critical one!), all the "short questions" I could've asked sitting and disturbing you in the same office.

I would like to express my gratitude to all the staff working at WUT's Faculty of Physics. You were very patient with all my delays and confusions I introduced.

I want to acknowledge the whole STAR Collaboration. Thanks to you, I had an opportunity to perform my studies on the data collected by the experiment, discuss my progress and get lots of feedback. I learned a lot by taking shifts or participating in the service work with the iTPC group.

During my studies, I have met many fantastic people who became my great friends.

Johannes, Mahbobeh, Andreas, Iuliia, Yurii, Gabriel, David, my stays in Nantes couldn't be better, and all of these thanks to you! Johannes, your contribution to my work with EPOS is substantial, and I highly appreciate it!

Jurku i Ewo, zostaliście moimi francuskimi rodzicami. Nigdy nie poznałam ludzi tak ciepłych, zaangażowanych, dobrych i bezinteresownych. Dziękuję za to, że wyciągnęliście mnie z najróżniejszych tarapatów i zawsze mogłam po prostu z Wami być. Dzięki Wam, Nantes było moim "drugim domem".

Daniel Kincses, thank you for all these jam sessions at Jazz Loft in Port Jefferson, crazy trips, and dozens of hours spent working on many scientific projects. But I am most grateful for your support 24h/7 with all my troubles. You are a fantastic friend! We are really great companions in this "scientific" journey, and I feel that this is just the beginning! Meg tudom csinálni!

I want to thank my parents Dorota and Tomek. Od początku mnie wspieraliście w realizacji wszystkich moich szalonych pomysłów. Dzięki Wam mogłam wyjechać na studia do Warszawy, a później kontynuować karierę naukową. Mamo, pokazałaś mi, czym jest sztuka, muzyka, kino. Dzięki Tobie, nie stałam się robotem, a jestem osobą wrażliwą na piękno otaczającego mnie świata. Tato, dzięki Tobie wiem, że nigdy nie można odpuszczać. Stałam się osobą ambitną, wytrwałą w dążeniu do celu. Najbardziej mnie cieszy to, że pokazałeś mi czym jest przygoda i aktywność. Sport stał się ogromnie ważną częścią mojego życia, która kształtuje mój charatker i pozwala przeżyć niezapomniane chwile.

Siostro, Aniu, nigdy nie przestaniesz być najważniejszą osobą w moim życiu. Prawie trzydzieści lat się mną opiekujesz i razem przeżyłyśmy niesamowite historie. Było wiele

wspaniałych, wiele niezwykle trudnych, jednak zawsze byłaś ze mną i wiem, że zawsze będziesz. Klaro, moja siostrzenico, jesteś oczkiem w mej głowie i najwspanialszym dzieckiem jakie poznałam.

Thanks to you, my family, I could have become who I am now.

I dedicated this thesis to **my friends**, because without you, I would not even start this adventure. Marta, Zuza, Jacek, Wojtek, Szymon i Patryk, Dorota, Julia, Asia, Szporki, Karol, Izerki, bez Was bym po prostu nie dała rady. Te wszystkie rejsy, wyjazdy, spotkania, pokazały mi, co w życiu jest najważniejsze, mimo że praca pochłaniała ogromną większośc mojego czasu. Zawsze jesteście dla mnie i mogę na Was liczyć. Chciałabym, żeby nasza przyjaźń nigdy się nie skończyła. Dziękuję Michale i Grzesiu, że przy mnie byliście i wytrzymywaliście moje przypływy euforii i niezadowolenia z pracy. Wasze wsparcie było bezcenne.

I want to also thank all my friends and coaches from Towarzysto Wisła Dla Wioślarzy (TWDW). Last year was very difficult for me due to the pandemic. I had to resign from all my travels, conferences, etc.. Still, thanks to rowing and the fantastic atmosphere in the club, I find myself and kind of relieved from all accumulated stress.

Jazz, my lovely puppy! Recently, you joined my little family and turned my world upside-down. You are just the best!

Table of Contents

INTRODUCTION

Physics is the empirical answer, not leaving place for the "believes". The theory has to be proven by the experiment in the agreed range of uncertainty. However, some of the physics fields are focused on studies of such extremely small ($\sim$ 1 fm) or located in the long-distance (many solar years form observer) objects that it becomes challenging to describe these phenomena both theoretically and experimentally.

One of the most intriguing puzzles is understanding of the beginning of the Universe. Scientists proposed as the answer the Big Bang model, which is nowadays broadly accepted. It explains the origin of the matter, but still, this description is not complete. We do not precisely understand the matter dynamics in the initial stages of evolution or what states and transitions matter goes through. This thesis broadens our knowledge in this topic and answers the questions: what are the properties of the expanding newly-created matter, how we can measure them and what we can improve in our theoretical description of processes occurring during the initial stages of the Universe existence. I am using both experimental and theoretical approach in the investigation of flowing nuclear matter.

Studying the properties of strongly interacting matter is one of the significant milestones for nuclear physics. Various experimental facilities have been designed to investigate the Quantum Chromo-Dynamical (QCD) phase diagram, such as the Relativistic Heavy Ion Collider (RHIC), the Super Proton Synchrotron (SPS), or the Large Ion Collider (LHC). There are also future Nuclotron-based Ion Collider fAcility (NICA) and Facility for Antiproton and Ion Research in Europe (FAIR) which scientific programs are dedicated to exploring high baryon density region. These programs are at the forefront of experimental efforts designed to map the thermodynamic and transport properties of strongly interacting QCD matter. Both theoretical and experimental approaches suggest a smooth cross-over phase transition from a hadronic state of matter to a Quark-Gluon Plasma (QGP) at low baryon chemical potential and high-temperature values, that is, in collisions at the LHC and top RHIC energies. At high baryon chemical potentials and low temperatures, a first-order phase transition is expected. Both transitions are foreseen to be connected by the Critical Point (CP), at which the phase transition is predicted to be second order. STAR experiment carried out an extensive research program to search for

CP.

The experimental data suggest that QGP behaves almost like an ideal fluid. Due to the short lifetime of the plasma state, many of its properties can only be inferred indirectly by comparing the final state measurements with transport model calculations. Among the current phenomena of interest are the interdependences between two collective flow effects, elliptic v_2 and triangular flow v_3. These are the observables characterising the shape and dynamics of the expanding matter. Both are very sensitive to the properties of the system at very early times of its evolution. The elliptic flow is mainly related to the initial geometry and collective expansion of the system, whereas triangular flow is sensitive to the initial state's fluctuations.

STAR is caring out an extensive research program to search for CP in the Beam Energy Scan program frame. The relevant part of the performed investigations concentrated on the measurements of v_1, v_2 and fluctuations. So far results for protons and antiprotons are the most intriguing: observation of the non-monotonic net-proton fluctuations, change of sign for net-proton dv_1/dy or large difference between v_2 of p and $\bar{p}$. These observations were that significant and interesting for the physicist community that the Beam Energy Scan II is being carried out at RHIC, providing new data that are already available. Here, the possible sources of the studied phenomena are explored- the effect of the initial state fluctuations and how in-medium interactions (characterised by transport coefficients) affect the observables used as probes of the CP. Since the triangular flow is susceptible to these effects, the measurements of v_3 for particles and antiparticles (focusing on p and $\bar{p}$) can provide an additional, vital experimental handle on initial-state fluctuations and shear viscosity.

The experimental research is complemented with developing the phenomenological model describing the matter's creation and its dynamics. The EPOS model is applicable to systems corresponding to small μ_B. It needs to undergo significant adaptations to describe better physical phenomena present at high baryon densities that occur at relatively low collision energies at which the BES studies are carried. Different ingredients of the EPOS model: hydrodynamical evolution, Equation of State and processes of hadronisation, need to be revised and improved. Each of them can give essential information about the nature of the phase transition (i.e. cross-over vs first order), the location and proprieties of Critical Point. It will enable EPOS to become one of the basic theoretical models for the previously mentioned experimental programs.

The hydrodynamical evolution included in the model is based on the Equation of State

(EoS). It characterises the relations between the thermodynamical quantities describing the evolving system. However, it cannot be studied directly in the experiment, and a phenomenological reference is needed. Although there are many models, it is challenging to acknowledge what experimental observables are sensitive to the changes in EoS and which as related to the other model ingredients. The possibility of changing only the EoS in the given model provides direct information about the searched effects.

In this thesis, a novel approach of heavy-ions studies is presented from both experimental and theoretical sides. The 2-particles cumulants of flow harmonics for identified hadrons have been studied at STAR for the first time as a function of transverse momentum and collision centrality. Moreover, a unique analysis of the impact on the several observables of the various EoS implemented in the EPOS model has been performed.

Some of the studies performed as a part of this thesis has been already published in [1–4]. Additionally, the results related to the flow harmonics for Au+Au collisions at $\sqrt{s_{NN}} = 200$ GeV measured at STAR are already under the internal STAR committee review. Furthermore, the rest of the obtained results are now being prepared for the publishing process for two articles: one dedicated to the v_n for experimental studies and the second related to the studies of EoS with EPOS model.

Chapter 1

High-energy nuclear collisions

In this chapter, the theoretical background of high-energy physics is introduced. Firstly, the concept of the Standard Model of particle physics and quantum chromodynamics is highlighted.

1.1 Standard Model and Quantum Chromodynamics

1.1.1 Standard Model

From the 1930s onwards one received a comprehensive insight into the knowledge of the most elementary structure of matter and its interaction. The few fundamental particles grouped into blocks governed by four fundamental forces were found to be the only ingredients creating the Universe. The relations between the given groups of *matter particles* and three of the forces are encapsulated in the Standard Model of particle physics. This theory was developed in the early 1970s, successfully describing nearly all experimental results and predicting a huge range of phenomena where some of them are still tested. The all particles are divided into two groups: **fermions** (matter particles) and **bosons** (interaction carriers).

Matter particles The matter which surrounds us consists of fundamental particles (no internal structure can be distinguished). They can be divided into two primary groups called quarks and leptons. There are six particle's species in each of them, and they are related to pairs called "generations". The first generation consists of the most stable and the lightest particles, while the second and the third particles are heavier and less stable. Consequently, the whole stable matter in the Universe is made from first-generation particles. The heavier ones nearly immediately decay to the more stable particles. The generations of the quarks are listed in the table 1.1. Nevertheless, each quark is characterised by a different quantum number called *colour*, which can come in the three various *colours* and

	Quarks			Leptons		
Generation	Symbol	Charge	Mass	Symbol	Charge	Mass
1	u	$2/3e$	$1.7 - 3.3 MeV/c^2$	e	$-e$	$0.511 MeV/c^2$
	d	$-1/3e$	$4.1 - 5.8 MeV/c^2$	v_e	0	$2 eV/c^2$
2	c	$2/3e$	$1.18 - 1.34 GeV/c^2$	μ^-	$-e$	$105 MeV/c^2$
	s	$-1/3e$	$80 - 130 MeV/c^2$	v_{mu}	0	$0.19 MeV/c^2$
3	t	$2/3e$	$169.8 - 174.2 GeV/c^2$	τ^-	$-e$	$1.68 GeV/c^2$
	b	$-1/3e$	$4.1 - 4.4 GeV/c^2$	v_τ	0	$18.2 MeV/c^2$

Table 1.1 – Elementary particles, their mass and charges as described in the Starndard Model of particles physics [7]

bound only in such ways as to create the colourless objects. This number was introduced to understand the possibility of obeying the statistical rule described by Enrico Fermi and Wolfgang Pauli called the exclusion principle. It states that no two fermions can occupy the same quantum state, be described by same quantum numbers [5]. The second group of fermions consists of six leptons, which are arranged into three generations. The tau, muon and electron have a sizable mass and an electric charge. The neutrinos are electrically neutral and were treated, for a very long time, as mass-less particles. Recently, it was discovered that they do have mass [6].

Force carriers In the Universe, the four fundamental forces can be distinguished:

— the electromagnetic force,
— the strong force,
— the weak force,
— the gravitational force (not included in SM).

It is predicted each force is carried by *gauge bosons*. The integer spin characterises them, and they obey Bose-Einstein quantum statistics. Bosons transfer discreet energy amount between matter particles. The electromagnetic interactions are exchanged by photons (γ) between charged particles, and similarly to gravitational forces, their range is infinite. It is described by Quantum Electrodynamics (QED). Contrarily, weak and strong forces are effective at the subatomic level. Very massive particles carry the weak interactions: W^+, W^-, Z^0. It is characterised by Quantum FlavourDynamics (QFD) and affects both quarks and leptons. Strong forces are mediated by eight gluons (g), and they are responsible for the colour exchange between quarks. The Quantum ChromoDynamics (QCD) is the theory

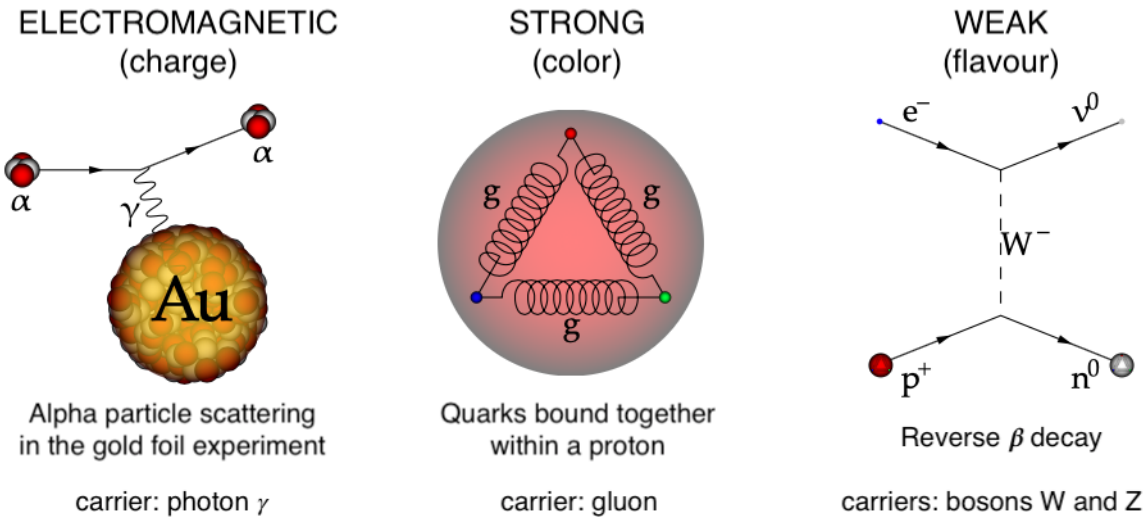

Figure 1.1 – Examples of interactions included in the Standard Model of particle physics. Names, what do they exchange and the carriers [8].

describing this type of interactions (more in the next subsection). The gravitational force is carried by hypothetical "graviton", which existence is not yet proven.

Standard Model does include electromagnetic, strong and weak forces, all their carriers, and describes how they interact with particles of matter. However, gravity is not a part of SM. In the Figure 1.1 there are presented examples of SM interactions.

Both bosons W and Z have mass a hundred times bigger than protons. In 1964 theorists Peter Higgs, François Englert, and Robert Brout proposed the theory explaining this puzzle by the mechanism BEH (Brout-Englert-Higgs). The assumed the existence of an invisible field that reacts with bosons W and Z, giving them mass, while it does not interfere with photons, leaving them massless. Just after the Big Bang, the so-called "Higgs field" was equal to zero and all the particles were massless moving with the speed of light. After cooling down, the Universe reached the critical temperature, and the filed spontaneously increased and, via interactions, gave particles mass. The BEH mechanism implies that the value of the elementary particles' mass depends on the strength of their interaction with the Higgs field. The particle which mediates in this field is called the Higgs boson and is one of the Standard Model's ingredients.

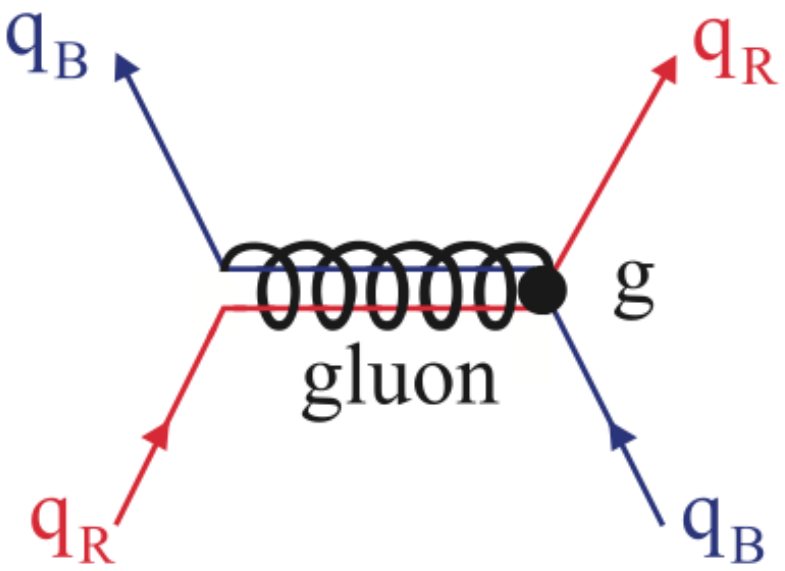

Figure 1.2 – the QCD interaction between coloured quarks via a coloured gluon $r\bar{b}$ [9].

1.1.2 Quantum Chromodynamics

Quantum Chromodynamics (QCD) is the theory describing the strong interactions between quarks. They are mediated by *gluons*, which are chargeless and massless. Similarly to photons, gluon is the vector particle, and its spin and parity are equal to $J^P = 1^-$. In QCD, there are six types or the strong charges called *colours* - the extra internal degrees of freedom. Quark can carry only one out of three possible colours and antiquark one anticolour; they can exchange them via gluons. It is assumed that the colour symmetry is the strict symmetry and the strong forces are colour independent. The example of the interaction is presented in Fig. 1.2, where the red quark interacts with the blue one exchanging the red-blue gluon. The gluon has its own color charge ($r\bar{b}$). As a consequence, the gluons can directly interact with each other.

The idea of introducing this extra quantum number was derived after observation of particles built up from three quarks of the same flavor: Δ^{++} - *uuu*, Δ^- - *ddd* and Ω^- - *sss*. To satisfy Pauli's exclusion principle, the new quantum number describing the systems had to be added. Greenberg introduced it in 1964 and by Han and Nambu in 1965 [10, 11]. Both baryons (qqq or $\bar{q}\bar{q}\bar{q}$) or mesons ($q\bar{q}$) have to be colour-singlets.

Potential of strong interactions

The potential between quarks in QCD can be expressed with the following equation:

$$V = -\frac{4}{3}\frac{\alpha_S}{r} + kr \tag{1.1}$$

where: α_s is the strong coupling constant, r is the distance between quarks, and k is the parameter experimentally estimated to be equal 0.87 GeV/fm. The proposed potential correctly explains the energy levels of charmonium and bottomium. In Figure 1.3 the dependence of the QCD potential on the distance between quarks. For small r the first part of the V (eq. 1.1) dominates. For the bigger distance, the second part dominates, which depends linearly on radii. It is related to the confinement of quarks in hadrons. The lines of the colour forces can visualise it pulled together by gluon-gluon interactions, creating a tube or a string. The stretching of the string causes the energy proportional to kr to reach the critical value where, for the energetic reason, it is more efficient to create the new pair of $q\bar{q}$. As a consequence, instead of one long string, there are two shorter. This process is called the *fragmentation of the strings*.

The asymptotic freedom and quark confinement

In the QCD there is defined the *coupling constant* α_s, which determines the strength of the force acting on quarks and gluons. In reality α_s is not constant and scales with Q^2 and can be expressed by the following :

$$\alpha_s(Q^2) \propto \frac{1}{\beta_0 ln(Q^2/\Lambda^2)} \tag{1.2}$$

where β_0 is one-loop approximation for the function [13], $\Lambda \approx 127MeV$ - scale constant [1] In the Fig. 1.4 the α_s dependance on the momentum exchange between particles is presented. There are two main scenarios possible for colored objects: *confinement* dominating in low energies [15–17] and *asymptotic freedom* at high energies [18–20].

Reactions with momentum exchange $Q < 1$ GeV are called the *soft processes*, which constitute the majority of the nuclear reactions. Thus the reactions with $Q > 1GeV$ are *hard processes*, which are just a percent of the whole occurring reactions. It is worth mentioning that the strength of the interactions between quarks is inversely proportional

1. At the mass of Z^0 boson value of $\alpha(m_Z) = 0.118 \pm 0.002$, consequently $\Lambda = 217^{+23}$ [14]

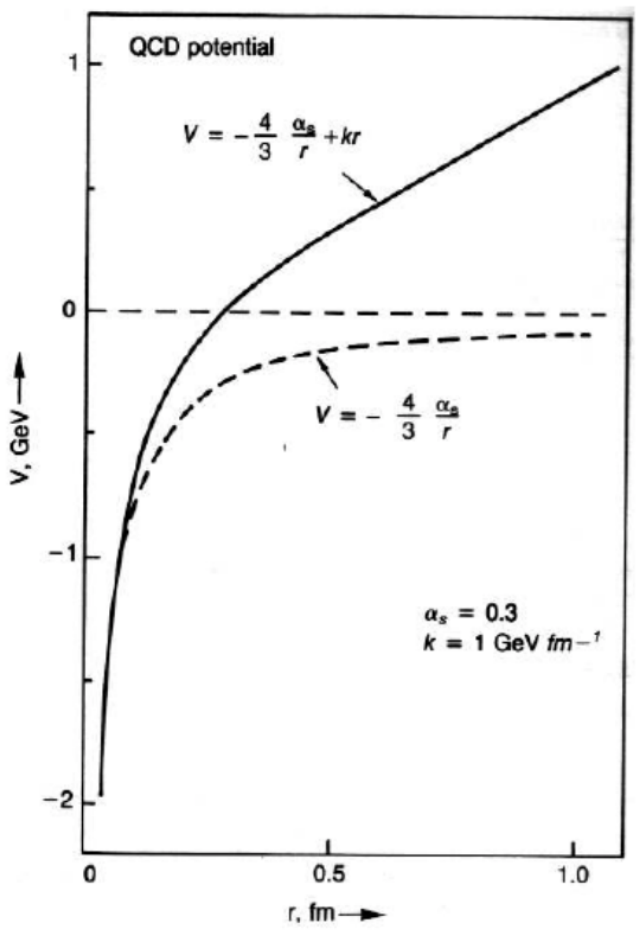

Figure 1.3 – QCD potential. The dotted line shows the short distance potential; the solid line includes the long distance potential [12].

to the momentum transfer: $r \propto \frac{1}{Q}$. As a consequence of the conservation of the coupling constant α_s two effects can be deduced:

Asymptotic freedom: phenomena of dissipation of the force acting on quarks where the distance between them decrease. At the asymptotically high Q^2 ($\rightarrow \infty$) the coupling constant $\alpha_s(Q^2) \rightarrow 0$, so at short distances (comparing to the radius of a nucleon), so the interactions between quarks and gluons are infinitely weak. Consequently, at high energies, quarks act like the "free" objects, not bounded. The predicted state where particles are in the asymptotic freedom and the system is in the thermal equilibrium is the strongly coupled *Quark-Gluon Plasma (QGP)*.

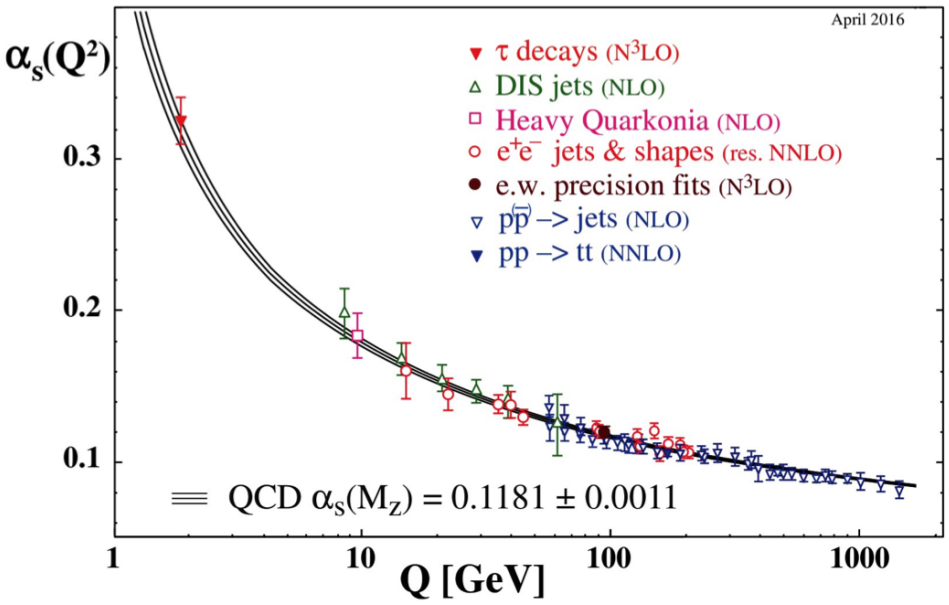

Figure 1.4 – QCD Coupling constant α_s dependence on the energy scale Q. The points refers to the pQCD calculations: NLO - next0to-leading order, NNLO - next-to-next-to-leading order, N^{3}NLO - next-to-NNLO [21].

Confinement of quarks: a state where quarks and gluons are bounded into hadrons. They are not expected to exist as separate particles. The energy per length of string is constant, so the energy required for the separation of partons is infinite. A simple example is meson which consists of two: quark and antiquark. As a consequence, quarks and gluons are bounded into hadrons and cannot exist as independent objects. Several models are explaining the production of new particles; one of them is the String model [22]. The string is an object: quark-antiquark, or quark-diquark, which is filled with the colour field. The energy of the string is proportional to the distance of separation. The string formation is based on momentum or colour exchange (depends on the model). If there is enough energy accumulated and the quarks are pulled apart, the string fragments. The newly created quarks and antiquarks immediately bound into hadrons [23].

There are two, main approaches to solve the Quantum Chromodynamics equations:

— *perturbative QCD*: used for $r \sim 1/Q$ and much lower the nucleon radius. The processes are *hard*, and it is possible to utilise the calculations similar for the QED.

— *non-perturbative QCD*: for large distances r and very small Q^2 ($\leq 1GeV^2$). It reports to the *soft* collisions. The calculations can be done based on the numeri-

cal calculation techniques on the space-time matrices called *lattice* or using phenomenological models (described in Section 1.2.4)

1.2 Relativistic heavy-ion collisions

To reproduce the Big Bang in the laboratory, heavy-ions are accelerated close to the relativistic speeds. As a result of their collision, a created system is described by the very high energy density where the two nuclei's energy is transformed into a fluid, so mainly into kinetic energy.

There are two possible scenarios of the system's evolution showed in Figure 1.5: one considers the Quark-Gluon Plasma (QGP) phase (right side) while the other one does not (left side). It is related to the energy of the collision and the reactions happening just after it. However, for low energies the QGP phase is not expected, at most the unbound state of quarks and gluons.

For the higher collision energies, the initial phase of the collision system is in the thermodynamic non-equilibrium *(pre-equilibrium)*, where the primary collisions occur, and the new matter is produced. Subsequently, the dynamics of partons (cascades) develop and the processes with low momentum transfer dominate. As a result of these interactions, after about 1 fm/c, the local equilibrium is reached. This state is called QGP. The system expands and cools. The so-called *chemical freeze-out* takes place where the inelastic interactions dissipate, and the chemical composition of the system is established - it reminds the hadronic gas. With the cooling, the particles stop to collide and exchange momentum - the *kinetic freeze-out*.

1.2.1 QCD Phase Diagram

As mentioned in Section 1.1.2, QCD is the theory of strong interactions. One of the crucial features of the theory is the self-coupling of gluons. It causes an increase of the coupling constant (α) with a decrease of momentum transfer, which gives rise to the phenomena of asymptotic freedom for high momentum exchange and confinement for low momentum exchange [24]. While confinement is responsible for all hadrons we observe in nature, the fundamental questions are (i) how a multi-parton system behaves at extremely high temperatures where the *deconfinement* regime is achieved and (ii) how and when the partons become bound into hadrons again. It is understood nowadays that

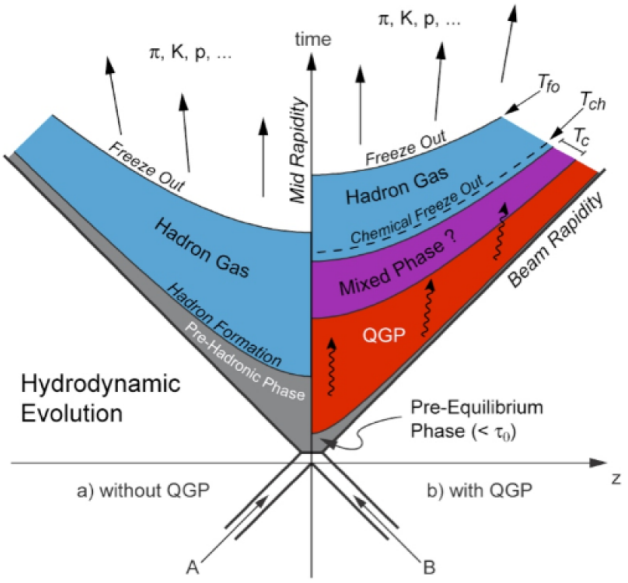

Figure 1.5 – Space-time system evolution created in the collision of ions: a) with the QGP creation, b) without QGP phase [23]

.

at the extremely high temperatures above 170 MeV the partons (quarks and gluons) are in a state of QGP.

The QCD phase diagram in Fig. 1.6 illustrates the phases of the strongly interacting matter at different temperatures T and baryochemical potentials μ_B. The baryochemical potential is the partial derivative of the internal energy on a number of the particles and entropy of the system:

$$\mu_B = \frac{\partial U}{\partial N}_{S,V=const} \tag{1.3}$$

This variable describes how internal energy will change if one baryon is added or subtracted. In the QCD Phase Diagram, μ_B can be interpreted as a measure of the imbalance between baryons and antibaryons in the system, so $\mu_B = 0$ MeV corresponds to equity between baryons and antibaryons and $\mu_B > 0$ MeV the advantage of the matter.

The QCD phase diagram is still not well-understood. The possible structure of it is shown in Fig. 1.6. Except for the two states of matter described before - hadronic matter and Quark-Gluon Plasma, there is a phase of colour superconductors in the diagram. It is a hypothetical state where the quarks are bounded into Cooper pairs, and then they condensate and create the phase analogical to the electrical superconductors. At very high densities, the preferred phase is the colour-flavour-locked (CFL) with the equal number of

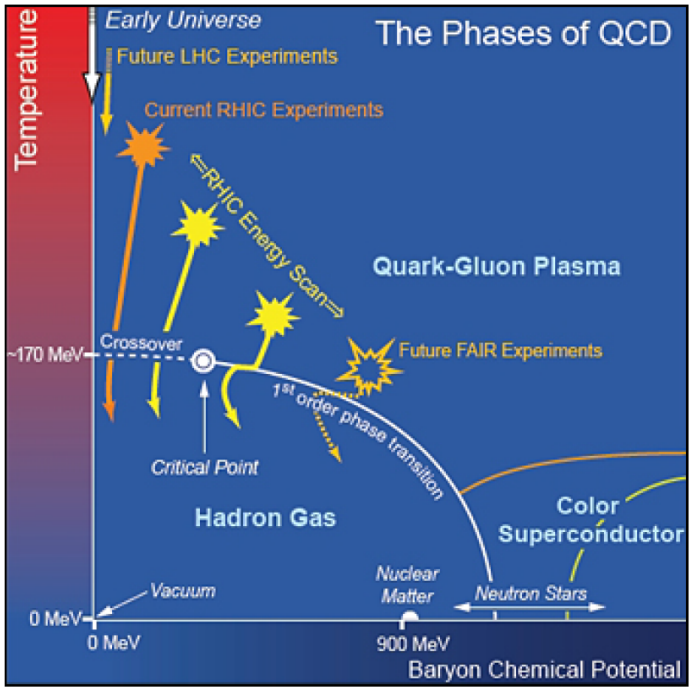

Figure 1.6 – Proposed structure of the QCD Phase Diagram of strongly interacting matter [23].

quarks u, d and s (in Fig 1.6 it is located under the yellow line). For example, in neutron stars, the superconductors are in the non-CLF phase with not an equal number of quarks u, d and s (phase between orange and yellow curve).

Depending on the μ_b between hadronic matter and QGP, there can occur various phase transitions:

— first-order phase transition: where the Gibbs Free Energy G is continuous while its derivatives do not; the entropy, volume, density, internal energy, enthalpy, baryonic and energy density change incrementally,

— second-order phase transition: G is continuous, its derivatives as well, but its second derivatives do not, the heat capacity and thermal expansion factor changes rapidly,

— "cross-over" transition: there are no discontinuities, but the parameters change drastically.

In the highest temperature and low μ_B region, the phase of matter changes via a “cross-over” transition. At the higher μ_B, the first-order phase transition is assumed to take place. Between those two cases, there is a so-called Critical Point (CP) which correspond to the second-order phase transition [25, 26]. Studies of the QCD phase diagram, the properties

of strongly interacting matter, and the phase transitions' nature are the vital parts of the Beam Energy Scan (BES) program [27].

In heavy ion (Au+Au) collisions at BES energies, the created matter is characterised by higher baryon density and lower temperatures than those obtained at the LHC. The program covers a broad range of collision energies, vital for precision studies of the phase transition between QGP and hadronic matter in different areas of its phase diagram. Colliding gold nuclei with precisely calculated energies gives a possibility to "scan" parts of the phase diagram, study the properties of matter, and pinpoint the possible CP location. The increase of the collision energy moves the system's thermalisation to higher T and lower μ_B. More horizontal shift on the phase diagram can be introduced colliding ions or nucleons with lower (more to the left side of diagram) or higher (oppositely) atomic mass.

1.2.2 Quark-Gluon Plasma

The QGP is the state of the matter characterised by thermal equilibrium, which exists at extremely high temperatures and densities, where the quarks and gluons are not confined. They can propagate in the whole volume occupied by the system. This state was predicted in the frame of QCD in the 70s. It is claimed that the QGP existed in the few milliseconds after the Big Bang. Nowadays, this state can be reproduced in high-energy experiments via collisions of ions.

Although in QGP, the quarks and gluons are not confined, the remnant interactions make it behave similarly to the dense liquid (plasma). It can be created via a) heating or b) squeezing the medium. Experimentally, squeezing is not possible, as well as heating with the external source. The increase of the temperature and density is gained via collisions of the atomic nucleus accelerated to the ultra-relativistic velocities.

The direct investigation of the QGP is impossible because it rapidly changes into the hadronic gas (after a few fm/s). Basing on the experimental measurements, one can study the signatures of the QGP, such as:

— direct photon production - prompt photons originating from the pQCD and thermal from QGP phase, interact weakly with the QGP, and they carry the information about the evolution of the system. The presence of QGP can be deduced in the investigation of the momentum spectra of direct photons. If there is a surplus of thermal photons over immediate ones, one can assume that the QGP phase took place. However, photons are produced rarely, and their identification is challenging, so this method is not highly effective. As the photons can also originate from the

decays, their identification is very complicated.

— dileptons production - similarly to photons, leptons interact with QGP weakly. Studies of invariant mass spectra of various leptons created in the p-p or p-Pb collisions prove that they originate from decays of mesons (ρ, ϕ, ω), while in collisions of Pb-Pb the surplus of produced leptons is disproportional to the size of the collided system. It is explained by the meson characterisation (mass, ratios of decay branches) modification happening during the QGP phase, which finally causes the increase of decays to the dilepton's channels. The surplus of leptons is proportional to the duration of the QGP phase.

— charm suppression - quarkonia (for example $c\bar{c}$, $b\bar{b}$) are produced at the beginning of the evolution of the system and originate from the lepton decay channels. In the presence of QGP, the colour charge of quarks is screened by other quarks and gluons (similarly to the Debye'a effect) so that the interactions between quarks $c\bar{c}$ are weaker, the dissociation of this pair takes place and the J/ψ($c\bar{c}$ particle cannot be produced (in other words: the freely moving colour charges "hide" the coupling potential $c\bar{c}$). The charm's suppression is studied in reference to p-p collisions or corresponding to the Drell-Yan effect.

— strangeness production enhancement - strange quarks produced at the freeze-out surface are less suppressed than originating from string decays. A vast number of strange particles can be treated as a signature of the existence of the QGP phase.

— elliptic flow - the flow of matter in the transverse direction in non-central collisions. More information in Chapter 2, in Section 2.3.

— jet suppression - jets strongly interact with QGP medium, and as a result, their energy relevantly decreases. The missing energy of the jet can state the existence of the QGP phase.

— inelastic (dynamic) fluctuations - for example, the fluctuations in the kinematic distributions or global characteristics (like average transverse momentum or multiplicity of the collision) are studied using event-by-event methods. Such fluctuations can be treated as a signature of QGP. Moreover, the significant increase of the fluctuation can be related to the Critical Point.

1.2.3 Equation of State

Equation of State (EoS) is the formula describing the states of the matter and its transitions. It expresses the relations between various parameters such as pressure, tem-

perature, energy density, speed of sound, and former. It is not trivial to characterise the whole phase diagram area. Consequently, such features of QCD as chiral symmetry breaking or confinement, are not fully understood.

The non-perturbative QCD is applied for the calculations of the dynamics of the matter at extreme densities and temperatures. For the description of the system where partons are expected to be in the deconfined state, the *lattice* calculations can be used. These are the numerical calculations performed on the discrete time-space grid [28]. The obtained EoS is derived from the first principles. It provides quantitative information on the deconfined state QGP and *cross-over* transition, the region of the QCD phase diagram characterised by the extremely high temperatures and low baryon chemical potential. In Figure 1.7 the relations between energy density/pressure and temperature are presented. The energy density rapidly changes at $T \sim 190$ MeV, which is caused by the rapid increase of the effective degrees of freedom. The pressure does not change that rapidly because during the strong phase transition, the speed of sound, expressed with $c_S = \sqrt{\partial P/\partial \epsilon}$, is reduced. At the extremely high temperature, the ϵ nearly reaches the value corresponding to the ideal massless gas limitation.

Although the full potential of Lattice calculations for QCD is increasing by applying more advanced algorithms and hardware technology [30], the region of the diagram at *non-zero* μ_B is still not completely understood. It is not possible to predict based on the first principles the existence and location of the CEP. In order to extend to the finite chemical potential, the Taylor series expansion in powers of μ_B/T [28, 31, 32] is applied to the Lattice calculations. The following equation can express the expansion of the pressure:

$$P(T, \mu_B) = T^4 \Sigma_n c_{2n}(T) (\frac{\mu_B}{T})^{2n} \tag{1.4}$$

the coefficients are:

$$c_n(T) = \frac{1}{n!} \left. \frac{\partial^n P/T^4}{\partial(\mu_B/T)^n} \right|_{\mu_B=0} = \frac{1}{n!} \chi_n(T) \tag{1.5}$$

where χ_n are *the susceptibilities of the baryon number*. However, only few of the expansion coefficients are known [33–35] and they do not allow to investigate the region of QCD phase diagram closer to CEP.

There are various attempts performed to generate the Equation of State, which will allow one to characterise the whole QCD phase diagram, starting from $\mu_b = 0$ finishing on cold neutron stars [36]. These EoS introduce the first-order phase transition for finite baryochemical potential and relatively lower temperatures - the region studied in the

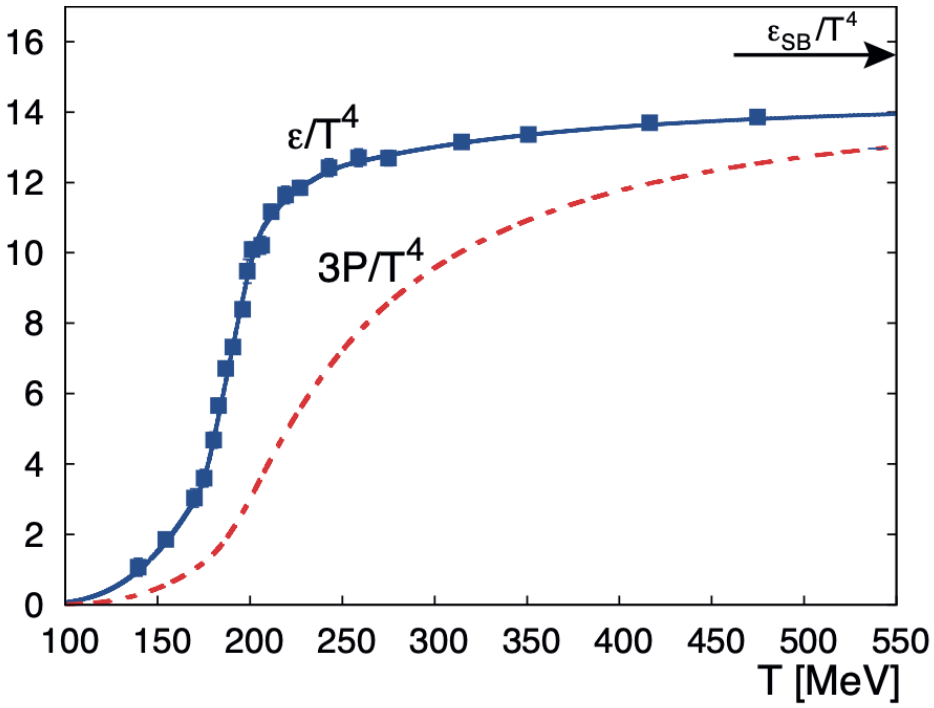

Figure 1.7 – Pressure $3P/T^4$ (dashed curve) and energy density ϵ/T^4 (solid curve) in function of temperature T from lattice calculations [29].

BES program. Nevertheless, some of them provide information about the Critical Point location and properties of this transition [30, 37]. One such EoS is described in Section 6.6.1.

Transport coefficients

To describe the state and dynamical properties of the expanding matter, one should investigate *the transport coefficients*.

The QGP is treated as a nearly perfect fluid [38], and its motion is described with hydrodynamics. Several parameters called *transport coefficients* are investigated to characterise the expanding bulk. The speed of sound c_S, which corresponds to the mechanical wave, is characteristic of the given state of matter. The *shear viscosity* η/s is expected generically to rise slowly above critical temperature (T_c - where the CP is expected), drastically below and has a minimum at T_c [39]. On the other hand, the *bulk viscosity* ζ/s peaks close to T_c, as a consequence of long-range critical correlations breaking the conformal symmetry [40]. It decreases on both sides of T_c, making the shear viscous effects dominate in given regions. Observation of the strong variations of bulk viscosity is expected close to CP.

However, it is impossible to measure transport coefficients directly in the experiment. They can be extracted from the real data, comparing them with the viscous fluid dynamical, phenomenological simulations.

1.2.4 Monte Carlo Event Generators

The processes occurring just after the collisions are incredibly complex. Although the experimental potential is high, and the applied technologies are extraordinarily sophisticated and precise, they do not allow one to follow each step of the created system's evolution. It is still impossible to detect single partons in the deconfined state and measure their properties directly. The particles identified in the experiment already hadronised and cooled.

Multiple theories are describing the properties of strongly-interacting matter created in the collision. To reproduce such scenarios, various MC Event Generators are created [41, 42]. These are the computer software that simulates the states and dynamics of the medium according to the given theory. The random number generators and MC methods are applied. For the soft interaction (low momentum transfers), the phenomenological

models are incorporate, while in the case of hard processes, the perturbative solutions are utilised.

1.3 Heavy ion collision characterization - concepts and definitions

The most important definitions and concepts for these studies are outlined in this subsection: firstly, these corresponding to the collision characterisation, then related to the particle dynamics.

1.3.1 Collision Geometry

The accelerated to the relativistic speeds nuclei appear as flat discs (depending on the collision energy) due to the Lorentz contraction along the beam directions, referring to the centre of mass (CM) frame (left part of Fig. 1.8). If A is the atomic mass number of the nuclei, the transverse radius can be estimated as $R = 1.2A^{1/3}$. During the collision, the incoming nuclei do not overlap completely. The quantity called *centrality of the collision* describes how big is this overlap region. The systems where the collisions are "head-on", and these more peripheral are relevantly different (Fig. 1.9). The *eccentricity* (ϵ) is the parameter describing the distortion from the round overlap region of collided nuclei. Higher values of ϵ correspond to more peripheral collisions.

To characterise the newly-created matter, one needs to categorise the *centrality* of the collision. There are several ways to extract information about the overlap region's size and finally classify the given event. Centrality definition is crucial in the studies of the system's evolution as the dynamics of the matter depends on the number of participants or the size of anisotropy in the overlapping region.

There is an *impact parameter* $\boldsymbol{b}$ introduced, which is equal to a shorties distance between the centres of the collided nuclei, measured in the moment of the nucleus overlapping (left part of Fig. 1.8). The smaller b, the more central collision is. However, it is impossible to measure it directly in the experiment. On the right side of Fig. 1.8 the particles' classification is presented. The nucleons which take part in the interactions occurring during the collision are called *participants*, while these which continue unaffected - *spectators*.

Assuming that the multiplicity of particles is a monotonic function of $\mathbf{b}$, in the experiment, the information about the centrality of the collision can be extracted, for example,

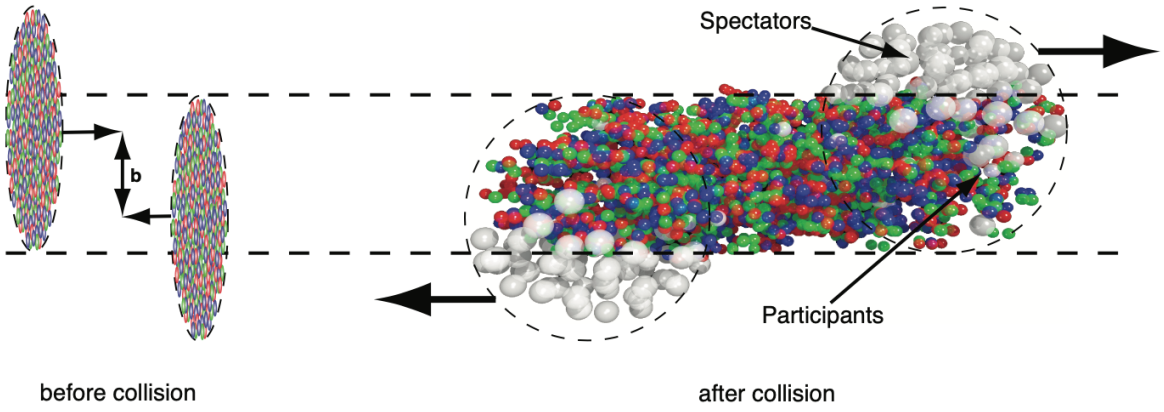

Figure 1.8 – Left: Approaching ions just before the collision, impact parameter ***b***, Right: Participants zone, where the new matter is created and unaffected spectators [43]

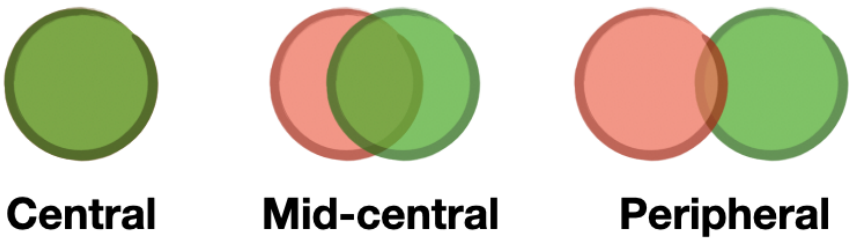

Figure 1.9 – Three heavy-ions collisions: central, midcentral and peripheral (This thesis)

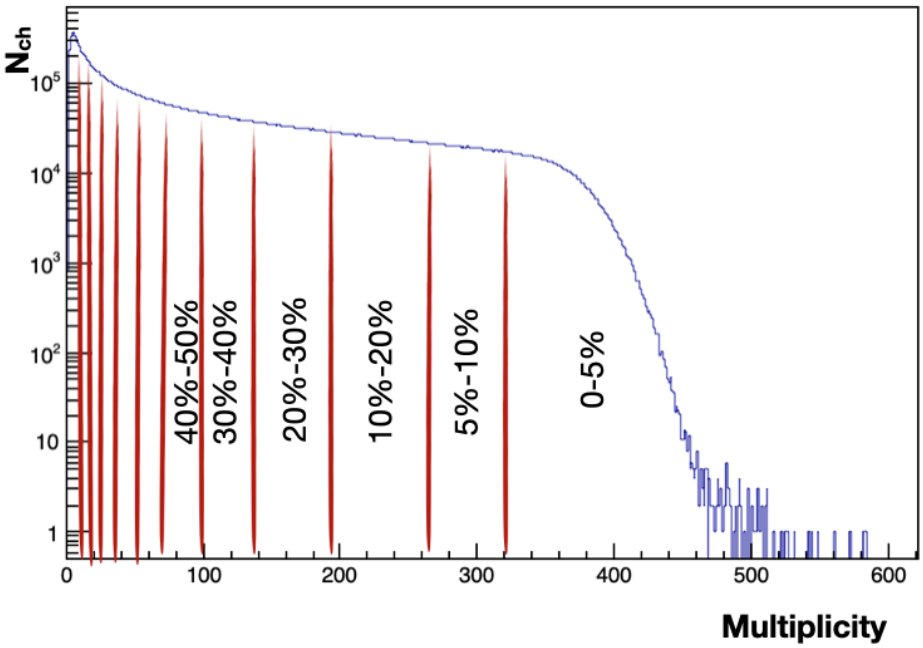

Figure 1.10 – The charged particles distribution measured at STAR experiment for Au+Au collisions at $\sqrt{s_{NN}} = 39$ GeV with drawn lines corresponding to the centrality division (This thesis)

using the distribution of the detected charged particles (Fig. 1.10). The more particles are measured, the more central the collision is.

As the shape of the overlap region is ellipsoidal, consequently, such anisotropy is transferred to the anisotropy in the emission of the created particles (Fig. 2.1).

1.3.2 Reaction and participant plane

In the studies of the anisotropies in the created matter dynamics, the coordinate system's choice is crucial. The same definition of the reference plane for the direction of the particle motion measurement has to be established to investigate all collisions. There are two possible choices: *reaction* and *participant plane*.

Reaction plane (Ψ_{RP}) - expanded between beam direction and impact parameter. As the impact parameter cannot be directly measured, the reaction plane angle cannot be derived straight from the experiment. It is estimated from the event-by-event azimuthal particle distribution.

Participant plane (Ψ_{PP}) - can differ from the reaction plane as the distribution of

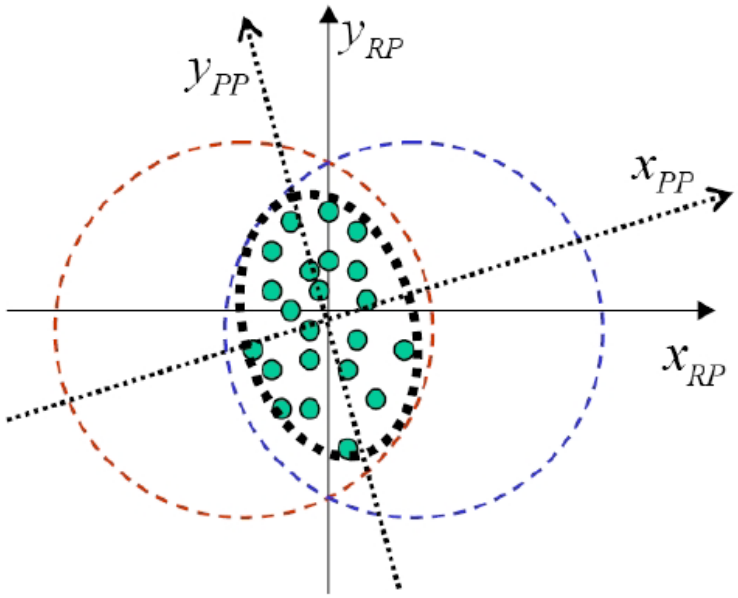

Figure 1.11 – The reaction and participant planes coordinate systems [38].

participants is not uniform in the overlap region.

Both systems are illustrated in Fig. 1.11. It is relevant in flow measurement to distinguish between these two coordinate systems.

1.3.3 Kinematics

To characterise the kinematics of the matter, the coordinate system needs to be established. At RHIC, the z-axis is parallel to the beam axis, x- and y-axes form the plane perpendicular to the z-axis, while y-axes points vertically up. Although the prime interaction point is located at $(0, 0, 0)$ - coordinate, it does not necessarily correspond to the place of the collision. The primary vertex (position of the collision) has to determined.

1.3.4 Energy of the collision

In the CM frame the energy of the collision is calculated using the beams 4-vector $E(E, 0, 0, p_z)$:

$$E_{CM} = \sqrt{(2E)^2} = 2E \tag{1.6}$$

The CM energy per nucleon pair is denoted as $\sqrt{s_{NN}}$.

1.3.5 Transverse momentum

A particle's measured momentum is decomposed to vectors corresponding to x, y, z direction. However, due to particles' relativistic motion, the Lorentz invariant variables are introduced, such as the transverse momentum. It can be expressed with following:

$$p_T = \sqrt{p_x^2 + p_y^2} \tag{1.7}$$

1.3.6 Rapidity

The momentum component parallel to the z-axis is rarely used, contrarily to the additively invariant under Lorentz transformations variable called *rapidity*. Rapidity is defined as:

$$y = ln[\frac{1}{2}\left(\frac{E + p_z}{E - p_z}\right)] \tag{1.8}$$

1.3.7 Pseudorapidity

To determine the rapidity of particle the particle mass has to be known. The variable which may be used in the charaterization of the direction of the particle's motion is *pseudorapidity*:

$$\eta = -ln[tan\left(\frac{\theta}{2}\right)] \tag{1.9}$$

where $tan(\theta) = \sqrt{x^2 + y^2}/z$. For the determination of η only the (x, y, z) coordinates needed; consequently, the information about the particle's momentum is not required. For particles with mass relevantly smaller than momentum, the energy $E = \sqrt{m^2 + p^2} \to p$, therefore $y \to \eta$.

Chapter 2

Azimuthal anisotropy in heavy-ion collisions

The heavy-ion collisions are invaluable for creating and investigating nuclear matter, dynamics, and phase transitions. Similarly to the early stages of the universe, the collision's newly-created, dense and extremely hot system will cool down and expand. The obtained medium goes through various phases changing its energy densities and temperatures, while quarks and gluons experience multiple interactions forming the QGP (if it is created). It expands collectively and finally becomes dilute enough to hadronise. Such collective expansion is named *flow*. Studies of flow have a relevant contribution to the experimental studies of EoS and transport properties of QGP. The particles are not produced uniformly in all directions. Such anisotropy is one of the most significant experimental signatures of the presence of flow in the system obtained in heavy-ion collision [38, 44–46]. Studies of this observation are crucial because anisotropies in flow are highly sensitive to the system properties at the first moments of its evolution - the spatial asymmetries immediately decrease. The flow can be built only during the first fm/c of the system's lifetime. In Fig. 2.1 the non-central collision is illustrated. Part of the ions passes by leaving the ellipsoidal overlap region. This anisotropy in the shape of the collided matter bulk results in the anisotropies in the final-state observables.

2.1 Source of collective flow

The azimuthal anisotropy characterises the expansion of highly-compressed matter created in non-central heavy-ion collisions. It is one of the most significant observables used in studies of hot and dense matter. The process of creation of collectivity can be described in several stages:

— During the non-central collisions, the shape of the overlapping nucleus in the beam axis direction resembles an almond or an ellipse.

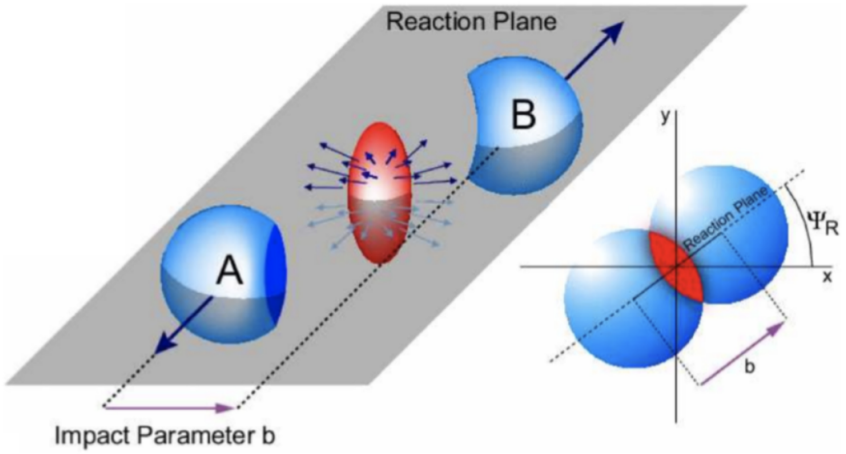

Figure 2.1 – Heavy-ion collisin with depicted overlap region and reaction plane. Drawn by Thomas Ullrich

— The newly created gradient of density is transformed into the pressure gradient via interactions such as hadron or parton scattering.
— After thermalisation, pressure on the almond's external surface vanishes and reaches the maximum inside of it, showed in Fig. 2.2 (pressure is related to the energy density). The gradients are higher in perpendicular to the beam direction.
— Consequently, particles in transverse direction have higher acceleration and, therefore, higher flow velocities in-plane.
— The final result of the differences in values of gradients of pressure and scattering is the anisotropy in production and motion of the newly-created matter.

In Figure 2.2, the evolution of the initial transverse energy density profile is illustrated. The expansion of the almond-shaped system and buildup of the collective motion is governed by sound velocity (c_s) [1]. It is a significant feature because it varies between different EoS (see Section 1.2.3).

Once it was realised that the ideal hydro does not describe the system's evolution correctly, the corrections for the viscous effects were taken into account [39, 48–50]. The *shear viscosity* ($\frac{\eta}{s}$) term was introduced. It defines how "imperfect" fluid is [2]. Since then, it became an interesting probe in studies of the EoS (left panel of Fig. 2.3).

1. c_s - distance traversed per unit of time by a sound wave propagated through an elastic medium.
2. In the case of a perfect fluid, the kinetic energy of the flow is not transformed into heat and has low viscosity

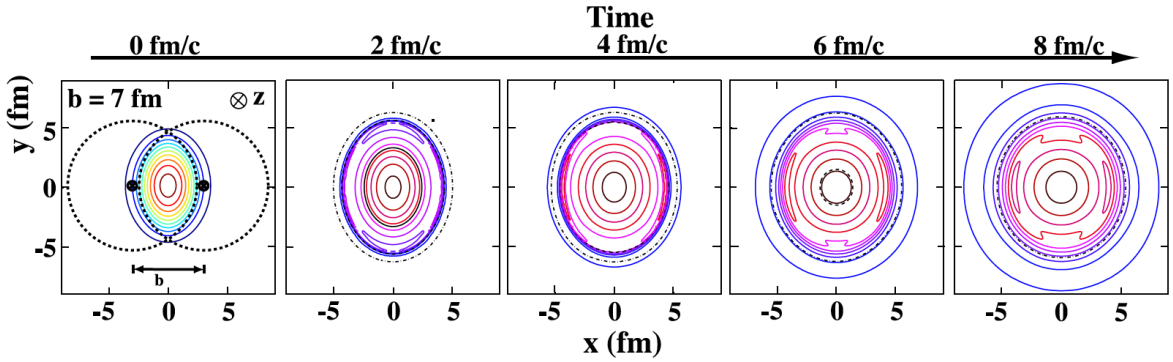

Figure 2.2 – The evolution of the initial transverse energy density profile of the system created in non-central heavy-ion collision. The x-axis is defined by the parameter b and z-axis goes along the beam direction [47].

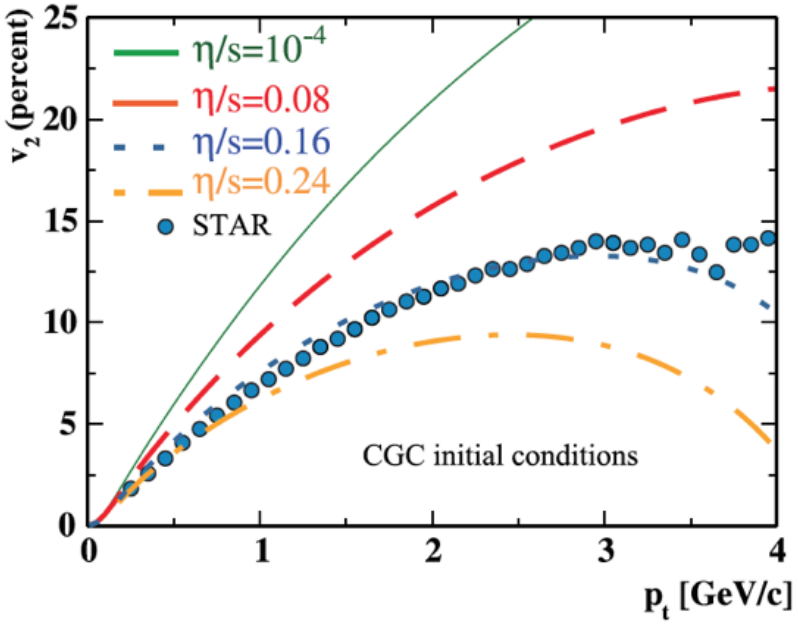

Figure 2.3 – Elliptic flow in function of transverse momentum dependence on shear viscosity over entropy of charged hadrons compared with STAR experimental data [43, 48]

Consequently, the shape of the measured flow is dominated by two effects illustrated in Figure 2.4 (valid for $n > 1$):

— for high multiplicities it origins from eccentricity ϵ_n

— at more peripheral collisions the shear viscosity dominates, which is inversely proportional to the number of participants.

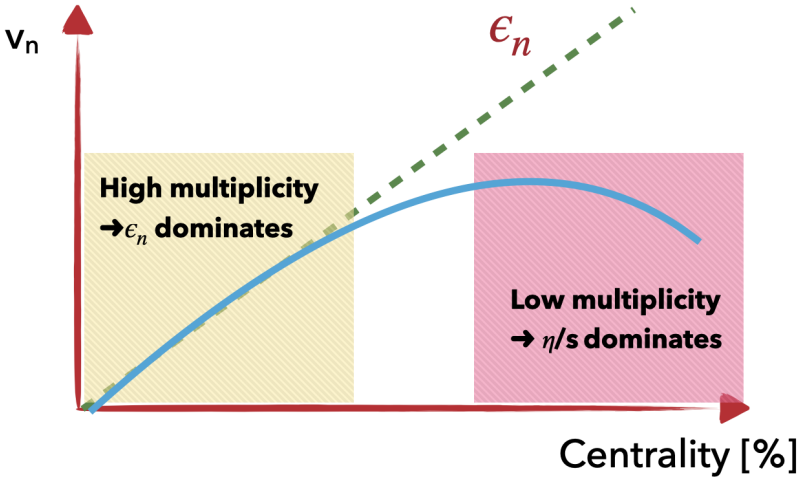

Figure 2.4 – The illustration of the relations between various effects dominating the creation of flow in function of centrality of the collision. (This thesis)

2.1.1 Non-flow contribution

The measured azimuthal correlations between particles also include contribution not solely originating from anisotropic flow, referred to as *non-flow*. These are correlations of particles not associated with the characterisation of the matter's dynamics in reference to the reaction plane. The most notable non-flow contributions correspond to such effects as jets, resonance decays, short-range correlations (Hanbury-Brown Twiss or momentum conservation) [51, 52]. There are few methods proposed to suppress non-flow, although it is problematic to estimate its contribution quantitatively into performed measurements. For example, considering the rapidity gap between correlated particles or various charge combinations of them. In two-particle correlations studies non-flow can by quantified by δ_n parameters:

$$\langle \cos[n(\phi_i - \phi_j)] \rangle = \langle v_n^2 \rangle + \delta_n \tag{2.1}$$

The non-flow contributions are the effects mainly concerning more than one particle, the δ_n is nearly inversely proportional to the multiplicity.

To suppress the not negligible non-flow, one can use the methods based on the multi-particle correlations. Although they are almost insensitive to non-flow, they are biased by the interference of several flow harmonics [53]. The various methods of measurements of azimuthal anisotropy are affected differently by non-flow.

Short-range correlations are characteristic for pairs of particles with similar η. In order to suppress this contribution of non-flow, the difference between pseudorapidity of particles is ensured by introduction of $\Delta\eta$. In Figure 2.5 the ratio of measured $v_2\{2\}$ with $\Delta\eta_1 = 0.0$ and 0.3 to $v_2\{2\}$ with $\Delta\eta_2 = 0.6$ for Au+Au collisions at $\sqrt{s_{NN}} = 200$ GeV as a function of centrality is presented. The higher value of minimal difference in particles' η, the more non-flow contribution is eliminated.

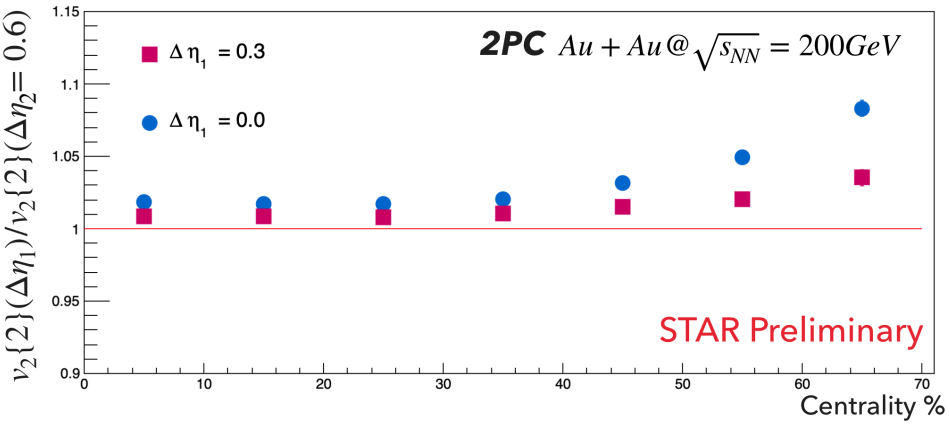

Figure 2.5 – Ratio of the centrality dependent $v_2\{2\}$ with $\Delta\eta_1 = 0.0$ and 0.3 to $v_2\{2\}$ with $\Delta\eta_2 = 0.6$ for Au+Au collisions at $\sqrt{s_{NN}} = 200$ GeV. The transverse momentum range: $0.2\text{GeV/c} < p_T < 4.0\text{GeV/c}$ [4]

2.1.2 Flow fluctuations and initial eccentricity

Even on the fix impact parameter one can observe the event-by-event fluctuations of flow in magnitude and direction. The *flow fluctuations* can be expressed by [38]:

$$\sigma^2_{vn} = \langle v_n^2 \rangle - \langle v_n \rangle^2 \tag{2.2}$$

The geometry of the *participant zone* can variate in both the eccentricities ε_n [3] and the direction of the major axes (Fig. 1.11). The Figure 2.6 shows the various ε_n with corresponding shapes.

3. ε - parameter characterizing the shape of conic ($\varepsilon = 0$ - circle, $\varepsilon > 0 \& \varepsilon < 1$ ellipse, etc.)

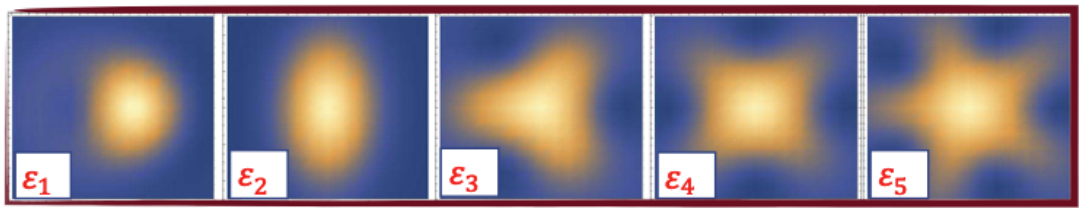

Figure 2.6 – Eccentricities ε_n with the corresponding participant zone shape [54].

It is challenging to identify the fluctuations. However, higher-order cumulant measurements $(v\{n\}, n \geq 4)$ are not sensitive to both non-flow and fluctuations of eccentricity. They are precisely equal to $v_{2,RP}$ - the flow projection on the reaction plane. Simultaneously, due to a lack of possibility of separating the non-flow contributions from flow fluctuations through correlation measurements, the participant plane cannot be measured [55].

2.2 Flow harmonics

The azimuthal distribution of particles is anisotropic in reference to the reaction plane. It can be expressed by the Fourier decomposition, where each of the coefficients reports to the shape of the matter flow: v_1 - directed flow, v_2 - elliptic flow (see Fig. 2.7), v_3 - triangular flow [43]:

$$E\frac{d^3N}{d^3p} = \frac{1}{2\pi}\frac{d^2}{p_T dp_T dy}(1 + \Sigma_{n=1}^{\infty} 2v_n cos(n(\phi - \Psi_{RP}))) \tag{2.3}$$

where:
N - number of particles, n - denotes the harmonic ϕ - azimuthal angle, Ψ_{PR} - reaction plane angle.The sinus terms are absent as a result of symmetry with respect to the Ψ_{PR}.

The flow harmonic coefficients v_n are influenced by eccentricities ε_n, fluctuations, system size, speed of sound $c_s(\mu_B, T)$ and transport coefficient $\frac{\eta}{s}(\mu_B, T)$. Investigation of these parameters gives unique information about the states of the matter obtained during the evolution of the system (more in Section 1.2.3).

2.2.1 Directed flow

The hot and dense matter is created in the overlap region of the collision, and it deflects the remaining nuclear matter (see Fig. 2.8 and 2.9). The spectators in the positive

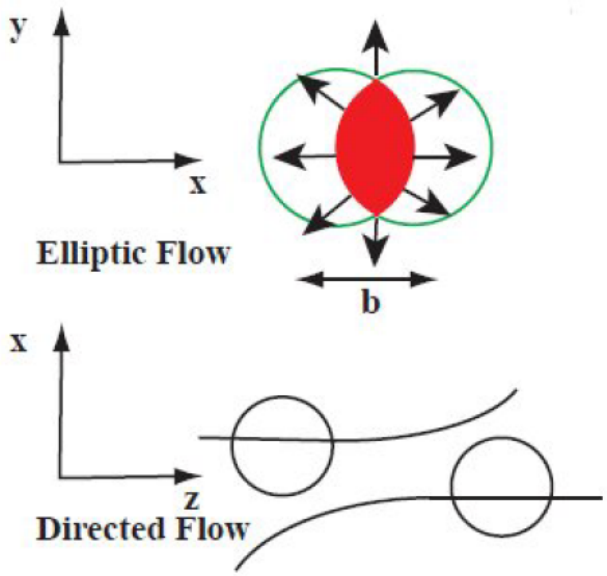

Figure 2.7 – Illustrations of directed and elliptic flow [38].

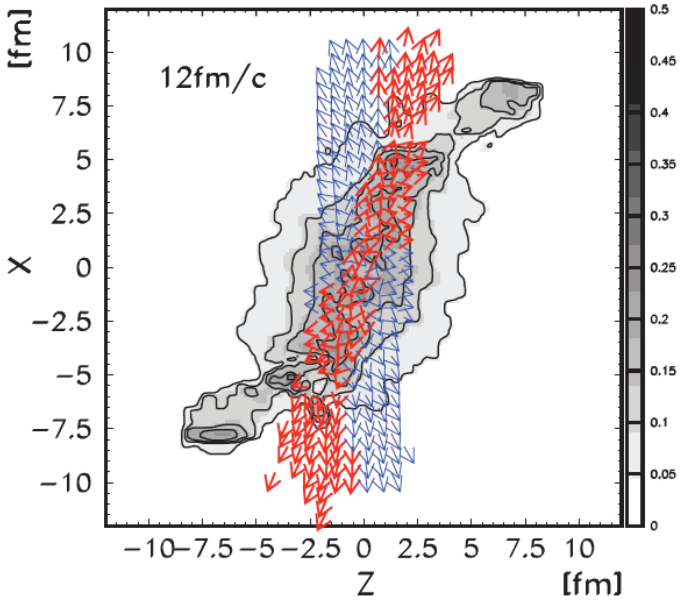

Figure 2.8 – The net-baryon density in the reaction plane ($\tau = 12fm/c$), the velocity arrows at $|y| < 0.5$ corresponds to fluid elements of anti-flow - thin arrows and normal flow - bold arrows [56]

rapidity part are deflected to $+x$ direction, so $\langle p_x \rangle > 0$ and oppositely the remnants from negative rapidity are pushed to $-x$ with $\langle p_x \rangle < 0$. This process occurs during the whole time of the collision of heavy-ions. Consequently, the deflection is the excellent probe of the compressibility of the new matter. At low energies such as obtained at AGS, the directed flow is the leading mechanism and nearly linearly depends on the rapidity. On the other hand, at higher energies (top RHIC and LHC), the linearity of directed flow is predicted to break; the so-called "wiggle" can be created - the directed flow in the function of rapidity switches the sign three times (Fig 2.8). It can originate from various physical mechanisms, such as the QGP phase's presence in the created system's evolution. It can be treated as a signature of the QGP phase transition [38, 57].

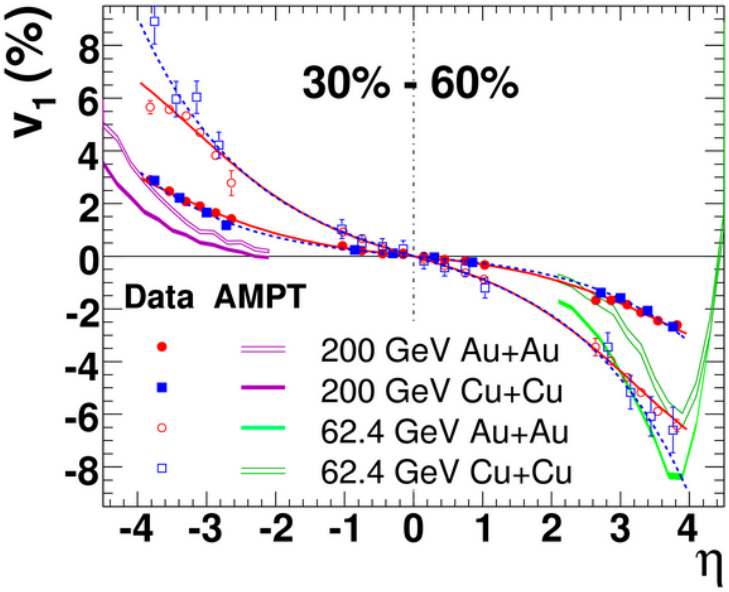

Figure 2.9 – System dependence of directed flow $v_1(\eta)$ measured at STAR experiment for mid-central (30%60%) Au+Au and Cu+Cu at 200 GeV and 62.4 GeV [57].

STAR conducts extensive studies in the broad range of the collision energies and systems of the directed flow in the function of rapidity [58, 59]. The most intriguing results are observed for protons and antiprotons. The significant differences between v_1 of these particles are present for all studied energies for Au+Au collisions, while in the case of pions, this dissimilarity is negligible. The increasing difference oppositely to the collision energy can be explained by the interplay between the v_1 of p related to the baryon number originating from the initial beam rapidity and transported close to the mid-rapidity region, and protons' v_1 coming from the particle-antiparticle pairs created

in the vicinity of the mid-rapidity.

2.2.2 Elliptic flow

The second harmonic of the Fourier decomposition corresponds to the expanding matter's elliptical shape - v_2. It depends mainly on the initial geometry, so the size of the overlap region of the collided nuclei. However, the tiny v_2 signal is also observed for central collisions, which is explained by the fluctuation in the initial state of the occurring processes. The strength of the elliptic flow signal gives information about the differences between particle yields in the direction "in-plane" and "out-of-plane".

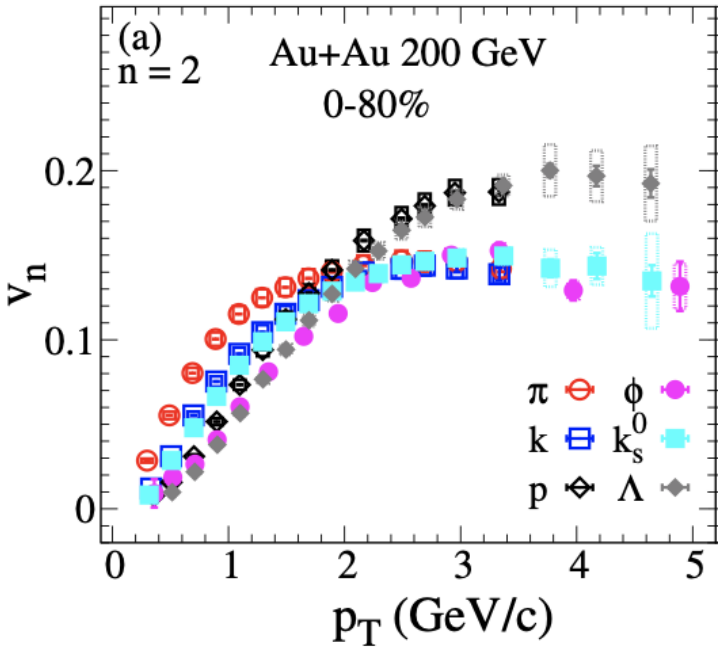

Figure 2.10 – $v_2\{2\}$ p_T-differential of identified hadrons for Au+Au collisions at $\sqrt{s_{NN}} = 200$ GeV. Part of the article which is now under review in STAR Collaboration (as a Primary Author)

2.2.3 Triangular flow

In simple models, all odd ε_n coefficients vanish because of symmetry $((\phi)\&(-\phi)$ or $(\phi)\&(\phi+\pi))$[60], whereas in a realistic event-by-event treatment, the fluctuations break this symmetry. They can originate inter alias from (Fig. 2.11):

— the shape of the incoming nuclei
— the interaction mechanism
— distribution of binary collisions and the degree of formalization [61].

The fluctuations strongly affect the observables of the QGP.

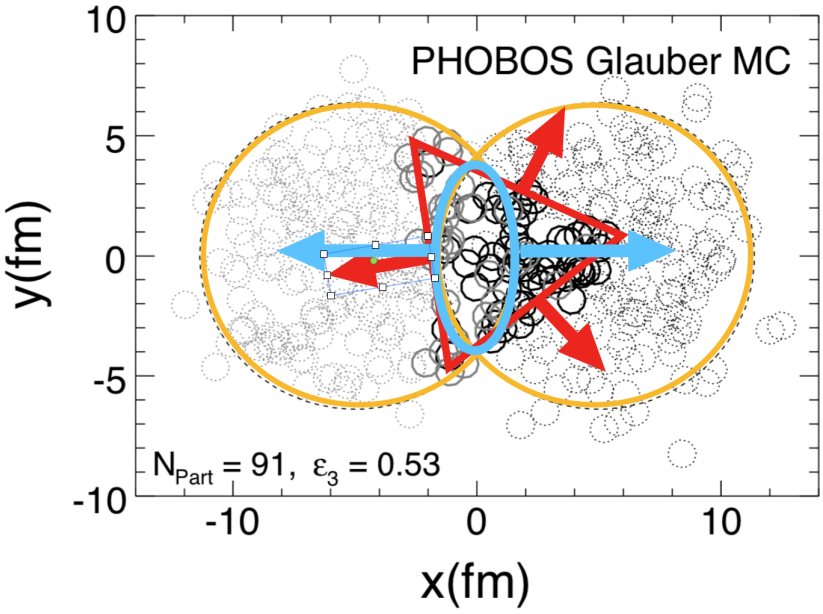

Figure 2.11 – Distribution of nucleons on the transverse plane for a $\sqrt{s_{NN}} = 200$ GeV Au+Au collision event with $\epsilon_3 = 0.53$ from Glauber Monte Carlo. The nucleons in the two nuclei are shown in gray and black. Wounded nucleons (participants) are indicated as solid circles, while spectators are dotted circles [62]. For the better visualization with the yellow color the collided ions are selected, with blue the ellipsoidal area corresponding to ϵ_2 and with red triangular - ϵ_3.

The third coefficient of the Fourier decomposition of the flow arises from event-by-event fluctuations (Section 2.1.2). It leads to a triangular anisotropy in azimuthal particle production through the collective expansion of the medium. It is also very sensitive to the viscosity of expanding medium [62]. What is more, it has been proven not to be dependent on the size of the system (Fig. 2.12)[63]. The triangular flow clarifies the fluctuations and viscous effects, while the measurements of v_2 are dominated by other components (already mentioned initial eccentricities).

The study of v_3 in the collision energy function provides information about the changes of transport coefficients in various points on the phase diagram. As a consequence, it becomes a unique tool in the investigation of matter transitions.

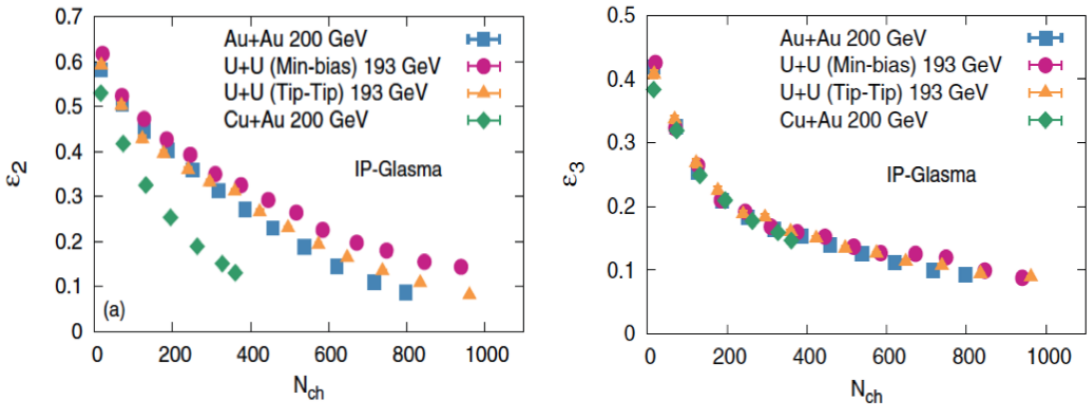

Figure 2.12 – ϵ_2 and ϵ_3 dependence on the system size [63]

Transverse momentum dependence

The evolution illustrated in Figure 2.2 underlines the initial dynamics' dependence on the motion in the transverse direction.

The Figure 2.10 presents the results of measurements of elliptic flow of various particles' species collected at STAR experiment in the Au+Au collisions at $\sqrt{s_{NN}} = 200$ GeV. The so-called *mass ordering* is visible up to $p_T = 2$ GeV/c. It means that the lighter particles exhibit higher elliptic flow for the given p_T range than heavier protons. For the intermediate transverse momentum (i.e. $2.0 < p_T < 5.0$GeV/c) particles are dividing into two groups: mesons (quark-antiquark) and baryons (3 (anti)quarks) (see Fig. 2.10). It is explained by the interplay between elliptic and radial flow, which strongly affects the particle spectra and by the shift of the heavier particles to higher p_T. Consequently, the more extensive depletion of spectra is achieved for the directed along with the symmetry plane values of p_T. As the elliptic flow expresses the relative difference between yields of particles in-plane to the out-of-plane, so described processes reduce that flow. Finally, the mixture of these components makes the v_2 higher with decreasing mass at a lower p_T. Consequently, the studies of the flow in the function of p_T and particle mass are excellent probes in investigating the relations in the dynamics creation of the matter and EoS.

2.2.4 Beam energy dependence

The anisotropic flow originates from the eccentricity-driven hydrodynamic evolution of the system. Consequently, measurements of this quantity are sensitive to the initial-state

geometry and EoS or transport properties of the medium. Accordingly, investigation of anisotropic flow is at the forefront of ongoing studies of T and μ_B dependence η/s, which is substantial transport coefficients in search of the matter transitions. The BES program gives the possibility to perform such studies as a function of beam energy providing the unique opportunity for understanding the relations between these quantities.

In [64] authors suggest that the related with T and μ_B, η/s could have a minimum at the CP vicinity. In Fig. 2.13 the good agreement of theoretical calculations of azimuthal flow from [65] with the experimental data is shown. In these computations, the η/s increases with the lowering of the collision energy but is constant for the whole process of the fireball evolution at given $\sqrt{s_{NN}}$. Accordingly, the studies of v_n as a function of beam energy give substantial constraints into the theoretical studies of relations $\eta/s(T, \mu_B)$

In higher energy collisions, the partonic phase is longer and consequently, the hadronic contribution to the elliptic flow is reduced. Figure 2.14 shows the elliptic flow's dependence on the collision energy. The apparent continuous increase from RHIC to LHC energies is visible. In the case of much cooler systems (lower collision energy), the matter is more trapped inside the created bulk and squeezed-in what results in negative elliptic flow - the push in out-of-plane direction is more substantial than in-plane one.

2.2.5 Collision Centrality

The flow measurements as a function of the centrality give direct information about the relation between eccentricity and the anisotropy in the matter expansion. The collided system's initial geometry is influenced by the eccentricity and distribution of nuclei in the overlap region. The flow originates from the anisotropies in initial geometry, so it should proportionally increase with the eccentricity. As it is directly related to the collision's centrality, the v_n is expected to be proportional to the number of charged hadrons N_{ch}. However, as mentioned before, the QGP is not *a perfect fluid*, but the viscous one. The effects of the viscosity dominate the low multiplicity events, which result in lowering the flow. While in the most central collisions, the created flow is mainly dominated by the eccentricity, so the N_{ch} as illustrated in Figure 2.4.

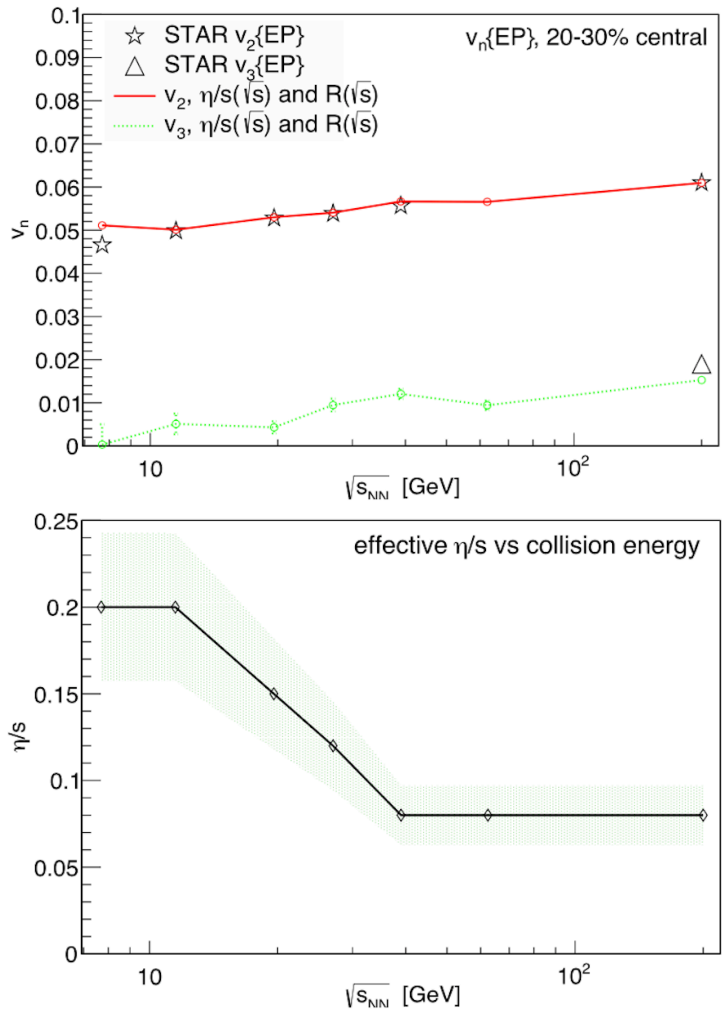

Figure 2.13 – The left panel: p_T integrated $v_2, 3$ coefficients vs. $\sqrt{s_{NN}}$. The $\sqrt{s_{NN}}$ dependent η/s. The experimental data from the STAR collaboration [66]. The right panel shows the effective values of η/s used to describe the experimental data at different collision energies. The green-band represents lines represents the results obtained using the estimated uncertainty [65]

2.3 Coalescence and NCQ-scaling

Particles can be created in the process of coalescence [4] of some primordial particles. Their distributions are expected to reflect the distributions of the primordial ones. If this process does not have relevant influence on the distributions of original particles, basing on the coalescence probability B_A the following formula can be applied for the nucleon

4. Coalescence in high energy physics is the process where two or more particles merge during contact to create a single daughter particle [68].

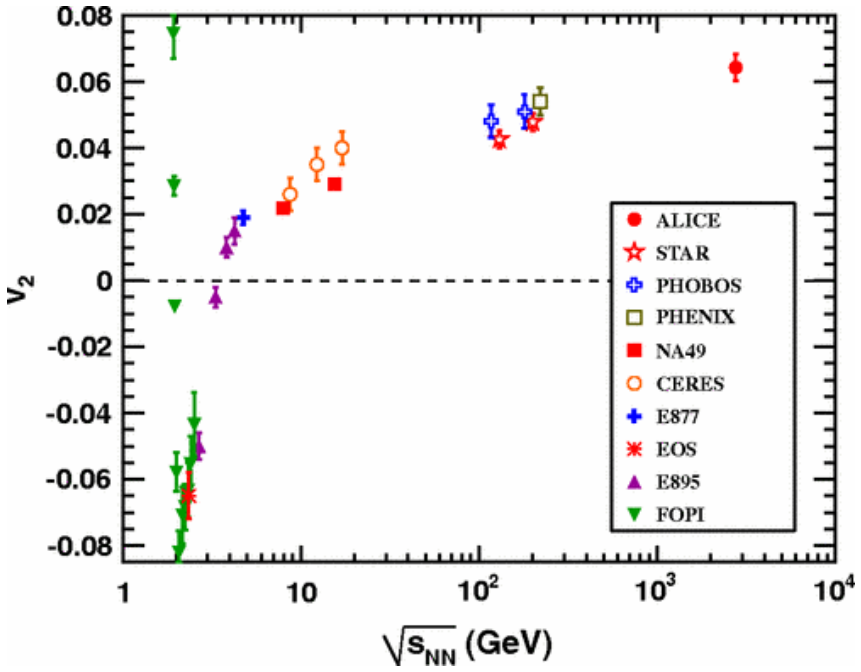

Figure 2.14 – Comparison of integrated elliptic flow in the centrality classes similar to $20-30\%$ in function of collision energy [67]

coalescence into light nuclei with A as an atomic number [38]:

$$\frac{E_A d^3 n_A}{dp_A} = B_A \left(\frac{E_p d^3 n_p}{d^3 p_p} \right)^A \tag{2.4}$$

If one focuses on the momentum distribution and neglect the possibility of the anisotropy in the spatial distribution, they can conclude that the nuclei A distribution 2.4 gets less uniform. Consequently, there can be found, such flow scaling relation:

$$v_{n,A}(p_{T,A} \approx A v_{n,p}(p_{T,A}/A) \tag{2.5}$$

A few collaborations like E877 [69] (at AGS), or PHENIX [70] and STAR [71] (at RHIC) made an observation that deuterons' flow are indeed consistent with the coalescence model predictions. In [38] author states that the *constituent quark* coalescence is relevant in the process of production of particle at the intermediate p_T.

Experimental studies were performed at RHIC [72, 73] and were treated as proof of the QGP phase's presence. Nowadays, many physicists argue about that. STAR showed in [73] that at the intermediate p_T ($\sim 2-4$ GeV/c) the significant scaling with the number

of constituent quarks (NCQ) is kept for both mesons and baryons. In the smaller scale by similarity to the light nucleons, it is assumed that if the hadrons are created via coalescence of constituent quarks, their particle yields would be proportional to the quark density to the power equivalent to the Number of Constituent Quarks (NCQ) forming the given hadron. As a result of the intensified production of particles in this intermediate p_T region, one can conclude that the elliptic flow can also be scaled with NCQ: $v_2(p_T) \approx nv_2(p_T/n)$ (where n correspond to ncq of baryon $n = 3$ or mesons $n = 2$) [74]. If the probability of the coalescence is small such scaling equations can be applied for the identified hadrons (first one for mesons, second for baryons):

$$\frac{d^3n_M}{d^3p_M} \propto [\frac{d^3n_q}{d^3p_q}(p_q \approx p_M/2)]^2 \text{ and } \frac{d^3n_B}{d^3p_B} \propto [\frac{d^3n_q}{d^3p_q}(p_q \approx p_B/3)]^3 \tag{2.6}$$

where: n_q correspond to the given quark, and p_q to its momenta. Indexes M -meson, and B - baryon. Although the violation of scaling can be present for lower p_T, it does not guarantee that the hadrons are not formed by the process of coalescence in this region. It can be caused by the break down of the formulas 2.6 describing the mechanism of coalescence. In Figure 2.15 there are results published by STAR collaboration showing the test of the NCQ-scaling of the v_2.

Anisotropic Flow Measurements at STAR in the frame of BES

BES I is the first phase of a scientific program run at RHIC completed in 2011. It is based on Au+Au collision data collected in 2010-2014 at $\sqrt{s_{NN}} = 7.7$, 11.5, 14.5, 19.6, 27, and 39 GeV. This was complemented by earlier 62.4, 130 and200 GeV and later 54.4 GeV collected data sets [76]. There are four physical goals:

— search for the vanish of the signatures of the QGP
— search for the possible first-order phase transition
— search for the possible CP
— investigate the transport properties of the strongly interacting matter as a function of T and μ_B [77–80].

The important observations made in this program's frame are related to the anisotropies in flow of the matter. Several of them are described and discussed in this Section.

In Figure 2.16 the v_2 dependence on p_T measured using four-particle cumulant method is shown for three centrality ranges and five collision energies
(from $\sqrt{s_{NN}} = 7.7$ GeV -2.76 TeV). The differences in v_2 signal for the inclusive charged hadrons between all the examined collision energies are little. It is striking because the

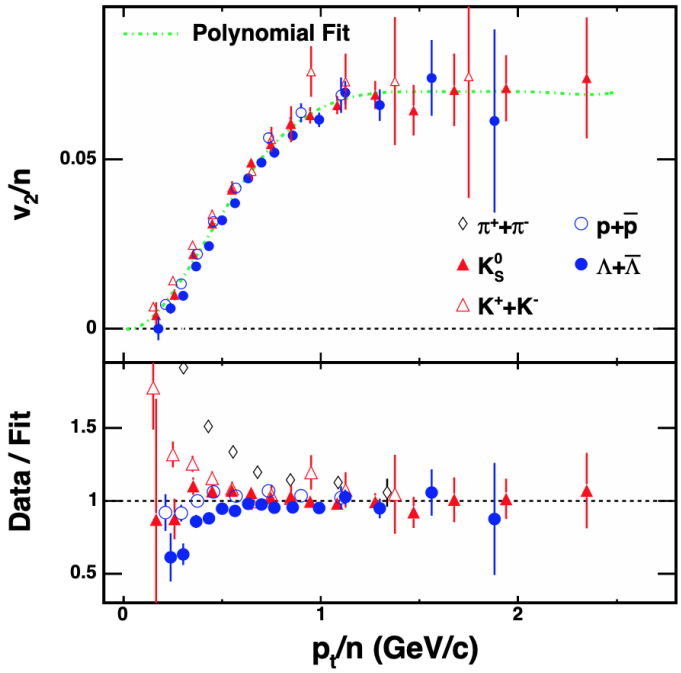

Figure 2.15 – Test of the constituent quark number scaling of elliptic flow for minimum bias Au+Au collisions at $\sqrt{s_{NN}} = 200$ GeV. The dashed lines are polynomial fits [75]

ranges of energies (changes by a factor of 400) and initial energy densities (factor ~ 10) are wide.

Another observation done by STAR is illustrated in Fig. 2.17. It shows the *ncq-scaling* of v_2 vs. $(m_T - m_0)/n_q$ for identified hadrons in $0 - 80\%$ centrality range of Au+Au collisions at $\sqrt{s_{NN}} = 7.7 - 62.4$ GeV [66]. The scaling holds within $10\% - 15\%$ for most of the particles and antiparticles. Due to the lack of the required statistic, it cannot be explained why the ϕ meson does not follow the trend at lower examined energies. Using the hybrid model calculation, the weak dependence of $v_2(p_T)$ on the collision energy is understood as a consequence of the interplay of the hydrodynamic and hadronic transport phase [81].

As the v_3 is more sensitive to the viscous damping, it is treated as a crucial observable in probing the QGP and pressure gradients formation in the early phase of plasma. In Fig. 2.18 the variation of the $v_3^2 2$ for the charged hadrons in several centrality bins at various collision energies: from 7.7 GeV to 2.76 TeV. At energies below 14.5 GeV, $v_3^2 2$ is nearly consistent with zero at more peripheral collisions. This observation agrees with the assumption that in the low-energy, peripheral collisions, the low viscosity QGP phase is

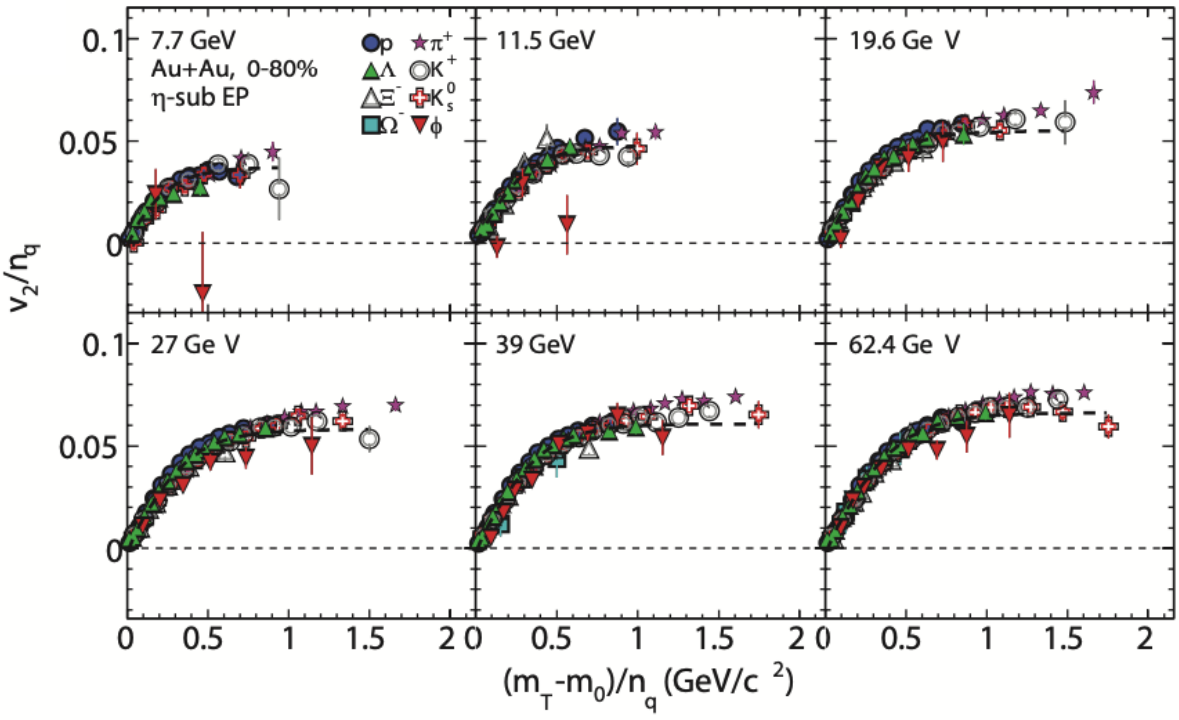

Figure 2.16 – The variation of $v_2(p_T)$ for charged hadrons produced at mid-rapidity from 7.7 GeV up to 2.76 TeV [66, 77]

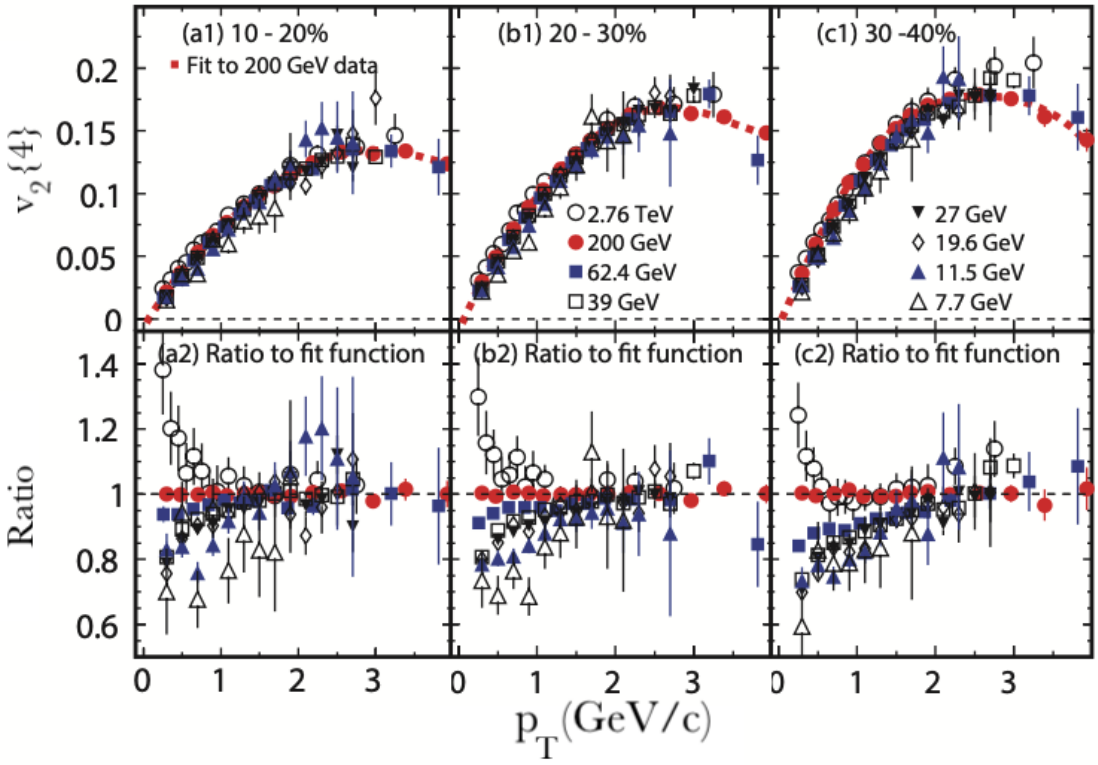

Figure 2.17 – Quark-number (n_q) scaled elliptic flow, v_2/n_q as a function of $(m_T - m_0)/n_q$, for identified particles produced in $0 - 80\%$ central Au+Au collisions at $\sqrt{s_{NN}} = 7.7 - 62.4$ GeV, where n_q is the constituent valence quark number of each hadron and $(m_T - m_0)$ is the transverse kinetic energy of the particle [73, 77]

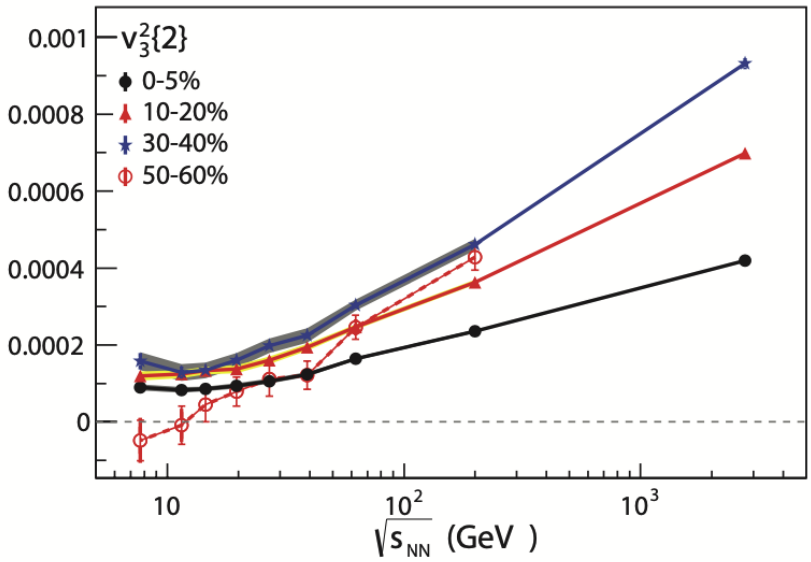

Figure 2.18 – The variation of $v_3^2\{2\}$ for charged hadrons produced at mid-rapidity from 7.7 GeV up to 2.76 TeV [66] for different bins in collision centrality [77, 82]

absent [81]. In more central collisions, the $v_3^2 2$ is positive and does not change relevantly between collision energies < 20 GeV. For the higher energies, the measured triangular flow increases linearly with the $log(\sqrt{s_{NN}})$ for the all examined centrality ranges [66].

The left panel of Figure 2.19 shows p_T-integrated v_n for $0 - 40\%$ central Au+Au collisions as a function of $\sqrt{s_{NN}}$ [83]. The essentially monotonic with beam energy trend for $v_{2,3,4}$ was observed. It is expected since the temperature increase with the $\sqrt{s_{NN}}$. However, the viscous coefficient $''$ [83] shows non-monotonic behaviour over the same beam energy range (right panel of Fig. 2.19). A similar non-monotonic trend is predicted by the hybrid viscous hydrodynamical calculations in [65].

The results of the BES I were so promising that the second phase of this program was planned (data taking in 2019-2020) [76]. The goals are similar but extended with the study of chiral symmetry restoration. BES II provides a substantial improvement in the data collection. The range of the gold ions beams energy is broadened down to $\sqrt{s_{NN}} = 3.0$ GeV by the successful implementation of the fixed-target (FXT) at the entrance of the STAR TPC. The collected data sets have one-order-of-magnitude more extensive statistics in collider mode and two-orders-of-magnitude higher statistics in FXT mode. BES II extends the STAR experiment's reach across a crucial energy regime of high baryon densities: $\mu_B \sim 200 - 720$ MeV. The more technical aspects, such as the introduction of the FXT

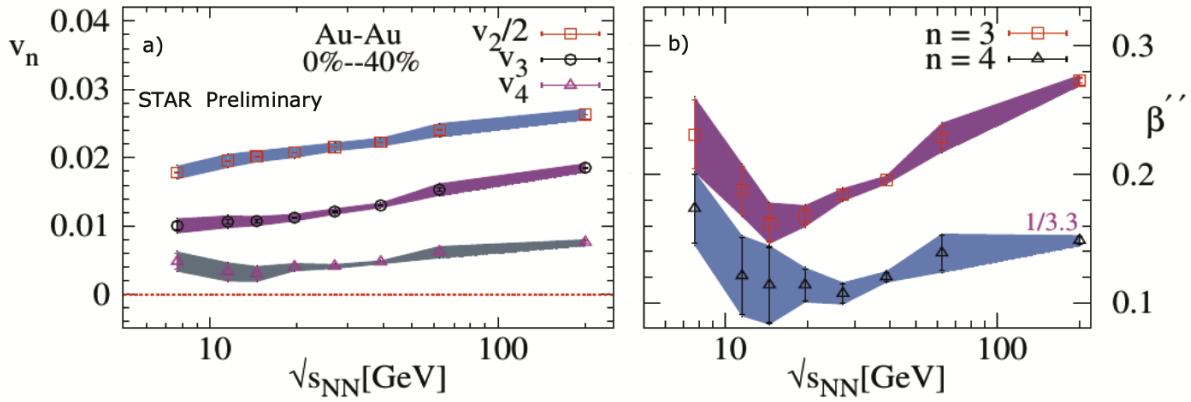

Figure 2.19 – $\sqrt{s_{NN}}$ dependence of the p_T -integrated v_n (left panel) and the estimated viscous coefficient $\beta'' \propto \eta s$ (right panel). Results are shown for $0-40\%$ central Au+Au collisions; the shaded lines are the systematic uncertainty [77, 83]

are described in Chapter 3.

2.3.1 Particle - antiparticle flow difference

As a part of the BES program, the different behaviour between particles and their anti-equivalents in elliptic flow analysis has been reported [59, 84, 85]. The substantial increase of v_2 ratio baryon - anti-baryon with the decrease of collision energy was observed. There are some indications that the growing contributions from hadronic interactions in the system evolution or the stopping power with decreasing energy of collision can be responsible for the differences between $v_2(X)$ and $v_2(\bar{X})$ [86, 87]. The discrepancies in the case of mesons (π and K) were suggested in [88] to be a consequence of the chiral magnetic effect induced by the strong magnetic field in non-central collisions.

Scenario 1: "Viscous Corrections"

In [89] authors propose that the new viscous corrections to v_n at finite μ_B obtained by solving the equations of viscous hydrodynamics coupled with conserved currents assuming conformal and boost-invariant symmetries. They are enhanced at higher baryon density and give the leading order contribution to the differences in v_n between particles and

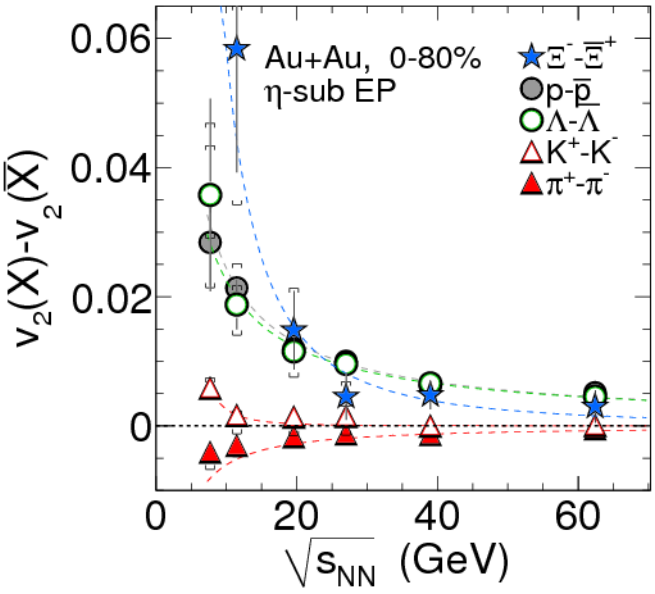

Figure 2.20 – Data published by STAR experiment in [84]. The difference in v_2 between particles (X) and the corresponding anti-particles ($\bar{X}$)) as a function of $\sqrt{s_{NN}}$ for $0-80\%$ central Au+Au collisions. The dash lines in the plot are fits with a power-law functions

antiparticles. They are expressed with the following equation:

$$\frac{\delta v_n}{\epsilon_n} = \frac{K}{256}\frac{\Gamma(3n)}{\Gamma(4n)}\left(\frac{128}{B^3}\right)^n \Gamma^2\left(\frac{n}{2}\right)\frac{n^3(n-1)}{3n-1}\Big\{-\frac{27}{4}(3n^2{+}3n{+}2){+}9\gamma\left(\frac{3n}{2}+1\right)\left(k-\frac{3f'}{4f}\right)\Big\} \tag{2.7}$$

where: K is the Knudsen number proportional to the $\frac{\eta}{s}$, B is the parameter related to the (position-dependent) freeze-out time τ_f, δf is the deviation from the equilibrium Boltzmann distribution. Concluding, the applied viscous corrections to the perfect fluid hydrodynamics explain the differences between v_n of particles and antiparticles. Also, the correction are dependent on the μ_B so consequently they explain the relation of differences with the energy of collision. Authors performed simulations using the corrections - the results are illustrated in Figure 2.21.

Scenario 2: "Mean field theory"

In [90], the researchers suggest that studied differences can be explained by the *mean field theory* assumptions. Attractive potential makes particles trapped in the system and

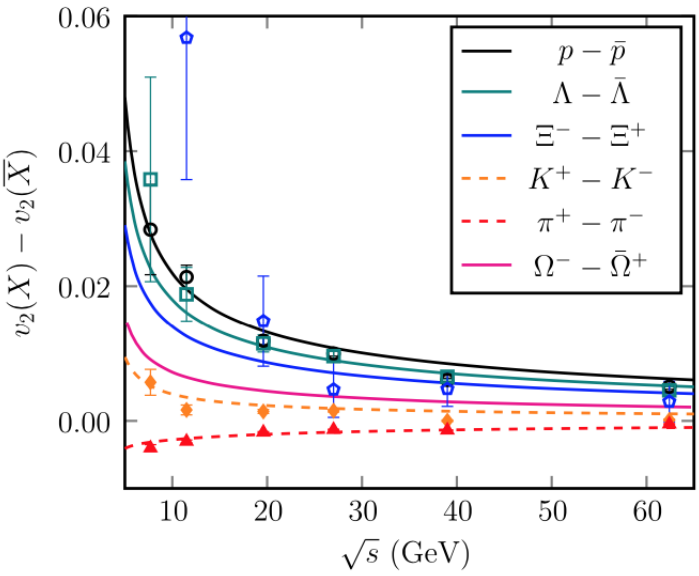

Figure 2.21 – Particle's and antiparticle's elliptic flow difference as a function of $\sqrt{s}$. Comparison of STAR published data [85] and simulations using the procedures proposed in [89].

pushed more in the direction perpendicular to the participant plane. On the other hand, the repulsive potential causes the motion out of the system in the direction along the plane. Protons (three quarks) are affected by the repulsive potential, while antiprotons ($\bar{q}\bar{q}\bar{q}$) by attractive. Consequently, the first ones have a stronger push along the participant plane, making their elliptic flow relevantly higher than antiprotons trapped in the system. The described effects are more pronounced in lower energy collisions, which could explain the dependence of the observed differences in flow on the $\sqrt{s_{NN}}$.

Scenario 3: "Transported protons"

The another theoretical scenario [91, 92] is based on the interplay between so-called *transported* and *produced* protons. Authors distinguish quarks that build the hadrons from collided ions - transported, and these created during the evolution of the system - produced. In the Figure 2.22 the different possible scenarios of the particle production using UrQMD [93, 94] are presented. The produced protons $p(0iq)$ (notation presented in Fig 2.22)and antiprotons are expected to behave similarly; they are both created in the early stages of the system evolution characterised by the relatively high energy density in lower energy collisions. The transported protons $p(3iq)$ are transferred from forward rapidity

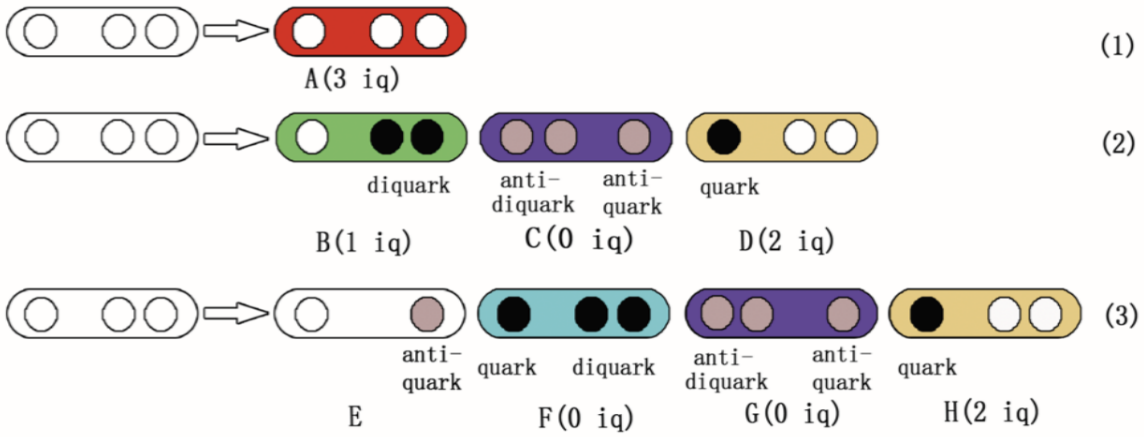

Figure 2.22 – Particle production in a string-excitation scheme in UrQMD. White circles, black circles and grey circles stand for initial quarks, produced quarks and produced antiquarks, respectively. In case (1), no quark pair is created. In case (2), one diquark-antidiquark pair and one quark-antiquark pair are spontaneously created in the colour flux-tube between the initial quark and the initial diquark. Similarly, in case (3), two quark-antiquark pairs and one diquark-antidiquark pair are created, and one meson is produced [91]

to mid-rapidity. As a consequence of the effect of nuclear stopping, which is stronger for lower energies, their elliptic flow variate from v_2 of $p(0iq)$ and $\bar{p}$. Moreover, transported protons' dynamics is affected by the process of the system evolution - they are present when the anisotropy of the initial geometry of the overlap region is being transformed into the anisotropy in expanding the matter. In contrast, the produced protons can only experience a part of these processes. The elliptic flow of $p(3iq)$ is expected to be higher than the flow of produced protons and anti-equivalents. The increasing power of nuclear stopping with the decrease of the collision energy explains the dependence of the observations on the $\sqrt{s_{NN}}$. Authors made simulations using UrQMD, and the results of the $v_2(p_T)$ are shown in Fig. 2.23, where transported protons flow is substantially higher than produced ones and the differences increase with the decrease of the collision energy.

As many proposed theoretical scenarios explain the observed differences in particles' elliptic flow and antiparticles, more experimental references are needed to verify and extend the theoretical suggestions.

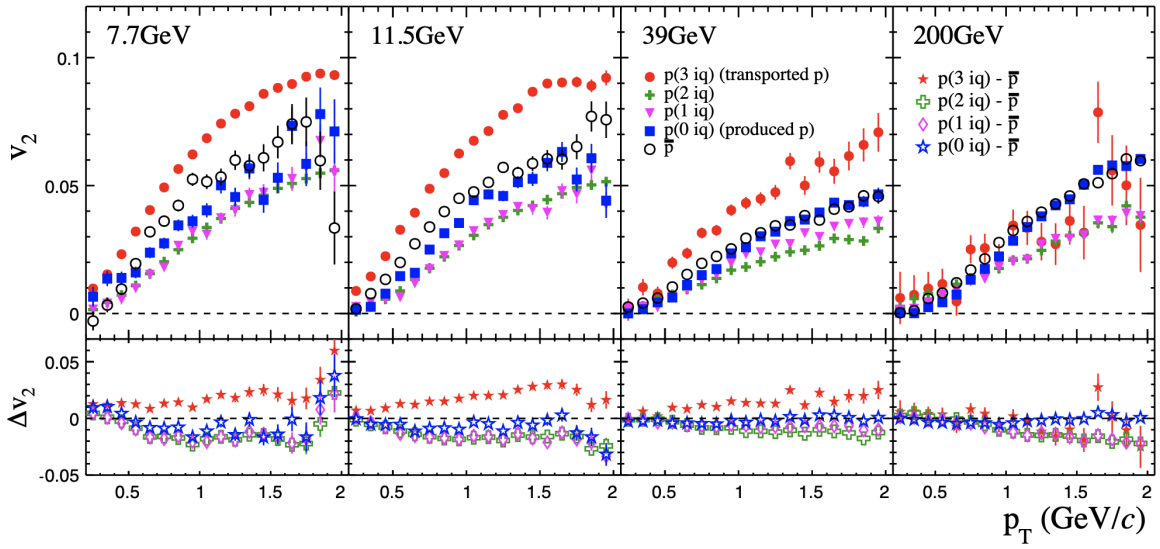

Figure 2.23 – Upper panel: The elliptic flow of p(3 iq), p(2 iq), p(1 iq), p(0 iq) and p as a function of the transverse momentum pT for $0-80\%$ central Au+Au collisions at $\sqrt{s_{NN}} = 7.7, 11.5, 39200$ GeV. The lower panels show the difference of $v_2(p_T)$ between $p(3iq)$, $p(2iq)$, $p(1iq)$, $p(0iq)$ and p, respectively [92]

2.4 Analysis method

In the flow analysis, the two-particle cumulants method is used. It is derived from the following calculations.

2.4.1 Direct cumulants

The flow measurements can be performed using equation:

$$v_n = \langle cos[n(\phi - \Psi_{RP})]\rangle, \tag{2.8}$$

so the coefficients depend on the values of transverse momentum (p_T) and rapidity (y) - *differential flow*. The *integrated flow* is determined by the weighted average (the weight is the invariant distribution, and the quantities with corresponding symbols are shown in Fig. 2.24) [53]:

$$v_n \equiv \frac{\int_0^\infty v_n(p_T)\frac{dN}{dp_T}dpT}{\int_0^\infty \frac{dN}{dp_T}dpT} \tag{2.9}$$

As mentioned in Section 1.3.2, the reaction plane Ψ_R cannot be measured experi-

mentally. However, it is possible to study flow using the azimuthal correlations between detected particles. The 2-particle cumulants (2PC) can be described by a Fourier decomposition $1 + 2v_n^2 \cos n\Delta\phi$. The v_n corresponds to harmonics of the single-particle anisotropy. The measurements are strongly affected by the contribution of the so-called *short-range non-flow* correlations [95–97]. The multi-particle cumulants method cannot completely remove them, but it can significantly suppress them.

The Fourier expansion of the distribution of the **probability** $P(\phi)$ characterizes the particle production azimuthal not-uniformity:

$$P(\phi) = \frac{1}{2\pi} \sum_{n=-\infty}^{\infty}$$

$\mathrm{v}_n \mathrm{e}^{in\phi}, \mathrm{v}_n = \mathrm{v}_n e^{in\Psi}$(2.10)with: v_n corresponding to magnitude and Ψ to phase. In the heavy-ion collisions the event-by-event flow fluctuations are present and can be characterized by a probability distribution $p(v_n)$, which shape can be similar to Gaussian or integrated out the angle ϕ Bessel-Gausssian v_n distribution:

$$p($$

$\mathrm{v}_n)= 1 \frac{}{2\pi\delta_n^2 e^{-|v_n - v_n^0|^2/(2\delta_n^2)}, p(v_n) = \frac{v_n}{\delta_n^2} e^{-\frac{(v_n)^2+(v_n^0)^2}{2\delta_n^2}} I_0\left(\frac{v_n^0 v_n}{\delta_n^2}\right)}$(2.11)where I_0 is modifued Bessel function, andv_n^0 is the driven by the average overlap region geometry component (for $n = 2$, v_n^0 is sizable). As a consequence of the finite multiplicity M of the event, using the flow vector $\boldsymbol{Q_n}$ and normalized by per-particle vector $\boldsymbol{q_n}$ becomes a convenient method. They can be expressed by following:

$\mathrm{Q}_n \equiv \sum_i e^{in\phi_i} = Q_n e^{in\Psi_n}, \mathrm{q}_n = \equiv \frac{\sum_i e^{in\phi_i}}{M} = q_n e^{in\Psi_n}$(2.12)where sum is over all particles in the event, and ϕ, Ψ_n are illustrated in the Fig. 2.24. Vector's $\boldsymbol{q_n}$ direction and magnitude are not same as the real flow, it consists of two additional ingredients:

$$\boldsymbol{q_n} = \boldsymbol{v_n} + s_n^{stat} + s_n \tag{2.13}$$

where s_n^{stat} are fluctuations related to finite multiplicity of particles and s_n is the non-flow contribution originating from short-range correlations. Both of them variate from event to event. The first one becomes negligible as a consequence of averaging over large number of

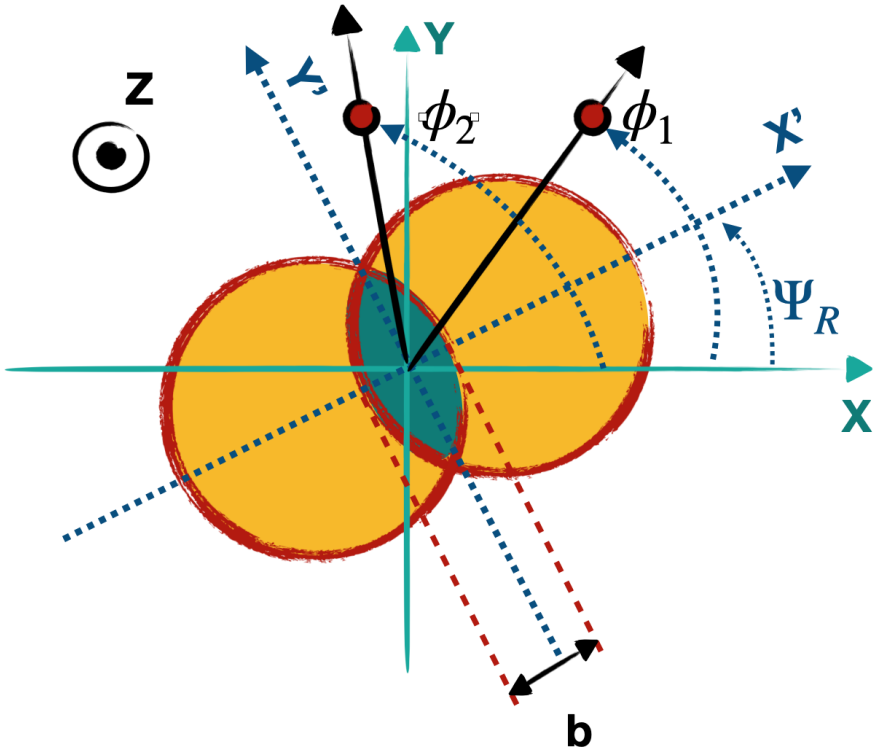

Figure 2.24 – Schematic illustration of a non-central ion collision, where red circles correspond to newly-formed particle 1 and 2. This thesis

events or because of introducing multi-particle correlation method of analysis. Cancelling of the second term is more challenging, there are numerous sources of the short-range correlations, such as: HBT [5], resonance decays or dijets.

The *single-event* average 2-particles azimuthal correlations are defined with given expression [53]:

$$\langle 2 \rangle = \langle e^{in(\phi_{2i-1}-\phi_{2i})} \rangle \tag{2.14}$$

Following, using double brackets denoting the average over all selected events:

$$\langle\langle 2 \rangle\rangle = \langle\langle e^{in(\phi_{2j-1}-\phi_{2j})} \rangle\rangle \equiv \frac{\sum_{events}(W_{\langle 2 \rangle})_i \langle 2 \rangle_i}{\sum_{events}(W_{\langle 2 \rangle})_i} \tag{2.15}$$

To minimise the influence of the multiplicity variations, the weight of the given event $W_{\langle 2 \rangle}$ are introduced. It is equal to the number of possible combinations of pairs of particles in

5. Hanbury-Brown and Twiss [98]

the event of the multiplicity M:

$$W_{\langle 2 \rangle} = M(M-1) \tag{2.16}$$

The cumulat $c_n\{2\}$ is equal to the averaged 2-particle azimuthal correlations (eq. 2.15). This leads to the following cumulant-based definition of harmonic flow v_n:

$$v_n\{2\} = \sqrt{c_n\{2\}} \tag{2.17}$$

2.4.2 Reference Flow

The calculation of the second order cumulant requires the separation of the diagonal and off-diagonal contributions of $|Q_n|^2$, what can be simply applied with [53]:

$$\langle 2 \rangle = \frac{|Q_n|^2 - M}{M(M-1)} \tag{2.18}$$

Then the averaging over all events is performed using eq. 2.15, and the reference flow with eq. 2.17.

2.4.3 Differential flow

In calculations of *differential flow* the two labels describing particles are introduced [53]:

— ***R**eference **F**low **P**article* - RFP

— ***P**article **O**f **I**nterest* - POI

Firstly, the reference flow is calculated only for RFP. Secondly, the differential flow of POI is estimated, considering the RFP flow from the previous step as a reference.

Reduced 2-particle azimuthal correlations

The *reduced 2-particle azimuthal correlations* are described with following equations:

$$\langle 2' \rangle \equiv \langle e^{in(\psi_1 - \phi_2)} \rangle \equiv \frac{1}{m_p M - m_q} \sum_{i=1}^{m_p} \sum_{j=1}^{M}{}' e^{in(\psi_1 - \phi_2)} \tag{2.19}$$

where: m_p corresponds to the total number of POI, m_q to the number of both POI and RFP and M is the multiplicity of RFP. The ψ_i and ϕ_j are the azimuthal angles of i-th and

j-th particles labeled accordingly PIO and RFP. The sum $\sum'$ is over all different indices. The reduced, averaged over all events 2PC are defined as:

$$\langle\langle 2' \rangle\rangle = \equiv \frac{\sum_{events}(w_{\langle 2' \rangle})_i \langle 2' \rangle_i}{\sum_{events}(w_{\langle 2' \rangle})_i} \tag{2.20}$$

where the weights of events are calculated as:

$$w_{\langle 2' \rangle} = m_p M - m_q \tag{2.21}$$

Differential cumulants

The two p- and q- vectors are introduced into the *differential cumulats* calculations (this q vector does not correspond to the same vector as in eq. 2.13). First one correspond to all m_p POI. In order to reduce the impact of the autocorrelations, the second vector is formed and it corresponds only to the m_q POI which are also labeled as RFP:

$$p_n \equiv \sum_{i=1}^{m_p} e^{in\psi i} \tag{2.22}$$

$$q_n \equiv \sum_{i=1}^{m_q} e^{in\psi i} \tag{2.23}$$

Thus, the average reduced single and all-event 2PC can be expressed with:

$$\langle 2' \rangle = \frac{p_n Q_n^* - m_q}{m_p M - m_q} \tag{2.24}$$

$$\langle\langle 2' \rangle\rangle = \frac{\sum_{i=1}^{N}(w_{\langle 2' \rangle})_i \langle 2' \rangle_i}{\sum_{i=1}^{N}(w_{\langle 2' \rangle})_i} \tag{2.25}$$

If the detectors used in collecting the data have the uniform azimuthal acceptance, the differential second order cumulant is defined as:

$$d_n\{2\} = \langle\langle 2' \rangle\rangle \tag{2.26}$$

Finally, the estimation of the differential flow $v_n'\{2\}$ is equivalent to:

$$v_n'\{2\} = \frac{d_n\{2\}}{\sqrt{c_n\{2\}}} \tag{2.27}$$

2.4.4 Particle weights

As the detection of the dynamics of the particles is not ideal (more in Chapter 3), the calculations of 2PC using the real, experimental data have to be modified. The weighted Q-vector is introduced [53]:

$$Q_{n,k} \equiv \sum_{i=1}^{M} w_i^k e^{in\phi_i} \tag{2.28}$$

w_i is the weight of the i-th particle and M is the multiplicity of RFP in the event. In case of two-particle azimuthal correlations the $k = 2$. Accordingly:

$$p_{n,k} \equiv \sum_{i=1}^{m_p} w_i^k e^{in\psi i} \tag{2.29}$$

In case of particles which are labeled only POI the $w_i = 1$, while for the particles labeled as RFP have non-unit weight. In situation when the particle is labeled simulatanously POI and RFP (in total there are m_q partciles), the q-vector is introduced:

$$q_{n,k} \equiv \sum_{i=1}^{m_q} w_i^k e^{in\psi i} \tag{2.30}$$

Then, for RFPs the next step of calculations is:

$$S_{p,k} \equiv \left[\sum_{i=1}^{M} w_i^k\right]^p \tag{2.31}$$

$$\mathcal{M}_{abcd...} \equiv \sum_{i,j,k...=1}^{M} w_i^a w_j^b w_k^c ... \tag{2.32}$$

In case of particles labeled **both** POI and RFP:

$$s_{p,k} \equiv \left[\sum_{i=1}^{m_q} w_i^k\right]^p \tag{2.33}$$

And anagously:

$$\mathcal{M}'_{abcd...} \equiv \sum_{i=1}^{m_q} \sum_{i,j,k...=1}^{\prime M} w_i^a w_j^b w_k^c ... \tag{2.34}$$

where the first sum is over all POIs and second over RFPs. The event weight is here:

$$W_{\langle 2\rangle} \equiv \mathcal{M}_{11} \tag{2.35}$$

so that the weighted single-event 2PC:

$$\langle 2 \rangle \equiv \frac{1}{\mathcal{M}_{11}} \sum_{i,j=1}^{\prime M} w_i w_j e^{in(\phi_i - \phi_j)} \tag{2.36}$$

Continuing, the reduced single-event 2PC here are:

$$\langle 2' \rangle \equiv \frac{1}{\mathcal{M}'_{01}} \sum_{i=1}^{m_p} \sum_{j=1}^{\prime M} w_j e^{in(\phi_i - \phi_j)} \tag{2.37}$$

where the event weights are now:

$$w_{\langle 2' \rangle} \equiv \mathcal{M}'_{01} \tag{2.38}$$

The weighted average 2PC are defined as:

$$\langle 2 \rangle = \frac{|Q_{n,1}|^2 - S_{1,2}}{S_{2,1} - S_{1,2}} \langle \langle 2 \rangle \rangle = \frac{\sum_{i=1}^{N} (\mathcal{M}_{11})_i \langle 2 \rangle_i}{\sum_{i=1}^{N}} (\mathcal{M}_{11})_i) \mathcal{M}_{11} \equiv \sum_{i,j=1} {}' w_i w_j = S_{2,1} - S_{1,2} \tag{2.39}$$

Finally, the 2-particle azimuthal correlations are expressed with the following equations:

$$\langle 2' \rangle = \frac{p_{n,0} Q^*_{n,1} - s_{1,1}}{m_p S_{1,1} - s_{1,1}} \langle \langle 2' \rangle \rangle = \frac{\sum_{i=1}^{N} (\mathcal{M}'_{01})_i \langle 2' \rangle_i}{\sum_{i=1}^{N} (\mathcal{M}'_{01})_i} \mathcal{M}'_{01} \equiv \sum_{i=1}^{m_p} \sum_{j=1}^{M} {}' w_j = m_p S_{1,1} - s_{1,1} \tag{2.40}$$

2.4.5 Subevent cumulants

The main goal of introduction of the *Subevent cumulat* method is the reduction of the non-flow contribution [53, 59, 99, 100]. This method's general picture is illustrated in Fig. 2.25. The two vectors A and B corresponding to particles from a given pseudorapidity range ensure no self-correlations are taken into account. The average distance (in η) between correlated particles is higher than zero, which provides the reduction of the short-range non-flow contribution originating from, for example, HBT (more in Sec. 2.1.1).

Each event is divided into subevent A and B, which consists of accordingly M_a and M_b particles. The two-particle correlator which considers event-by-event weights can be described using flow vectors:

$$\langle 2 \rangle_{a|b} \equiv \langle e^{in(\phi_1^a - \phi_2^b)} \rangle = \frac{Q_{n,a} Q^*_{n,b}}{M_a M_b} \tag{2.41}$$

where :

$$Q_{n,o} \equiv \Sigma_i e^{in\phi_i^o}, o = a, b \tag{2.42}$$

Particles in subevent A are correlated with particles from subevent B, ensuring no self-correlations in calculations.

The $\Delta\eta$ gap between subevents

As mentioned before and underlined in equation 2.13 the non-flow contribution is measured using described above methods. The more non-flow is suppressed, the more detailed studies of the anisotropies in particles' yields are. The short-range correlations are present for particles close in the pseudorapidity. To suppress their contribution in the flow measurements, the η gap between subevents is introduced.

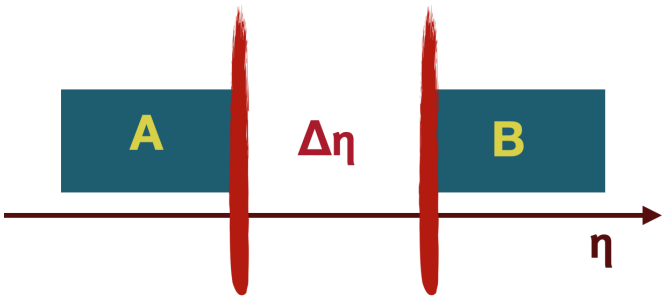

Figure 2.25 – An event divided into two subevents A and B with the η gap between them. This thesis

Chapter 3

The STAR experiment at RHIC

Various experimental facilities have been designed to investigate the QCD phase diagram such as the Relativistic Heavy Ion Collider (RHIC) [101], the Super Proton Synchrotron (SPS) [102], Alternating Gradient Synchrotron (AGS) [103], Schwer Ionen Synchrotron (SIS) [104], or the Large Ion Collider (LHC) [105]. There are also future Nuclotron-based Ion Collider fAcility (NICA) [106], Facility for Antiproton and IonResearch in Europe (FAIR) [107] or Japan Proton Accelerator Research Complex (J-PARC) [108]. Their scientific programs are dedicated to exploring different regions of the diagram (Figure 3.1). The extremely high collision energies obtained at LHC provide creation of systems at temperatures about to 170 MeV and $\mu_B \approx 0$, where the cross-over transition occurs and the QGP is created. On the other hand, SPS accelerate ions to much lower energies giving the access to investigation of the phase diagram at finite μ_B and lower T, where the first order phase transition is expected to be present. RHIC provides the whole spectra of collision energies for several systems. The unique scientific program conducted there, allows to perform studies of system evolution in different regions of the QCD phase diagram what is substantial in search for the signatures of phase transitions.

In this chapter the STAR experimental setup is described.

3.1 Relativistic Heavy-Ion Collider RHIC

In the 2000 year, RHIC, one of the biggest accelerators, was built in Brookhaven National Laboratory (BNL) in New York State [110–112]. The primary goal was to accelerate gold ions and collide them with the energy $\sqrt{s_{NN}} = 200$ GeV. Then the physics program called Beam Energy Scan (BES I) conducted at RHIC became more diverse, and new collision systems and energies were applied to explore a wider range of the QCD phase diagram. There were performed studies of collisions obtain at energies between $\sqrt{s_{NN}} = 7.7 - 200$ GeV for systems including: Au (max 100 GeV/nucleon) , U, Ru, Al, d, ^{3}He, Zr ions, and protons (max $\sqrt{s_{NN}} = 510$ GeV) [113]. Now, this program is extended -

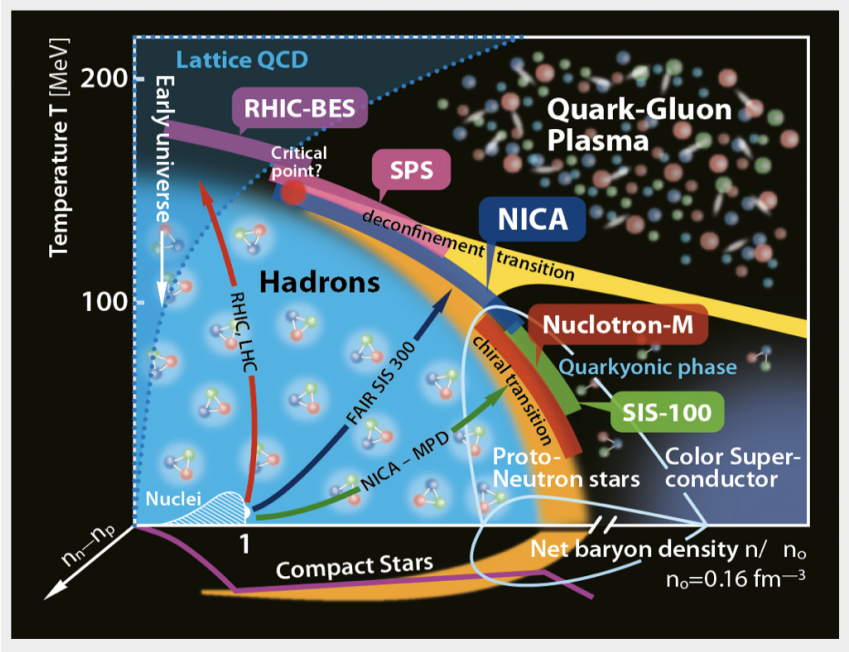

Figure 3.1 – The QCD phase diagram with depicted regions studied in different experimental programs [109]

BES II [76]. The statistics of performed collisions is increased and more collision energies (such as $\sqrt{s_{NN}} = 54.4$ GeV) are provided. However, there is also, an energy bottom limit of the accelerator performance in the collider system. To decrease the collision energy, the golden shield was located inside the STAR experiment replacing one of the beams. The new Fix Target program allows studying even more diverse phase diagram regions - characterized by lower temperature and higher baryochemical potential ($\mu_B \approx 720$ MeV), where Au+Au collisions happen with $\sqrt{s_{NN}} = 3.0$ GeV.

RHIC consists of the two separate accumulation rings: "Blue" and "Yellow", each of length 3.8 km. There are 1740 superconducting magnets (dipoles, quadrupoles, sextupoles and corrector magnets) used in RHIC to provide high-precision collimation and maintenance of the beam trajectory. They are made of niobium and titanium alloy processing at 4.6 K, and in the arc, dipoles generating the 3.45 T magnetic field [114]. To stabilize the polarized-proton spin, the Siberian Snake devices are used [115].

In Figure 3.2 the whole structure of the acceleration complex is illustrated [116].

In order to prepare the proton beam, several stages can be listed:
1) Firstly, in the Optically Pumped Polarized Ion Source (OPPIS) [117] the polarized hydrogen ions are created,

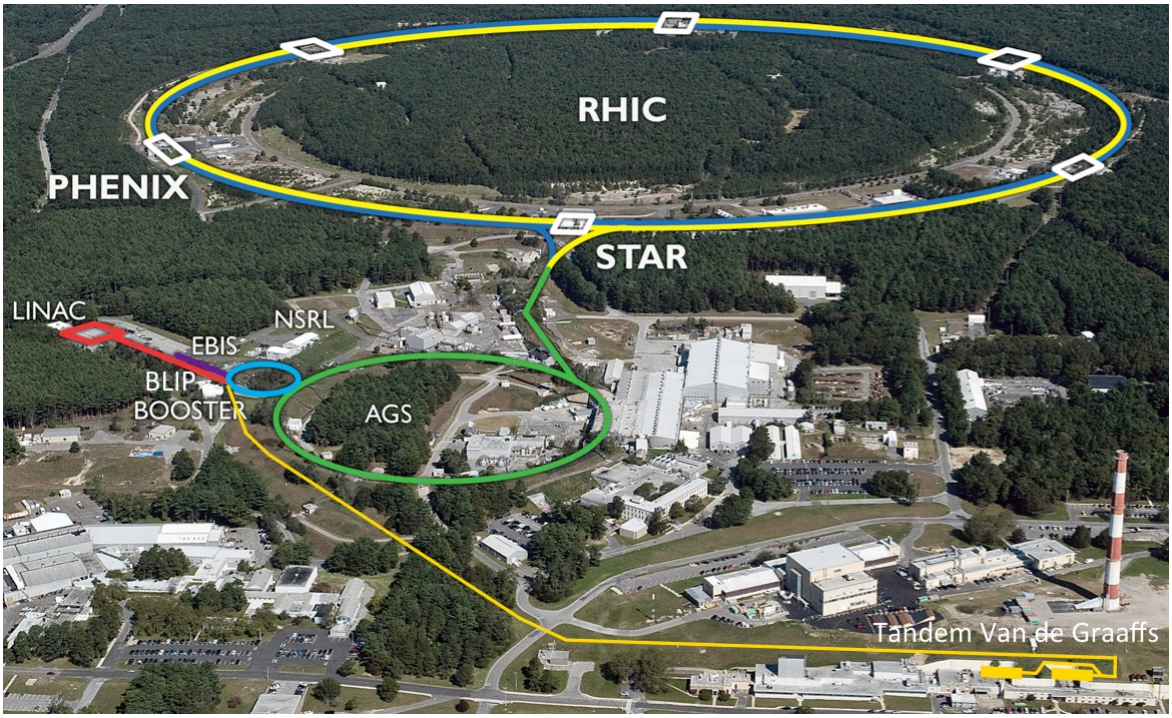

Figure 3.2 – The RHIC accelerator complex [110].

2, 3) It is accelerated by Radio Frequency Quadrupole (RFQ) and Linac up to 200 GeV.
4, 5) Subsequently, they are stripped to protons and get more acceleration in the Booster (up to 2.5 GeV), and in Alternating Gradient Synchrotron (AGS) (reaching 25 GeV of energy).
6, 7) Finally, beams are injected in the RHIC's rings, and they continue being accelerated until they reach the nominal energy.

The preparation of heavy-ion beams can be described in such steps as:
1) It starts in Laser Ion Source (LION), where they are produced.
2) Next, they are transported to an Electron Beam Ion Source (EBIS) where after acceleration they achieve the energy of 17 keV/nucleon.
3) Their charge is also multiplied (+32 in case of Au) [118].
4) The subsequent acceleration is performed in RFQ and Linac (up to 2 MeV/nucleon).
5) then in Booster (100 MeV/nucleon), where they are also stripped changing their charge (for Au +77).
6) The nominal charge is established in AGS (+79 for Au) where the ions continue being accelerated, reaching the energy of 8.87 GeV/nucleon.

7) In the end, the ion beams are injected into the RHIC, where they achieve the nominal energy.

Several experiments consisting of complexes of detectors are constructed at the RHIC. However, only one is currently operational - STAR (Solenoid Tracker at RHIC, see Subsection 3.1.1). PHOBOS [119] in 2005 and BRAHMS [120] in 2006 completed their scientific programs and operations. The last one, in 2015, PHENIX [121] was decommissioned for the development purpose, the sPHENIX is expected to start collecting data in 2023 [122, 123].

3.1.1 STAR

Solenoid **T**racker **a**t **R**HIC was designed and constructed to study the properties of the QGP created in the heavy-ion collisions and investigate the data from the polarized proton collisions to explore cold-QCD. It is multi-purpose, mid-rapidity detector, which consists of over ten various subsystems used to investigate multiple observables, the structure is illustrated in Fig. 3.3.

The STAR experiment consists of such detectors as:

— Time Projection Chamber (TPC) - responsible for tracking [124],
— Time of Flight (TOF) - used for particle identification [125, 126],
— Barrel Electromagnetic Calorimeter (BEMC) - particle energy measurement [127],
— Heavy-Flavor Tracker (HFT) - the short-lifetime decay vertices reconstruction [128],
— Muon Telescope Detector (MTD) - identification of di-muon decays (from J/ψ and Υs [129]),
— Vertex Position Detector (VPD) - position of the primary collision vertex, and start the time counting for the fast-timing detectors (TOF or MTD) [130];

In last two years the upgrade of the STAR experiment took place. The three new systems were installed (illustrated in the Figure 3.4 with the short description) [131]:

— Event Plane Detector (EPD) [132]
— endcap Time Of Flight (eTOF) [133]
— Inner Time Projection Chamber (iTPC) [134]

As part of this project, I was engaged in the iTPC software development, what is shortly described in Appendix 9.

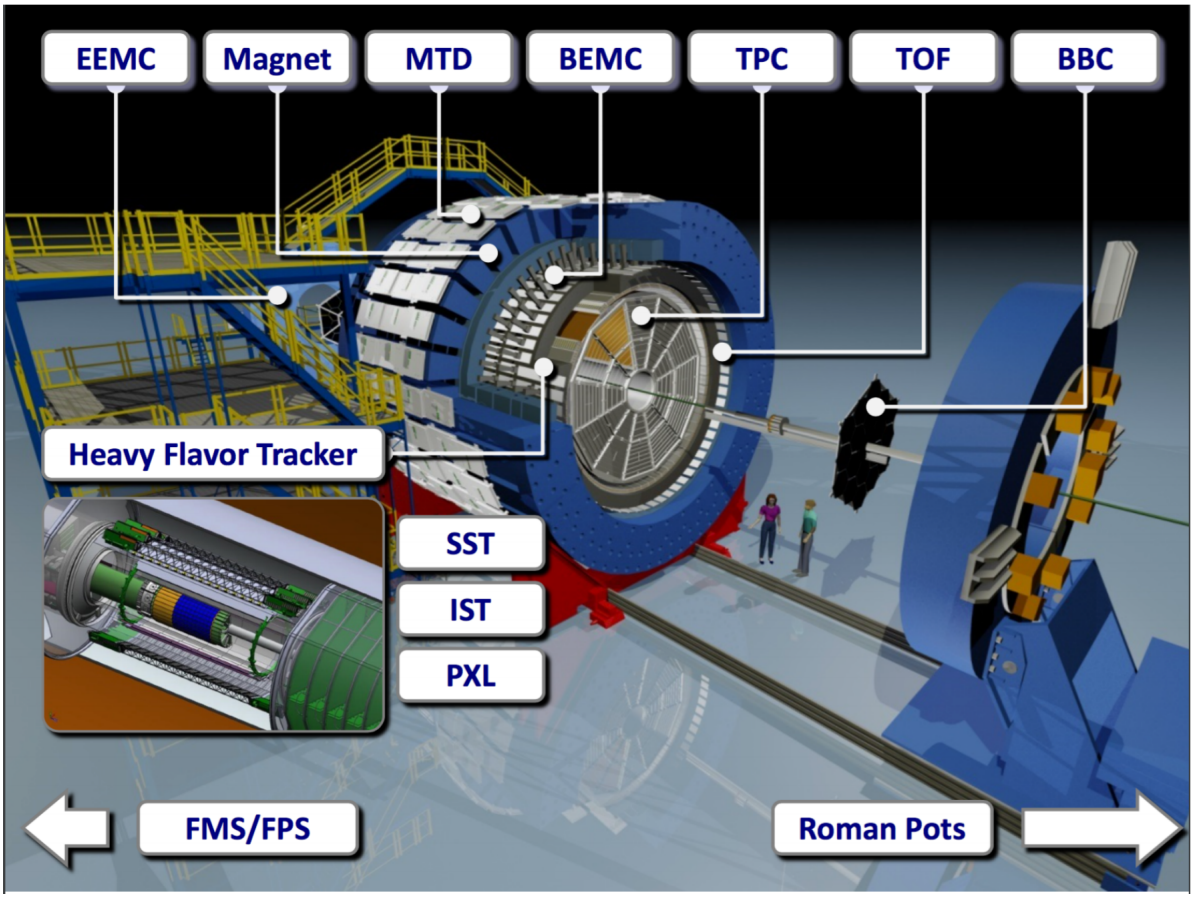

Figure 3.3 – STAR experiment schematic illustration with depicted detector subsystems. The TPC, TOF are the detectors of the special interest to this thesis. Figure courtesy of A. Schmah (STAR Collaboration).

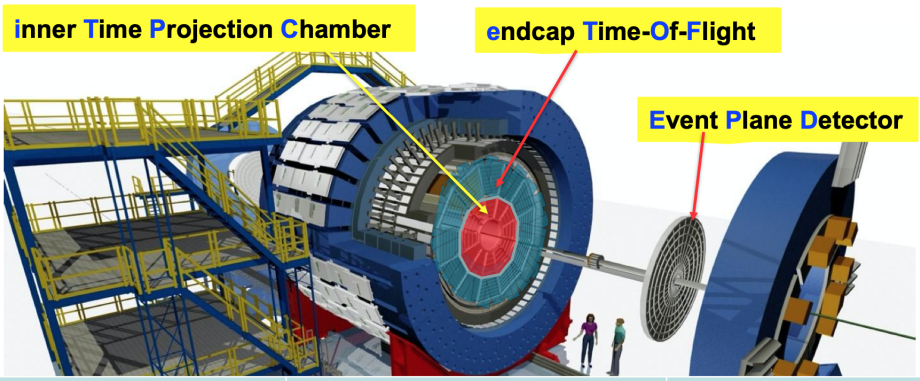

iTPC upgrade	eTOF upgrade	EPD upgrade
Continuous pad rows Replace all inner TPC sectors	Add CBM TOF modules and electronics (FAIR Phase 0)	Replace Beam-Beam Counter
$\|\eta\| < 1.5$	$-1.6 < \eta < -1.1$	$2.1 < \|\eta\| < 5.1$
$p_T > 60$ MeV/c	Extend forward PID capability	Better trigger & b/g reduction
Better dE/dx resolution Better momentum resolution	Allows higher energy range of Fixed-Target program	Greatly improved Event Plane info (esp. 1st-order EP)

Figure 3.4 – STAR experiment schematic illustration with depicted detector subsystems. The TPC, TOF are the detectors of the special interest to this thesis. Figure courtesy of A. Schmah (STAR Collaboration).

As the TPC, iTPC, TOF, and VPD detectors are the most vital for this analysis, they are described in details in the subsequent sections.

Time Projection Chamber

Time Projection Chamber (TPC) is one of the most relevant STAR detectors used in nearly all performed analysis. It is 4.2 m long, and its diameter is equal to 4 m. The Figure 3.5 shows the scheme of TPC [135]. The chamber is filled with the P10 mixture of gases: 90% argon Ar and 10% methane CH_4. It is designed to register particles' tracks (normally it reconstructs the multiplicities equal more than 3000 tracks) and measure their momenta (in range of 100 MeV/c to 30 GeV/c). It covers the full azimuthal angle ($0 < \phi < 2\pi$) and ± 1.8 units of pseudo-rapidity ($-1 < \eta < 1$). The basic parameters of TPC are listed in Table 3.6.

The inner filed cage is located 0.5 m from the centre of the beam pipe, while the outer one in a distance of 2 m. The operating at a high voltage of 28 kV central membranes (CM) provides the uniform electric field of 135 V/cm. It is placed at the centre of TPC ($z = 0$). The solenoidal magnet gives the magnetic field of 0.5 T. Both fields are directed along the beam. The collision occurs close to the centre of the TPC. The primary charged

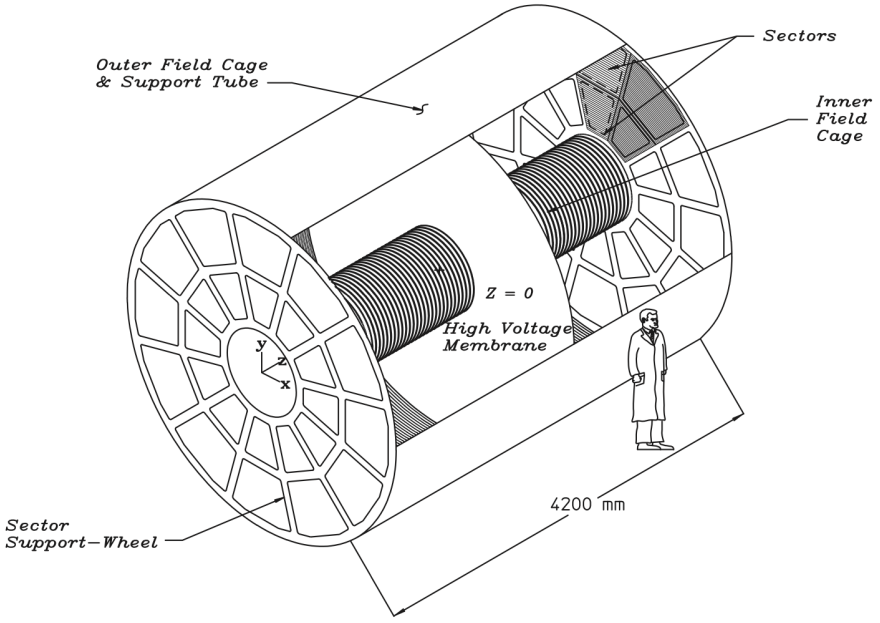

Figure 3.5 – The schematic profile of TPC detector at STAR [135]

particles transverse the TPC and interact with the gas. Consequently, the gas gets ionized. Affected by the electric uniform field, the secondary electrons drift to the readout end-caps of the TPC. The registered signals are used in the high-resolution reconstruction of the primary particles' trajectories. The typical drift velocity of the gas is 5.45 cm/μs. The end-cap readout plane is a system based on the Multi-Wire Proportional Chambers (MWPC).

One of the TPC sectors is shown in Fig. 3.7 . The whole sector can be divided into outer and inner sub-sectors. The outer sub-sector on the left of the Fig. 3.7 consists of densely packed pads in the 32 rows. There is inner sub-sector built of smaller pads on the right in the picture, arranged in widely spaced 13 pad rows. Recently, the inner part was replaced with iTPC sectors. New sectors include the Continuous Pad Coverage of 72 rows. iTPC upgrade improves the detection of the ionization energy loss of particles for about $15\% - 30\%$. The coverage of pseudo-rapidity η is extended from 1.0 to 1.5. The p_T cut-in is lowered from 125 MeV/c to 60 MeV/c.

The identification of particles (PID) is performed by measuring the ionization energy loss (dE/dx). The Bichsel formula [1] [136] provides the mean rate of energy loss for a

1. improved versio of the Bethe-Bloch formula [14].

Item	Dimension	Comment
Length of the TPC	420 cm	Two halves, 210 cm long
Outer Diameter of the Drift Volume	400 cm	200 cm radius
Inner Diameter of the Drift Volume	100 cm	50 cm radius
Distance: Cathode to Ground Plane	209.3 cm	Each side
Cathode	400 cm diameter	At the center of the TPC
Cathode Potential	28 kV	Typical
Drift Gas	P10	10% methane, 90% argon
Pressure	Atmospheric + 2 mbar	Regulated at 2 mbar above Atm.
Drift Velocity	5.45 cm / μs	Typical
Transverse Diffusion (σ)	$230\mu m/\sqrt{cm}$	140 V/cm & 0.5 T
Longitudinal Diffusion (σ)	$360\mu m/\sqrt{cm}$	140 V/cm
Number of Anode Sectors	24	12 per end
Number of Pads	136,608	
Signal to Noise Ratio	20 : 1	
Electronics Shaping Time	180 ns	FWHM
Signal Dynamic Range	10 bits	
Sampling Rate	9.4 MHz	
Sampling Depth	512 time buckets	380 time buckets typical
Magnetic Field	0, $\pm$0.25 T, $\pm$0.5 T	Solenoidal

Figure 3.6 – Table including the basic parameters of TPC [135]

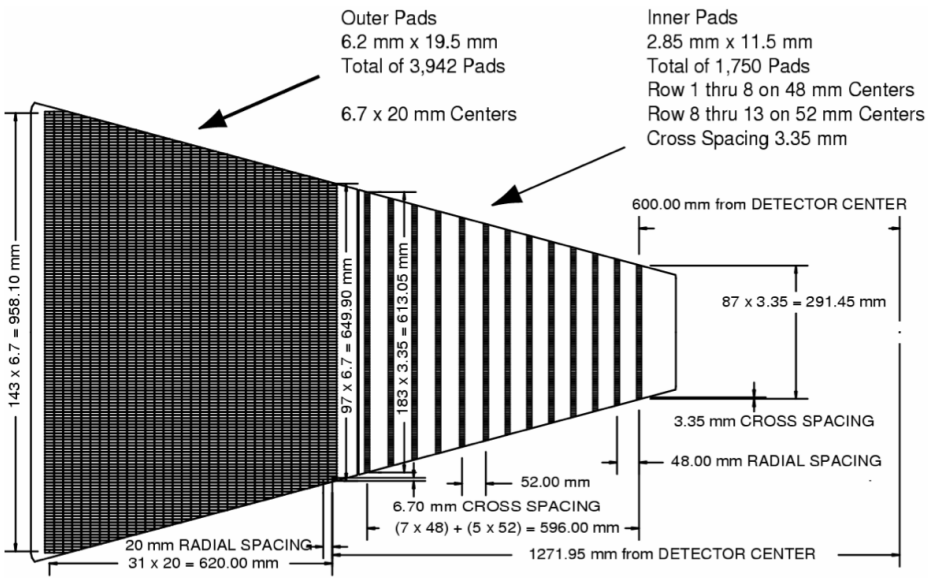

Figure 3.7 – The anode pad plane with one full sector [135].

charged particle [137]:

$$-\langle\frac{dE}{dx}\rangle = 2\pi N_a r_e^2 m_e c^2 \rho \frac{Z}{A}\frac{z^2}{\beta^2}\left[ln\left(\frac{2m_e\gamma^2 v^2 W_{max}}{I}\right) - 2\beta^2\right] \tag{3.1}$$

where: $2\pi N_a r^2 m_e c^2 = 0.1535$ MeV cm^2/g and $\gamma = 1/\sqrt{1-\beta^2} = 1/\sqrt{1-(v/c)^2}$.

N_a: Avogadro's number
r_e: classical electron radius
m_e: electron mass
ρ: density of absorbing material
Z: atomic number of absorbing material
A: atomic weight of absorbing material
z: charge of incident particle [e]
W_{max}: maximum energy transfer in single collision
I: mean excitation potential

The calculations of the loss of the energy are performed in the function of the momentum transfer. Various species of particles having the same momentum, loose in the different way their ionization energy (dE/dx). In Figure 3.8 the example of dE/dx distribution in function of particles' momentum at $\sqrt{s_{NN}} = 39$ GeV with the fitted by the Bichsel function lines [138]. They correspond to given particle specie. It is visible that the identification with TPC of protons up to $p < 1$ GeV/c is clear. For the studies of the higher momentum range, the Time Of Flight detector is used.

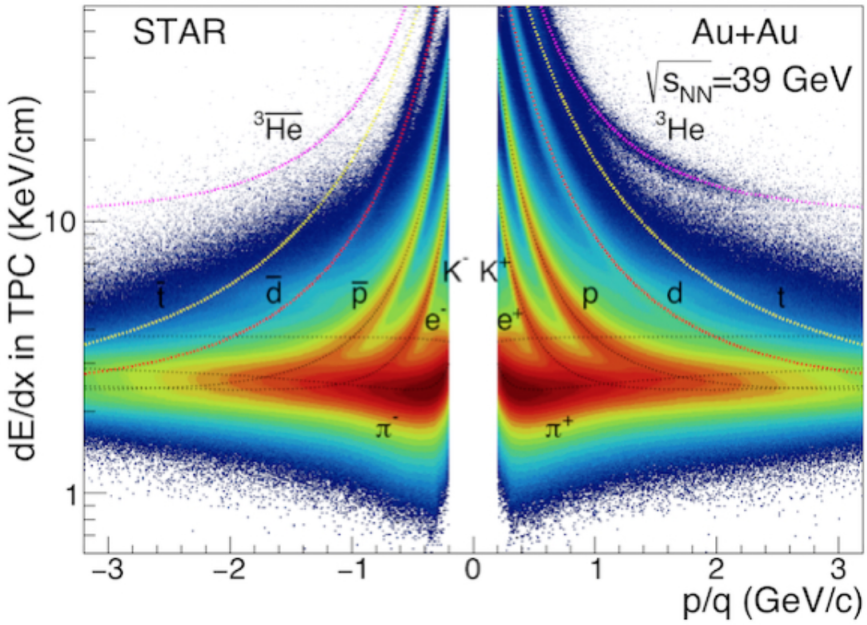

Figure 3.8 – The ionization energy loss distribution of charged particles at $\sqrt{s_{NN}} = 39$ GeV. The solid lines are from the Bichsel functions [138].

Time of Flight

Time of Flight is the fast-timing detector, which main goal is to register the time of the motion of the particle. It is dedicated for the identification of the particles with momentum $p \geq 1$ GeV/c.

The TOF detector is placed outside of the TPC. The geometry of TOF's trays, modules and pads are illustrated in Figure 3.9. On each side of TPC (east and west), 60 trays cover $-1 < \eta < 1$ of pseudo-rapidity and full azimuthal angles. The tray is build of 32 Multi-gap Resistive Plate Chamber (MRPC) modules illustrated in Figure 3.10.

In the construction of MRPC the two electrodes with a voltage 7 kV and a stack of resistive glass plates are used. There are six uniform gas gaps between plates, which are filled with the uniform, high electric fields. The MRPC proceeds in the avalanche mode: when the particle transverse the module, they cause the simultaneous avalanches in the gas gaps. The created signal is the superposition of the avalanches. The distance (L) between TOF and the vertex of the collision is know, the speed (β) and mass (m) of particles can be calculated using following equations:

$$\beta = \frac{v}{c} = \frac{L}{c\Delta t} \tag{3.2}$$

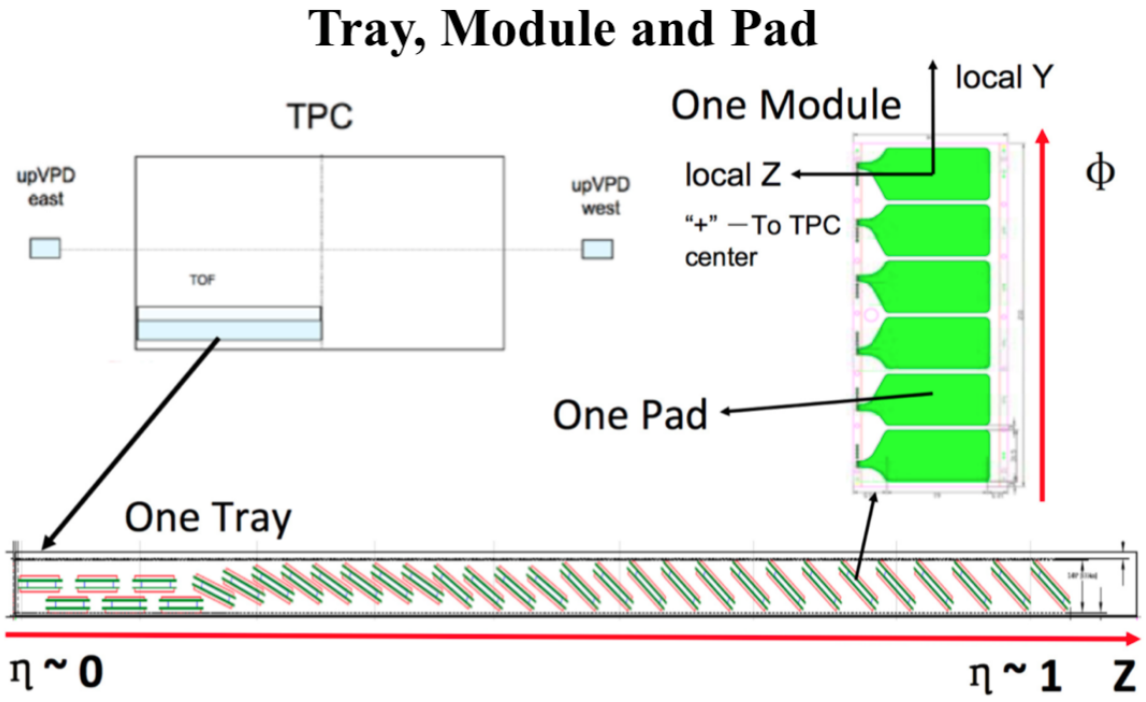

Figure 3.9 – The details of TOF trays, modules and pads [126]

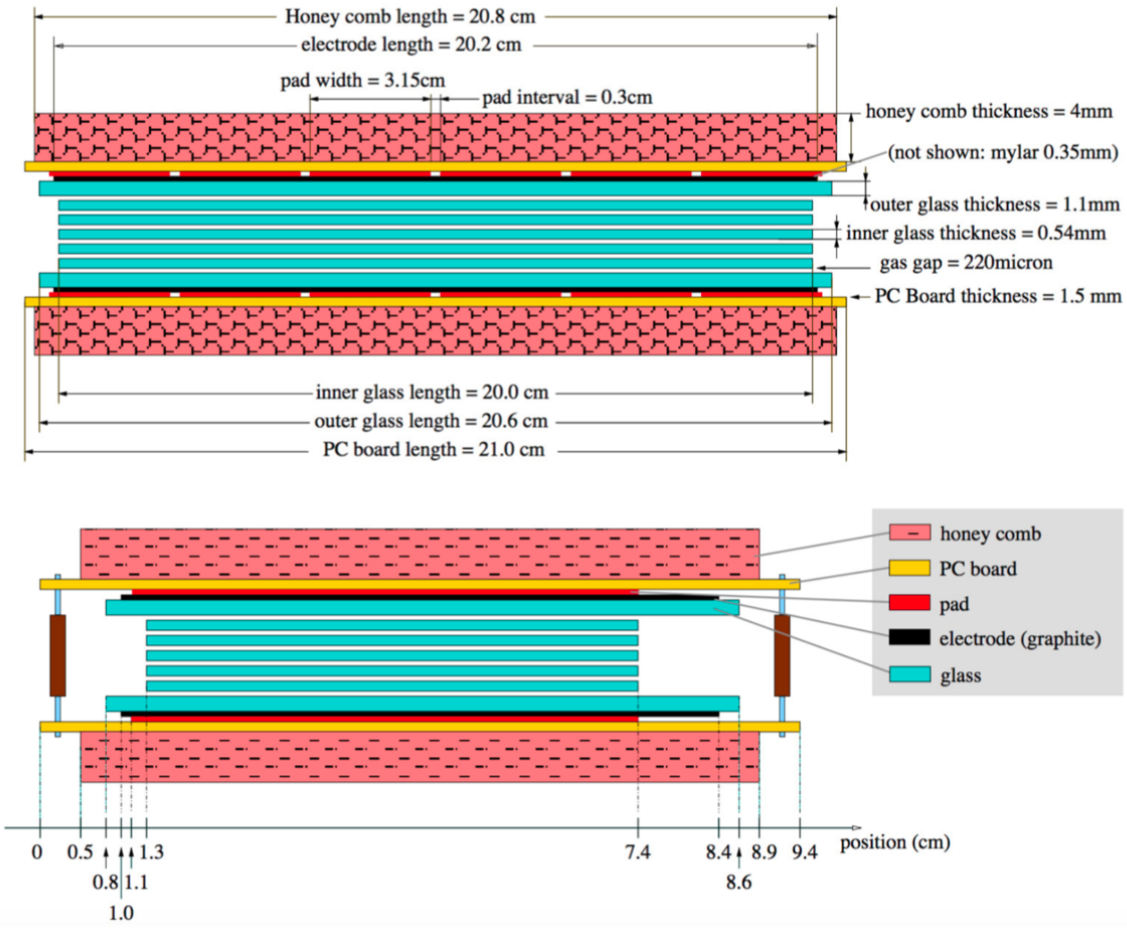

Figure 3.10 – The two-side view on the Multi-gap Resistive Plate Chamber (MRPC) modules [126]

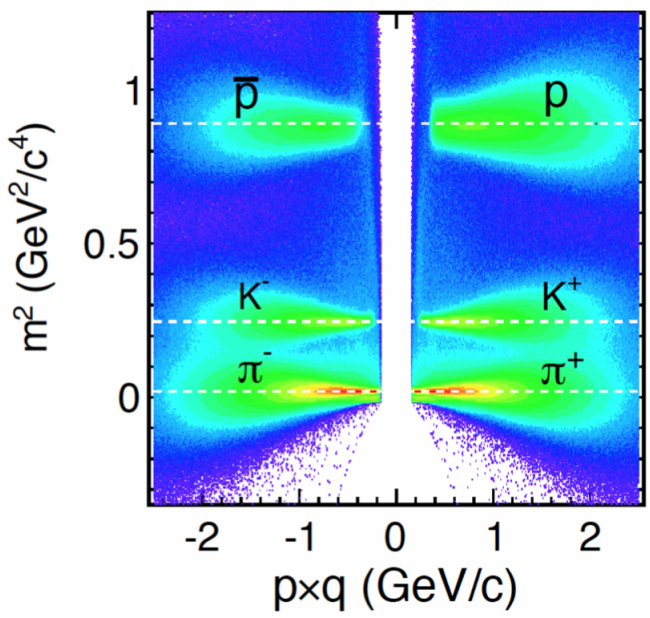

Figure 3.11 – The mass square distribution as a function of rigidity at $\sqrt{s_{NN}} = 39$ GeV. This thesis

$$m^2 = p^2(\frac{1}{\beta} - 1) \tag{3.3}$$

where $\beta = p/E$ and $E = \sqrt{p^2 + M^2}$, p is the measured by TPC momentum of the particle and Δt is measured by TOF time difference between start and stop time (given by the VPD). Figure 3.11 shows the example distribution of mass square (Eq. 8.7) in function of ridigity at $\sqrt{s_{NN}} = 39$ GeV measured with Time of Flight detector.

Vertex Position Detector

Vertex Position Detector (VPD) measures the position of the primary collision vertex and provides the "start-time" for the fast-timing detectors (TOF or MTD). VPD is the 2x19 channel detector, before the pseudo Vertex Position Detector (pVPD) consisted only of 2x3 channels. It is used as a minimum-bias trigger for Au+Au collisions.

VPD consists of the pair of detectors located symmetrically in the distance 5.7 m from the centre STAR, on the beam pipe on either side of the detectors' complex. The construction of VPD reminds the revolver - the 19 photo-multiplier tubes (PMTs) surround the beam-pipe, illustrated in Fig. 3.12. It registers the neutral remnants from the collided ions (spectators) and produced from π^0 photons.

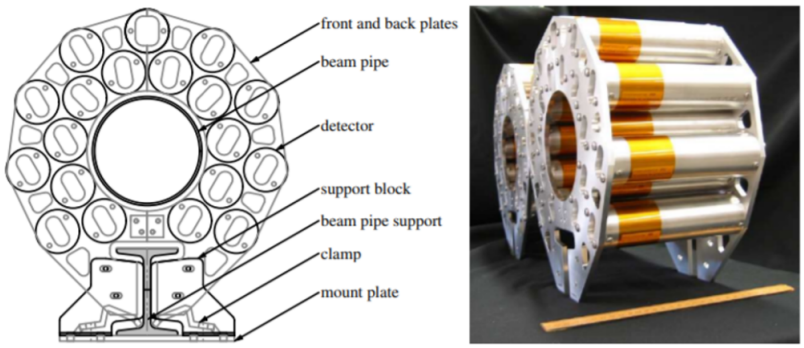

Figure 3.12 – The left panel is schematic drawing of one of the VPD assemblies, and the right panel is a photograph of both VPD assemblies [130]

For the determination of the location of the collision vertex (Z_{vtx}) the measured times at east (T_{east}) and west (T_{west}) sides are used:

$$Z_{vtx} = c(T_{east} - T_{west})/2 \tag{3.4}$$

Thus, the start-time for other detectors can be calculated with:

$$T_{start} = (T_{east} + T_{west})/2 - L/c \tag{3.5}$$

where c is the speed of the light and L is the distance between the center of the STAR and assembly.

Chapter 4

Analysis

The data's selections, events, tracks are described in this chapter, and the particles identification and applied corrections to the experimental analysis.

4.1 Data samples

The studies are performed on the data recorded by STAR experiment during Au+Au collisions at $\sqrt{s_{NN}} = 27, 39, 54.4$ and 200 GeV. The data sets are selected using the STAR software and subsequently stored in PicoDst root files [139]. PicoDst files contain only the most relevant to the analysis pieces of information. The main goals of usage of this type of files are:

— Have relevantly smaller size than previously used by STAR MuDst files
— Contain most of the essential information or most of the physics analysis
— Store data in plain ROOT
— Allow working in STAR-independent environment
— Compatible with ROOT5/6, Windows, Linux, macOS [140].

The events collected during the beam or detectors' calibration tests are rejected and when any miscalibration is observed. The example luminosity of the events registered in the run 17 by STAR for Au+Au collisions at $\sqrt{s_{NN}} = 54.4$ GeV are presented in Figure 4.1.

In the performed analysis, there were chosen three sets of produced data listed in Table 4.1. Several selection criteria were applied to remove events of low quality and/or suppress background.

4.2 Event selection

For the best quality event selection, the pileup (average number of collisions per bunch crossing) removal techniques were applied. The TPC detector's measured quantities had

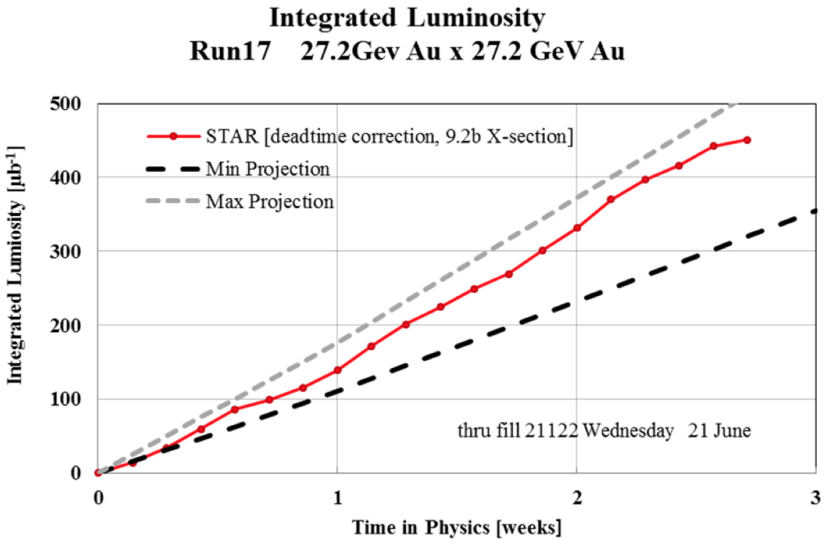

Figure 4.1 – The integrated luminosity in function of time of the events registered by STAR for Au+Au collisions at $\sqrt{s_{NN}} = 54.4$ GeV [141].

Trigger Name	Production	Vertex Cut	Trigger ID
*AuAu*27_*Production*	P11id	$\|V_Z\| < 50$cm	360001
			360002
*AuAu*39_*Production*	P10ih	$\|V_Z\| < 40$cm	380001
			3800023
*AuAu*54_*production*_2017	P17ii	$\|V_Z\| < 40$cm	580021
*AuAu*200_*production*_2011	P 11id	$\|V_Z\| < 30$cm	350003, 350013, 350023, 350033, 350043

Table 4.1 – The data sets used in analysis, and the basic selection criteria.

to be validated with corresponding measurements performed by fast-timing detectors such as TOF or VPD to avoid the pileup events. Firstly, the multiplicities of events detected by TPC (*Refmult*) are compared with the related distribution of these registered by TOF (*TOFmatch*). In Figure 4.2 the plots of the relation between *TOFmatch* and *Refmult* before and after cuts are presented. The green curve in the right-hand side plot corresponds to the difference between distributions of the Refmult before and after the corrections.

Secondly, the Vertex Z relation using data registered by TPC and VPD detectors is investigated (Fig. 4.3). The events selected in the final analysis have to be characterized by the exact value of V_Z confirmed by both detectors.

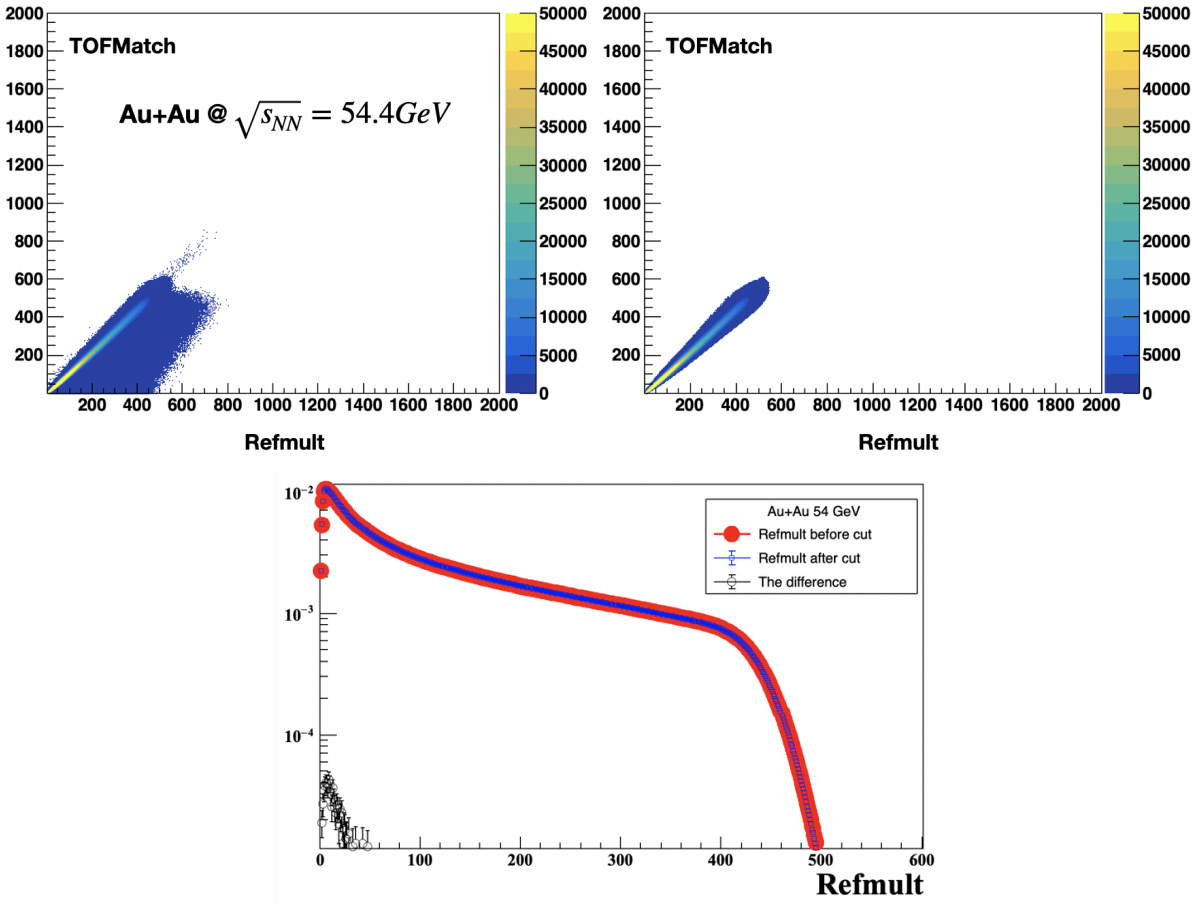

Figure 4.2 – The Quick Analysis (QA) distributions of relations between multiplicity of events detected by TPC and TOF for Au+Au collisions at $\sqrt{s_{NN}} = 54.4$ GeV before and after the pileup removal technique application. On the right the distribution of *Refmult* before (red) and after (blue) applying cuts, and the difference (green). (The plot is normalized to unity) This thesis

4.3 Track selection

The most important selection criteria are listed in Table 4.3. The application of stricter limits can highly decrease the statistics so that there has to be a compromise between the quality of the selected data and the sufficient amount of data for the given analysis.

The Distance of Closest Approach (DCA) corresponds to the shortest distance between the particle's track's main vertex and the point where it was registered. If the value of DCA is close to 0 cm, the probability that the particle is primary does not originate from the resonance decay, is high. The bigger DCA, the further the primary vertex of the particle from the collision vertex. Figure 4.4 illustrates the particles' tracks, collision

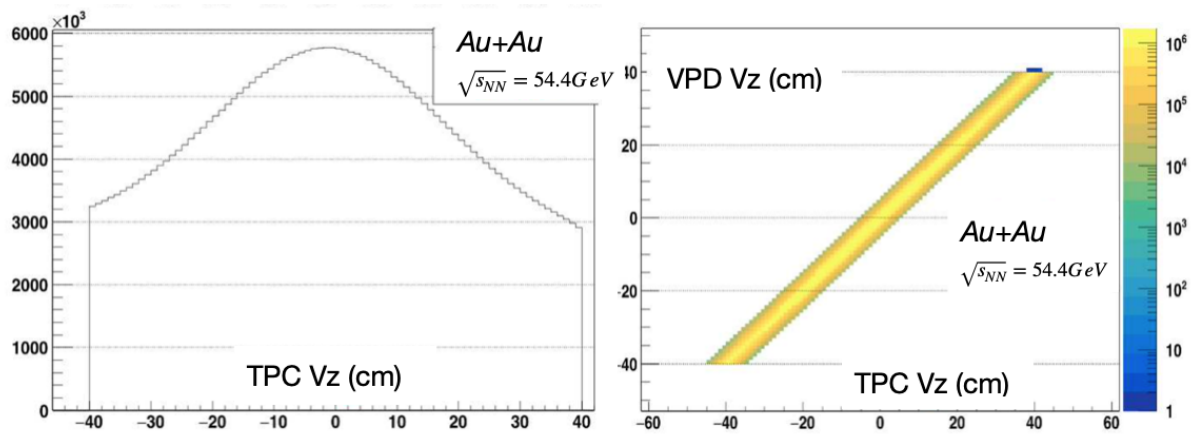

Figure 4.3 – The Quick Analysis (QA) TPC V_Z distribution on the left, and on the right the relation between the Vertex Z from TPC and VPD. This thesis

$\sqrt{s_{NN}}$	Number of events (min bias)
27 GeV	3.6e+10
39 GeV	3.0e+09
54.4 GeV	1.4e+11
200 GeV	5.0e+8

Table 4.2 – Numbers of events after application of selection criteria.

$\sqrt{s_{NN}}$	DCA	$nHitsFit$	$Nhits/Hitmax$	p_T $[GeV/c]$	η
27 GeV	< 3 cm	> 20	> 0.52	$\langle 0.2, 4.0 \rangle$	< 1
39 GeV	< 3 cm	> 20	> 0.52	$\langle 0.2, 4.0 \rangle$	< 1
54.4 GeV	< 3 cm	> 20	> 0.52	$\langle 0.2, 4.0 \rangle$	< 1
200 GeV	< 3 cm	> 15	> 0.52	$\langle 0.2, 4.0 \rangle$	< 1

Table 4.3 – Track selection criteria

vertex with DCA depicted.

The condition of the minimum number of hits fitted with the one curve used to reconstruction the track of particle ($nHitsFit$) is applied to reject fake tracks.

The distributions of variables are illustrated in Figures 4.5.

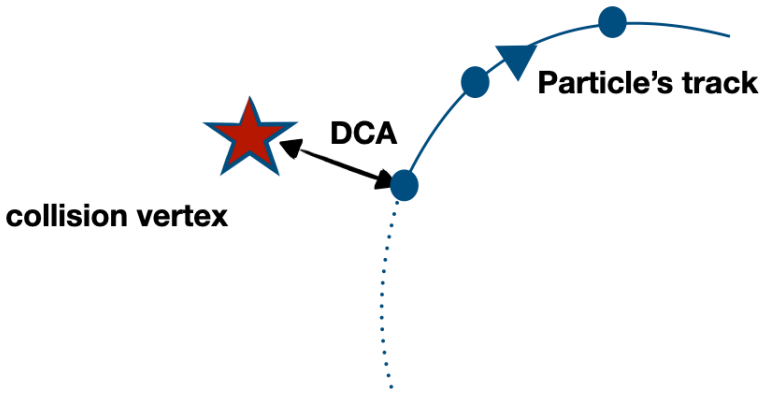

Figure 4.4 – Illustration of the collision vertex and reconstructed particle track with depicted Distance of Closest Approach. This thesis

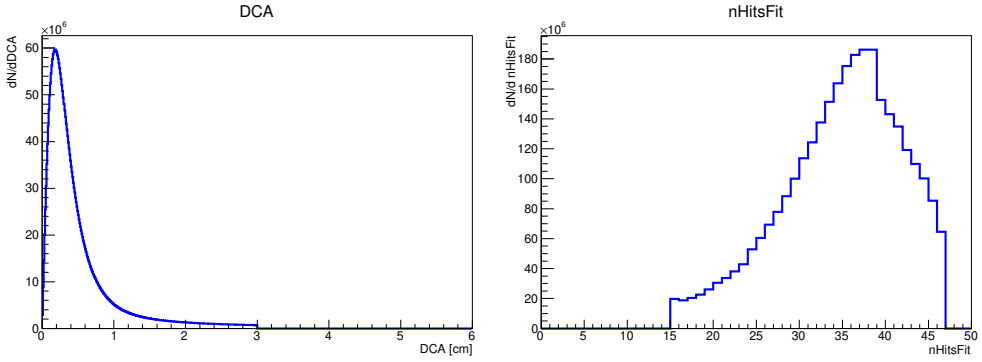

Figure 4.5 – DCA and number of hits in the reconstructed track histograms for Au+Au collisions at $\sqrt{s_{NN}} = 39$ GeV. This thesis

4.4 Particle Identification

The identification of pions, kaons, and protons is accomplished by combining TPC and TOF detectors information. For the TPC data, the $N\sigma$ method is applied, where σ is the standard deviation from the Bethe-Bloch parameterization of the energy loss signal dE/dx. Figure 4.6 shows the average dE/dx of measured charged particles by TPC plotted as a function of "rigidity" (i.e. momentum/charge) of the particles. The TOF identification is based on tracking inverse particle's velocity in a unit of the speed of light $1/\beta$, which depends on the mass square of the given particle (Figure 4.7). Finally, the whole p_T range is divided into bins, and the combination of these methods is applied for each bin accordingly. The selection of these criteria was based on the previous STAR

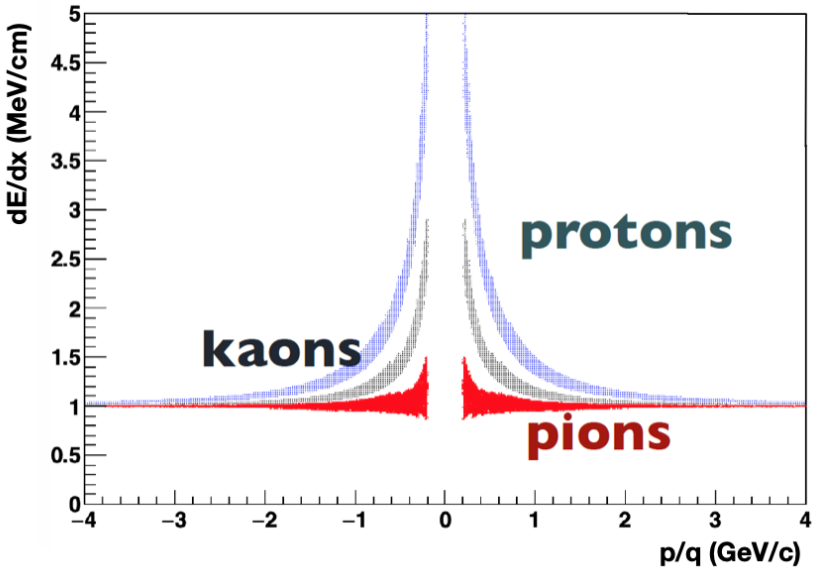

Figure 4.6 – The dE/dx of charged tracks at midrapidity ($|y| < 1.0$) plotted as function of rigidity (p/q) in Au+Au collisions at $\sqrt{s_{NN}} = 39$ GeV. This thesis

publications and expected to be the most reliable and precise [73].

4.5 Efficiency and Acceptance corrections

The construction and calibration of the detectors are performed with high precision. However, there are present some imperfections in acceptance and reconstruction efficiency. Due to such inadequacies, some of the particles are lost in collecting the data.

4.5.1 Acceptance correction

The STAR detectors do not cover perfectly 100% of acceptance - particles are not reconstructed, for example, in the $x-y$ plane along the gaps between the TPC sectors, or some of the particles are missing due to the possible failure in the reconstruction software. Several corrections are applied to the analysis of the already collected data to increase the investigated data quality.

In the proposed method, one has to create the histograms, including the particles' distributions in the η, ϕ plane. The histograms are divided into multiple groups depending on:

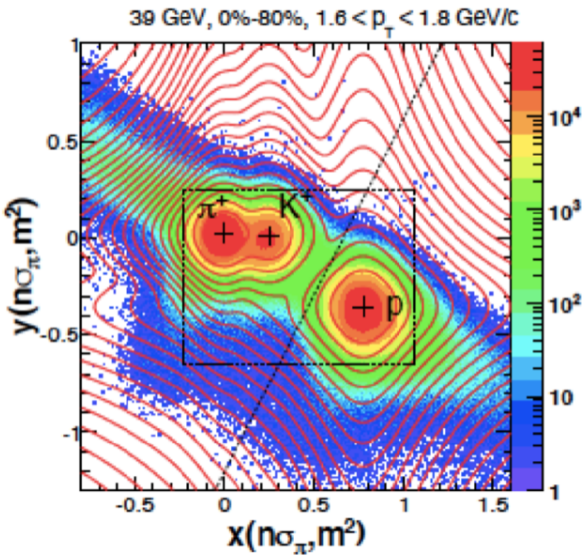

Figure 4.7 – The combined information from TPC and TOF with depicted selected regions corresponding to identified hadrons species for collision Au+Au at $\sqrt{s_{NN}} = 39$ GeV. This thesis

— particle *sigitta* [1]
— the Z vertex of the event
— the centrality of the event

Each cell refers to the particle's $1/weight$ value, which is applied in the final analysis. The Figure 4.8 illustrates the examples distributions of particles' η, ϕ, which are not uniform. Assigning the proper weight to the particle results in this distribution's flattening, which is treated as an acceptance correction.

The particles' ϕ distribution for the Au+Au collisions at $\sqrt{s_{NN}} = 39$ GeV for all centrality ranges before and after acceptance correction are shown in Figure 4.9. The application of particles' weights makes the distribution flat.

4.5.2 TPC Tracking Efficiency

Another issue is the imperfection of the tracking efficiency. For instance, particles with very low p_T could not be taken into account by the reconstruction software. The method used to correct such effects is based on the *embedding simulated events*. They are propagated through the *Starsim* algorithms, which provides the same conditions as in the

1. Sigitta of a track is the distance from the centre of the reconstructed track curvature to the centre of its base.

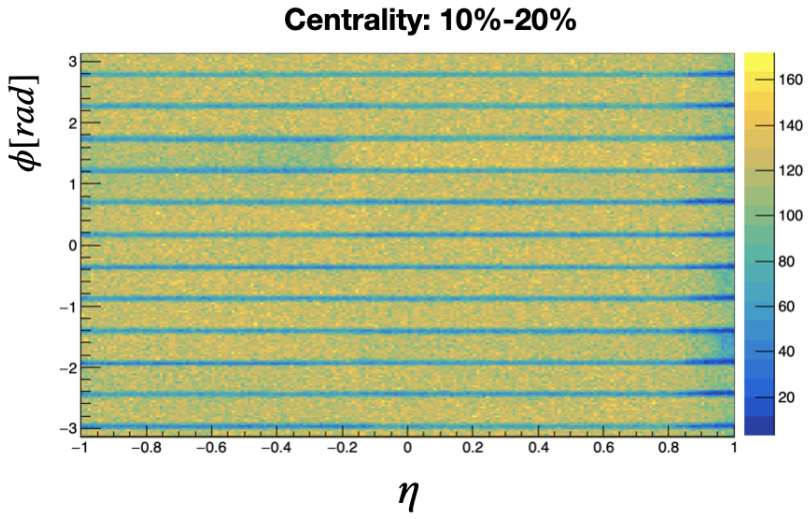

Figure 4.8 – The ϕ, η particle distribution for Au+Au collisions at $\sqrt{s_{NN}} = 39$ GeV. This thesis

detector geometry and reconstruction procedure. The efficiency of the given detector (in this case, TPC) corresponds to the probability of detecting the given particle specie. It can be expressed as a ratio of "matched" tracks (a reconstructed track that matches one of the pre-reconstructed simulated tracks) to the numbers of embedded MC tracks.

The impact of the application of the TPC Tracking Efficiency as an additional to the Acceptance correction was investigated. In Figures 4.10 the $v_2\{2\}$ in function of p_T (as the efficiency correction strongly depends on transverse momentum) for Au+Au collisions at $\sqrt{s_{NN}} = 39$ GeV is shown. In the bottom panels there are ratios between data corrected with *efficiency+acceptance/acceptance*. The parameters of the fitted function used for the correction can be found in [142].

The effect of the correction is small $\sim 1\%$. In conclusion, the TPC Tracking Efficiency correction has such a negligible effect that it is not applied in the analysis as an addition to the acceptance correction.

4.6 Systematic uncertainty analysis

As listed in previous sections, several data selection criteria are applied to prepare the data sets for analysis. The removal/suppression of undesired effects in the reconstruction of particles' characteristics strongly limits the statistics, and in various studies, the applied

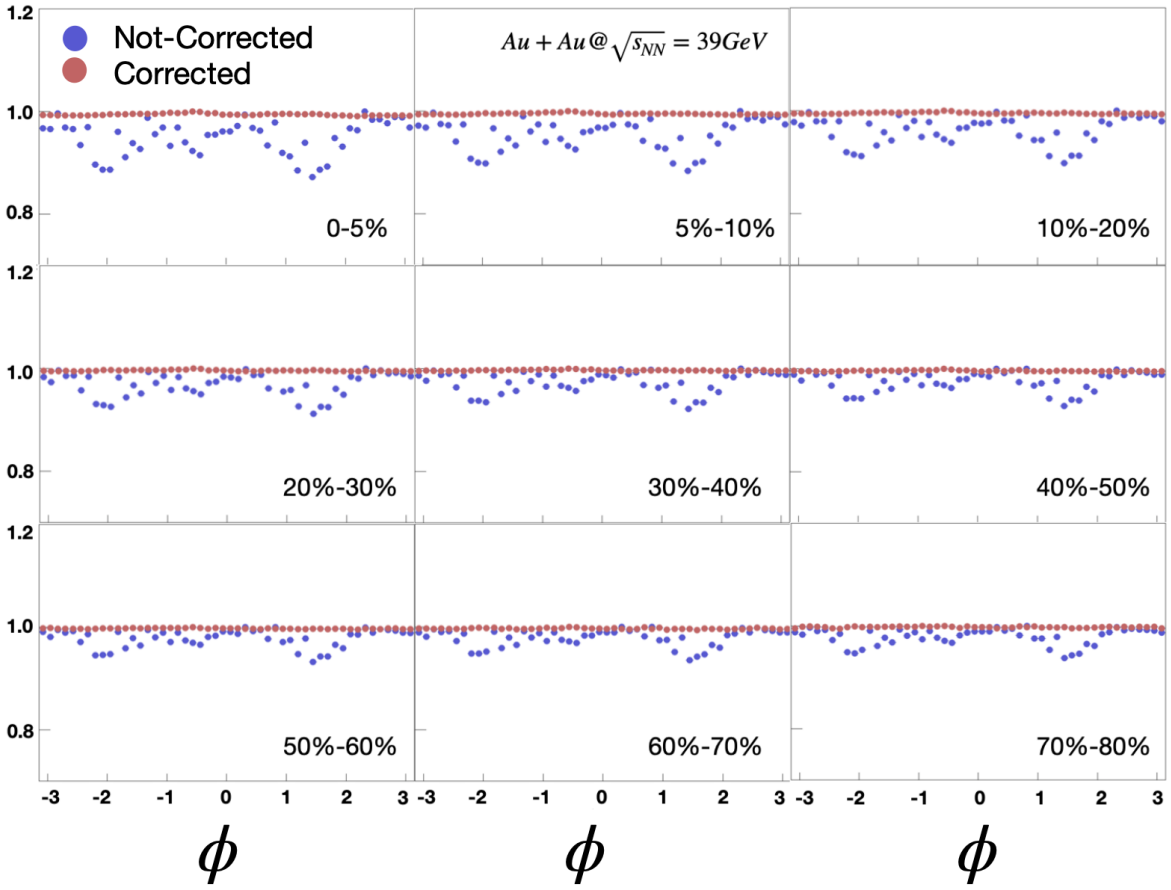

Figure 4.9 – The ϕ distributions for Au+Au collisions at $\sqrt{s_{NN}} = 39$ GeV at 9 centrality bins before and after application of acceptance correction. This thesis

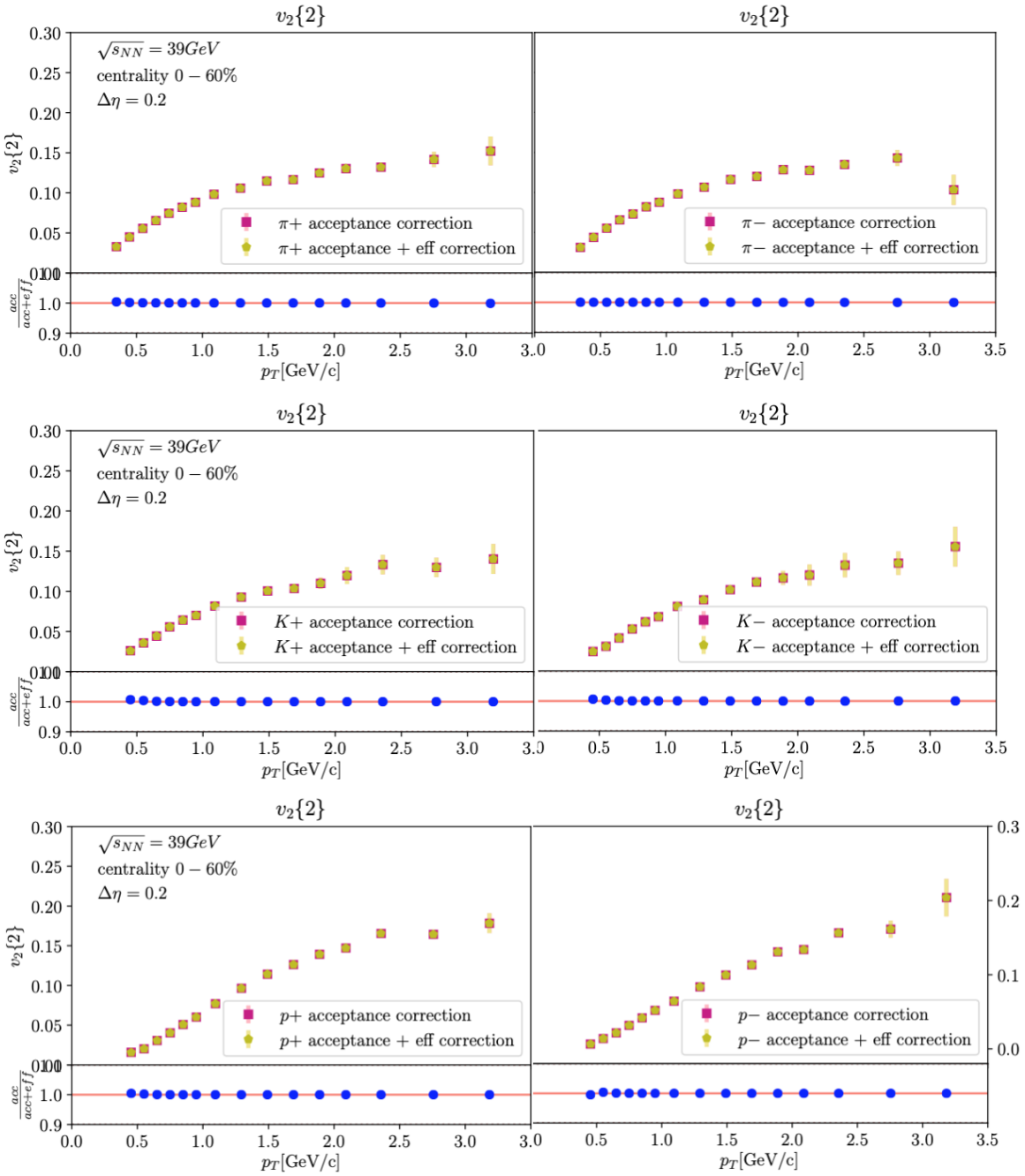

Figure 4.10 – Difference between data corrected with *efficiency+acceptance* and *acceptance* in $v_2\{2\}(p_T)$ of identified hadrons for Au+Au $\sqrt{s_{NN}} = 39$ GeV. This thesis

criteria differ. In order to consider all possible discrepancies between available, reasonable criteria application, systematic uncertainties are introduced.

In the performed analysis, there are four sources of systematic uncertainty studied:
a) maximum value of DCA:
The whole analysis was performed twice for: one default DCA event cut and the second value of default DCA±1 cm.
b) events characterized only positive or both positive and negative V_Z:
The events chosen for the analysis had only V_Z, or default their V_Z was in range $-V_Z$ to $+V_Z$. c) introduced $\Delta\eta$:
The selection of the minimum difference between particles' η is not trivial. With that the part of *non-flow* contribution is compressed, but also it can significantly decrease the statistics. Sometimes, the selection of this criteria is treated as additional study. In case of this thesis it is considered as the systematic uncertainty.

d) minimum number of hits in the reconstructed particle's track:
Similarly, to the DCA selection criteria, in the systematic untertainty analysis, the two separate studies of flow was performed for default and slightly changed *nHitsFit*.

Other sources of systematic uncertainties were negligible (like originating from particle identification) in comparison to those listed above.

The example plots of $v_n\{2\}(p_T)$ for different data selection criteria are shown in Figures 4.11 and 4.12.

The final systematic uncertainty is calculated as weighted average of the deviation from the ratio equal unity:

$$\sigma_{sys} = \frac{\sum_i^N ratio_i * 1/\sigma_{i,stat}}{\sum_i^N 1/\sigma_{i,stat}} \tag{4.1}$$

Where: σ_{sys} is the systematic error, N is the number of points in ratio, $\sigma_{i,stat}$ is the statistical uncertainty of given ratio point. The point's weight is inversely proportional to the $\sigma_{i,stat}$ of it. The Tables 4.4 and 4.5 consist of percentage contribution of each of source of the systematic uncertainties for v_2 and v_3 measurements.

The rounded sums of listed systematical uncertainty contributions are included in Table 4.6.

particle	DCA	nHits	V_z	$\Delta\eta$
pions	4.1%	0.3%	3.2%.	0.2%
kaons	1.1%	0.4%	2.1%.	0.3%
protons	4.4%	0.3%	2.5%.	0.2%

Table 4.4 – Contributions to systematic uncertainties of v_2 of identified hadrons for Au+Au $\sqrt{s_{NN}} = 39$ GeV.

particle	DCA	nHits	V_z	$\Delta\eta$
pions	9.7%	2.7%	4.6%.	1.0%
kaons	5.8%	5.0%	0.6%.	2.0%
protons	9.5%	1.4%	8.7%.	0.7%

Table 4.5 – Contributions to systematic uncertainties of v_3 of identified hadrons for Au+Au $\sqrt{s_{NN}} = 39$ GeV.

v_n	pions	kaons	protons
v_2	5.3%	4.4%	4.7%
v_3	11.1%	7.9%	11.9%

Table 4.6 – Systematic uncertainties of v_n of identified hadrons for Au+Au $\sqrt{s_{NN}} = 39$ GeV.

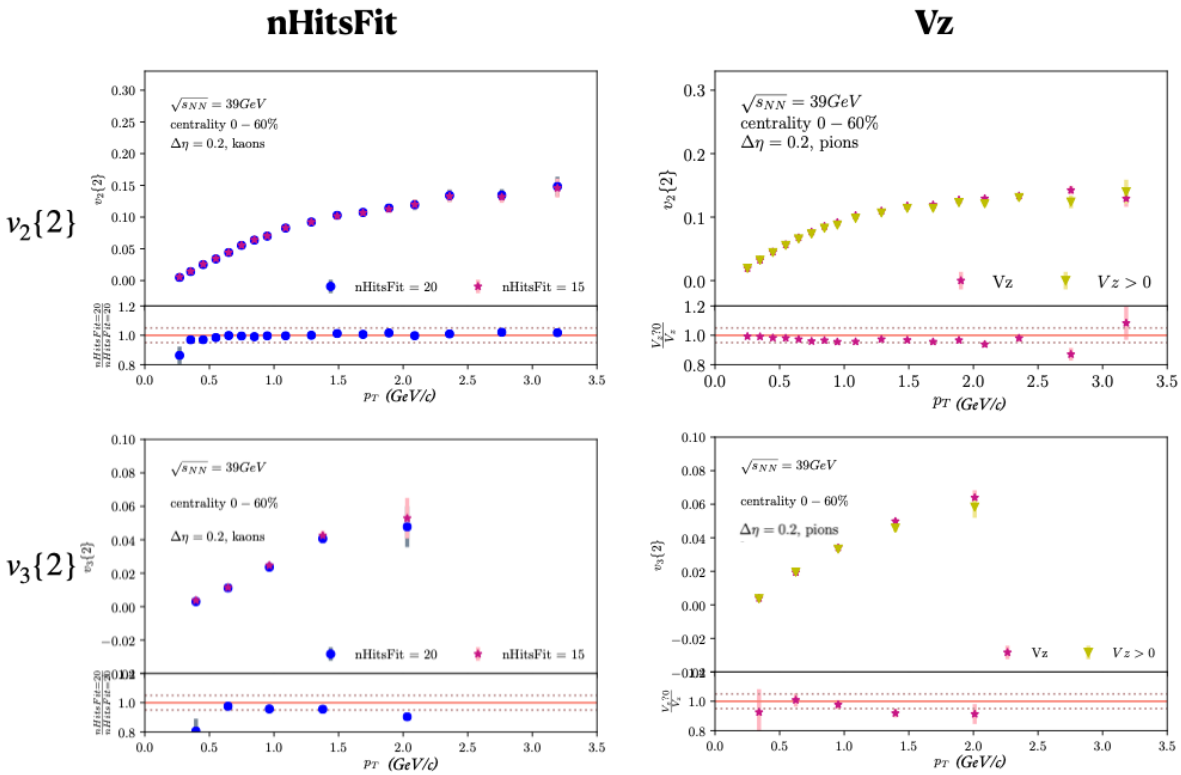

Figure 4.11 – First column consists of the $v_2\{2\}(p_T)$ (top) and $v_3\{2\}(p_T)$ (bottom) panels with different $\Delta\eta$ between sub-events, the right one correspond to two possible requirements considering DCA for Au+Au at $\sqrt{s_{NN}} = 39$ GeV. The bottom panels correspond to ratios of two data sets. This thesis

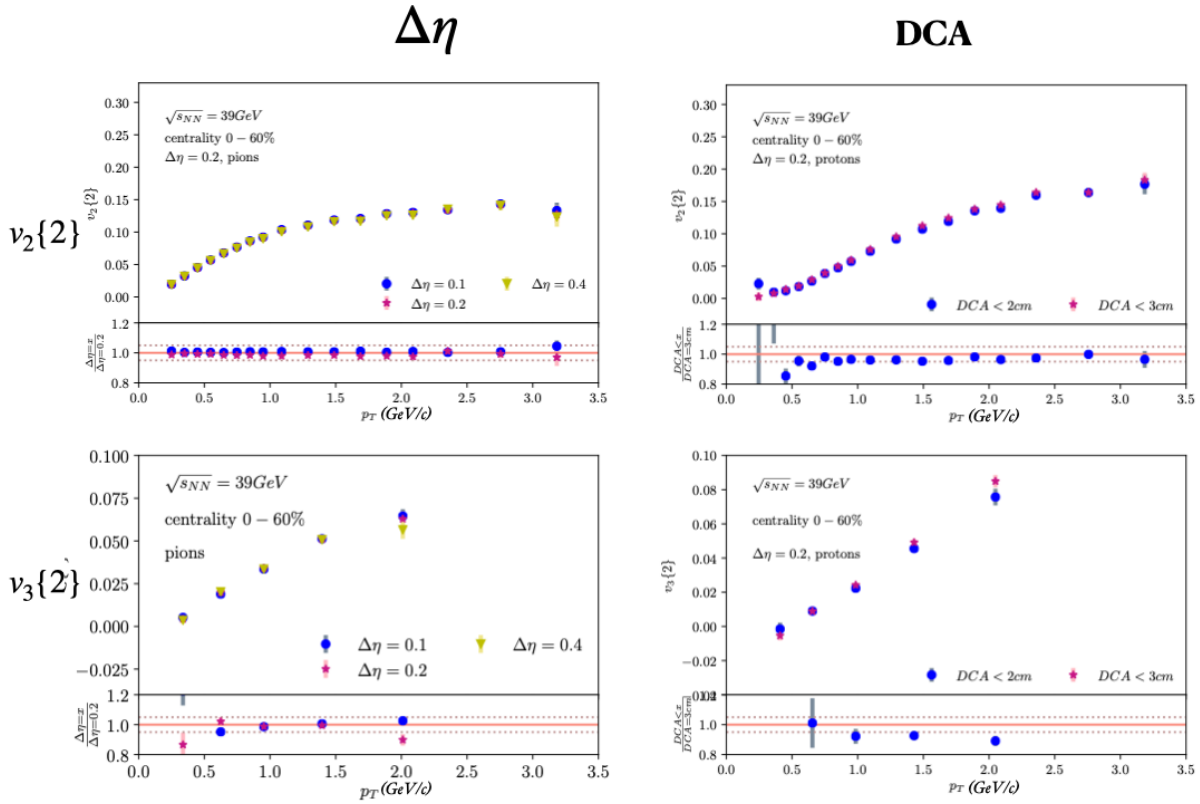

Figure 4.12 – First column consists of the $v_2\{2\}(p_T)$ (top) and $v_3\{2\}(p_T)$ (bottom) panels with two different minimums hits in the particle track requirement, the right one correspond to events with V_Z positive and in whole range for Au+Au at $\sqrt{s_{NN}} = 39$ GeV. The bottom panels correspond to ratios of two data sets. This thesis

Chapter 5

Beam Energy dependence of elliptic and tringular flow

This is one of two most substantial chapters of this thesis. It consists the main results of the studies performed in frame of this PhD project. In this chapter, the studies of azimuthal anisotropies in newly-created matter's dynamics using experimental STAR data is described. Firstly, the comparisons with already published by STAR data are shown. Then, the flow studies for Au+Au at $\sqrt{s_{NN}} = 200$ GeV are reported. Subsequently, the measurements for low beam energies are shown and discussed in two options: *integrated* and p_T-*differential*.

5.1 Comparison with published STAR results

The comparison with already published results for elliptic flow was performed. The Collaboration had already obtained results for v_2 of identified hadrons for various centralities [73]. As the purely technical aspects of different flow harmonics' calculations do not differ relevantly, such comparison could give information about possible mistakes in performed computations. In Figures 5.1, 5.2, and 5.3 the comparisons between various centralities for Au+Au collisions at $\sqrt{s_{NN}} = 39$ GeV are shown. In the bottom panels, there are ratios between data from this work and already published by STAR.

Both data sets are in a reasonable agreement. The methods used in both studies are different: in published data authors used the Event Plane method [73], while in this work the 2PC one. Another source of possible discrepancies is different binning of two data sets. Consequently, the ratio is between data obtained in this analysis and the fit to the published data. That is why the data sets are not expected to overlap, but the difference up to 10% is considered acceptable.

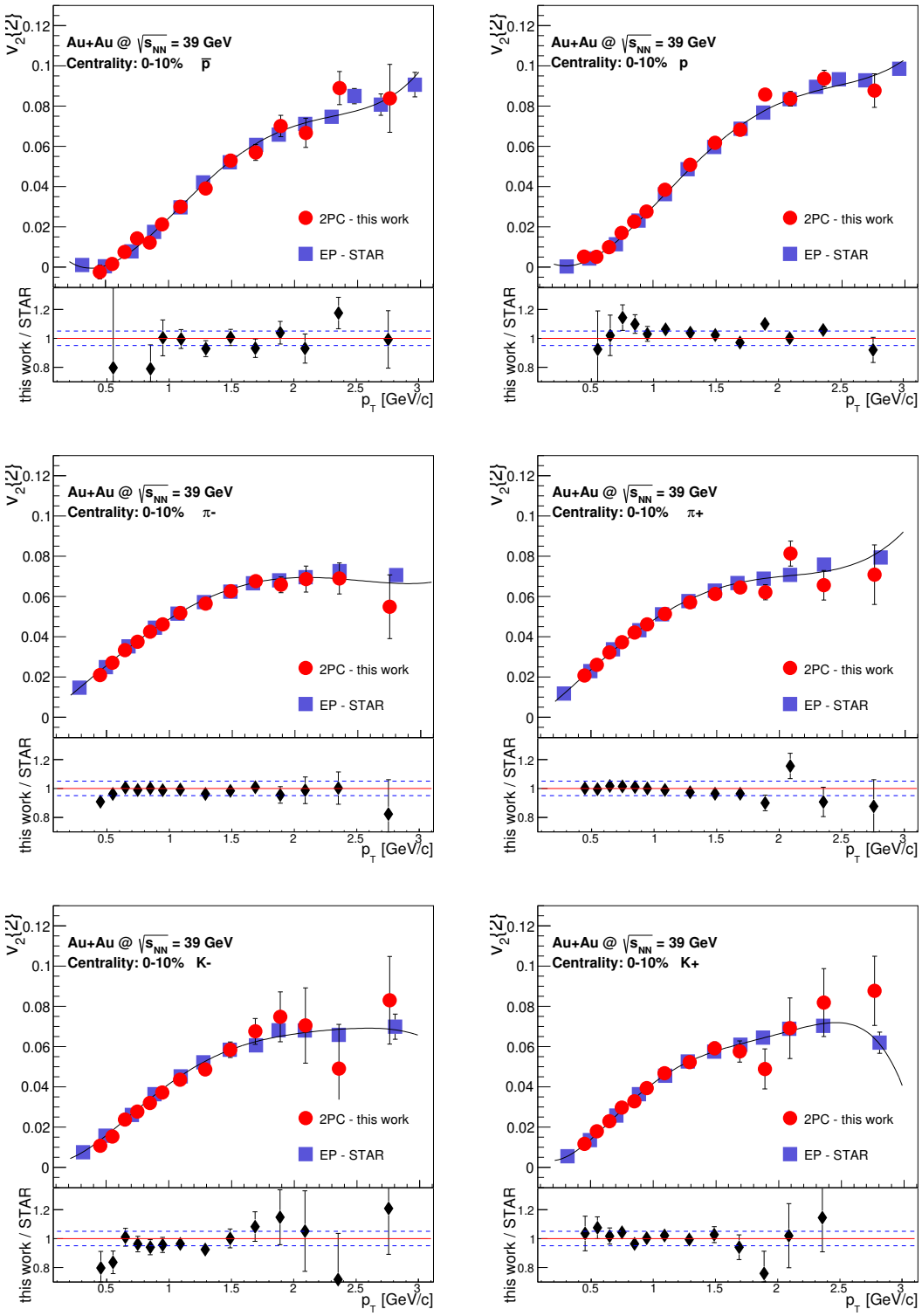

Figure 5.1 – Comparison of 2PC flow and STAR published flow measurements using Event Plane method [73] for Au+Au at $\sqrt{s_{NN}} = 39$ GeV at $0 - 10\%$ centrality. In the bottom panels there is a ratio between *this work* to fit to the STAR published data, where the dotted lines correspond to the 5% difference.

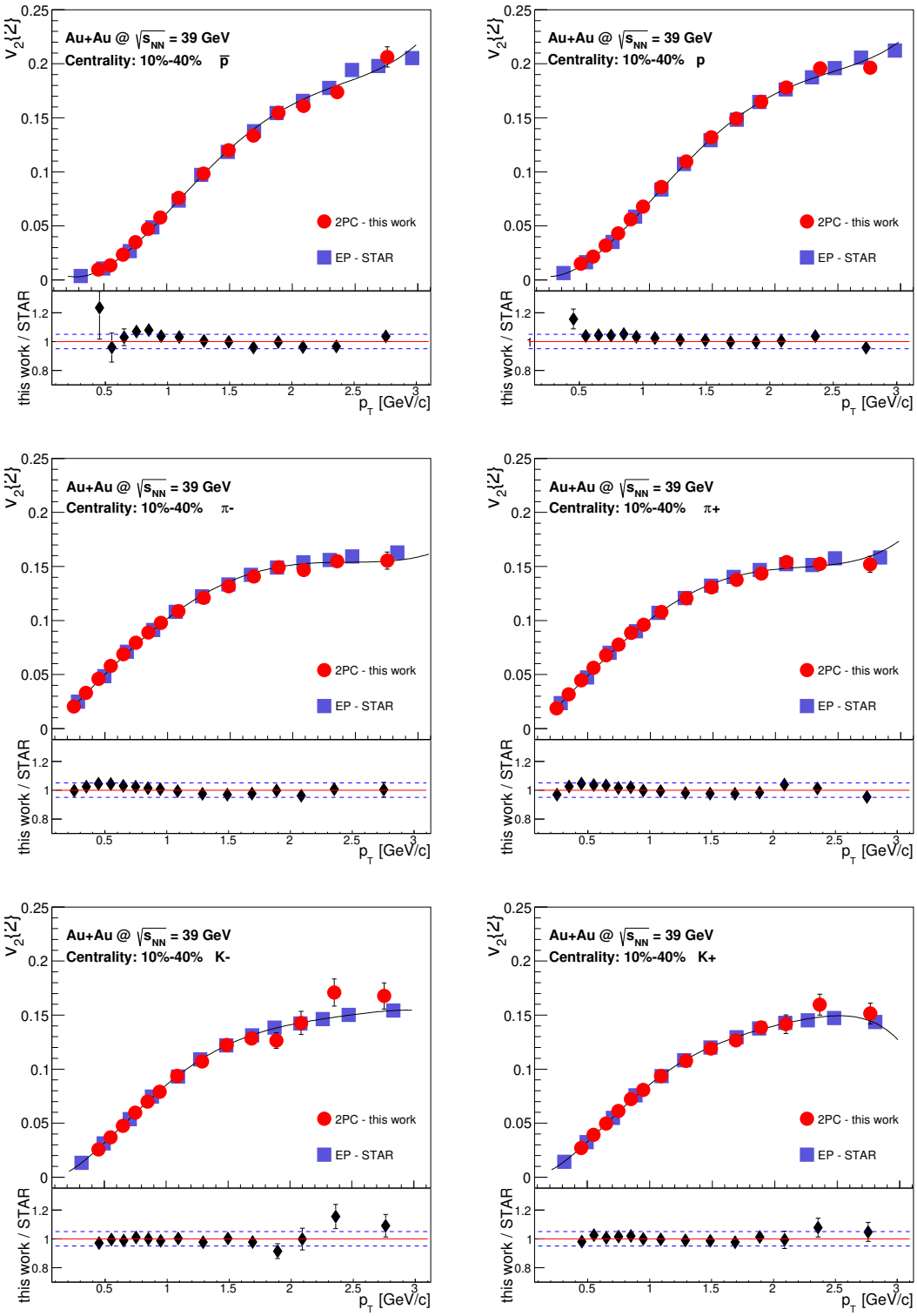

Figure 5.2 – Comparison of 2PC flow and STAR published flow measurements using Event Plane method [73] for Au+Au at $\sqrt{s_{NN}} = 39$ GeV at $10\% - 40\%$ centrality. In the bottom panels there is a ratio between *this work* to fit to the STAR published data, where the dotted lines correspond to the 5% difference.

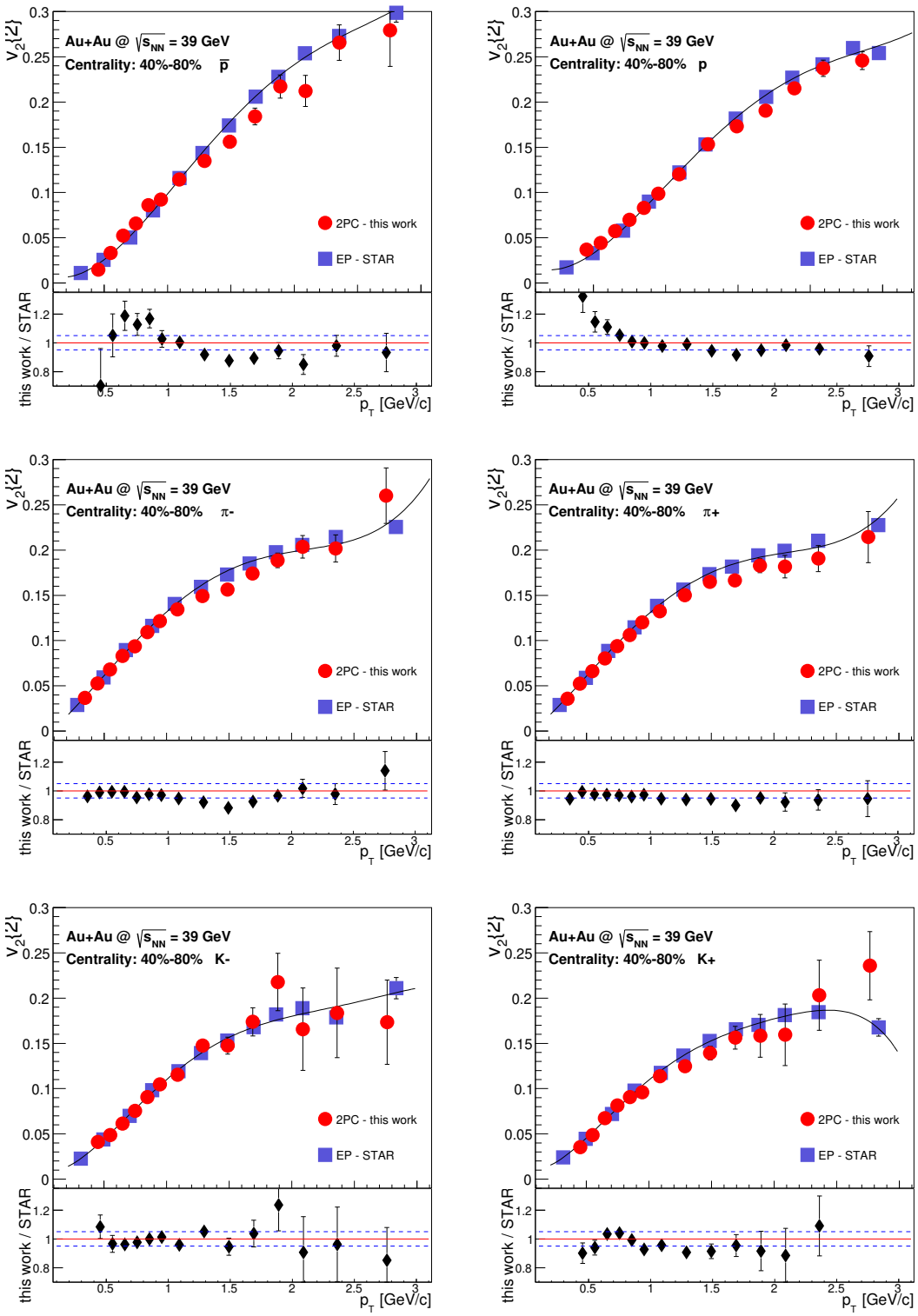

Figure 5.3 – Comparison of 2PC flow and STAR published flow measurements using Event Plane method [73] for Au+Au at $\sqrt{s_{NN}} = 39$ GeV at $40\% - 80\%$ centrality. In the bottom panels there is a ratio between *this work* to fit to the STAR published data, where the dotted lines correspond to the 5% difference.

5.2 Flow of identified hadrons for Au+Au collisions at $\sqrt{s_{NN}} = 200$ GeV

The top RHIC energy is the baseline for the beam energy studies of the flow harmonics at STAR. This section consists of the first results of the identified hadron $v_{3,4}$ measurements STAR, which are already under revision of the Collaboration and will be soon published. In Figure 5.4 the difference between particles and antiparticles flow are shown. As they are negligible, the rest of the analysis was performed for the hadrons of both signs.

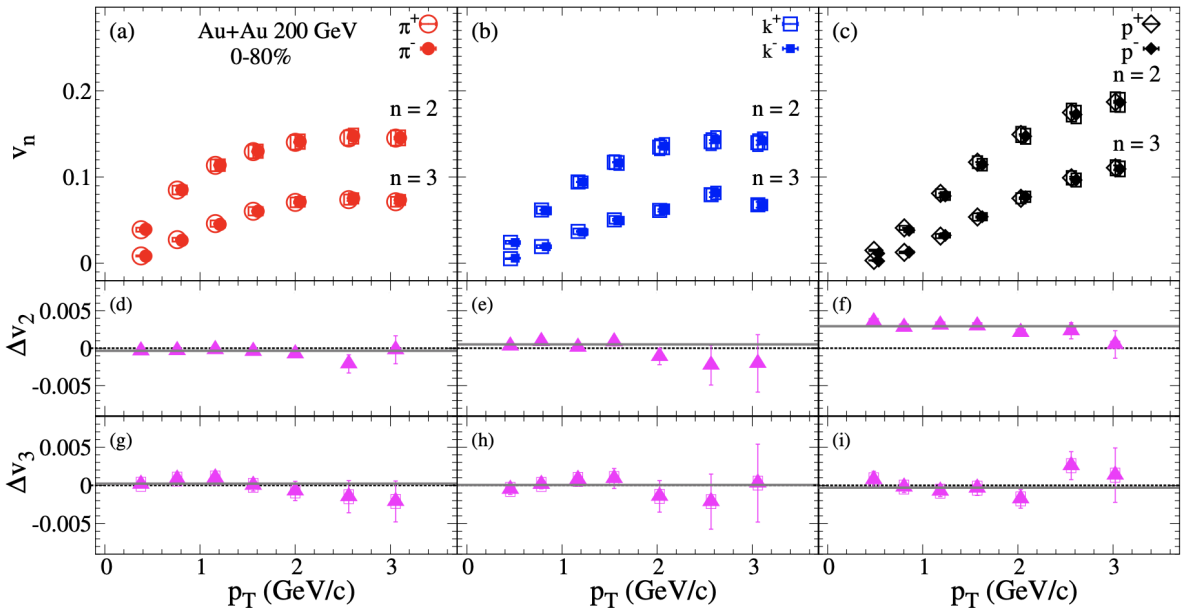

Figure 5.4 – The particles and anti-particles elliptic and triangular flow for $0-80\%$ central Au+Au collisions at $\sqrt{s_{NN}} = 200$ GeV, using the two-particle cumulant method. The lower panels (d)-(i) represent the v_2 and v_3 difference between particles and anti-particles. This thesis

A clear centrality dependence of $v_{2,3,4}$ as a function of p_T is observed for π, K, and p at midrapidity ($|y| < 1.0$) of the Au+Au collisions at $\sqrt{s_{NN}} = 200$ GeV as shown in Fig. 5.5. The measurements show a mass order dependence for the presented flow harmonics. The v_n values are found to be higher in peripheral collisions (30-80% centrality) compared to those in central collisions (0-30% centrality). This observation is consistent with the picture in which the initial spatial anisotropy being the mean driving force of final momentum anisotropy.

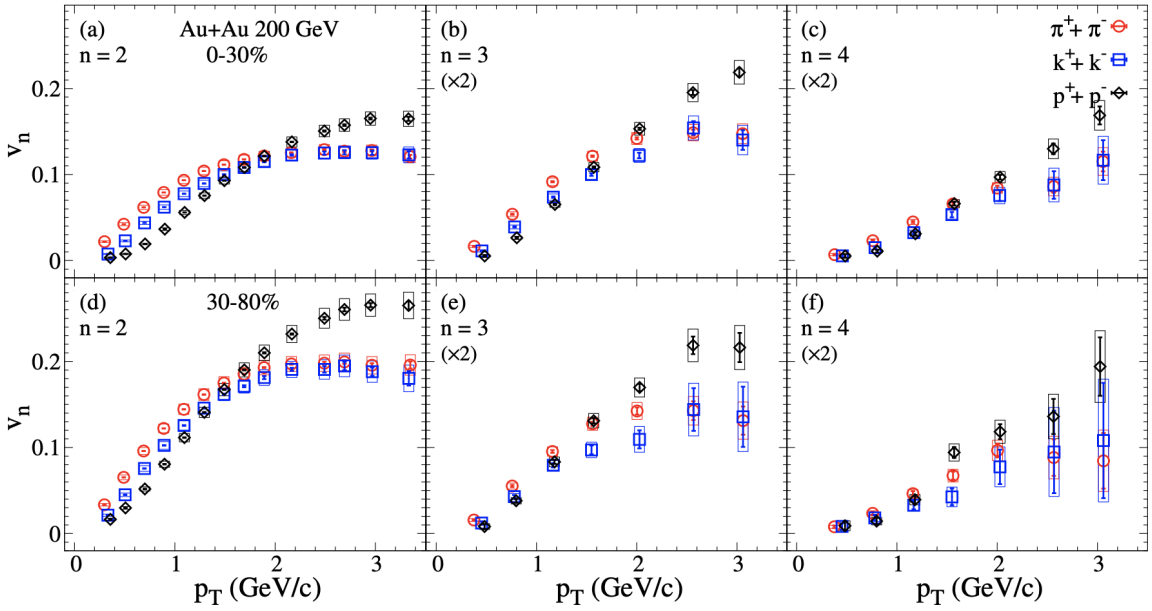

Figure 5.5 – The transverse momentum dependence identified particles v_2, v_3, and v_4 for 0–30% and 30˘80% central Au+Au collisions at $\sqrt{s_{NN}} = 200$ GeV. This thesis

Figure 5.6 shows the scaled kinetic energy dependence of $v_{2,3,4}$ for π, K, and p at midrapidity ($|y| < 1.0$) of 0-30% and 30–80% central Au+Au collisions at $\sqrt{s_{NN}} = 200$ GeV. The measurements indicate a scaling for the v_n/nq vs KE_T/nq for both presented centrality. These scaling properties of v_2, v_3 and v_4 may indicate that the measured collective flow develops during the partonic phase.

5.3 Flow of identified hadrons for Au+Au collisions at BES energies

Since the increasing with lowering the collision energy difference between particles and antiparticles flow was observed, the studies of systems obtained at BES energies (below 200 GeV) requires the distinguishing particles' signs. The relations between positive and negative particles flow are described in this section in great details.

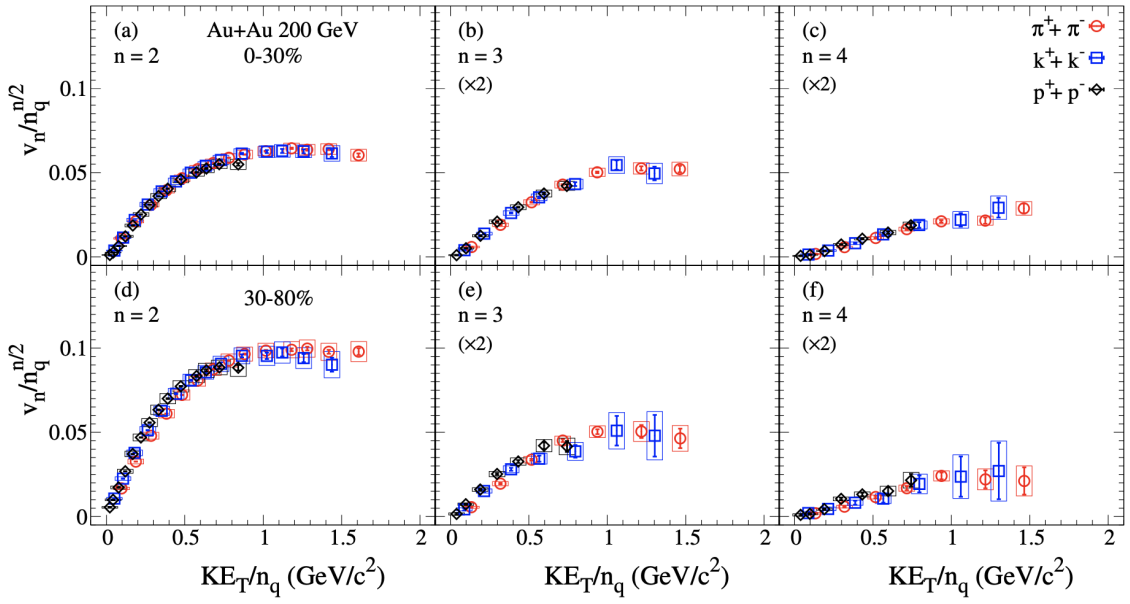

Figure 5.6 – The transverse mass dependence identified particles v_2, v_3, and v_4 for 0˘30% and 30˘80% central Au+Au collisions at $\sqrt{s_{NN}} = 200$ GeV. This thesis

5.3.1 Integrated flow harmonics

Described in Section 2.2.5 integrated flow over transverse momenta provides information about the dependence of the flow on the multiplicity of the collision. The examined data (Fig. 5.7 and 5.8) show the clear particle species dependence of both v_n for all the collision energies. As these are integrated by the p_T measurements, such differences can be explained by looking into distributions of transverse momenta of given types of particles. Protons' spectra is dominated by the higher p_T in comparison to remnant mesons [143], what results in the higher integrated v_n. For the centralities up to $\sim 30\%$ the $v_n\{2\}$ increase nearly linearly, from the mid-central collisions the curves flatten. Finally, in peripheral collisions, the $v_n\{2\}$ is dominated by the viscous effects, which causes a decrease of measured flow.

The triangular flow shows similar differences between $v_3\{2\}$ of various species. As it is a *fluctuation-driven* quantity, the non-zero signal corresponds to the possible overlap region's granularities' presence. However, the measured signal due to the high uncertainties does not provide the information about the dependence of $v_3\{2\}$ on the collision's centrality.

In Figures 5.9 and 5.10 the dependence of the $v_n\{2\}$ on the collision energy is pre-

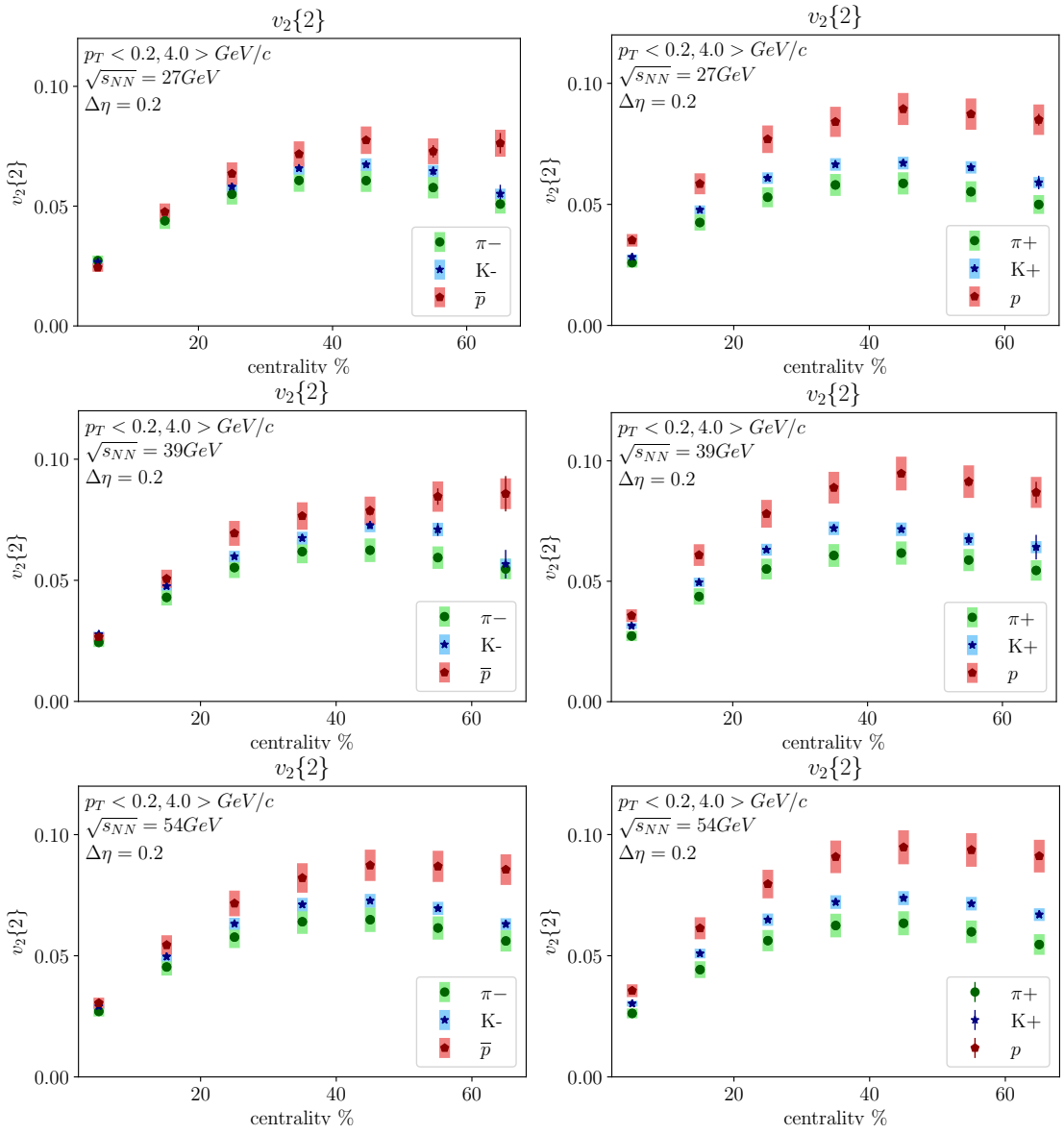

Figure 5.7 – 2PC integrated over p_T $v_2\{2\}$ for Au+Au collisions at $\sqrt{s_{NN}} = 27, 39$ and 54.4 GeV in function of centrality. The $\Delta\eta = 0.2$ and the p_T range is 0.2 to 4.0 GeV/c. This thesis

sented. As the eccentricity does not differ relevantly in these range of $\sqrt{s_{NN}}$ between bins of centrality, all the differences originate from the transport proprieties of the matter. The general trend shows that increase of both flow harmonics with the collision energy. However, the effect is not substantial.

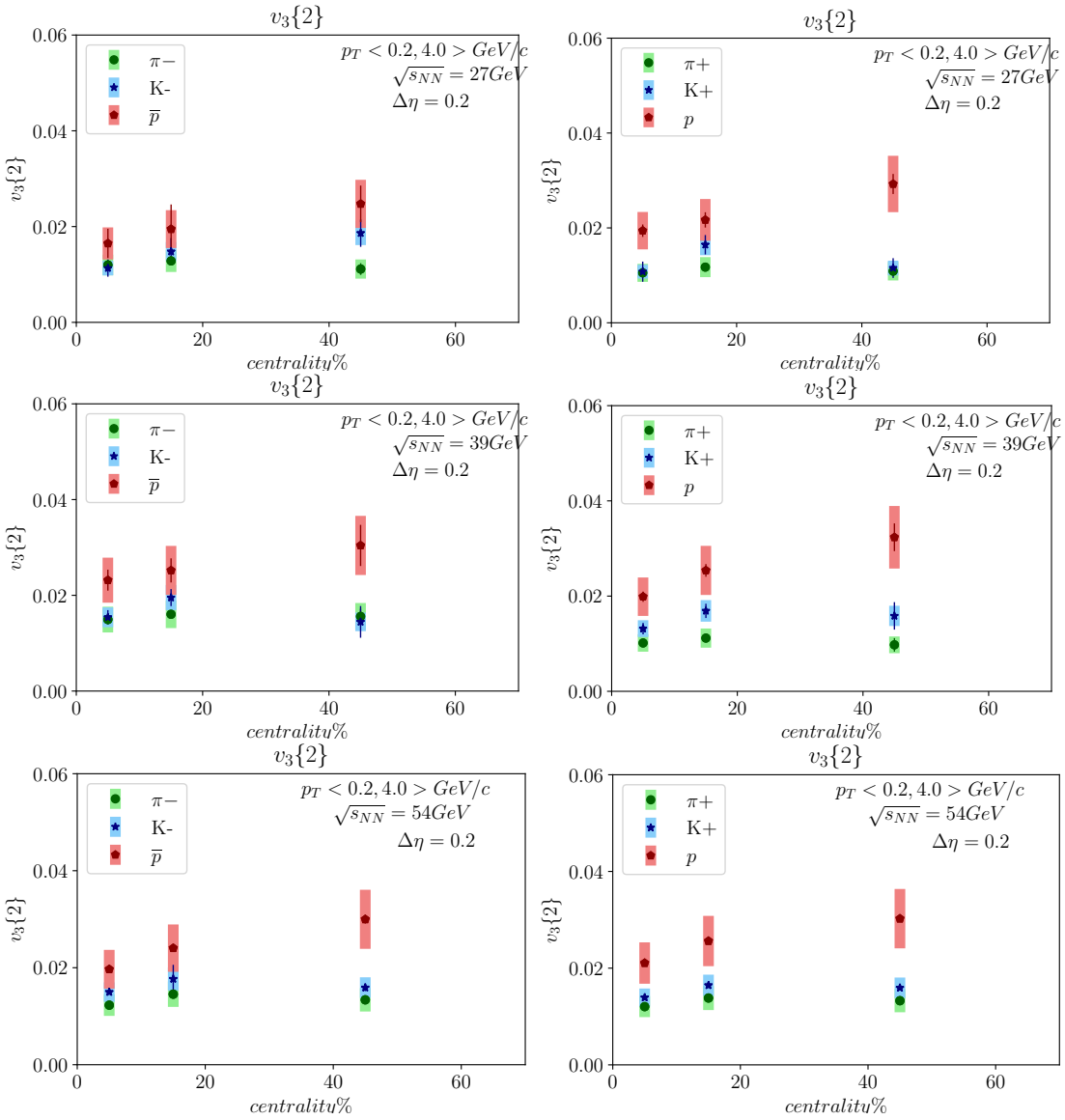

Figure 5.8 – 2PC integrated over p_T $v_3\{2\}$ for Au+Au collisions at $\sqrt{s_{NN}} = 27, 39$ and 54.4 GeV in function of centrality. The $\Delta\eta = 0.2$ and the p_T range is 0.2 to 4.0 GeV/c. This thesis

5.3.2 p_T-differential flow harmonics

The studies of p_T-differential flow harmonics were performed for the $0 - 60\%$ centrality range. The triangular flow's signal is small, so the high statistics are needed for the reasonably performed investigation. Nonetheless, the measured flow in the peripheral collisions is dominated by the viscous effects (see the previous section), and in order to avoid such contribution, these centralities are eliminated.

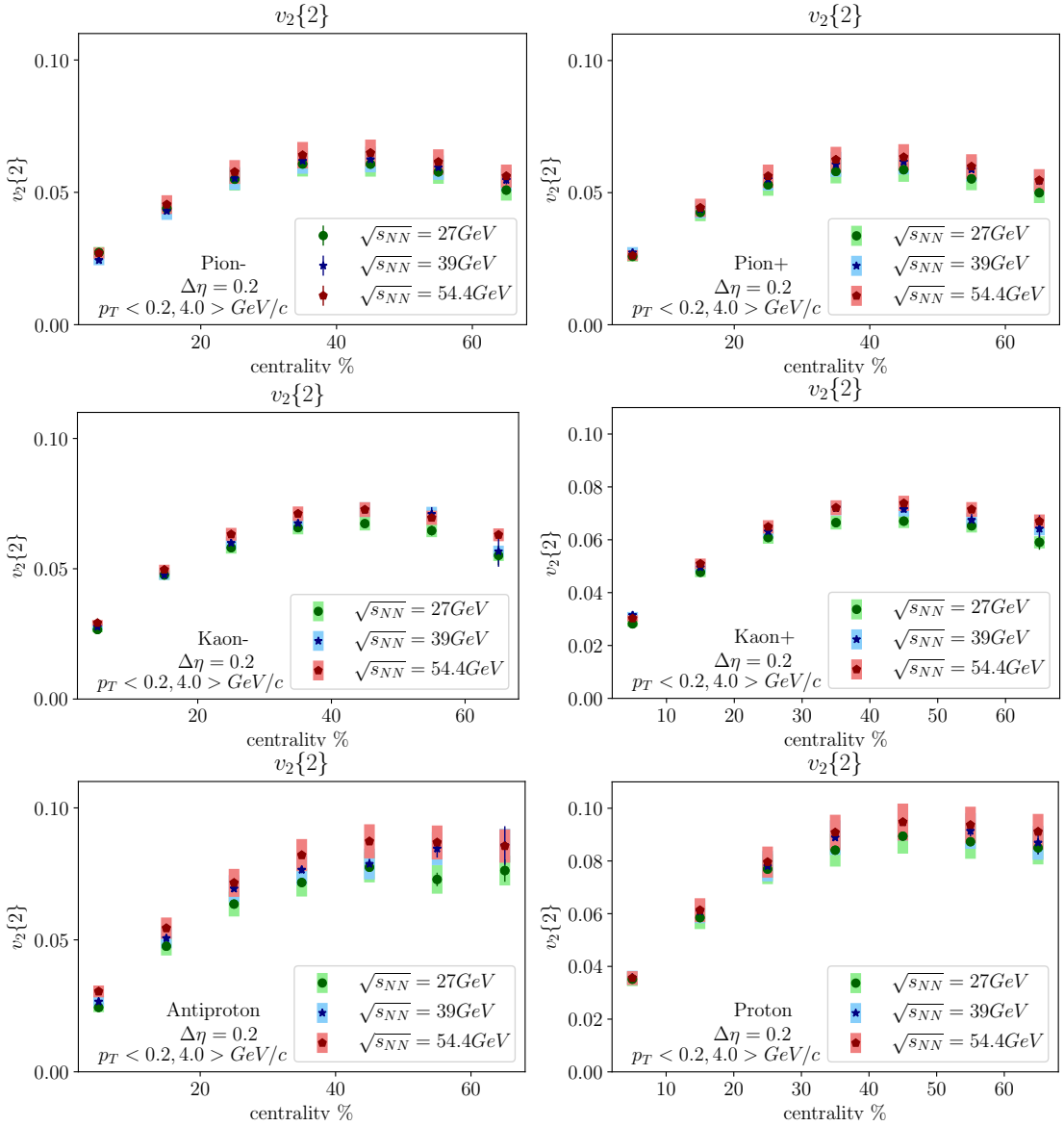

Figure 5.9 – The energy dependence of 2PC integrated over p_T $v_2\{2\}$ for Au+Au collisions at $\sqrt{s_{NN}} = 27, 39$ and 54.4 GeV in function of centrality. The $\Delta\eta = 0.2$ and the p_T range is 0.2 to 4.0 GeV/c. This thesis

For all three energies $\sqrt{s_{NN}} = 27, 39$ and 54.4 GeV the mass ordering is visible. Up to $p_T \sim 1.5$ GeV/c, the elliptic flow curves are parallel and increasing inversely to the mass of particles. At higher transverse momenta there is a clear split between baryons (protons' flow is relevantly higher) and mesons (pions' and kaons' flow is similar, start to overlap).

The triangular flow keeps similar trends as the elliptic one, although the uncertainties are high. The mass ordering for all the energies is visible for low p_T, and since the last

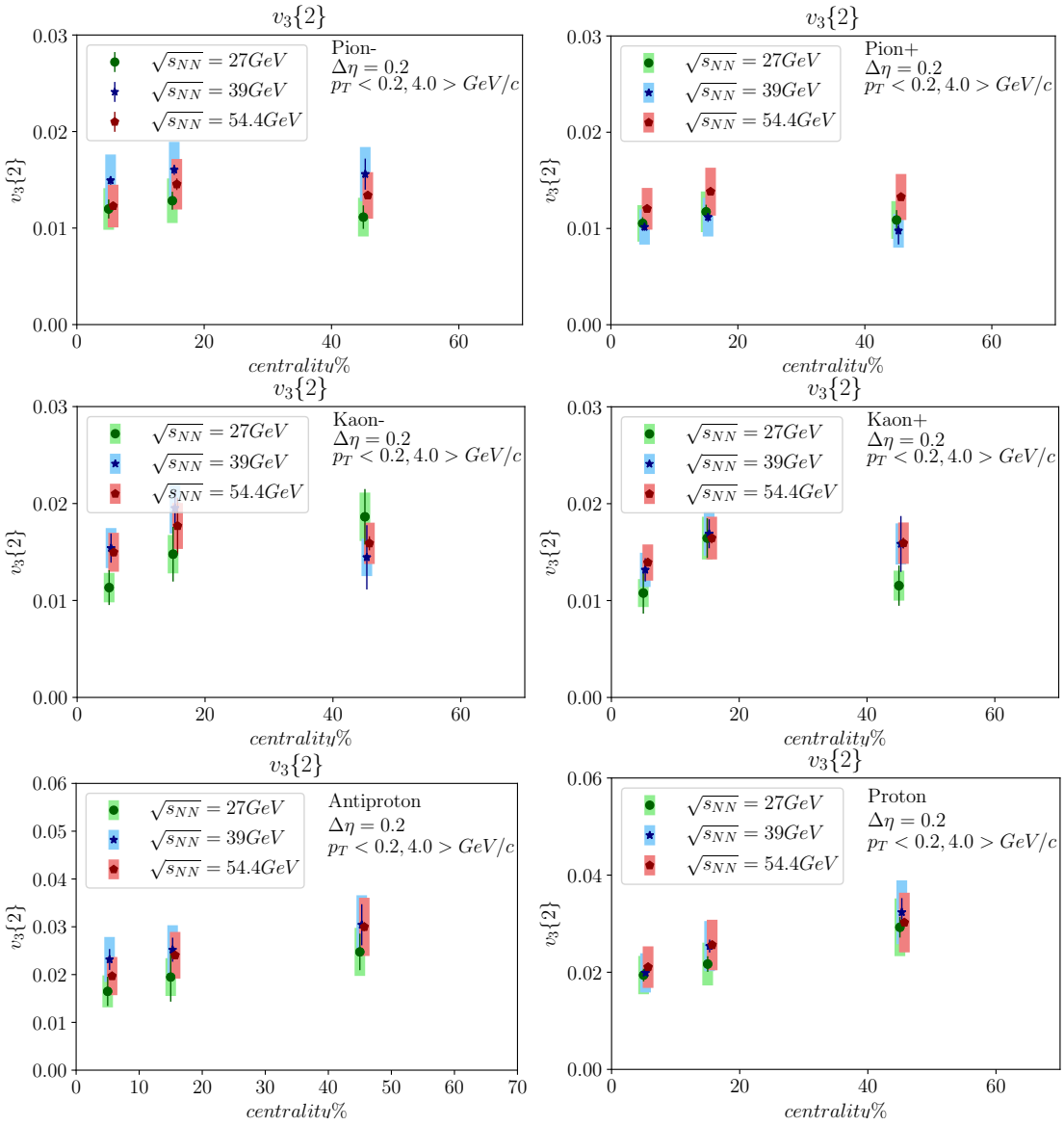

Figure 5.10 – The energy dependence of 2PC integrated over p_T $v_3\{2\}$ for Au+Au collisions at $\sqrt{s_{NN}} = 27, 39$ and 54.4 GeV in function of centrality. The $\Delta\eta = 0.2$ and the p_T range is 0.2 to 4.0 GeV/c. This thesis

bins were merged, it is impossible to make a statement about the higher-p_T region.

n_q flow scaling

The number of constituent quarks scaling was performed on the data from all three energies for both elliptic and triangular flow. The negative particles do not break the

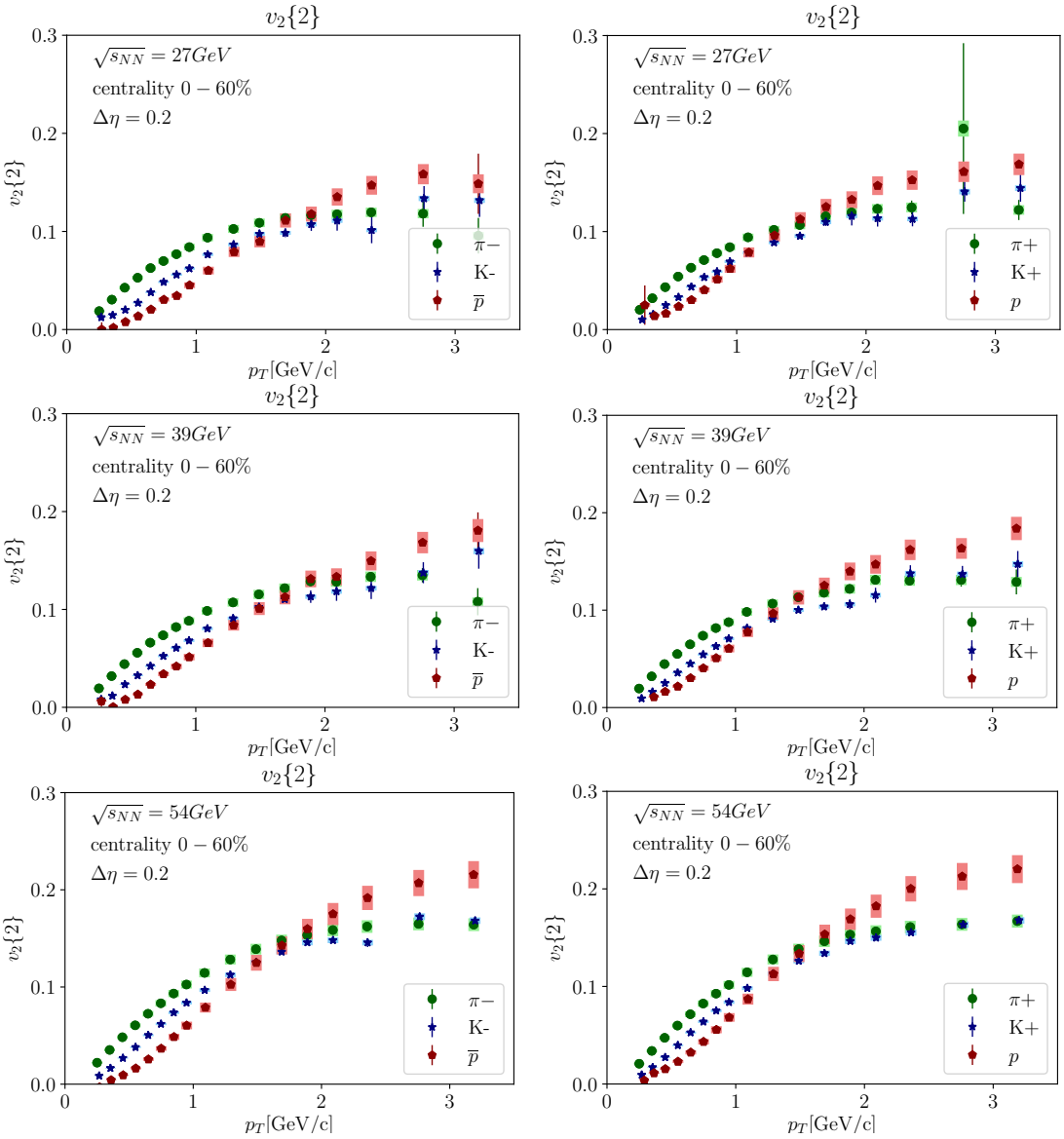

Figure 5.11 – 2PC p_T-differential $v_2\{2\}$ for Au+Au collisions at $\sqrt{s_{NN}} = 27, 39$ and 54.4 GeV in centrality $0-60\%$. The $\Delta\eta = 0.2$. This thesis

scaling, while there is a visible deviation in protons, especially in triangular flow.

5.3.3 Particle-antiparticle flow difference

Studies of differences in the flow between particles and antiparticles are still ongoing. The theoretical models are developing; however, authors need bigger constrain from the experimental side. In this project, several investigations are proposed, which could be used

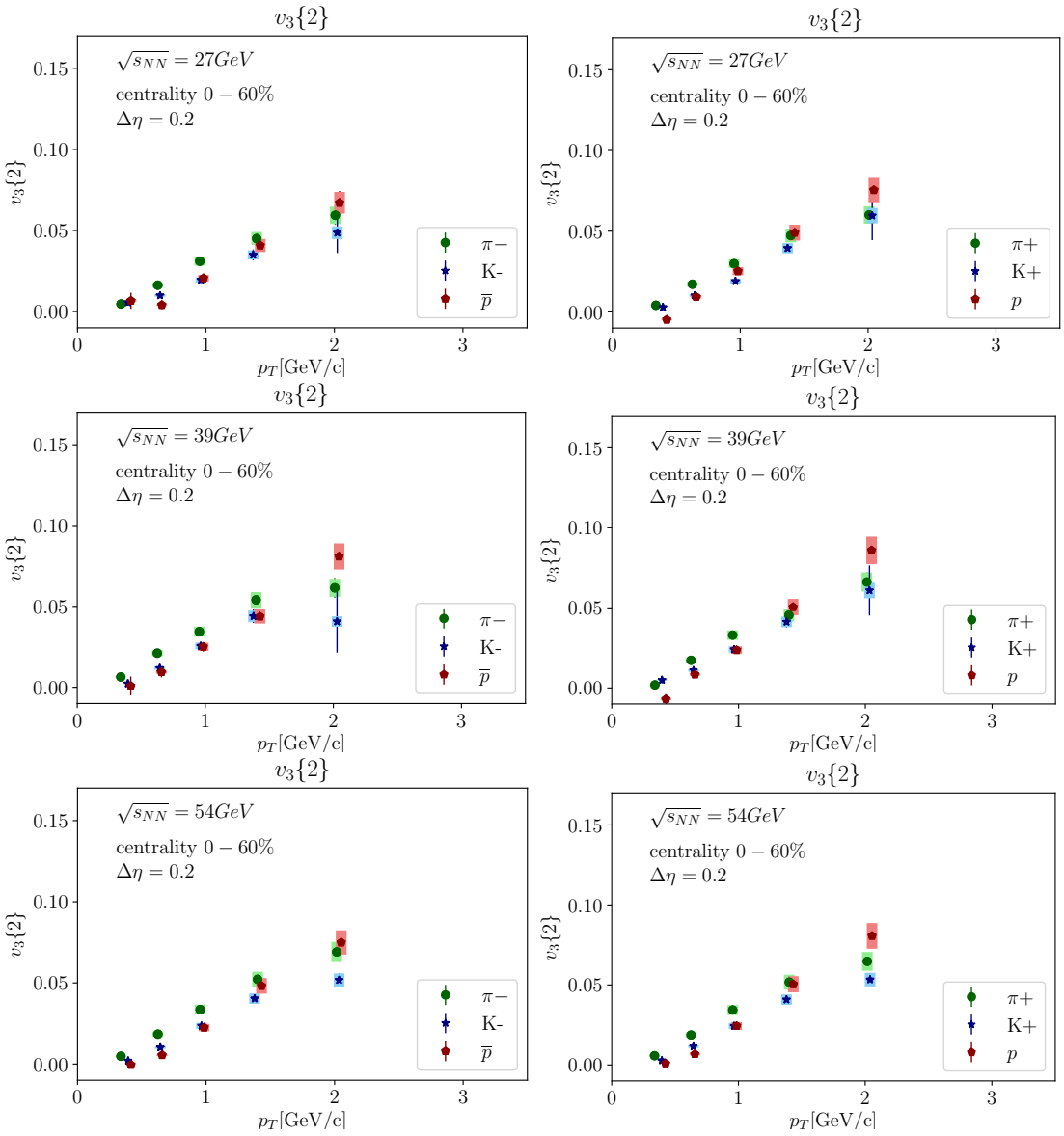

Figure 5.12 – 2PC p_T-differential $v_3\{2\}$ for Au+Au collisions at $\sqrt{s_{NN}} = 27, 39$ and 54.4 GeV in centrality $10\% - 60\%$. The $\Delta\eta = 0.2$. This thesis

to validate or reject some of the theoretical scenarios.

5.3.4 Triangular flow

Firstly, the 2-Particle Cumulants method was applied in the investigation of the differences in p_T-differential elliptic flow of particles vs. antiparticles for Au+Au collisions at $\sqrt{s_{NN}} = 27, 39$ and 54.4 GeV and shown in Figure 5.15.

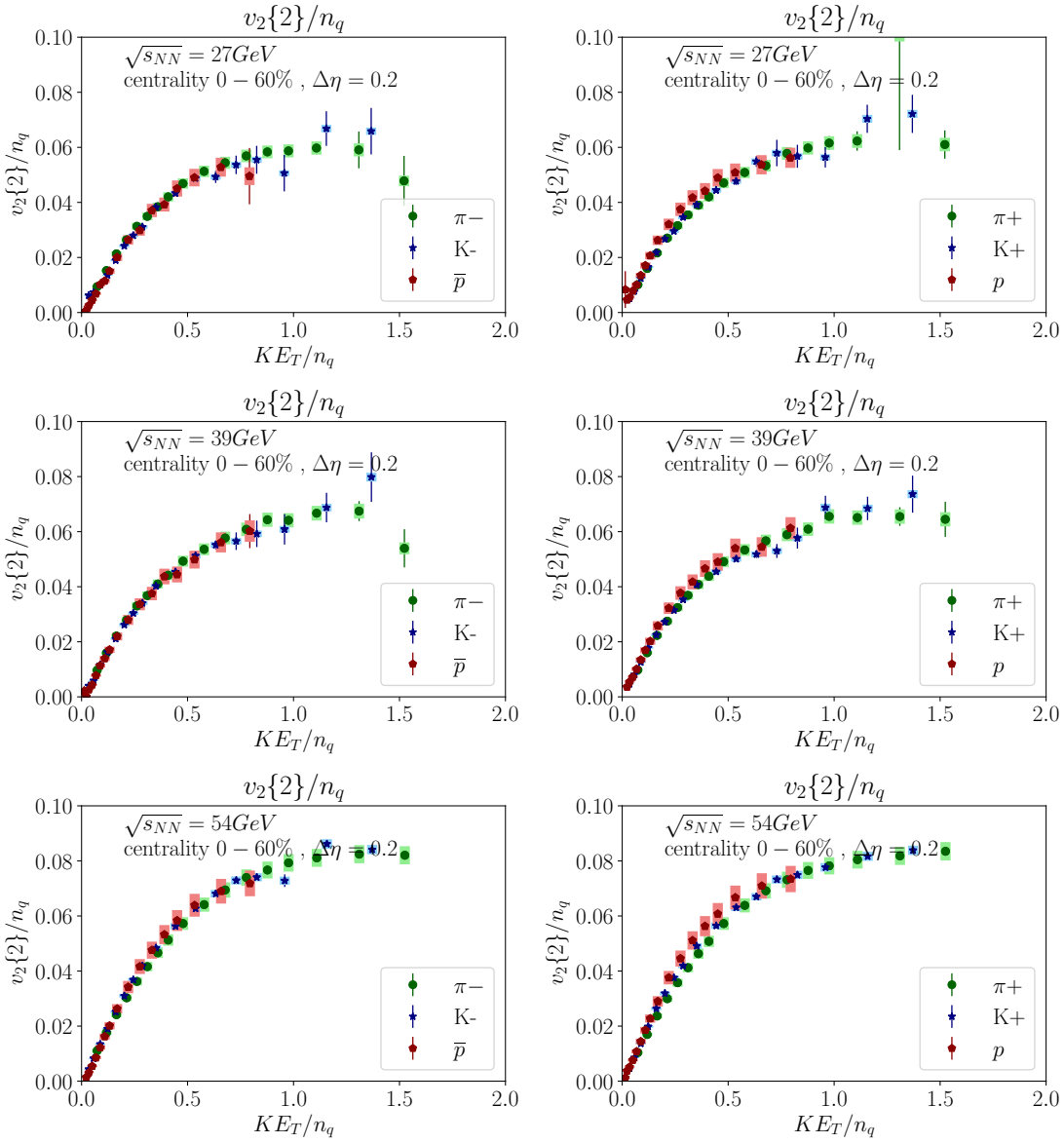

Figure 5.13 – 2PC p_T-differential $v_2\{2\}$ for Au+Au collisions at $\sqrt{s_{NN}} = 27, 39$ and 54.4 GeV in centrality $0-60\%$ scaled with number of constituent quarks $(v_n\{2\}/n_q^{n/2}$ in function of transverse kinetic energy KE_T. This thesis

In Section 2.3.1, in proposed **Scenario 1 "Viscous Corrections"**, authors relate the differences in v_n with the implementation of the viscous corrections in flowing matter. As triangular flow is more sensitive to such effects than elliptic one, investigating the differences between particles and antiparticles $v_3\{2\}$ was performed. Fig 5.16, the differences for all energies between the flow of kaons positive and negative is close to zero.

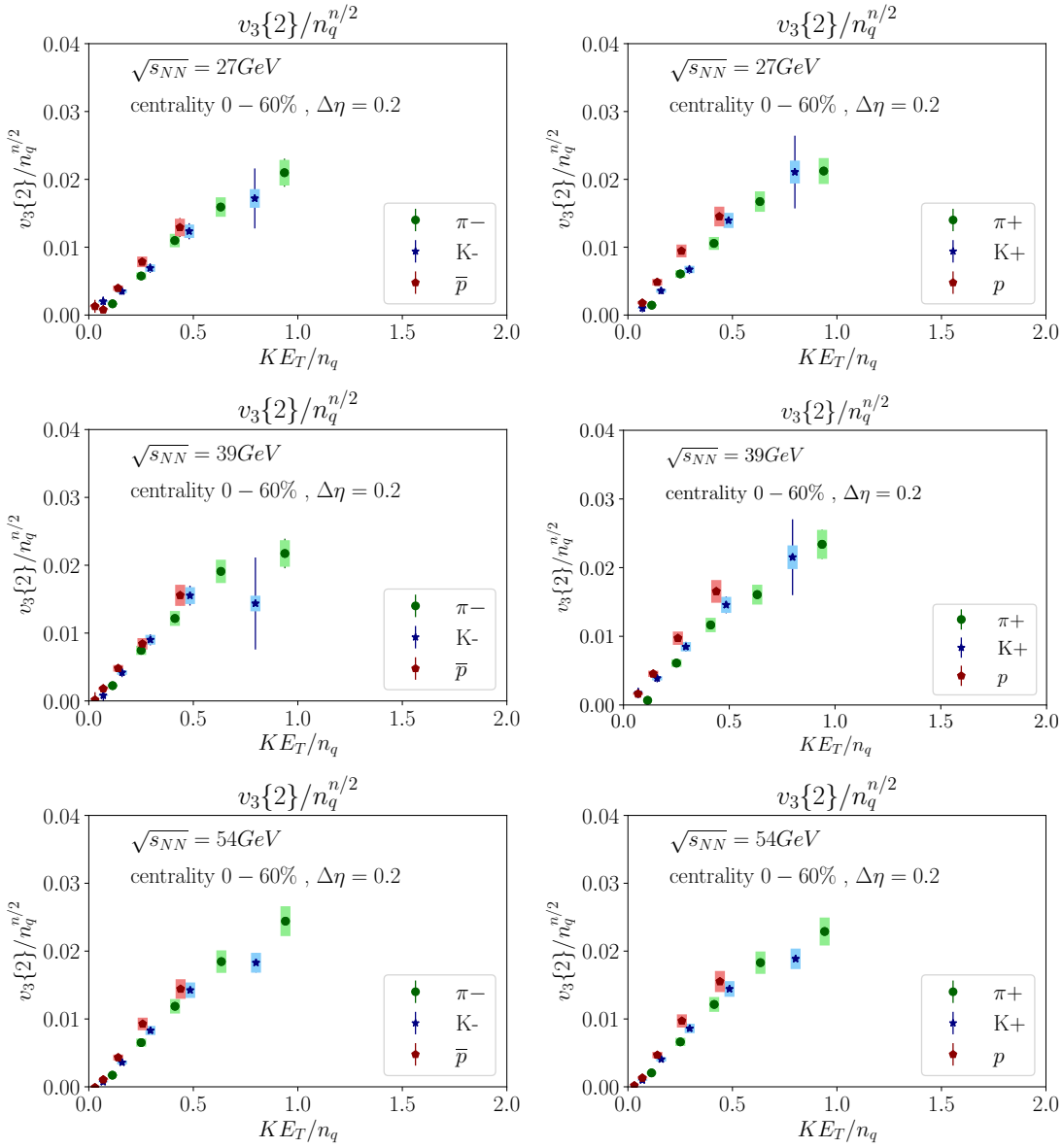

Figure 5.14 – 2PC p_T-differential $v_3\{2\}$ for Au+Au collisions at $\sqrt{s_{NN}} = 27, 39$ and 54.4 GeV in centrality $0-60\%$ scaled with number of constituent quarks ($v_n\{2\}/n_q^{n/2}$ in function of transverse kinetic energy KE_T. This thesis

Pions' differences in $v_3\{2\}$ do not variate significantly (< 0.01). The only exception is $\sqrt{s_{NN}} = 39$ GeV, where π^- v_3 is slightly higher than π^+. In the case of protons' and antiprotons' triangular flow, the higher p_T, the bigger difference observed. Figure 5.17 shows that the collision energy dependence of elliptic and triangular flow differences between particles and antiparticles. The same trends are visible: the growing difference between

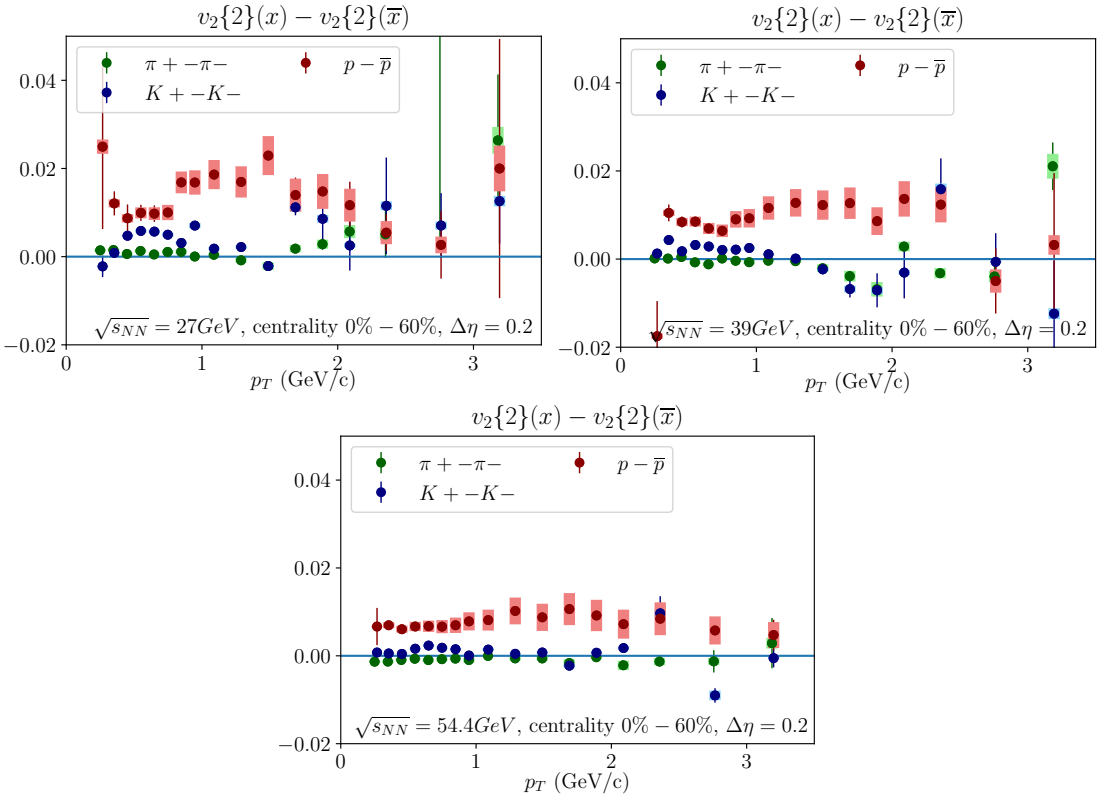

Figure 5.15 – Difference in 2PC p_T-differential $v_2\{2\}$ of particles and anti-equivalents for Au+Au collisions at $\sqrt{s_{NN}} = 27, 39$ and 54.4 GeV in centrality $0 - 60\%$. This thesis

baryons with the collision's energy decreases, while both positive and negative mesons have nearly equal $v_3\{2\}$. These results are vital for the theoretical models' development and validation of the proposed **Scenario 1 "Viscous Corrections"**.

n_q-scaling

It is claimed that the n_q scaling is the proof of the common origin of hadrons' flow [72, 73]. It is built during the QGP phase where quarks are deconfined, and they are boosted as separate particles. Subsequently, they are bounded into hadrons, but their flow is already established. Due to such an approach, breaking the scaling means that the flow of given particle specie does not originate completely from the QGP phase.

In Figure 5.18 the range of breaking the scaling of protons and antiprotons is illustrated. In top row there is ratio of p and $\bar{p}$ $v_2\{2\}/n_q$ to the fit of pions' $v_2\{2\}/n_q$ and in bottom one to koans' $v_2\{2\}/n_q$. In both cases, protons break relevantly the scaling - more than 10% for $KE_T/n_q < 0.6$ GeV. While antiprotons violate scaling only up to 10%

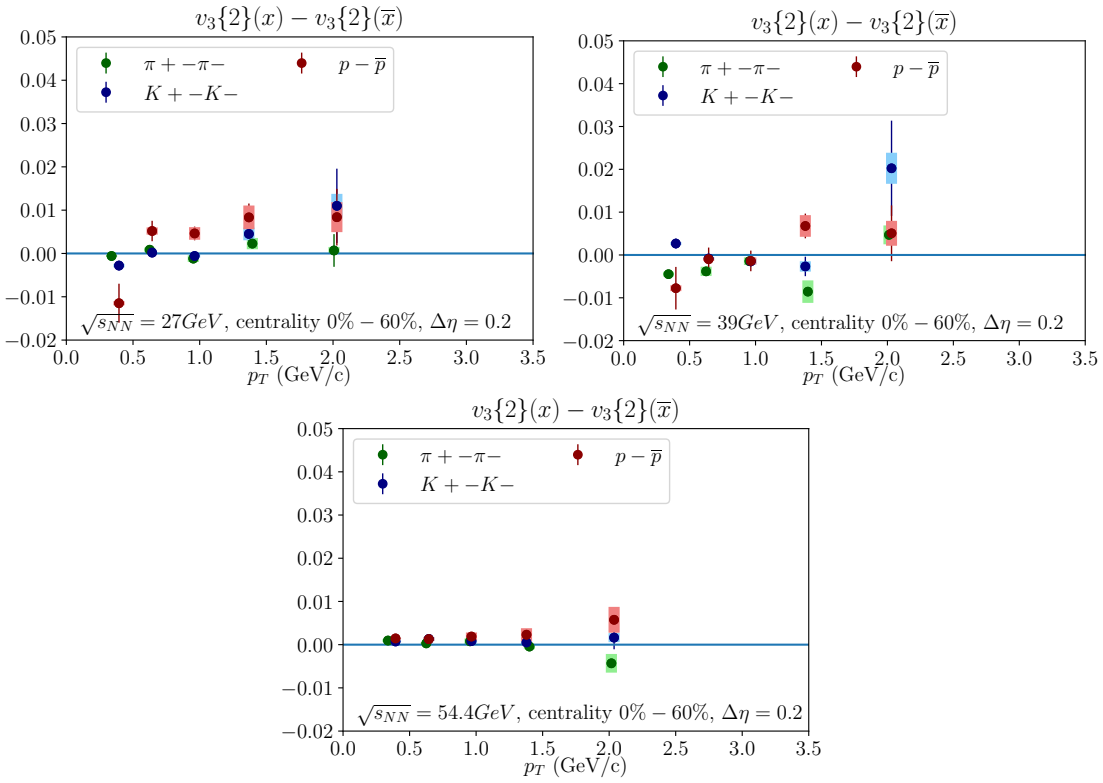

Figure 5.16 – Difference in 2PC p_T-differential $v_3\{2\}$ of particles and anti-equivalents for Au+Au collisions at $\sqrt{s_{NN}} = 27, 39$ and 54.4 GeV in centrality $0 - 60\%$. This thesis

for the Au+Au collisions at $\sqrt{s_{NN}} = 54.4$ GeV, and for lower energies it is up to 5%. The energy dependence is not clear, and could be caused by lack of consideration of the systematic uncertainties in the ratio computation.

These studies provide the starting point for investigating protons flow's various origins, as suggested in **Scenario 2 "Mean field theory"**.

Another theoretical approach explains the differences between particles' and antiparticles flow' using the *Mean field theory*. Kaon as s meson consists of quark and anti-quark, and is characterized by relatively high mass. According to the **Scenario "Transported protons"**, the effect of the potential on kaons is negligible comparing to protons. In such case, if the mass factor is cancelled by scaling, the antiprotons behave oppositely to protons concerning the scaled flow of kaons. In Figure 5.19 the ratio of p and $\bar{p}$ $v_2\{2\}/n_q$ to fitted kaons' $v_2\{2\}/n_q$ is shown for Au+Au collisions at $\sqrt{s_{NN}} = 39$ GeV. The ratio for negative particles is equal to unity within the uncertainties, while for protons, it is more than 10% higher. If the ratios of p and $\bar{p}$ were the mirror reflection to K, it could be treated

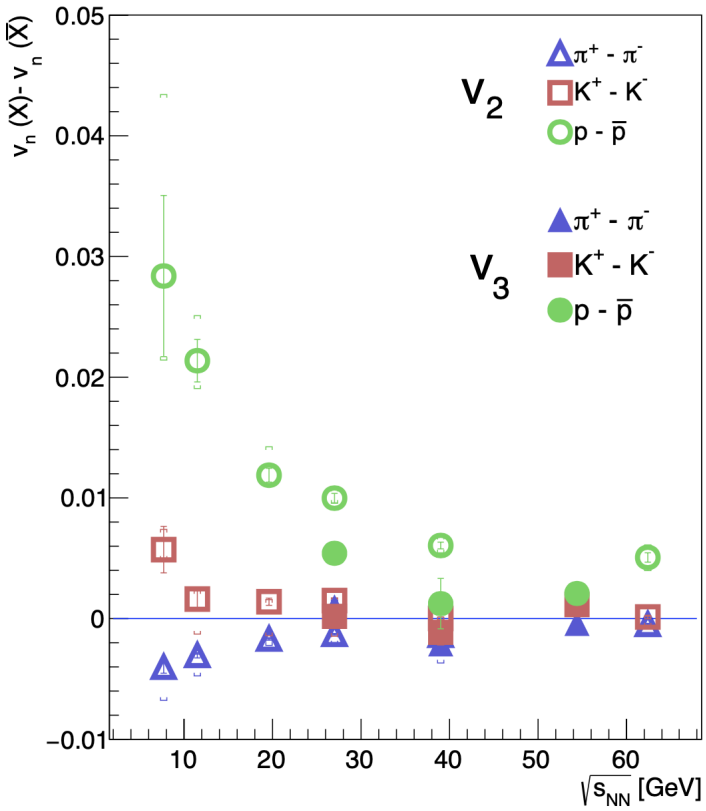

Figure 5.17 – The difference in Event Plane v_2 (data from [84]) and in 2PC $v_3\{2\}$ between particles (X) and the corresponding anti-particles ($\bar{X}$) as a function of $\sqrt{s_{NN}}$ for $0-80\%$ central Au+Au collisions. This thesis

as evidence favouring the explanation included in **Scenario "Transported protons"**. However, this theoretical approach cannot be validated with performed studies.

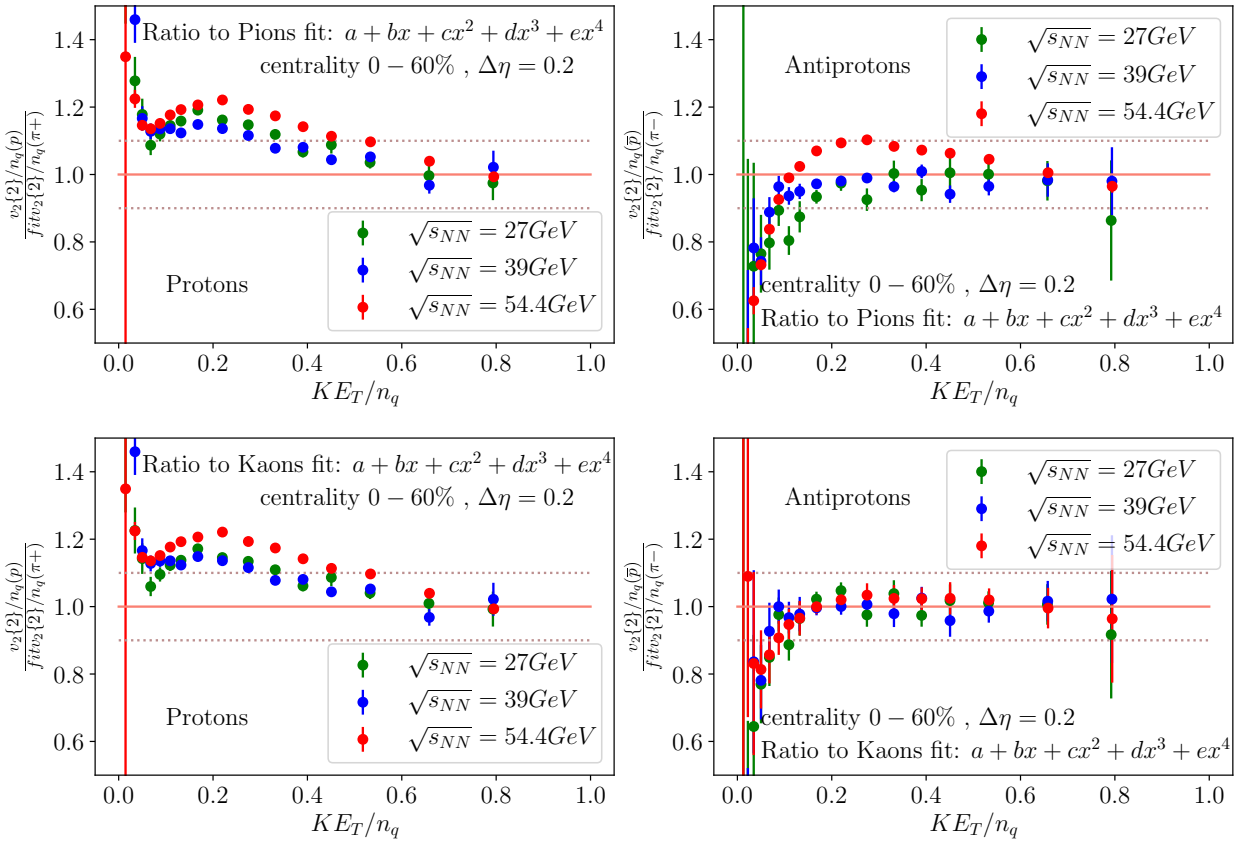

Figure 5.18 – Collision energy dependence of ratios of protons' and antiprotons' $v_2\{2\}/n_q$ to fit of (top row) fit to pions' $v_2\{2\}/n_q$ and (bottom row) kaons' $v_2\{2\}/n_q$ in function of transverse kinetic energy. This thesis

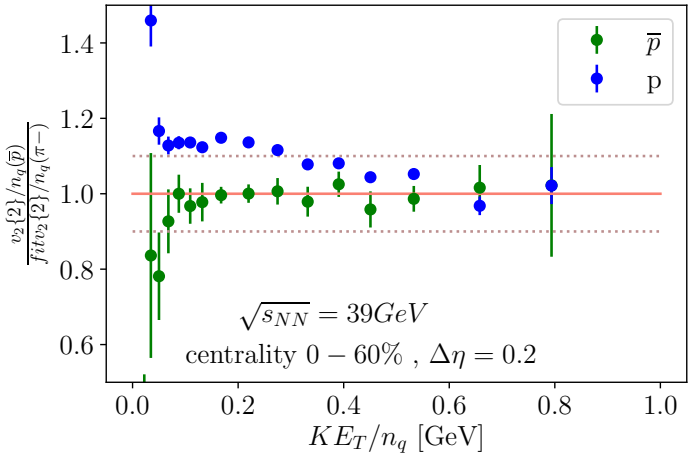

Figure 5.19 – Collision energy dependence of ratios of protons' and antiprotons' $v_2\{2\}/n_q$ to fit of kaons' $v_2\{2\}/n_q$ in function of transverse kinetic energy. This thesis

Chapter 6

EPOS Model

The second part of this thesis is focused on the development of the phenomenological MC model EPOS. The possibility of the choice of the family of the new EoS was introduced into the model. It allowed me to study the impact of changes of the EoS on the final experimental observables.

EPOS is an abbreviation of **E**nergy conserving quantum mechanical multiple scattering approach, based on **P**artons (parton ladders), **O**ff-shell remnants, and **S**aturation of parton ladders.

The EPOS is a phenomenological model based on the MC techniques. It gives a possibility to investigate various observables (like particle production, momenta distribution or flow correlations), providing a better understanding of the evolution of the system created in the elementary collisions such as proton-proton and during complex reactions with heavy-ions. The theoretical framework included in the model provides the coherent description of the space-time expansion of matter based on the precise spectrum of studies of both elementary processes such as electron-positron annihilation or lepton-nucleon scattering and more compound collisions of protons or nucleus'. This model was designed to describe processes present after collisions at $\mu_B \approx 0$, at very high energies like top RHIC or obtained at LHC and for various systems, such as Au+Au, Pb+Pb or p+p.

The EPOS model consists of several phases of evolution:

— initial stage (based on the Parton Gribov-Regge theory),
— core/corona division,
— hydrodynamical evolution,
— hadronization,
— hadron rescattering,
— resonance decays.

In this chapter, all of these stages are described as well as the new developments of the generator.

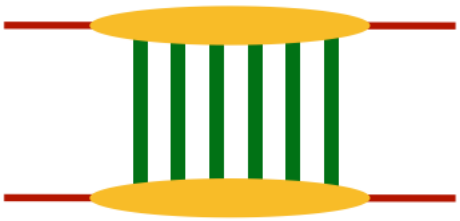

Figure 6.1 – Hadron-hadron scattering. Red incoming lines represents the hadrons and each green thick line Pomeron - the exchanges happen in parallel. This thesis

6.1 Initial Stage of the evolution

In the model's theoretical framework, the crucial element is the sophisticated treatment of the hadron-hadron scattering and the initial stage of the collisions at ultra-relativistic energies. It is highly relevant in the understanding of possible parton-hadron phase transition. In the EPOS model, the merged approach of Gribov-Regge Theory (GRT) and the eikonalised parton model is utilised to provide proper treatment of the first interactions happening just after the collision - satisfying conservation laws and equal treatment of subsequent Pomerons. **This part of the thesis is based on the book [144].**

6.1.1 Parton-Based Gribov-Regge Theory

Gribov-Regge Theory

The **Gribov-Regge** approach is an effective field theory focusing on the soft aspects of the particle interactions [145]. Numerous elementary interactions can happen simultaneously and they are represented by the complex, theoretical objects called "Pomerons". The single exchange of Pomeron is parametrized with the elastic amplitude T expressed by:

$$T(s,t) \sim is^{\alpha_0+\alpha' t} \tag{6.1}$$

where: s, t are the Mandelstam's variables [1], α Regge Pole [146]. Multiple Pomeron exchange occur in parallel (Fig. 6.1).

1. Mandelstam variables are Lorentz-invariant variables describing the kinematics of particle reactions, carring th einformation about the momenta of particles before and after collisions

Elastic amplitude: The n Pomeron exchange amplitude can be expressed with:

$$T_n(s,t) \propto \int d^2b \times e^{ikb} - \frac{s \times \omega(s,b)^n}{n!} \tag{6.2}$$

where b is the impact parameter, k is the transverse momentum of outgoing hadrons, while ω is:

$$\omega(s,b) \propto \frac{y e^{\alpha_0 - 1}}{R^2 + \alpha' y} \times exp\left[-\frac{1}{4}\frac{b^2}{R^2 + \alpha' y}\right] \tag{6.3}$$

where $y = ln\left[\frac{s}{s_0}\right]$ and R is a free parameter. The total elastic amplitude is:

$$T(s,t) = \sum_{n=1}^{\infty} T_n(s,t) \propto \int d^2b \times e^{ikb} \times y(s,b) \Rightarrow y(s,b) = 1 - se^{\omega(s,b)} \tag{6.4}$$

The multiple Pomeron exchanges respect the Froissard limit [147] and their total amplitude can be used in calculation of the total cross-section:

$$\sigma_{tot} = \int 2\Re[y(s,b)]d^2b \tag{6.5}$$

Inelastic amplitude: The production of particles is governed by the field theory. Utilizing the cutting rules the inelastic cross section can be expressed by following:

$$\sigma_{inel}^{h_1 h_2} = \int d^2b\{1 - exp(-G(s,b))\} \tag{6.6}$$

where $G(s,b)$ is proportional to the Fourier transformation of $T(s,t)$ and is an equivalent to the one elementary interaction (green line on the Fig. 6.1). Although the cross-sections of all elementary interactions are respected identically, subsequent Pomerons are not treated equally in particle production. Moreover, energy conservation is not ensured.

Parton Model

Feynman proposed the Parton Model during his studies of proton-proton collisions [148]. It introduces the components of protons. Consequently, they stopped being treated as elementary particles.

The Parton Model considers quarks and gluons. The momentum distributions f_{h_1} and f_{h_2} represent the partons of projectile and target. It considers the hard processes and the inclusive cross-section of the parton jets' production with the squared transverse

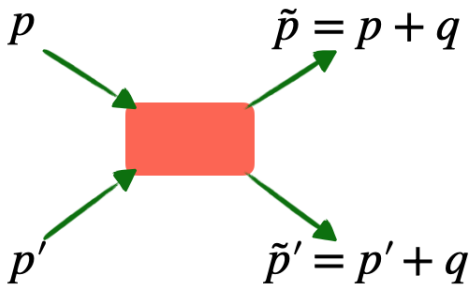

Figure 6.2 – Elastic scattering amplitude T. This thesis

momentum p_T^2 bigger than some cutoff Q_0^2 can be expressed by following equation:

$$\sigma_{incl}^{h_1 h_2} = \Sigma_{ijT}^2 \int dx^+ \int dx^- f_{h_1}^i(x^+, p_T^2) f_{h_2}^i(x^-, p_T^2) \frac{d\hat{\sigma}_{ij}}{p_T^2}(x^+ x^- s)\theta(p_T^2 - Q_0^2) \tag{6.7}$$

where i, j are the parton flavors and $\frac{d\hat{\sigma}_{ij}}{p_T^2}$ reports to the elementary parton-parton cross-section. However, similarly to the GRT, in this approach there is no clear solution for the way of energy sharing in the exclusive calculations - the generation of the event.

Parton-Based Gribov-Regge Theory

Combining these two approaches - Parton-based Gribov-Regge Theory (PBGRT) - provides the solution for some of the imperfections from each of the model separately. It is a realistic treatment of both soft and hard processes occurring in the medium evolution. Here, the rigorous approach to the multiple scattering aspect and particle production ensures the proper energy sharing and overall conservation.

In the Figure 6.2 the fundamental two-body elastic scattering with amplitude T is illustrated. Each of incoming particle has 4-momenta p and p', and outgoing: $\tilde{p} = p + q$, $\tilde{p'} = p' + q$ respectively, where q correspond to transferred momentum. The total cross-section can be expressed as:

$$\sigma_{tot}(s) = \frac{1}{2s} 2\Im T(s, t = 0) \tag{6.8}$$

The Fourier transform $\tilde{T}$ of T is:

$$\tilde{T}(s, b) = \frac{1}{4\pi^2} \int d^2 q_\perp e^{-i\vec{q}_\perp \vec{b}} T(s, t) \tag{6.9}$$

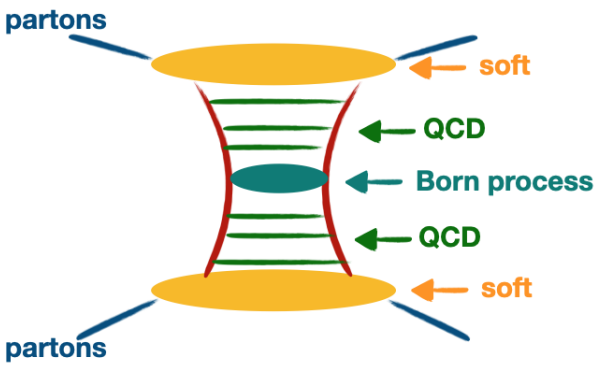

Figure 6.3 – Elementary interaction in PBGRT. This thesis

if $t = -q_\perp^2$, the profile function $G(s,b)$ is:

$$G(s,b) = \frac{1}{2s} 2\Im\tilde{T}(s,b) \tag{6.10}$$

Consequently the total cross-section can be expressed as

$$\sigma_{tot}(s) = \int d^2b G(s,b) \tag{6.11}$$

This profile function can be understood as a probability of interaction at the given impact parameter. It can be applied to partonic profile functions and hadronic or nuclear functions that can be derived from the partonic one.

In the Figure 6.3 the schematic elementary interaction ladder depicted, where blue lines corresponds to incoming and outgoing partons. The ladder consists of three contributions:

— **soft**: non-perturbative QCD, the virtuality of partons is smaller than the saturation factor Q_s^2; in the description and parametrization the phenomenological Regge theory is used,

— **semi-hard**: getting closer to the center of the ladder causes the increase of virtuality: $Q^2 > Q_s^2$; consequently it becomes harder

— **hard**: perturbative QCD used in the discription, the DGLAP equations are used for the virtuality of partons [149]; in the center of the diagram there is a $2 \to 2$ interaction called Born proccess.

The contributions of the semi-hard combination of partons originate from the sea, or valance quark are considered as well.

Moreover, the equal treatment of subsequent pomerons in particle production is pro-

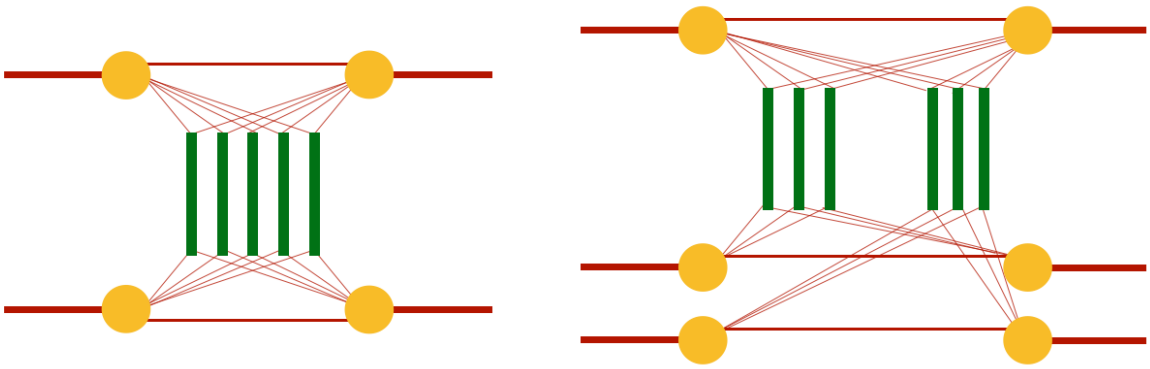

Figure 6.4 – Proton-proton (left) and proton-nucleus (right) scattering. The total energy is conserved: from each incoming proton/nucleus, the energy is shared among several "constituents". Consequently, each Pomeron obtains only a part of the total energy. This thesis

vided. In Figure 6.4, the proton-proton and proton-nucleus collisions are illustrated. The green lines correspond to the elementary interactions and are the sum of soft, semi-hard and hard contributions - the treatment is coherent.

Finally, in the EPOS model calculations of the cross-sections and particle production, the same formalism is used. It is based on the Feynman diagrams of the QCD-inspired effective field theory and provides energy conservation. The nucleons are divided into a certain number of "constituents" carrying the incident momentum fraction. The fractions sum to unity in order to ensure momentum conservation. For each nucleon, there can be (illustrated on the Fig. 6.5) :

— multiple or one *participants*, which take part in the elementary interactions (green lines) with constituents from the opposite side,
— one *spectator*, or
— one *remnant*, which does not interact ($nucleon - participants$)

The *parton ladder* is used for the representation of the evolution from the projectile to the target. There are two kinds of mention above *ladders*: open and closed. The first one corresponds to the interactions where the new particles are produced, while the closed one to elastic processes.

Applying the *cutting rule techniques*, the partial cross-section for exclusive event classes are obtained and simulated using the Markov chain techniques.

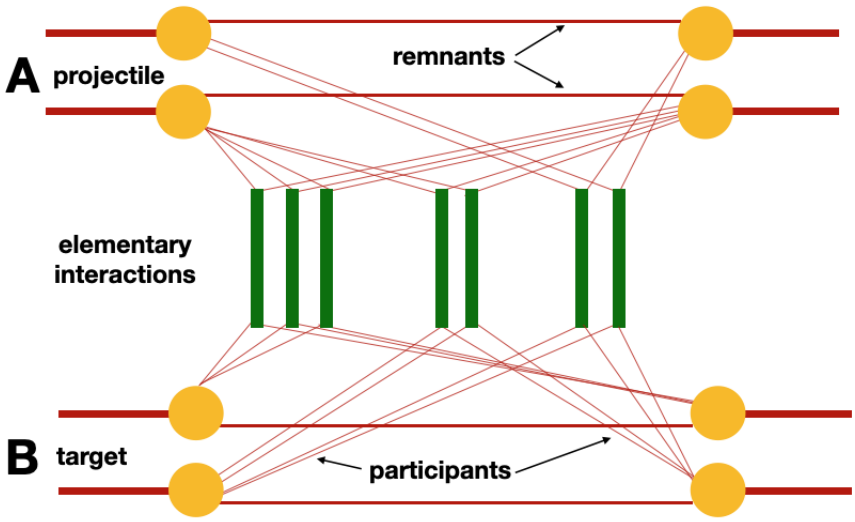

Figure 6.5 – The illustration of the nucleon-nucleon rescattering. Two projectiles A and two targets B interaction. The split between participants and remnants shows the momentum sharing between constituents ensuring conservation of given valuable. This thesis

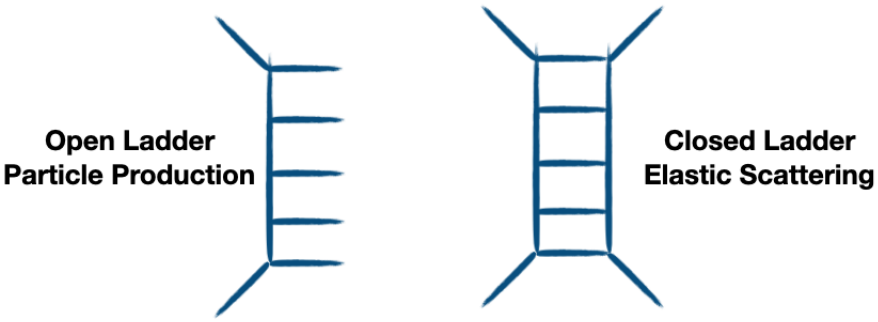

Figure 6.6 – left) open ladder, right) closed ladder. This thesis

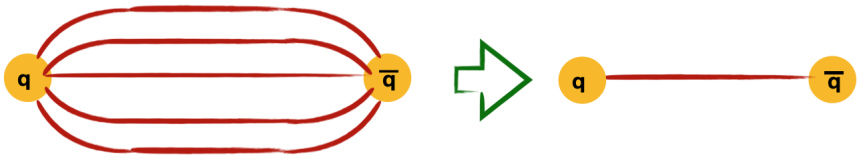

Figure 6.7 – Quark and antiquark connected with color-field and its simplification expressed with a single string. This thesis

6.1.2 String Model and Flux Tube Approach

The particle production is based on the String Model approach [22, 150], which describes the process of hadronisation. It uses strings as an analogy of the production of new particles. The QCD potential between quarks expressed with the eq. 1.1, is dominated at large distances by the linear part. It is used in the division (fragmentation) of the high-masses $q\bar{q}$ into multiple small-masses ones. The colour field stretched between the quarks is approximated with the one-dimensional string (Fig. 6.7).
The potential energy increases with the distance of separation of the original quarks. When the invariant mass of the system is big enough, the production of the new pair of $q\bar{q}$ is more energetically favourable than a continuation of stretching the string. The new particles are created via so-called *string fragmentation*.

Flux Tubes

In EPOS model the parton ladders are recognized as a quasi-longitudinal color field - elementary flux tubes and treated as classical strings [151]. The strings are divided into several segments $[\alpha_k, \alpha_{k+1}]$ with a corresponding velocity:

$$\{ V\ (\alpha) \equiv \frac{\partial X}{\partial \beta}(\alpha, \beta = 0) = V_k, in[\alpha_k, \alpha_{k+1}] \tag{6.12}$$

where $X(\alpha, \beta)$ is the 2D surface in 3+1 dimensional space-time. The interval with a constant V_k is called *a kink*. The length of the segment is given by the parton energy E_k, the velocity is the parton velocity p_k^μ / E_k. The intermediate gluons introduce the transverse motion into the *kinky string* string evolution. The schematic picture of the flux tube with the transverse kink is shown in the Fig. 6.8. The illustration is just two dimensional, the object is mainly longitudinal but there are pieces of the string moving transversely in the y-direction. The fragmentation of the flux tube occurs according to the string model via

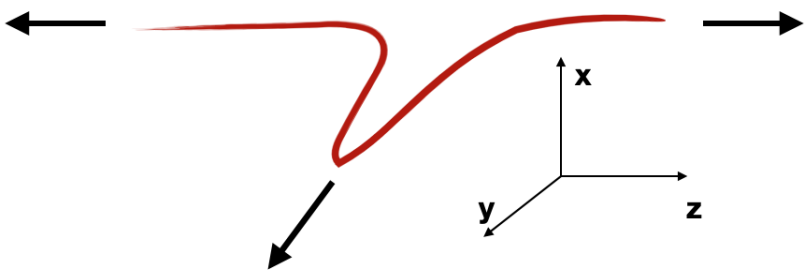

Figure 6.8 – The flux tube with the kink, moving transversely in R^3. This thesis

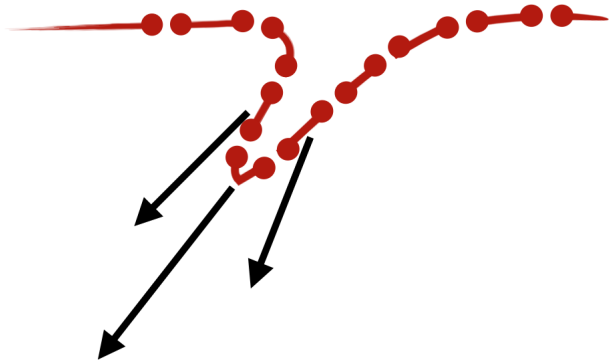

Figure 6.9 – Schematic illustration of the fragmentation of the string. The segments close to the kink will contribute to corona. This thesis

$q - \bar{q}$ or $qq - \bar{q}\bar{q}$ production (Fig. 6.10). This process happens with a given probability in the 3D+1 space-time, what is rigorously treated utilizing *the area law hypothesis* [152].

6.2 Core-Corona approach

If the density of the strings is very high, they cannot decay independently, and this situation is characteristic for the heavy-ions and the high-multiplicity $p - p$ collisions. In EPOS the dynamical process of division of the strings segments into *core* and *corona* is introduced in order to deal with this issue [151, 153, 154].

The separation is based on the abilities of a given string segment to leave the "bulk matter". As the criteria for the decision, if it goes to a given group, the transverse momentum of the element and the local string density is taken into account. If the string segment belongs to the very dense area, it will not escape but will build the *core*, which will be driven in the next step by the hydrodynamical evolution. When the segment origi-

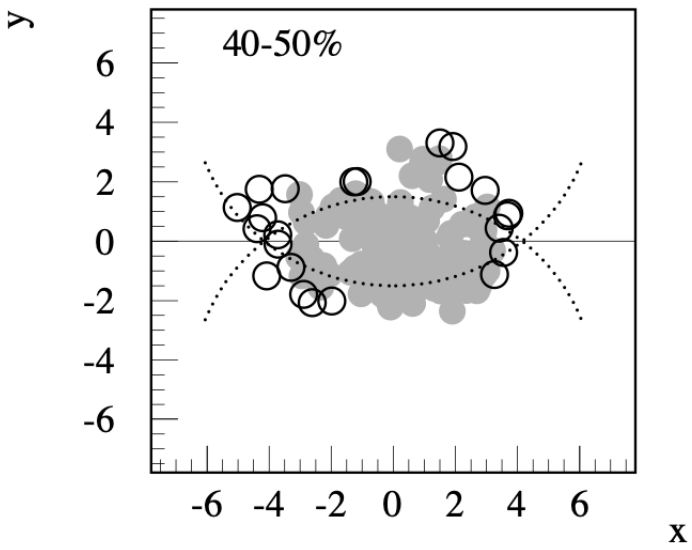

Figure 6.10 – The Monte Carlo simulation: full circles correspond to string segments contributing to core and open to corona. The big circles are just for the eye-guidance showing the surface of collided nuclei [154]

nates from the part of the string close to the kink, is characterized by the high transverse momenta, it escapes the bulk matter and join the *corona* and consequently will show up as a hadron (jet-hadrons). There is also a possibility that the string segment is close to the surface of the dense part of the medium, and its momentum is high enough to leave it; it also becomes a *corona* particle. The following equation is used for the determination of core and corona:

$$p_t^{new} = p_t - f_{Eloss} \int_\gamma \rho dL \tag{6.13}$$

where: is the trajectory of the segment, ρ density, $f_{Eloss} \neq 0$ constant for $p_t < p_{t,1}$, $f_{Eloss} = 0$ for $p_t > p_{t,2}$. If the p_t^{new} is positive for a given segment, it escapes and becomes a corona particle; in the opposite case, it contributes to the core.

6.3 Viscous Hydrodynamical evolution

As it has been studied [39, 40, 43, 155], the QGP does not expand like an ideal fluid, and the effect of the bulk viscosity has to be taken into account in the simulations. In EPOS, the 3D+1 hydrodynamics is applied, providing an excellent description of the collective expansion of the matter [151].

The thermalization occurs at the given proper time τ_0 and the core string segments provide the initial conditions. Their four-momenta is used in the computation of the flavour flow vector and energy-momentum tensor at given position x:

$$N_q^\mu(x) = \sum_i \frac{\delta p_i^\mu}{\delta p_i^0} q_i g(x - x_i), \tag{6.14}$$

$$T^{\mu,\nu}(x) = \sum_i \frac{\delta p_i^\mu \delta p_i^\nu}{\delta p_i^0} g(x - x_i), \tag{6.15}$$

where: g is a Gaussian smoothing kernel with a transverse width $\sigma_{perp} = 0.25$fm, $q \in u, d, s$ corresponds to the net flavor of string segment and its four-momenta is:

$$\delta p = \left\{ \frac{\partial X(\alpha,\beta)}{\partial \beta}\delta\alpha + \frac{\partial X(\alpha,\beta)}{\partial \alpha}\delta\beta \right\} \tag{6.16}$$

In order to convert the system into the coo-moving frame, the Lorentz transformation is used:

$$\Lambda^\alpha_{mu}\Lambda_\nu T^{\mu\nu} = T^{\mu\nu}_{com} \tag{6.17}$$

The EoS is computed as:

$$p = p_Q + \lambda(p_H - p_Q) \tag{6.18}$$

where: p_Q is the pressure of the ideal QGP (including bag pressure), and p_H - of a resonance gas, and:

$$\lambda = exp(-z - 3z^2)\Theta(T - T_C) + \Theta(T_C - T) \tag{6.19}$$

with:

$$\{\, z = x/(1 + x/0.77), x = (T - T_C)/\delta \tag{6.20}$$

where: $\delta = 0.24exp(-\mu_b^2/0.4^2)$. The compatibility of equation of state with the lattice data [156] is ensured by λ.

In EPOS there is applied the 3D+1 viscous hydrodynamics approach called vHLLE (viscous HLLE-based algorithm) [157]. The Minkowski coordinates $\{t, x, y, z\}$ are used as $\tau = \sqrt{t^2 - z^2}$, $\eta = \frac{1}{2}ln(t + z)/(t - z)$. The hydrodynamic equations are:

$$\partial_{\mu\nu}T^{\mu\nu} = \partial_\nu T^{\mu\nu} + \Gamma^\mu_{\nu\lambda}T^{\nu\lambda} + \Gamma^\nu_{\nu\lambda}T^{\mu\lambda} = 0 \tag{6.21}$$

where Γ is the Christoffel symbol. In order to avoid application of a higher order numer-

ical time integration scheme, the $\tilde{T}^{\mu\nu}$ is introduced as:

$$\{\, T^{\nu\mu} = \tilde{T}^{\mu\nu}, \mu, \nu \neq \eta, T^{\nu\eta} = \tilde{T}^{\mu\eta}/2, \mu \neq \eta, T^{\eta\eta} = \tilde{T}^{\eta\eta}/\tau^2, \tag{6.22}$$

so from eq. 6.3 $\tau T^{\mu\nu}$:

$$\{\ \partial_\nu(\tau T^{\tau\nu}) + \frac{1}{\tau}(\tau T^{\eta\eta}) = 0,$$

$\partial_\nu(xT^{\tau\nu}) = 0,$

$\partial_\nu(yT^{\tau\nu}) = 0,$

$\partial_\nu(\eta T^{\tau\nu}) + \frac{1}{\tau}(\tau T^{\eta\tau}) = 0,$
(6.23) where:

$$\partial \equiv (\partial/\partial\tau, \partial/\partial x, \partial\ \partial y, (1/\tau)\partial/\partial\eta) \tag{6.24}$$

To solve the equations of the relativistic viscous hydrodynamics, the calculations are performed in the Israel-Stewart framework [158, 159]. To satisfy the energy-momentum conservation in viscous case, the ideal-viscous splitting technique is used [160]. The Israel-Stewart equations are calculated simultaneously, and the correction of the momentum/energy expansion is performed according to the source terms in eq.6.3 and viscous fluxes.

6.3.1 Event-by-event treatment

In the simulations, the highly important is the definitive treatment of individual events - the generalization in considering smooth initial conditions for all events is not applied. The event-by-event (*ebe*) approach in hydrodynamical evolution is based on the random flux tube initial conditions [151]. It has a relevant impact on the final observables such as spectra or various harmonics of flow.

6.3.2 Equation of State

The viscous hydrodynamics uses Equation of State X3F ("cross-over" and "3 flavor conservation") which is compatible with Lattice QCD data (Fig. 6.11). It corresponds to $\mu_B = 0$ MeV so that it limits the possibility to describe the region of QCD phase diagram characterized by the finite baryon density [151]. To extend these limits, the new EoS has to be implemented.

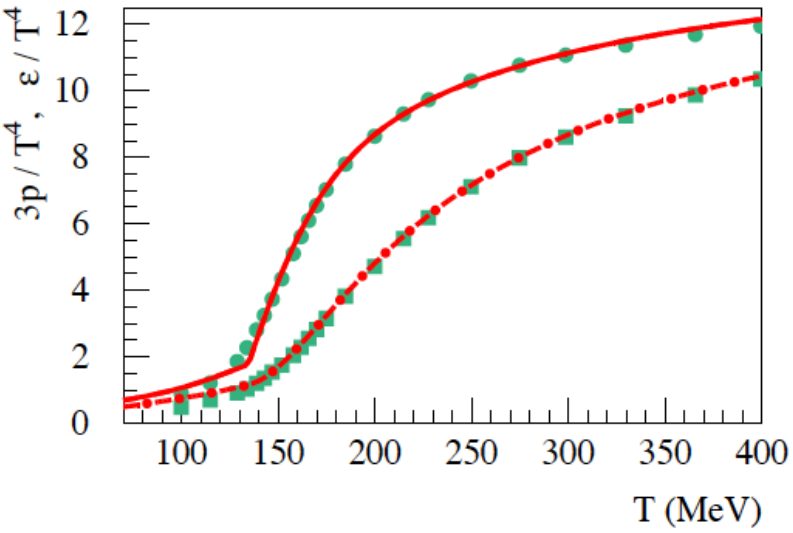

Figure 6.11 – The energy density (top line) and pressure (bottom line) relations with temperature for EPOS EoS [153] compared with Lattice data [156].

6.4 Hadronization

The expanding medium in the processes of hydrodynamical evolution reaching the given freeze-out condition is transformed into the particle spectra. In EPOS 3, the criteria characterizing the hadronization hypersurface is the energy density equal $0.57 Gev/fm^3$. The transformations are governed y the Cooper-Frye formula [161]:

$$E\frac{dN}{d^3p} = \int_\Sigma d\Sigma_\mu p^\mu f(T, p_\mu u^\mu, \pi^{\mu\nu}) \tag{6.25}$$

where $f(T, p_\mu u^\mu, \pi^{\mu\nu})$ corresponds to the particle distribution function, Σ is the hadronization hypersurface.

As a new development, the micro-canonical approach to the hadronization has been introduced.

6.5 Hadronic Cascades

The final part of the simulation uses so-called *hadronic afterburner* - UrQMD [162, 163].

When the density is very high and the mean free paths of constituent particles are

small about any macroscopic length scale, the hydrodynamic description can be used - in the initial phase of the QGP evolution. With the cooling of the system, the density and the mean free paths decrease; oppositely, the η/s increases. Finally, the differences in the mean free path of various particle species become relevant, and the collective description of the system becomes not adequate. When the density and the temperature are low enough, the kinetic theory is applied using the UrQMD code [162, 163].

The particles can interact only when they leave the hyper-surface of the freeze-out. The $2 \rightarrow n$ hadronic scattering is performed according to the measure reaction cross sections [164]. The 60 different baryonic species and their anti-particles, about 40 mesonic states are considered [162, 163]. There are implemented such interactions between hadrons as [165]:

— elastic scattering,
— string excitations,
— resonance excitations,
— strangeness exchange reactions

The hadronic scattering has a significant impact on the final observables [2].

6.6 New developments

One of the essential elements of this PhD project was to develop the code of the EPOS generator applying new Equations of State and make it possible to choose the one from the immense variety. The goal is to study the impact of the different EoS used in the evolution of the system on the final observables such as one-particle spectra or flow investigation. It is substantial to investigate which experimental measurements are sensitive to each implemented phase transition or strength of criticality of given EoS.

6.6.1 BEST EoS

Collaboration Beam Energy Scan Theory proposed the family of Equations of State describing same region of QCD phase diagram as studied in BES program [37, 166]. It covers the region of chemical potential in range $0 \leq \mu_B \leq 450$ MeV and T between 30 MeV and 800 MeV. The equations respect the lattice QCD results up to $\prime(\mu_B^4)$. They consider existence of *cross-over transition*, *first order phase transition* and give possibility to choose the location of *Critical Point*.

In the proposed EoS, the consistency with the derived from the first principle calculations is preserved. However, the problem with the limitation in the extraction of information about the medium characterized by the finite μ_B (described in Section 1.2.3) is still present. Although the Taylor series used to expend the region studied with the QCD EoS never goes beyond the μ_B higher than one at Critical Point, the universality class to which the CP belongs is known, and it is possible to study the behaviour of EoS in some limited neighbourhood of CP.

The calculations applied by BEST are based on such a strategy:

1. In the region close to CP, the suitable parametrization is used in the description of EoS universal scaling behaviour in the 3D Ising model;
2. The 3D Ising model phase diagram is mapped using a parametric change of variables (not universal) onto the QCD one;
3. Estimation of critical contribution to Lattice QCD expansion coefficients using the Ising model thermodynamics;
4. Reconstruction of the full pressure - compatible with Lattice QCD at $\mu_B = 0$ and consisting the proper critical behaviour.

Despite the possibility to locate the critical point on the thermodynamics and hydrodynamic simulations, the proposed approach depends on the choice of parameters in the mapping of Ising $\rightarrow$ QCD, which is not arbitrary. It is a consequence of a need to match QCD Lattice data which puts some limitations on the CP position.

Scaling and mapping 3D Ising model Equation of State to QCD

In these transformation close to the CP, firstly the Ising model EoS is parametrized and then mapped on the QCD diagram. The reduced temperature $r = (T - T_C)/T_C$, magnetic fields h, and magnetization M is introduced by following equations [167–170]:

$$M = M_0 R\Theta \tag{6.26}$$

$$h = h_0 R^{\sigma} \tilde{h}(\Theta) \tag{6.27}$$

$$r = R(1 - \Theta^2) \tag{6.28}$$

where M_0, h_0 report to normalization constants, α, β are the 3D Ising critical exponents [168], $\tilde{h}(\Theta) = \Theta(1 + a\Theta^2 + b\Theta^4)$ (where $a = -0.76201$ and $b = 0.00804$). The Gibbs free

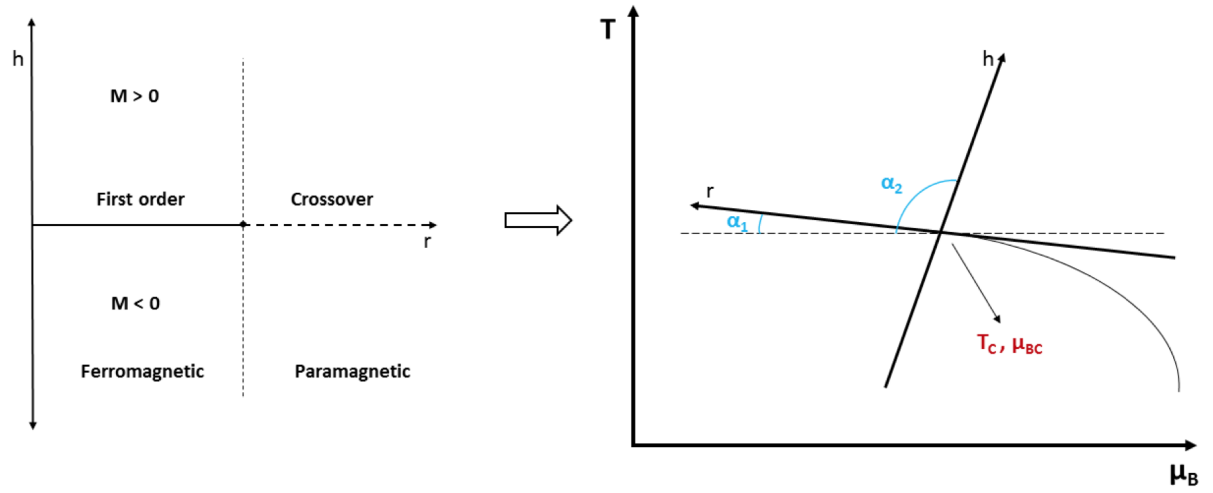

Figure 6.12 – The linear transformation is used in mapping the 3D Ising model diagram on the QCD one [166].

energy density can be expressed as a function of (R, Θ) parameters [167, 168]. Finally, considering the relation between Gibbs free energy density and pressure: $G/V = -P$, the scaling can be expressed with:

$$P_{Ising}(R, \Theta) = -h_0 M_0 R^{2-\alpha}[g(\Theta) - \Theta\tilde{h}(\Theta)] \tag{6.29}$$

In the Fig. 6.12 the non-universal mapping procedure is illustrated. Using six parameters the critical thermodynamics is linearly transferred to QCD (Ising variables to QCD coordinates: $(h, r) \mapsto (T, \mu_B)$):

$$\frac{T - T_C}{T_C} = w(r\rho \sin\alpha_1 + h \sin\alpha_2) \tag{6.30}$$

$$\frac{\mu_B - \mu_{BC}}{T_C} = w(-r\rho \cos\alpha_1 - h \cos\alpha_2) \tag{6.31}$$

where:
(T_C, μ_{BC}) is the location of CP, α_1 and α_2 are the angles between r and h axes and $T = const.$, w and rho reports to respectively global and relative rescaling of r and h. Such a description provides the possibility to locate the CP on the curve, set precise parameters characterizing the system, and satisfy the need for proper mapping from the Ising model to the QD phase diagram.

With the globally invertible second step, the map is ready:

$$(R, \Theta) \mapsto (h, r) \leftrightarrow (T, \mu_B) \tag{6.32}$$

The QCD pressure's critical input is:

$$P_{crit}^{QCD}(T, \mu_B) = f(T, \mu_B) P_{Ising}(R(T, \mu_B), \Theta(T, \mu_B)) \tag{6.33}$$

where $f(T, \mu_B)$ is a regular function with energy fourth dimension.

The coefficients derived from Lattice QCD are expressed by the ensured by matching with Lattice EoS at $\mu_B = 0$ "regular coefficients" ($c^{reg}(T)$) and these including the contributions coming from Ising CP:

$$c_n^{LAT}(T) = c^{reg_n(T) + c_n^{crit}(T)} \tag{6.34}$$

Finally, the full pressure can be calculated using the following equation:

$$P(T, \mu_B) = T_{n=0}^{4}{}^{2} c_{2n}^{reg}(T) \left(\frac{\mu_B}{T}\right)^{2n} + P_{crit}^{QCD}(T, \mu_B) \tag{6.35}$$

This equation ensures the matching with Lattice QCD at $\mu_B = 0$ and introduces the criticality in the correct universality class.

6.6.2 Microcanonical hadronization

The microcanonical hadronization is introduced as a consequence of difficulties in matching the dynamical properties of the bulk created in hydrodynamical evolution and the given hadronic system. Another reason is to ensure that the energy and flavor are conserved for small systems [171–175].

The hadronization hyper-surface $x^\mu(\tau, \varphi, \eta)$ is characterized by following equations:

$$\{ x^0 = \tau cosh\eta, x^1 = r cos\varphi, x^2 = r sin\varphi, x^3 = r sinh\eta, \tag{6.36}$$

respecting one of the chosen by the authors condition with given constant (FO):

— temperature: $T_H = const.$

— energy density: $\epsilon_H = const.$

Figure 6.13 – Hydronization hyper-surface, with elements $d\Sigma^\mu$ and flow momentum vector dP^μ. This thesis

The element of the hyper-surface is:

$$d\Sigma_\mu = \epsilon_{\mu,\nu,\kappa,\lambda}\frac{\partial x^\nu}{\partial \tau}\frac{\partial x^\kappa}{\partial \varphi}\frac{\partial x^\lambda}{\partial \eta}d\tau d\varphi d\eta \tag{6.37}$$

$$d\Sigma_0 = \{-r\frac{\partial r}{\partial \tau}\tau\cosh\eta + \frac{\partial r}{\partial \eta}\tau\sinh\eta\}d\tau d\varphi d\eta, \tag{6.38}$$

$$d\Sigma_1 = \{\frac{\partial r}{\partial \varphi}\tau\sin\varphi + r\tau\cos\varphi\}d\tau d\varphi d\eta, \tag{6.39}$$

$$d\Sigma_2 = \{-\frac{\partial r}{\partial \varphi}\tau\cos\varphi + r\tau\sin\varphi\}d\tau d\varphi d\eta, \tag{6.40}$$

$$d\Sigma_3 = \{r\frac{\partial r}{\partial \tau}\tau\sinh\eta - r\frac{\partial r}{\partial \eta}\tau\cosh\eta\}d\tau d\varphi d\eta \tag{6.41}$$

The flow of momentum vector dP^μ (Fig. 6.13) and charges dQ_A for each element are conserved:

$$dP^\mu = T^{\mu\nu}d\Sigma_\nu \tag{6.42}$$

$$dQ_A = J^\nu_A d\Sigma_\nu \tag{6.43}$$

The effective mass is the sum of all the surface elements:

$$M = \int_{\text{surface area}} dM \tag{6.44}$$

where $dM = \sqrt{dP^\mu dP_\mu}$. The volume and the four-velocity U^μ (ONLY if the pressure is 0, it is equal to velocity of fluid u^μ) of each element are known:

$$U^\mu = dP^\mu / dM \tag{6.45}$$

$$dV = u^\mu d\Sigma_\mu \tag{6.46}$$

The constructed effective mass decays microcanonically:

$$dP = C_{vol} C_{deg} C_{ident} \times \delta(E - \Sigma E_i)\delta(\Sigma \overrightarrow{p}_i) \prod_A \delta_{Q_A, \Sigma q_{Ai}} \prod_{i=1}^{n} d^3 p_i \tag{6.47}$$

where:
$C_{vol} = \frac{V^n}{2\pi)^{3n}}$ (volume),
$C_{deg} = \prod_{i=1}^{n} g_i$ (degeneracy),
$C_{ident} = \prod_{\alpha \in S} \frac{1}{n_\alpha!}$ (identical particles factor),
n_α correspond to the number of the species α of particles, and S reports to the set of the particle species. After the decay, the particles are boosted according to the velocities U^μ.

Chapter 7

The Equation of State at EPOS model

This is second of the most substantial chapters including main results of author of this thesis.

In this chapter, the introduction of the new Equation of State into the EPOS model is described. The proposed EoS is characterized in details in 6.6.1. The main goal of the presented studies is to investigate the influence introduced changes onto the final observables.

7.1 Implementation of EoS into the code of generator

The EPOS model includes the hydrodynamical description of the part of the evolution of the simulated system. This part of calculations uses tables including the information about the dependence of the temperature and μ_B on energy density (ϵ), speed of sound (c_s), pressure (P) in a given range. Such tables are generated using the relations included in Equation of State. Concluding, the hydrodynamical evolution is based on the EoS.

The source code of the generator is developed using the Fortran and C++ programming languages. The main introduced modification is a simplification of the part of the code related to using the information in EoS tables. There is the possibility of choosing and quickly adding the EoS, which is used in the simulations. There were performed various successful tests in order to validate the introduced changes.

7.1.1 Selection of the EoS parameters

The primary studies possible due to the modifications and development of EPOS model allow one to study the impact on final observables of the changes between the variety of EoS. As mentioned in Section 6.6.1, the BEST EoS is, in reality, the "family" of EoS, the

set of divers EoS tables. To obtain the EoS one needs to choose the set of parameters corresponding to mapping properties and locating the CP onto the QCD phase diagram.

The composition of the input parameters is crucial in setting the strength of the "criticality" of the transitions of the matter, moreover via changing the position of the CP one can expect the cross-over or the first-order transitions in the evolution of examined simulated systems. The structure of the parameter input file is:

MODE $\quad T_0 \quad \kappa \quad \mu_{BC} \quad \Delta_{\alpha_1,\alpha_2} \quad \omega \quad \rho$

where:

— MODE - corresponds to the CP location and choice of following parameters. In this studies the CP lies on parabola parallel to the chiral transition line - what reports to MODE = PAR;

— T_0 - the value of temperature at which the parabolic pseudo-critical line crosses the T axis;

— κ - the curvature of the transition line at the T axis;

— μ_{BC} - the chemical potential at the critical point: since both T_C and α_1 are determined by this choice, they do not need to be input;

— $\Delta_{\alpha_1,\alpha_2}$ - the difference between two angles (see Fig. 6.12)

— ω - the global scaling parameter in the mapping (the higher ω the less criticality in transitions of matter);

— ρ - the relative scaling in the mapping [166];

Example: PAR $\quad$ 155 $\quad$ -0.0149 $\quad$ 350 $\quad$ 90 $\quad$ 1 $\quad$ 2

The critical temperature, $\alpha_{1,2}$ can be easily calculated from the given parameters:

$$T_C = T_0 + \kappa/T_0\mu_{BC}^2 \qquad \alpha_1 = 180/\pi \left| \arctan(-\frac{2\kappa}{T_0\mu_{BC}}) \right| \qquad \alpha_2 = \alpha_1 + \Delta\alpha_1, \alpha_2 \qquad (7.1)$$

Critical Point location

In the performed studies various sets of parameters were chosen in order to investigate the wide range of properties of EoS. In order to study the critical behaviour the CP was placed on the T, μ_B plane close to the average temperature of the system simulated by EPOS model. Due to the fact that these are approximate estimations the temperature was extracted from the positive pion's p_T spectra distribution obtained for the simulated most central Au+Au collisions $(0 - 5\%)$. The used modified Hagedorn function for the fit is described in [176, 177], where A correspond to the so-called also *inverse slope parameter*, which can be treated as an approximate average temperature of the expanding system

$\sqrt{s_{NN}}$	T_C	T_0
7.7 GeV	153.4 ± 48.1 MeV	~ 169 MeV
27 GeV	174.4 ± 80.7 MeV	~ 184.3 MeV

Table 7.1 – Critical Temperature (T_C) and T_0 extracted from the fits from Fig. 7.1 and 7.2 and Eq. 7.1.

[23]:

$$E\frac{d^3\sigma}{dp^3} = A(e^{(ap_T+bp_T^2)} + p_T/p_0)^{-n} \tag{7.2}$$

The spectra with the fits are shown in the Figures 7.1 and 7.2. The extracted T_C and calculated with Eq. 7.1 T_0 are listed in the Table 7.1.

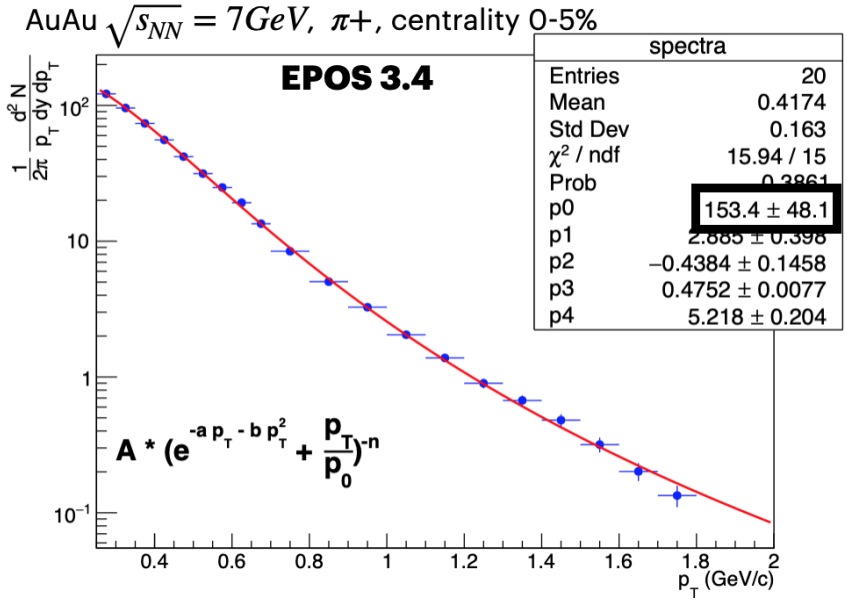

Figure 7.1 – The p_T spectra of positive pions from the most central Au+Au collisions $0-5\%$ at $\sqrt{s_{NN}} = 7.7$ GeV simulated with EPOS 3.4 model with a modified Hagedron fit. This thesis

Simulations

The two collision systems were studied: Au+Au collisions at $\sqrt{s_{NN}} = 7.7$ GeV and 27 GeV. The simulations using EPOS 3.4 model were performed using computer clusters at the Centre de Calcul de l'IN2P3/CNRS in Lyon [178]. In the simulations the given Equations of State were applied:

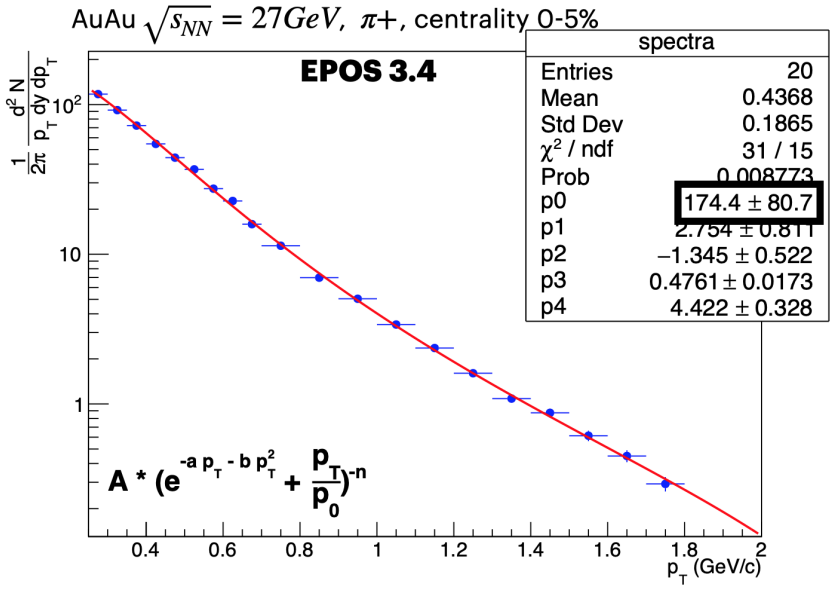

Figure 7.2 – The p_T spectra of positive pions from the most central Au+Au collisions $0-5\%$ at $\sqrt{s_{NN}} = 27$ GeV simulated with EPOS 3.4 model with a modified Hagedron fit. This thesis

— X3F cross-over, 3 flavour conservation (described in Sec. 6.3.2)
— BEST EoS with various parameters listed in Table 7.2.

7.2 Comparison of various EoS at EPOS model

7.2.1 Thermodynamical relations

The only element of the whole simulation performed by EPOS model which changes is the Equation of State. Concluding, all the presented data sets can be used in the direct comparison of the proposed EoS. Firstly, all the basic relations between thermodynamical properties are illustrated in the Figures 7.3, 7.4, 7.5, and 7.6. Also, the approximate CP's location is pointed on the plots for better visualisation. The "BEST 5" set of parameters was excluded due to the non-physical output.
The lower the parameter ω, the more visible the critical behaviour - drastic change (pick or break-down) on the illustrated surfaces. The highest peack in the Fig.7.6 for BEST 7 is present due to ω value 0.5, and they correspond to the critical behaviour of the system (rapid changes, fluctuations of thermodynamical properties of matter). Oppositely, in the BEST 4 the $\omega = 10$, what suppresses the criticality and makes the illustrated

Number	*MODE*	T_0	κ	μ_{BC}	$\Delta_{\alpha_{1,2}}$	ω	ρ	T_C	μ_{BC}	α_1	α_2	ωT_C	ωT_C
BEST 1:	PAR	155	-0.0149	350	90	1	2	143	350	3	93	143	286
BEST 2:	PAR	155	-0.0149	350	90	4	1	143	350	3	93	572	572
BEST 3:	PAR	155	-0.0149	420	90	0.75	2	138	420	4	94	103	207
BEST 4:	PAR	155	-0.0149	350	90	10	1	143	350	3	93	1432	1432
BEST 5:	PAR	169	-0.0149	420	90	0.25	2	165	3	86	179	23599	6749k
BEST 6:	PAR	169	-0.0149	420	90	1	1	153	420	4	94	153	153
BEST 7:	PAR	169	-0.0149	420	90	0.5	1	153	420	4	94	76	76
BEST 8:	PAR	174	-0.0149	440	90	1	1	157	440	4	94	157	157
BEST 9:	PAR	178	-0.0149	300	90	1	1	170	300	2	92	170	170

Table 7.2 – Sets of input parameters for the construction of nine BEST EoS used in the EPOS simulations.

surface in the Fig. 7.3 the most smooth one. The sets BEST 6 and 7 have CP placed in the approximate temperature of chemical freeze-out of system simulated by EPOS in Au+Au collision at $\sqrt{s_{NN}} = 7.7$ GeV. The BEST 8 is characterized by very high $T_C = 157$ MeV and $\mu_{BC} = 440$ MeV (what is nearly the top available potential). On the other hand, the last, ninth set of parameters correspond to the highest studied $T_C = 170$ MeV and lowest $\mu_{BC} = 300$ MeV, what places the system obtained at the examined Au+Au at $\sqrt{s_{NN}} = 7.7$ GeV approximately at the line of first-order phase transition. In case of simulations of Au+Au collisions at $\sqrt{s_{NN}} = 27$ GeV, the approximate T_C extracted from spectra fit is above the limit of the proposed BEST EoS. The simulated system is expected to go through, at least mostly, the cross-over transition.

7.2.2 Production of particles

The production mechanism highly depends on the potentials characterising the system. The higher the μ_B, the more produced baryons than antibaryons. Similarly in case of μ_q (charge) and μ_s (strange). Such relations are illustrated in Figure 7.7, where the most central $0 - 5\%$ collisions of Au+Au simulated with EPOS 3.4. model are compared with STAR data published in [143]. Various EoS sets of parameters were used in performed simulations; the numbers of EPOS' data sets correspond to these listed in the Table 7.2. The relations between particles' and antiparticles' production is reflected using ratios in Figure 7.8. The criteria for selecting the theoretical data are the same as applied by the experimentalists: $|y| < 0.1$ and $p_T < 2.0$ GeV/c.

The higher number of produced baryons than antibaryons proves that in EPOS simulations, the impact of non-zero baryon potential is kept for all the proposed EoS. The

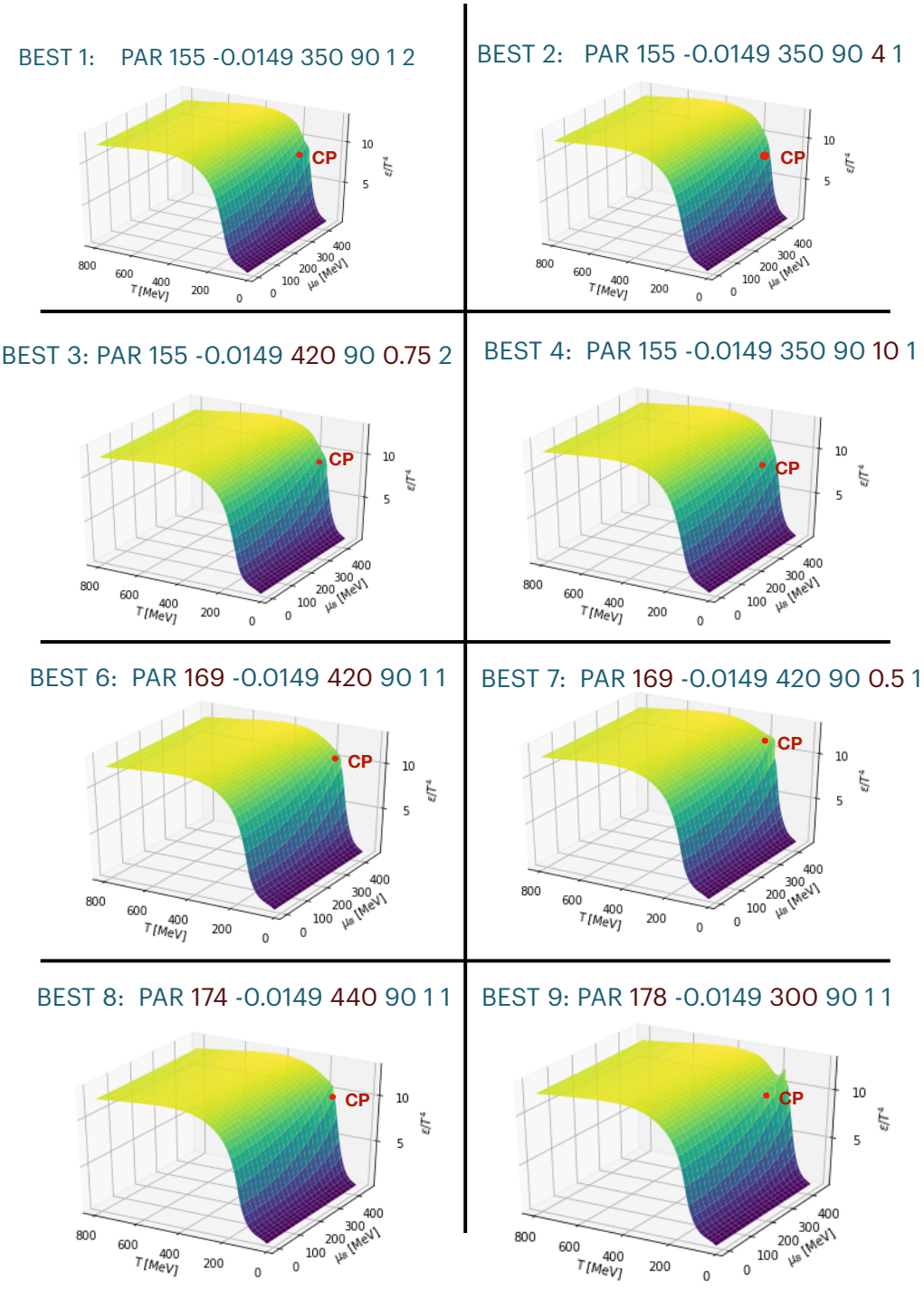

Figure 7.3 – Energy density (ϵ/T^4) dependence on T and μ_B. Some of the variables in sets of parameters are highlighted in order to underline the change which they introduce. This thesis

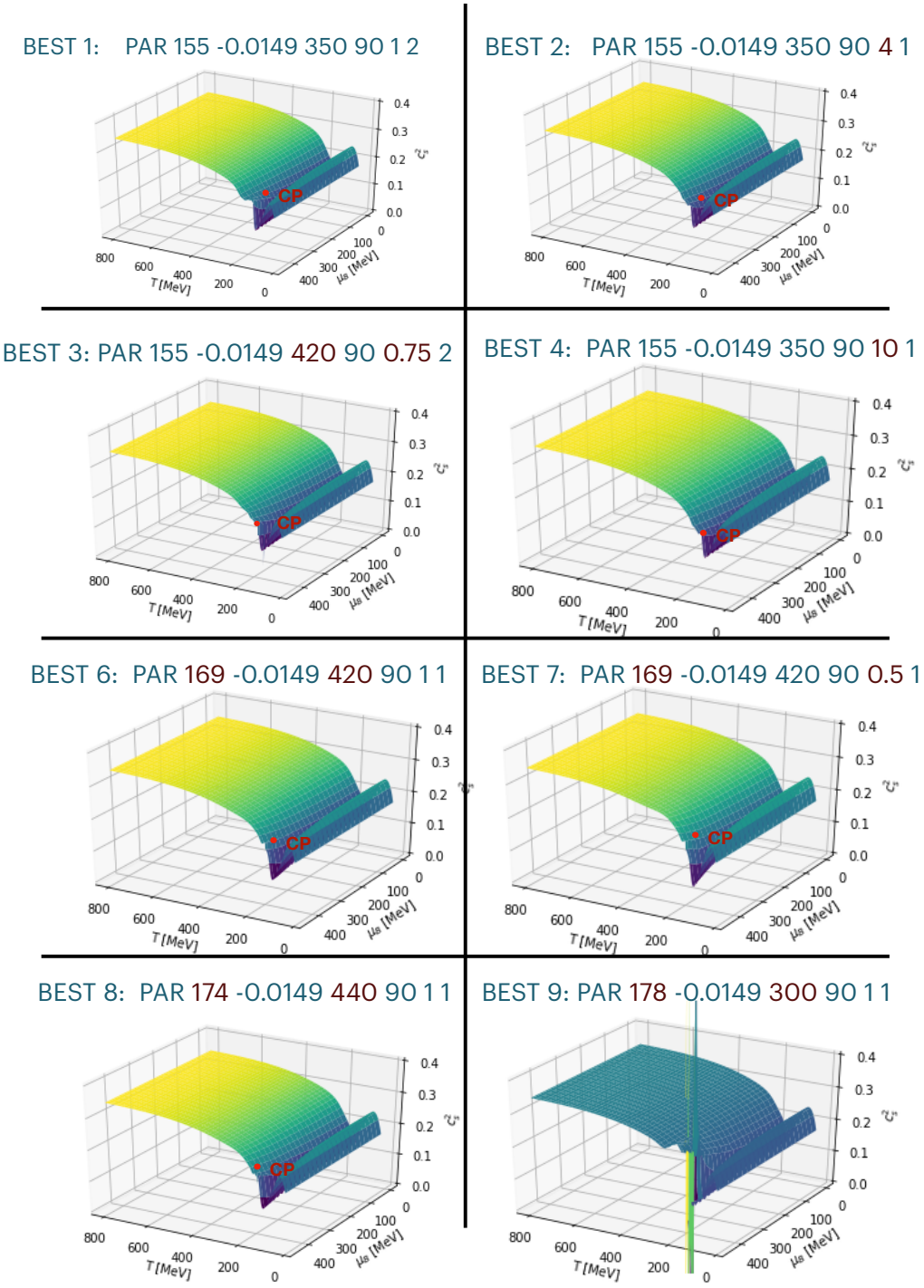

Figure 7.4 – Speed of sound (c_s^2) dependence on T and μ_B. Some of the variables in sets of parameters are highlighted in order to underline the change which they introduce. This thesis

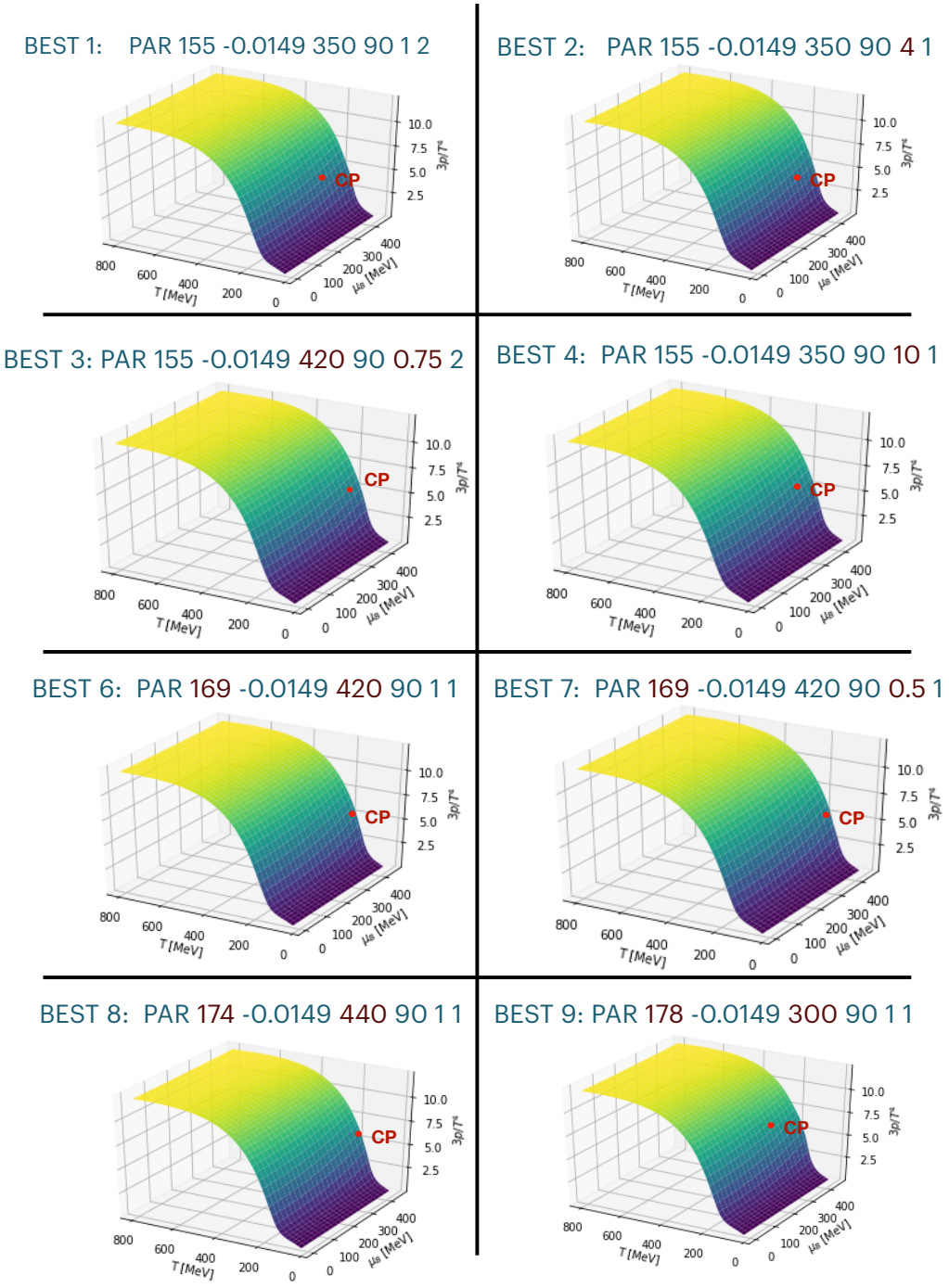

Figure 7.5 – Pressure ($3p/T^4$) dependence on T and μ_B. Some of the variables in sets of parameters are highlighted in order to underline the change which they introduce. This thesis

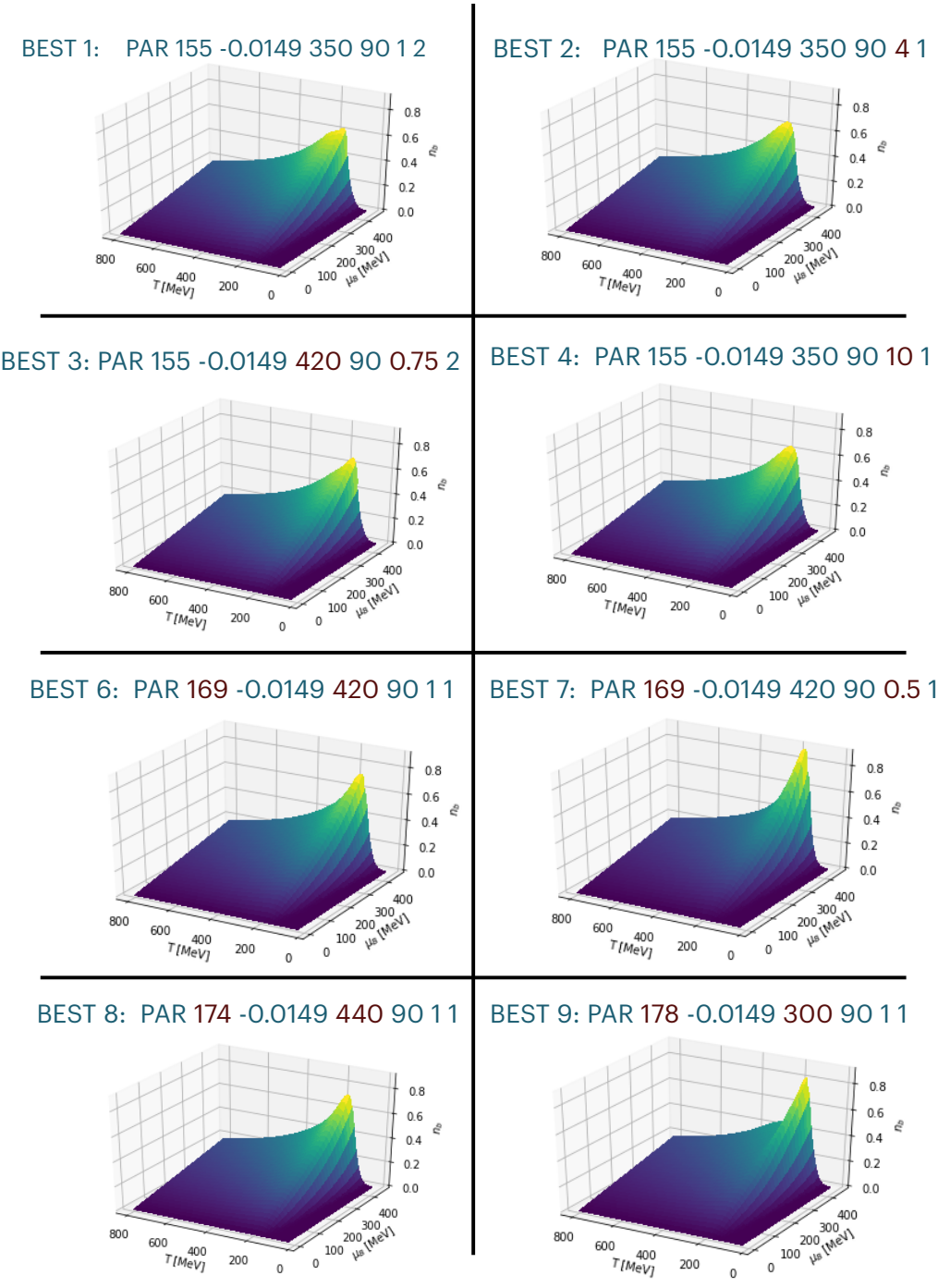

Figure 7.6 – Baryon density (n_b/T^3) dependence on T and μ_B. Some of the variables in sets of parameters are highlighted in order to underline the change which they introduce. This thesis

model reflects the experimental data reasonably, except for pions. The number of these both negative and positive mesons is overestimated. Nonetheless, their ratio is kept.

The possible reason for such discrepancies could be the too wide rapidity distribution of simulated data. In the experimental analysis, the selection of particles characterised by the $|y| < 0.1$ is very narrow. In such a case, even a small deviation in the rapidity distribution strongly affects the performed investigation.

In both Fig. 7.7 and 7.8 no relevant differences between simulations obtained with various EoS are observed. Notwithstanding the $X3F$ Equation of State corresponds to the *cross-over* transition, which is not expected to happen for cooling systems created in collisions of Au+Au at $\sqrt{s_{NN}} = 7.7$ GeV.

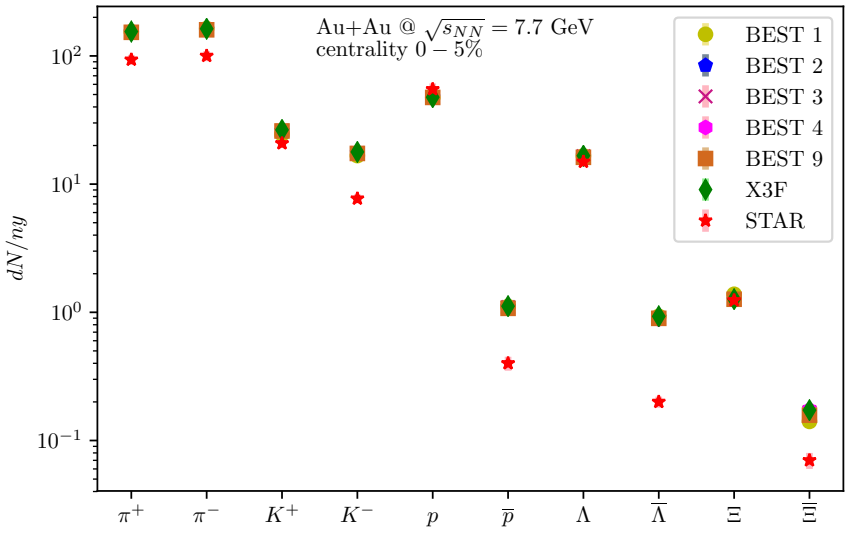

Figure 7.7 – Particle yields for Au+Au most central $0-5\%$ collisions at $\sqrt{s_{NN}} = 7.7$ GeV simulated with EPOS 3.4. model using various EoS and compared with STAR data [143]. This thesis

7.2.3 Dynamics of matter

In this subsection, the transverse momentum dependence of particle production is compared with experimental STAR data. Furthermore, simulations were performed for various EoS sets of parameters listed in Table 7.2. It gives a possibility to test the impact of different EoS introduced in the same generator framework on the final observables.

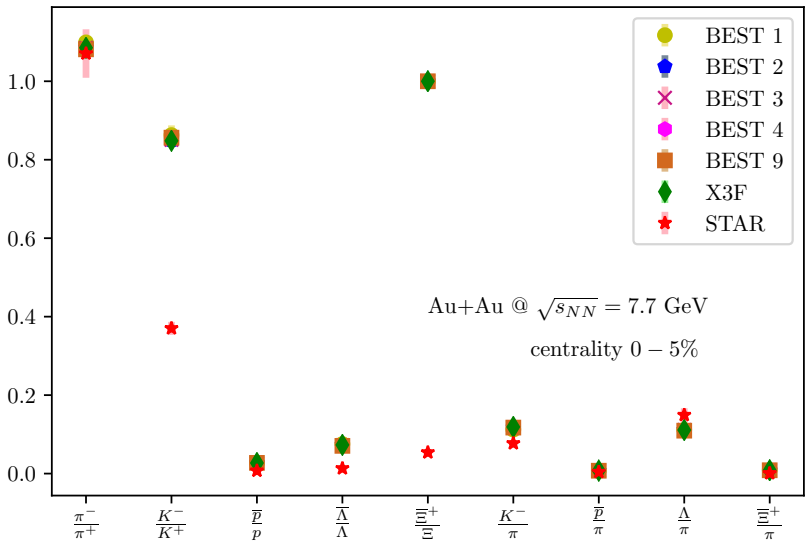

Figure 7.8 – Particle ratios for Au+Au most central $0-5\%$ collisions at $\sqrt{s_{NN}} = 7.7$ GeV simulated with EPOS 3.4. model using various EoS and compared with STAR data [143]. This thesis

Transverse momentum spectra

The fundamental observable studied in high-energy physics is the transverse momentum. One of the possible application is the calculation via proper fitting method the chemical freeze-out temperature of the examined system [143, 176, 177]. In these studies, there were two Au+Au collision energies considered: $\sqrt{s_{NN}} = 7.7$ and 27 GeV. In the Figures 7.9, 7.10,7.11, and 7.12 there are shown the particle spectra of identified hadrons from simulations with EPOS and comparisons with STAR data [143].

Au+Au at $\sqrt{s_{NN}} = 7.7$ GeV The slopes of the p_T spectra of the simulated data are similar to the experimental ones. It means that the relation between the amount of core and corona particles is correct. The more core particles, the p_T distribution gets flatten. As studied in the previous subsection, too many mesons are generated in the events of $0-5\%$ centrality in rapidity range ($|y| < 1.0$). It is reflected in the "height" of the distributions of pions and kaons, while in case of protons the agreement between EPOS and STAR spectra is better. Furthermore, Figure 7.7 shows that positive kaons production is closer to the experimental one than the negative, what is also repeated in their p_T spectra.

The data simulated using various EoS do not variate relevantly. The differences are present, what is visible in the bottom-ratio plots, but there is no clear trend showing the

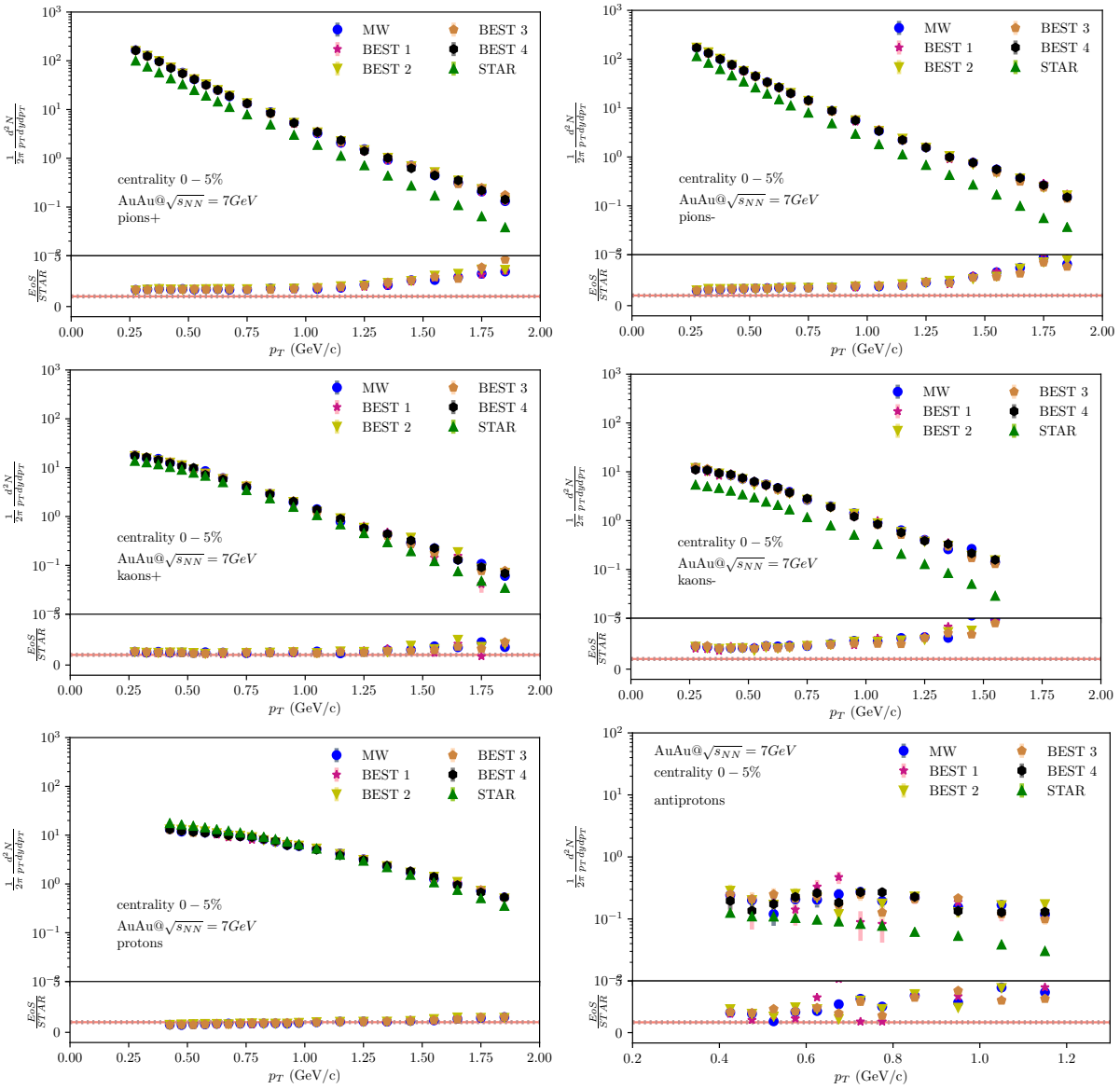

Figure 7.9 – The p_T spectra of the most central $0-5\%$ Au+Au collisions at $\sqrt{s_{NN}} = 7.7$ GeV of Pion+, Pion-, Kaon+, Kaon-, Proton, and Antiproton, simulated with EPOS 3.4. using various EoS (Tab 7.2). Compared with STAR data [143]. In the bottom panels there is a ratio between the simulated and experimental data. This thesis

impact of changes of EoS on p_T spectra. The points fluctuate, and even the error bars are plotted, they still look like the statistical fluctuations.

The plots of p_T spectra for peripheral Au+Au collisions in Figure 7.10 show the much better agreement between simulated and experimental data sets. However, the statistical fluctuations prevent making a final statement about the differences between EoS - the

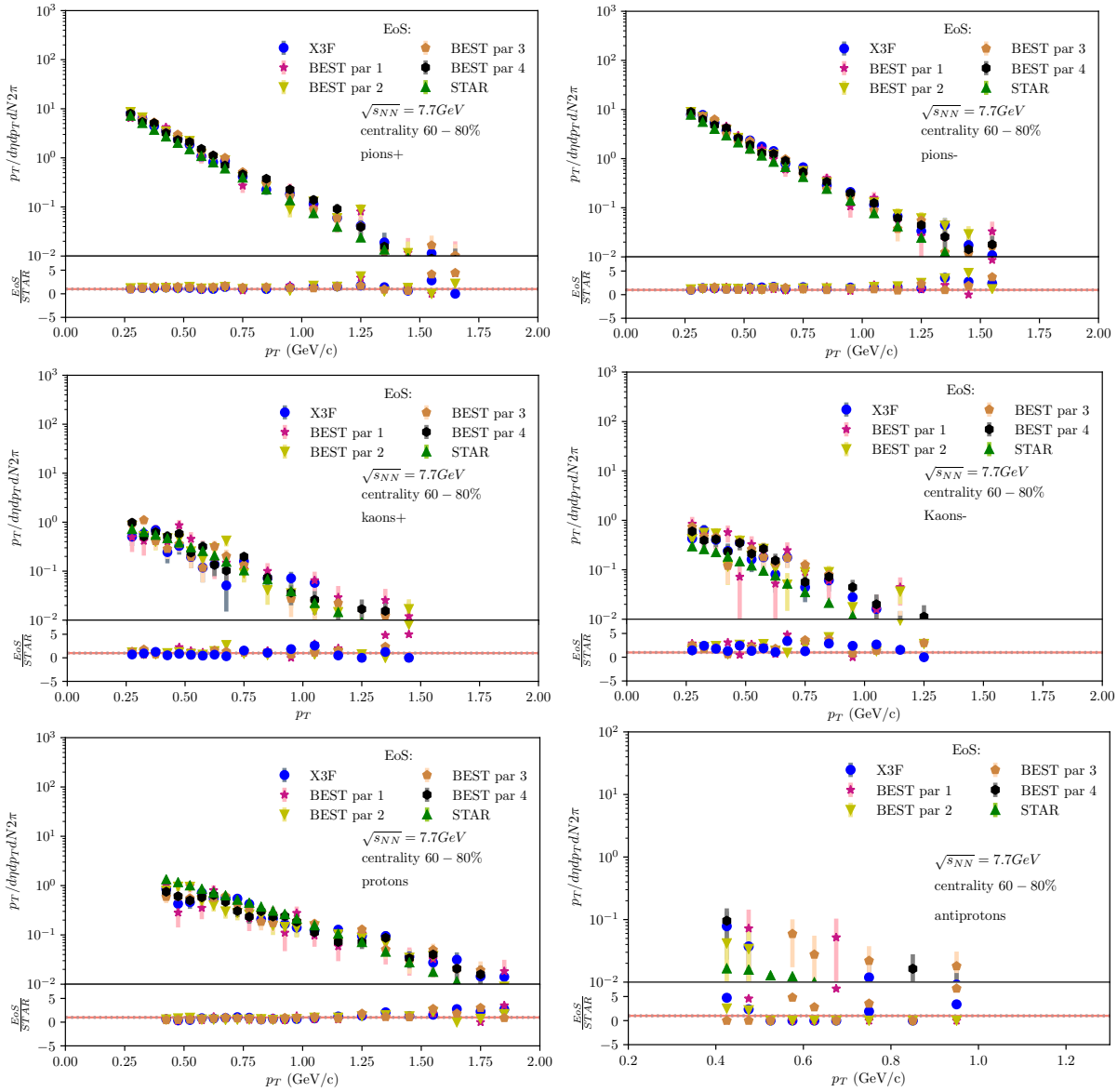

Figure 7.10 – The p_T spectra of the most peripheral 60% − 80% Au+Au collisions at $\sqrt{s_{NN}} = 7.7$ GeV of Pion+, Pion-, Kaon+, Kaon-, Proton, and Antiproton, simulated with EPOS 3.4. using various EoS (Tab 7.2). Compared with STAR data [143]. In the bottom panels there is a ratio between the simulations based on BEST EoS and X3F. This thesis

points of ratio variate around unity, but they are marked with high uncertainties.

Au+Au at $\sqrt{s_{NN}} = 27$ GeV The mesons' spectra up to $p_T < 1$ GeV/c are reasonably reproduced by the EPOS model. The model parameters are not yet adjusted to the lower

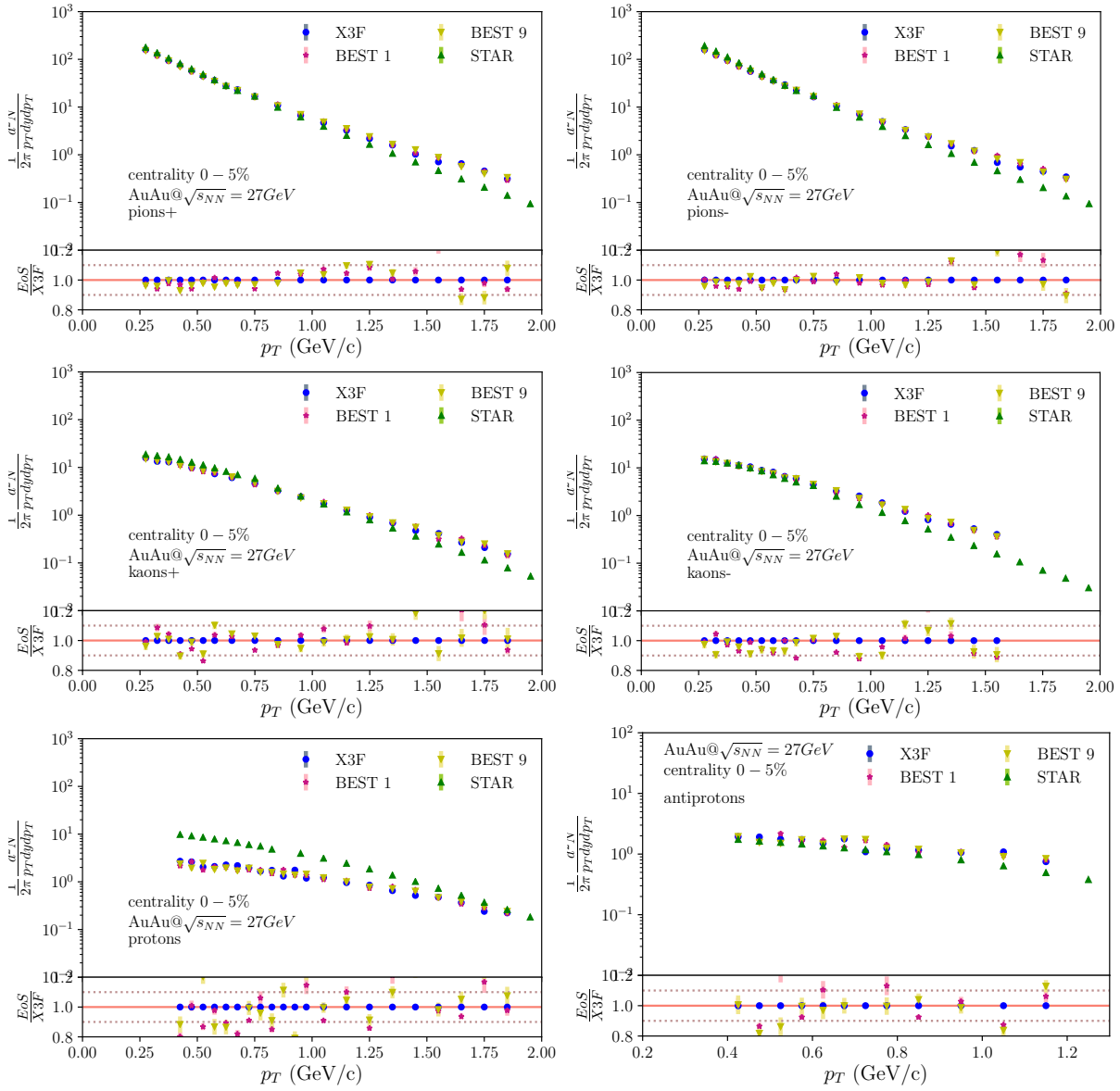

Figure 7.11 – The p_T spectra of the most central $0-5\%$ Au+Au collisions at $\sqrt{s_{NN}} = 27$ GeV of Pion+, Pion-, Kaon+, Kaon-, Proton, and Antiproton, simulated with EPOS 3.4. using various EoS (Tab 7.2). Compared with STAR data [143]. In the bottom panels there is a ratio between the simulated and experimental data. This thesis

collision energies (like in BES), such as the wrong magnitude of radial flow, resulting in a broader distribution of p_T spectra. The plotted spectra are too flat for protons, which can be caused by the not adequate fraction of corona particles over core ones. On the other hand, the clear overproduction of particles in a given range of rapidity is visible in spectra for peripheral collisions.

For both centralities, the differences between data sets based on various EoS are similar to these at $\sqrt{s_{NN}} = 7.7$ GeV: no clear trend, the ratios fluctuate.

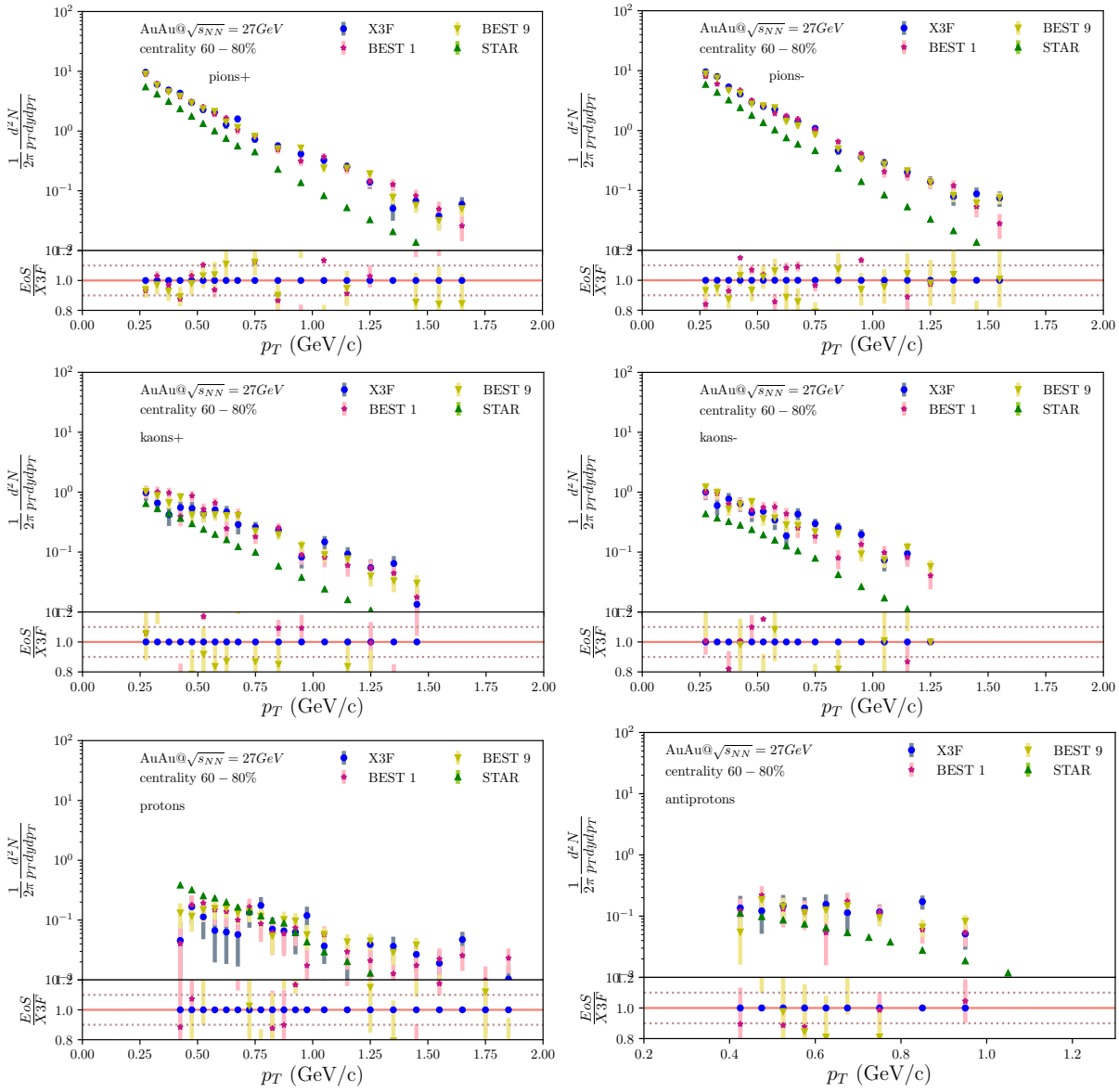

Figure 7.12 – The p_T spectra of the most peripheral 60% − 80% Au+Au collisions at $\sqrt{s_{NN}} = 27$ GeV of Pion+, Pion-, Kaon+, Kaon-, Proton, and Antiproton, simulated with EPOS 3.4. using various EoS (Tab 7.2). Compared with STAR data [143]. In the bottom panels there is a ratio between the simulations based on BEST EoS and X3F. This thesis

Elliptic flow

The simulated flow for Au+Au collisions at $\sqrt{s_{NN}} = 7.7$ GeV (Fig. 7.13) shows the good agreements with the STAR data. However, the high p_T part is marked with big statistic uncertainties. In case of Au+Au collisions at $\sqrt{s_{NN}} = 27$ GeV (Fig. 7.14) the differences between simulated and experimental data are more vital. The biggest discrepancies are visible for protons.

The anisotropies in flow are expected to be mostly built during the QGP phase, so in the simulations' hydrodynamic evolution. As this part is based on the EoS one could expect elliptic flow measurements to be sensitive to changes of EoS. However, as showed in Figures 7.13 and 7.14, the averaged over all events v_2 calculated using Event Plane method [43], does not emphasize such differences.

7.2.4 Event-by-event Fluctuations

The observables integrated over multiple events described in previous sections, do not indicate any sensitivity to changes of EoS. Nevertheless, the whole system is not expected to go through the transition simultaneously. More possible is partial participation in these processes, what could be studied in the event-by-event (*ebe*) fluctuations analysis [179]. Close to the CP, it is expected to observe multiple oscillations of several variables. In this subsection, the *ebe* investigations of elliptic flow and moments of particles' distributions are reported.

Event-by-event elliptic flow

In the Sec.7.2.3, the shown results correspond to the average overall available events. In addition, in Fig. 7.15 there is a distribution of v_2^{obs} (not corrected with resolution of event plane) of each event. The Gaussian-like shape with the centre in 0.0 does not differ between simulations based on various EoS.

The possible explanation is the attenuation of the searched differences by the subsequent after hydrodynamic evolution, hadronic phase.

Moments of particle distributions

The non-monotonic behaviour in the event-by-event fluctuations of globally conserved quantities is treated as one of the signatures of the presence of CP [180, 181]. The moments of distributions characterising the given fluctuations are:

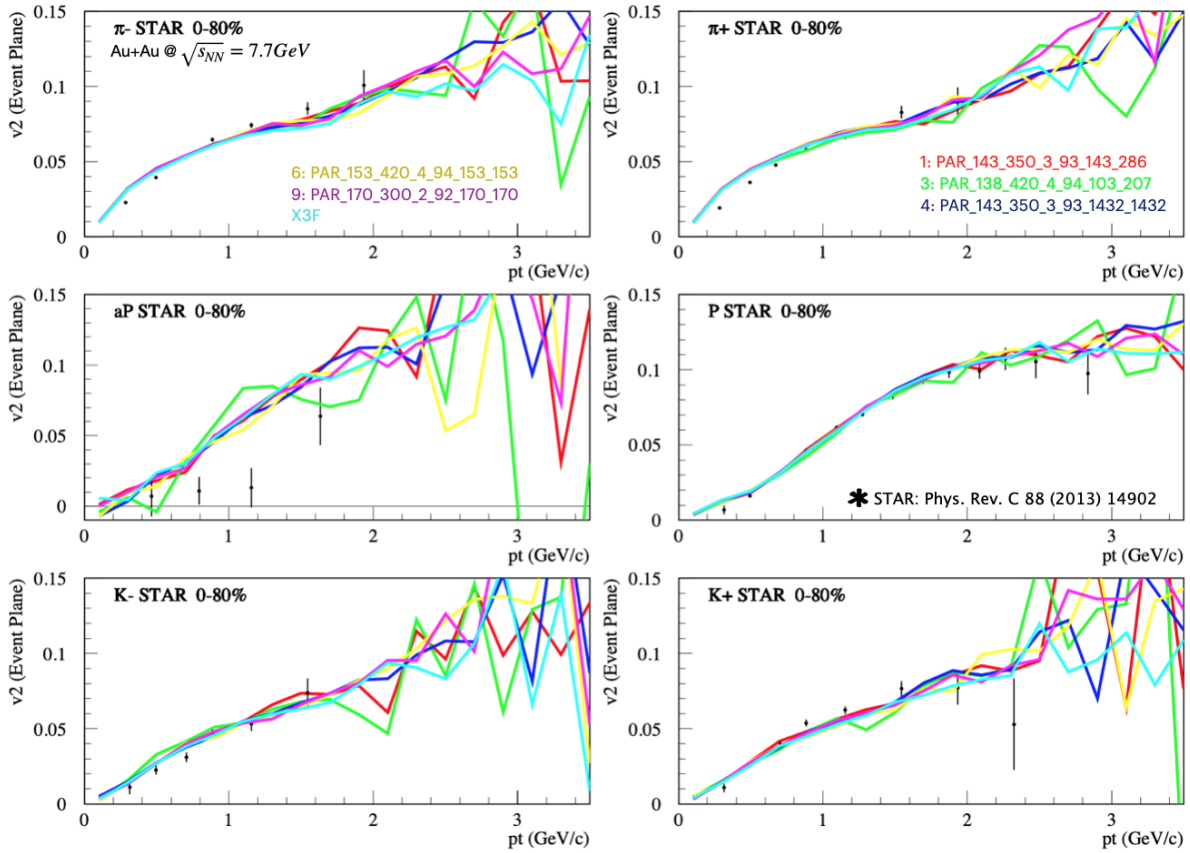

Figure 7.13 – Elliptic flow of pions, kaons and protons calculated using Event Plane method (described in [43]) for Au+Au collisions at $\sqrt{s_{NN}} = 7.7$ GeV, centrality $0-80\%$. Various data sets corresponds to simulated with EPOS 3.4. and experimental STAR data from [73]. This thesis

— the mean (M)
— the standard deviation (σ)
— the skewness (S), which corresponds to the asymmetry of the distribution
— the kurtosis (κ), reflecting the degree to which the distribution is peaked relative to the normal distribution.

They are linked with the corresponding higher-order thermodynamic susceptibilities, and the system's correlation length [182, 183], which are expected to deviate for large samples in equilibrium at the CP. As a result of slowing down in the vicinity of CP, in reality, the system is driven away from the thermodynamic equilibrium, and the maximum value of correlation length attains 1.5-3 fm [182]. During the fireball evolution after the hadronisation stage, the freeze-out signal information can dissipate [184]. However, if it survives,

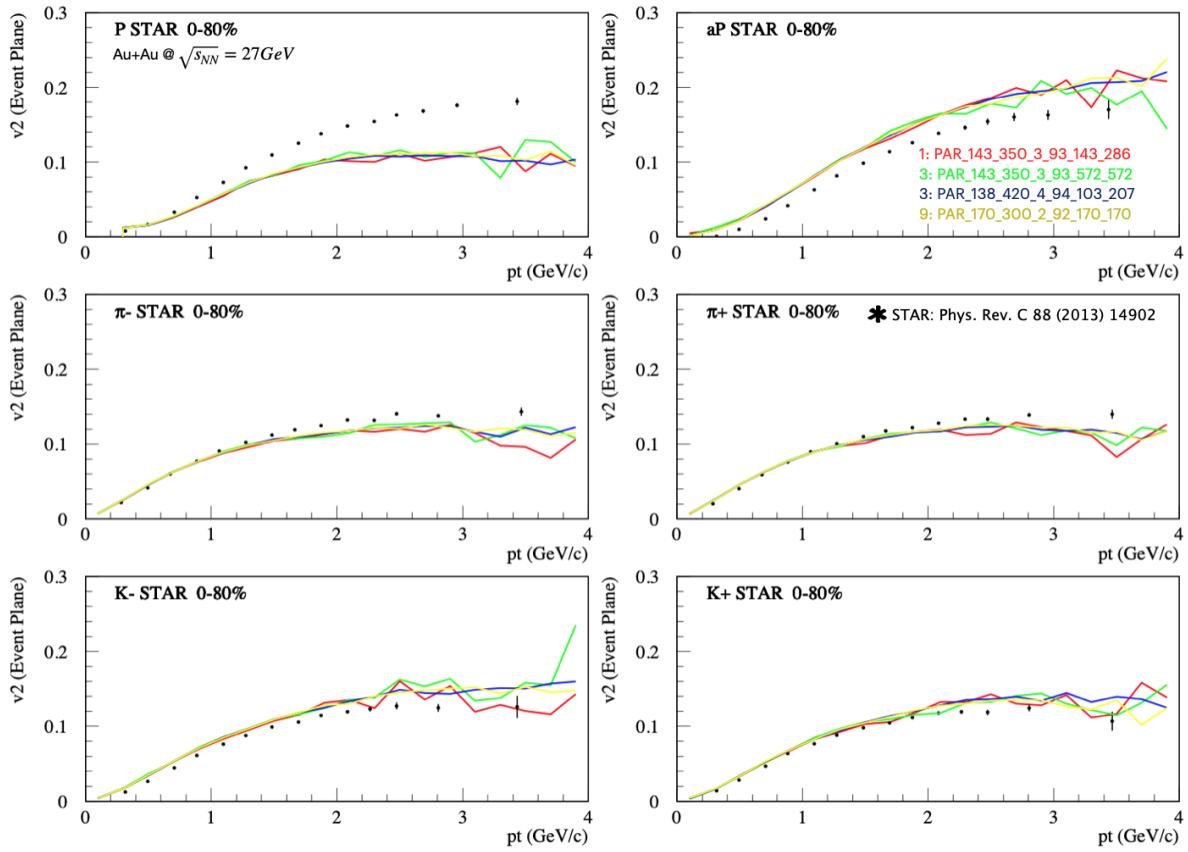

Figure 7.14 – Elliptic flow of pions, kaons and protons calculated using Event Plane method (described in [43]) for Au+Au collisions at $\sqrt{s_{NN}} = 27$ GeV, centrality $0 - 80\%$. Various data sets corresponds to simulated with EPOS 3.4. and experimental STAR data from [73]. This thesis

the higher moments can become useful in studies of CP's location. As the CP's location is changed in various used EoS, the moments of particle distributions are expected to be a useful tool in the performed investigation. In this section, the net-proton number is studied as a function of the number of participants and collision energy.

In Figures 7.16 and 7.17 the simulated with EPOS model moments of net-proton distributions as a function of number of participants (*Npart*) for Au+Au collisions at $\sqrt{s_{NN}} = 7.7$ and 27 GeV are plotted. The various EoS are used as an input to the hydrodynamical evolution.

The differences between data sets are visible, starting from the mean of the distributions of net-protons. For collisions, at $\sqrt{s_{NN}} = 7.7$ GeV the standard deviation is relevantly lower for the BEST9 data set, in which the CP is located at high T and low μ_B

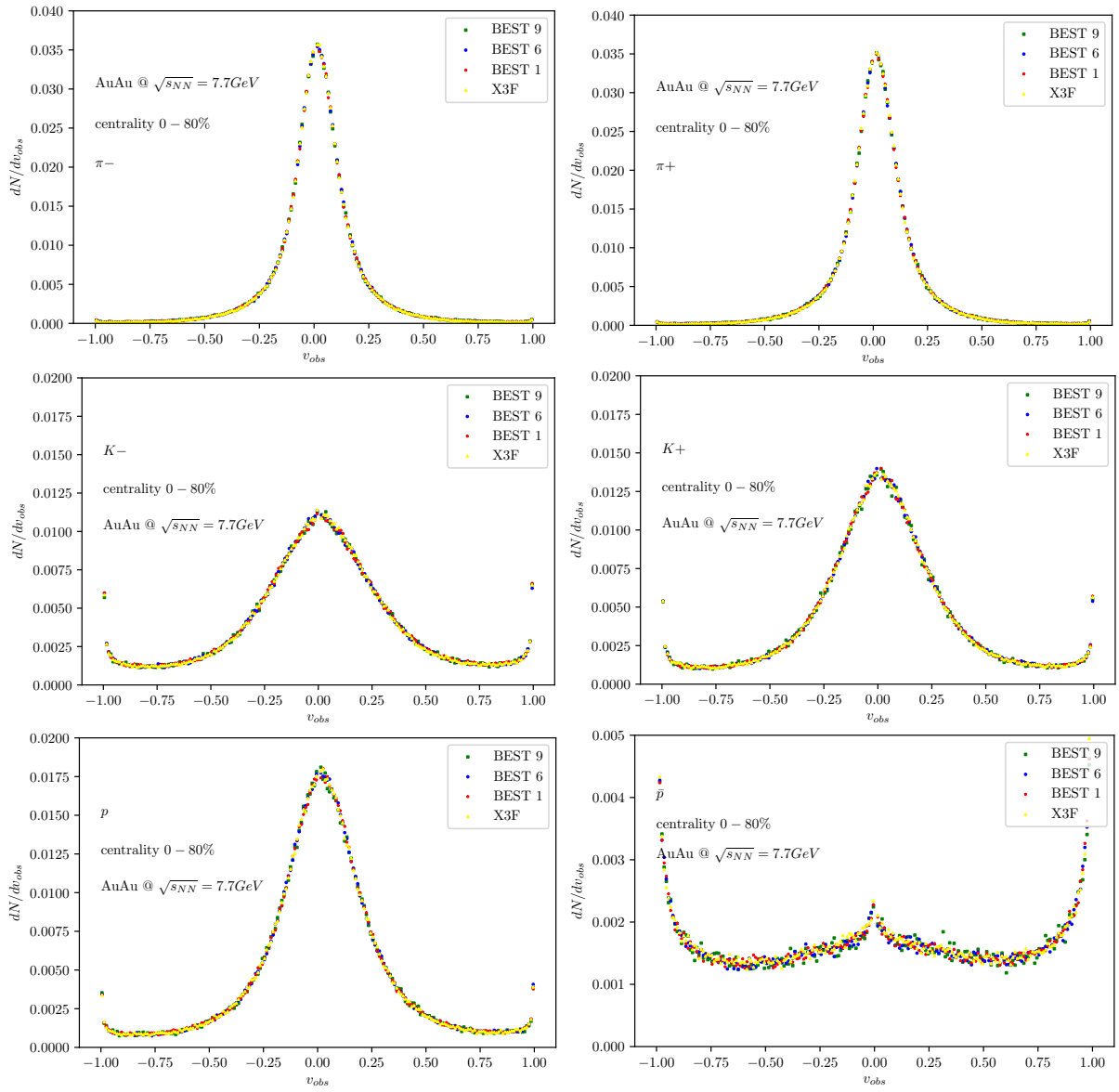

Figure 7.15 – The event-by-event v_2^{obs} distributions of pions, kaons, protons for Au + Au collisions at $\sqrt{s_{NN}} = 7.7$. GeV for centrality $0 - 80\%$. This thesis

(corresponding to systems obtained at higher $\sqrt{s_{NN}}$). The differences are becoming more negligible with the increase in the number of participants. The low-multiplicity events consist mostly of the *core* particles, so going through the hydrodynamical evolution. The effect of changes of EoS, as it is expected, is mostly enhanced there. For collisions at $\sqrt{s_{NN}} = 7.7$ GeV the statistic error bars are relevantly bigger than in case of collisions at $\sqrt{s_{NN}} = 27$ GeV. The clear separation between the various data sets is visible for the net-

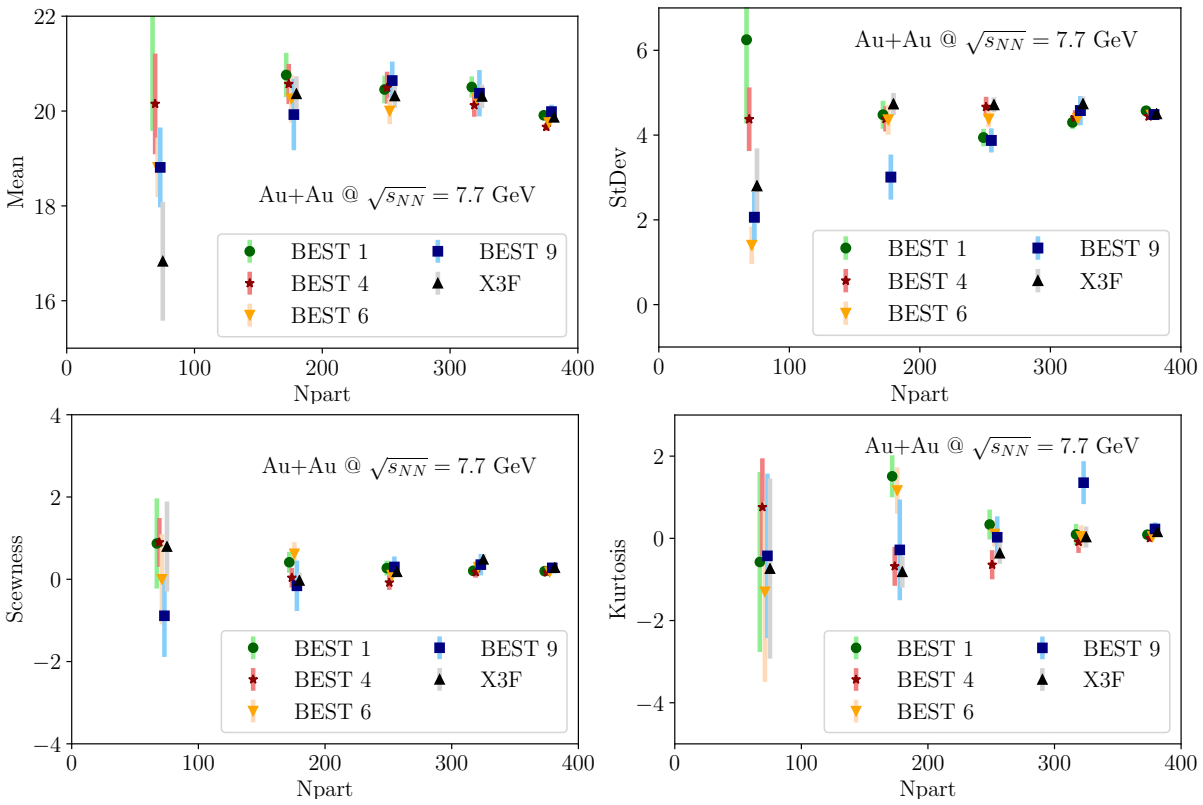

Figure 7.16 – Moments of particle distributions: mean, standard deviation, skewness and kurtosis for Au+Au collisions at $\sqrt{s_{NN}} = 7.7$ GeV as a function of number of participants. The shifts of the point on x-axis are applied for better visualisation. This thesis

proton distributions' means for $\sqrt{s_{NN}} = 27$ GeV. Similarly to the lower collision energy the differences are the multiplicity dependent for all the measured moments.

In Figure 7.18 the comparison between two examined collision energies $\sqrt{s_{NN}} = 7.7$ and 27 GeV are shown for $S\sigma$ and $\kappa\sigma^2$ as a function of number of participants. Only BEST9 data set does not show the energy dependence, where the lower energy correspond to the higher values of $S\sigma$, what is the expected trend [185]. The significant disparities are present for various EoS for the $\sqrt{s_{NN}} = 7.7$ GeV data even with the presence of high statistic uncertainties. Both $S\sigma$ and $\kappa\sigma^2$ for the $\sqrt{s_{NN}} = 27$ does not show the multiplicity dependence.

Figure 7.19 shows the $S\sigma$ and $\kappa\sigma^2$ integrated overall centralities as a function of the collision energy. The significant energy dependence is present for $S\sigma$ for all EoS. All the points at given energy are within the statistic errors, so no clear statement about the discrepancies between the EoS can be made. $\kappa\sigma^2$ shows bigger variations between

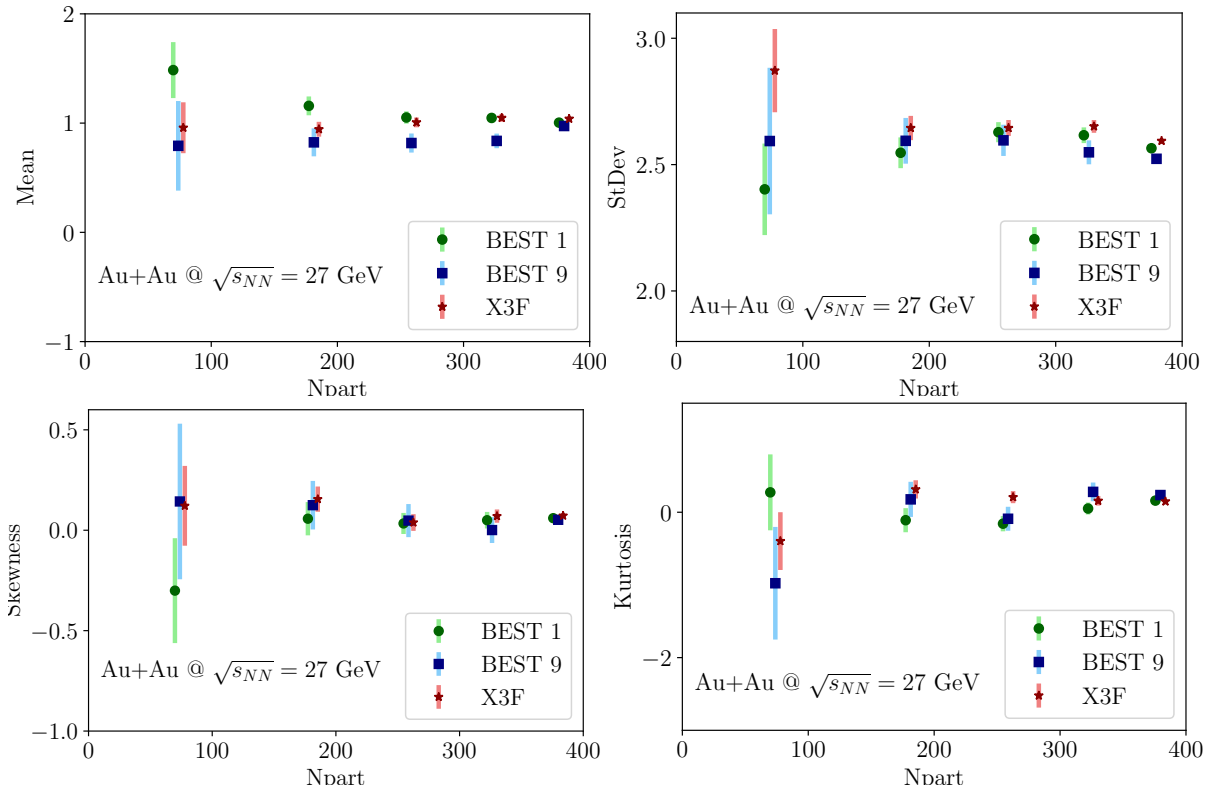

Figure 7.17 – Moments of particle distributions: mean, standard deviation, skewness and kurtosis for Au+Au collisions at $\sqrt{s_{NN}} = 27$ GeV as a function of number of participants. The shifts of the point on x-axis are applied for better visualisation. This thesis

different EoS data sets. At $\sqrt{s_{NN}} = 7.7$ GeV the highest point corresponds to the EoS where the CP is located at high T and low μ_B and the simulated system is expected to go through the first-order transition, while the negative value is related with BEST 4, where the criticality is the less pronounced. For data sets simulated at $\sqrt{s_{NN}} = 27$ GeV the differences are smaller; however, the BEST9 value is the highest. The energy dependence is not definite.

The measurements of the net-proton distributions' moments show the differences between data simulated using various Equations of State.

7.2.5 Two Particle Cumulants

This Section consists of comparison of the STAR data described in Section 4 (same data selection criteria) and simulated with EPOS 3.4 using EoS BEST1 (parameters: PAR 143 350 3 93 143 286). In Figures 7.20 and 7.21 the elliptic and triangular flow for Au+Au

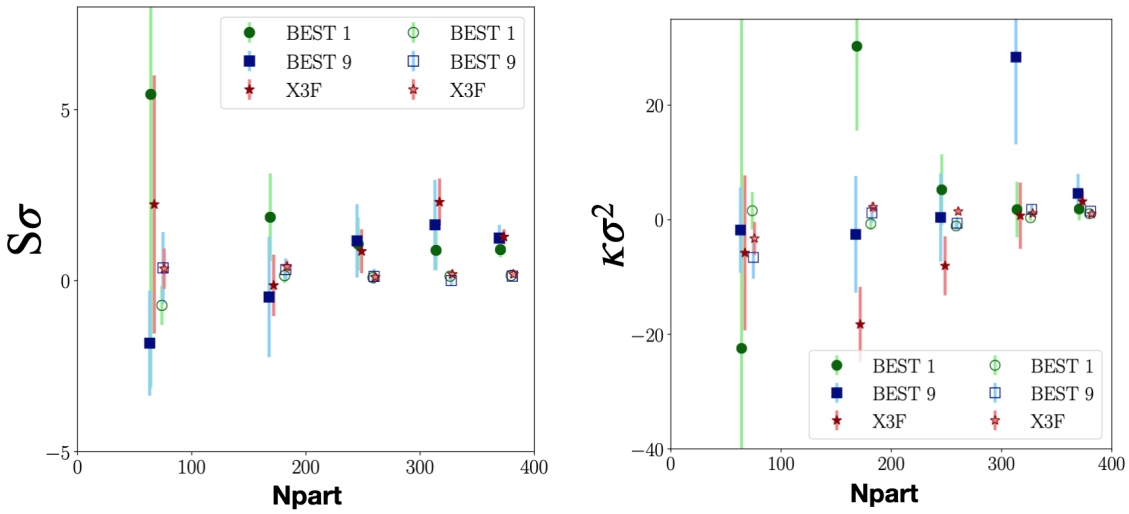

Figure 7.18 – The $S\sigma$ and $\kappa\sigma^2$ for Au+Au collisions at $\sqrt{s_{NN}} = 7.7$ (full markers) and 27 GeV (empty markers) as a function of number of participants. The shifts of the point on x-axis are applied for better visualisation. This thesis

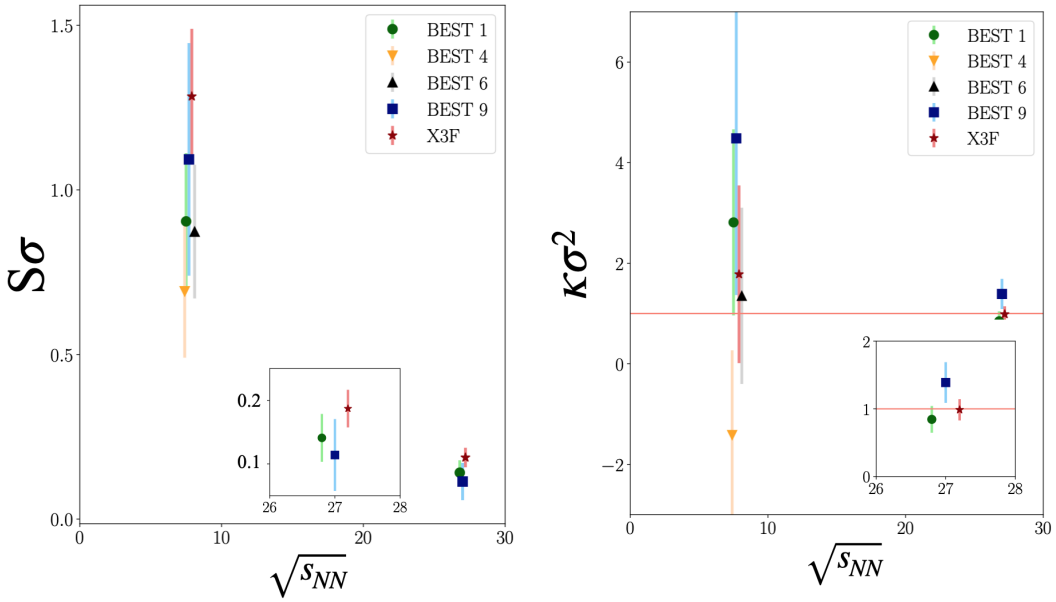

Figure 7.19 – The $S\sigma$ and $\kappa\sigma^2$ for Au+Au collisions at $\sqrt{s_{NN}} = 7.7$ (full markers) and 27 GeV (empty markers) as a function of the collision energy $\sqrt{s_{NN}}$. The zoomed windows correspond to the points got collisions at $\sqrt{s_{NN}} = 27$ GeV. The shifts of the point on x-axis are applied for better visualisation. This thesis

collisions at $\sqrt{s_{NN}} = 27$ GeV are shown.

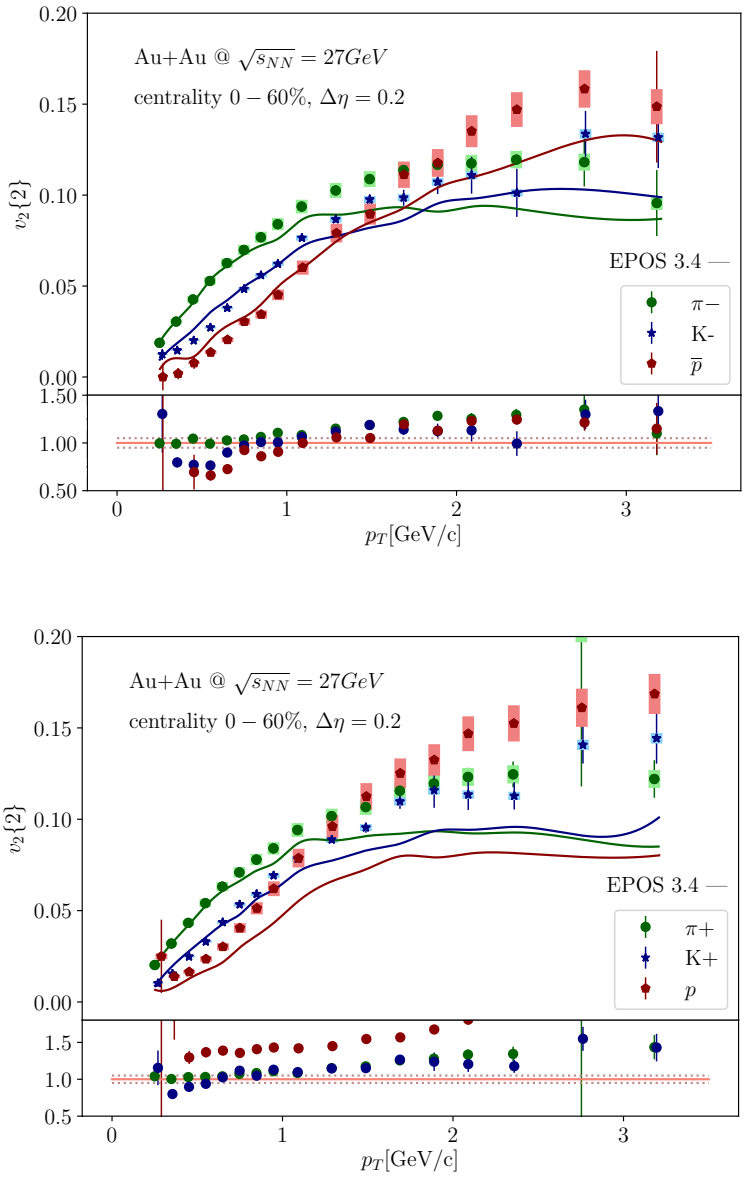

Figure 7.20 – $v_2\{2\}$ for Au+Au collisions at $\sqrt{s_{NN}} = 27$ GeV for positive and negative particles. Comparison of experimental STAR results (points) and simulated with EPOS 3.4 (line). This thesis

The elliptic flow of pions and kaons, both signs, is well reproduced up to $p_T < 1$ GeV/c. The trend of the mass splitting is kept in the model but for higher transverse momentum $v_2\{2\}$ is underestimated. The most relevant discrepancies are visible for protons, which significantly do not follow the experimental data in the whole range of p_T.

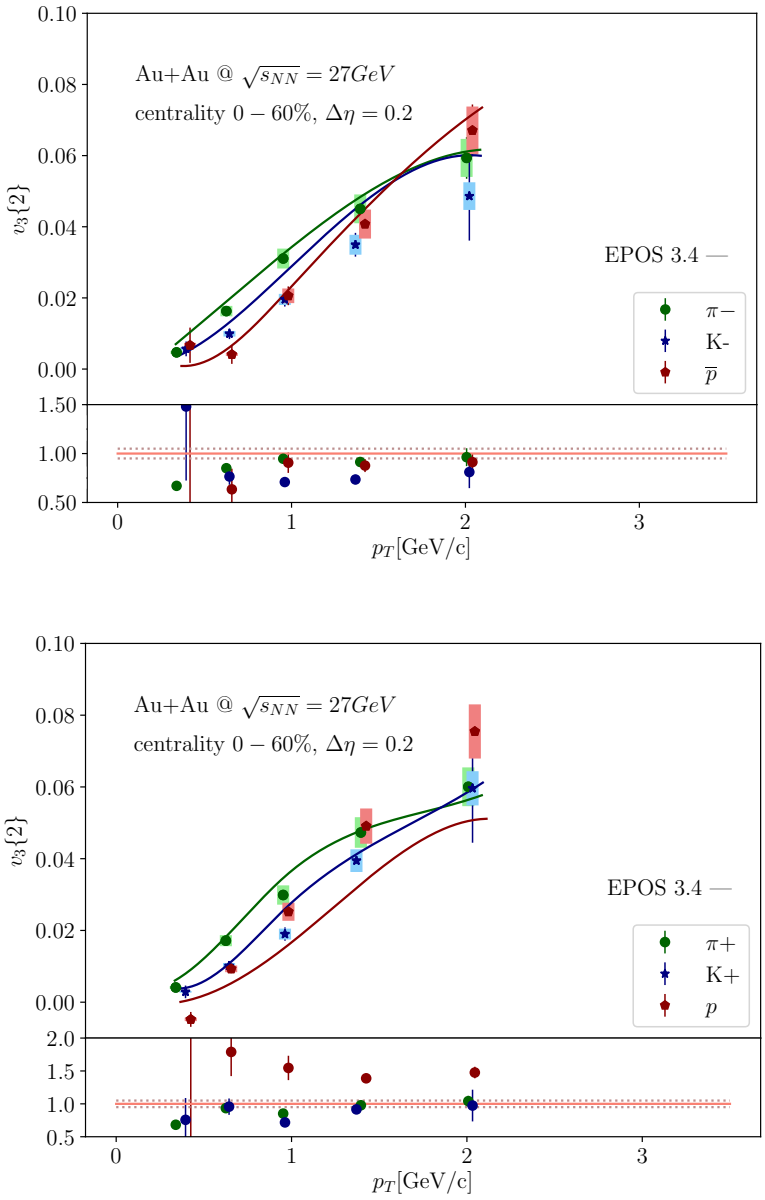

Figure 7.21 – $v_3\{2\}$ for Au+Au collisions at $\sqrt{s_{NN}} = 27$ GeV for positive and negative particles. Comparison of experimental STAR results (points) and simulated with EPOS 3.4 (line). This thesis

Triangular flow of both data sets are closer to the agreement than for the elliptic flow. The simulated with EPOS $v_3\{2\}$ of negative particles shows the trend of mass ordering, and reproduce the experimental data well. Triangular flow of $\pi+$ and $K-$ is consistent with STAR, while, protons' one is not.

CONCLUSION

7.3 Summary and discussion of results

In this thesis, detailed studies of the dynamics of newly-created matter in the heavy-ion collisions were presented and discussed. Both an experimental and a theoretical approach were applied to broaden the knowledge in this subject.

The first part of the thesis consists of studies of $v_2\{2\}$ and $v_3\{2\}$ calculated basing on 2-Particle Cumulants for the real data collected by the STAR experiment. Both harmonics as a function of centrality show clear particle species dependence, where the protons flow is the highest. The $v_2\{2\}$ is susceptible to the eccentricity, which varies with the centrality of the collision. Oppositely, such a dependence is not observed for the $v_3\{2\}$. The dominating viscous effects cause the elliptic flow attenuation at peripheral collisions (in EPOS approach the corona part dominates there and the jet contribution causes the vanishing of the flow). There is not a substantial enhancement of all particle species flow with increasing collision energy. The difference between the eccentricities in the given centrality bin at different collision energies in the studied range is negligible. Consequently, all the discrepancies between flow measured in collisions at various beam energies can be caused by matter reaction properties.

The p_T-differential $v_n\{2\}$ for all energies show the mass ordering and split for the higher p_T (≈ 2 GeV/c) to baryon and mesons. This observation is consistent with the studies at higher beam energies such as $\sqrt{s_{NN}} = 200$ GeV or LHC energies. This indicates a similar interplay between radial and higher-order flow harmonics. The scaling with the number of constituent quarks is kept for the Au+Au collisions at $\sqrt{s_{NN}} = 200$ GeV and for negative particles at lower examined energies. Although there is a small scale breaking for low KE_T for positive particles at BES energies, all these observations imply that flow originates mostly from the partonic phase of the system evolution. However, hadrons are created at the freeze-out hypersurface from the flowing fluid, where the mass effect of not present yet. It originates from the following hadronic rescaterring, mainly at low p_T.

Both elliptic and triangular flow do not differ between protons and antiprotons at $\sqrt{s_{NN}} = 200$ GeV. However, the relevant increase of such differences is present for lower

collision energies. In this thesis, a detailed investigation of possible sources of these differences was performed. Firstly, no p_T dependence of $v_2(p) - v_2(\bar{p})$ relations is indicated in examined data. It implies the lack of the differences between flow harmonics interplay of particles and antiparticles. Subsequently, the possible relation of observed discrepancies with the initial geometry of the collision was examined.The triangular flow shows increasing differences between flow of protons and antiprotons with the lowering of $\sqrt{s_{NN}}$, similar as observed for elliptic flow. This observation is substantial for the theoretical studies from [89] of additional viscous corrections to the measured flow. The violation by protons and antiprotons n_q-scaling of flow in the function of transverse kinetic energy was studied. Protons break the scaling relevantly, while antiprotons' do not. It can lead to the conclusion that these baryons' origin is not the same as it was suggested in [91, 92]. However, there is no clear energy dependence of the size of protons' scaling violation. In the proposed theoretical scenario, the lower the collision energy, the more immense contribution of transported protons is into the measured flow. Finally, the kaons were used as a neutral reference for investigating the mean filed potentials' effect on the p and $\bar{p}$ flow [90]. The mass-independent scaled $v_2\{2\}$ of protons is expected to behave oppositely to antiprotons' concerning kaons. The performed measurements do not confirm this scenario.

In the second part of the thesis, studies of various Equations of State implemented in the EPOS model were described. The development of the generator's code by introducing new EoS gave a unique possibility to investigate the impact of EoS on the final observables. Apart of the EoS, the whole structure of the model remained unchanged. Studies of yields, transverse momentum spectra and elliptic flow did not show any substantial effect of switching the EoS. The moments of net protons distributions gave important information about the variations of EoS. The differences between data sets are visible for all studied moments: mean, standard deviation, skewness, and kurtosis. It makes the investigation of fluctuation of the particle distributions the most adequate observable for studies of the EoS.

Data simulated with EPOS 3.4 were compared in various ways with the STAR ones: particles' yields, p_T-spectra, elliptic flow (Event Plane) and finally basing on 2-Particle Cumulants, $v_2\{2\}$ and $v_3\{2\}$. The model has the biggest problem with a reproduction of higher-p_T data and overestimates pions' production in a given range of rapidity. Implementation of the EoS considering the finite μ_B made a a major step in the model's development. The agreement with experimental data was not expected because the model has not yet been adjusted to describe lower collision energies. At BES energies, the ac-

celerated ions do not have such a flat shape as those at LHC. Consequently, the more spherical shape has to be considered in the description of the binary collisions. Furthermore, in the hydrodynamical evolution included EPOS model only the mean values are propagated. The extension of these calculation are needed to improve the reproduction of the large fluctuations in the CP vicinity.

In conclusion, the performed research significantly impact the studies of nuclear matter's dynamics and properties. Combining the experimental and theoretical investigation made it a unique work providing additional constraints in the model development, studies of thermodynamic relations in expanding matter, and factual information about the higher-order harmonics of flow.

7.4 Outlook

The research included in this thesis is a significant reference for both theoretical and experimental studies of the QCD phase diagram. The studies performed as a function of beam energy can be used to map the μ_B, T space with the view to investigating properties of the matter and its transitions. The BES I and II are programs that introduced a unique possibility for studying a broad range of the QCD phase diagram. The experimental studies of flow harmonics are an essential reference for developing the hydrodynamical phases in the MC models. The triangular flow measurements provide unique information about the initial stage fluctuations and constrain the studies of viscous effects in the medium. The performed development of EPOS is one of the first steps in preparing the model describing the evolution of the various systems (N+N, A+A) obtained due to the collisions at a wide range of beam energies. Absence of the MC model applicable for the low energies ($\sqrt{s_{NN}} < 20$ GeV) is one of the biggest problems for the characterization of the matter at finite baryonic densities or first-order phase transition.

On the other hand, investigation of the impact of the changes in the EoS withing a single model on the final observables is a milestone for the experimentalist looking for the signatures of phase transitions of the medium. I have tests the sensitivity to EoS of several experimental analysis types yet found only one susceptible to introduces variations in EoS. However, the hydrodynamical evolution included EPOS model only the mean values are propagated. The extension of these calculation are needed to improve the propagation of the large fluctuations in CP vicinity. More studies have to be performed to complete the research, such as studies of the space-time evolution using the HBT methods or extend

studies of the particles distributions' moments. These results are crucial for planning the scientific programs for new, still-under-construction experimental facilities such as NICA or FAIR.

Summarizing, the performed research in the frame of this thesis, provide substantial constrain onto the development of our present knowledge and plans for the future studies of the properties of the strongly interacting matter and its transitions.

Chapter 8

Appendix A: Useful equations

8.1 Thermodynamic quantities

Entropy density:

$$\frac{S}{T^3} = \frac{1}{T^3}\frac{\partial P}{\partial T} \tag{8.1}$$

Baryon density

$$\frac{n_B}{T^3} = \frac{1}{T^3}\frac{\partial P}{\partial \mu_B} \tag{8.2}$$

Energy density:

$$\frac{\epsilon}{T^4} = \frac{S}{T^3} - \frac{P}{T^4} + \frac{\mu_B}{T}\frac{n_B}{T^3} \tag{8.3}$$

Speed of sound:

$$c_S^2 = \left(\frac{\partial P}{\partial \epsilon}\right)_{S/n_B} = \frac{n_B^2\partial_T^2 P - 2Sn_B\partial_T\partial_{\mu_B}P + S^2\partial_{\mu_B}^2 P}{(\epsilon+P)(\partial_T^2 P\partial_{mu_B}^2 P - (\partial_T\partial_{\mu_B}P)^2)} \tag{8.4}$$

Baryon susceptibilities:

$$\chi_n^B = \frac{\partial^n(P/T^4)}{\partial(\mu_B/T)^n} \tag{8.5}$$

Speed of the particle:

$$\beta = \frac{v}{c} = \frac{L}{c\Delta t} \tag{8.6}$$

Mass square of particle:

$$m^2 = p^2(\frac{1}{\beta} - 1) \tag{8.7}$$

where $\beta = p/E$ and $E = \sqrt{p^2 + M^2}$, p is the measured by TPC momentum of the particle and Δt is the time.

Chapter 9

Appendix B: iTPC software development

As a member of the STAR Collaboration, I participated in the **service work**. This is a 2-months project which is not directly related to the topic of my analysis, however, it is profitable for the whole Collaboration.

During the installation of the new sectors of TPC called Inner Time Projection Chamber (iTPC) the various tests had to be performed in order to ensure the quality of the future performance of the detector. During my *service work* I was engaged in ADC tests and the first quality assurance (QA) of the data collected by iTPC during cosmic rays taking. *Only the short part of the performed studies description and few figures are placed in the Appendix.*

9.1 ADC tests

The measured in each sectors' pads voltage was investigated. The Figure 9.1 is the visualisation of the measured voltage signals in sectors 24 and 9. The not uniform distributions were studied and taken into account in the process of the reconstruction data. The Fig. 9.2 shows the two possible pad row mean voltage extraction: with the normal distribution mean and fitted with Landau one.

9.2 Data quality assurance

Before the injection of the beams into the RHIC there is approximately one month of the cosmic rays data-taking. The general characteristic of these data sets is well-known, so its analysis is a perfect tool for testing the quality of data-taking by the detectors. In Figure 9.3, the dependence of the particle energy loss in function of momentum registered by iTPC and TPC is shown. The reconstructed tracks corresponding to antiprotons in

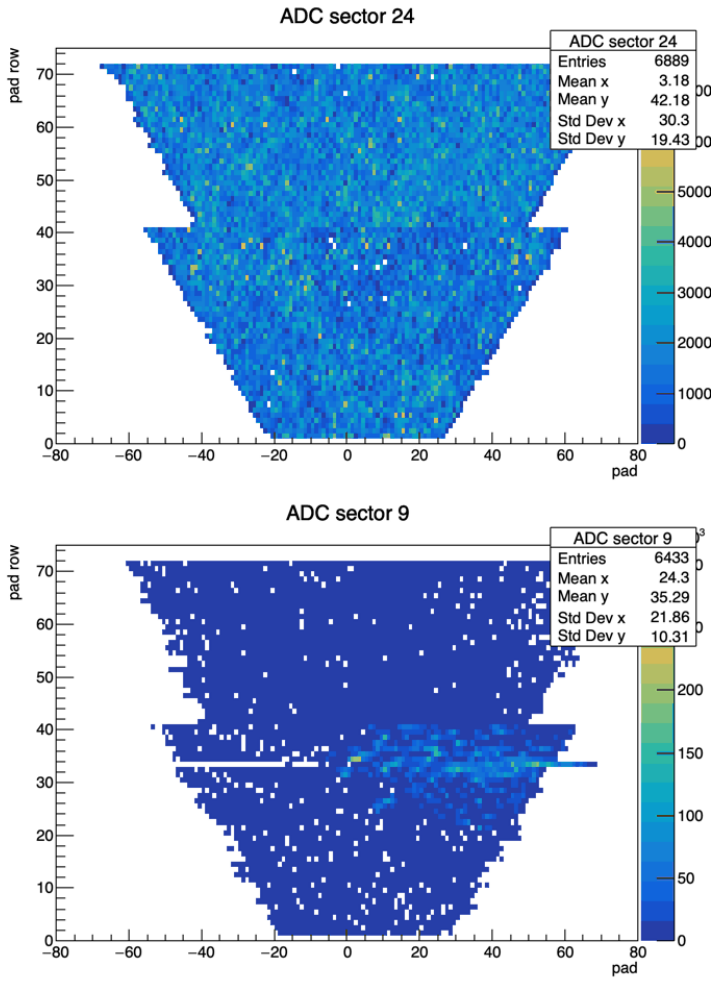

Figure 9.1 – The measured ADC in sector 24 (top) and 9 (bottom) in different pads. This thesis

collider mode, are not expected to be present in the cosmic rays (negative $q * p$). The particles originating from cosmic rays traverse the detector from the "top" to the "bottom", not from the inner to outer direction as these coming from the ion collisions. The rotation caused by the magnetic field makes the reconstruction of part the tracks looking like they refer to the negatively charged particles. The Figure 9.3 shows first example plots obtained in year 2019 during the 20^{th} and 25^{th} days of the data-taking.

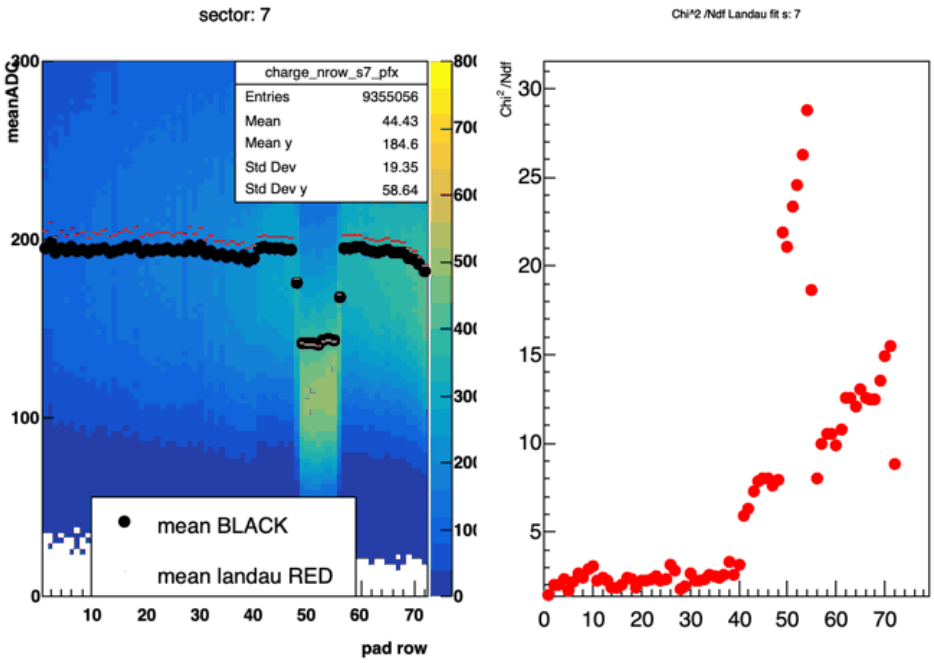

Figure 9.2 – The left panel: the measured ADC in sector 7 in different pads with the calculated for each row mean of values for normal and Landau distributions The right panel: the quality of the Landau fit to obtained distributions for each pad row. This thesis

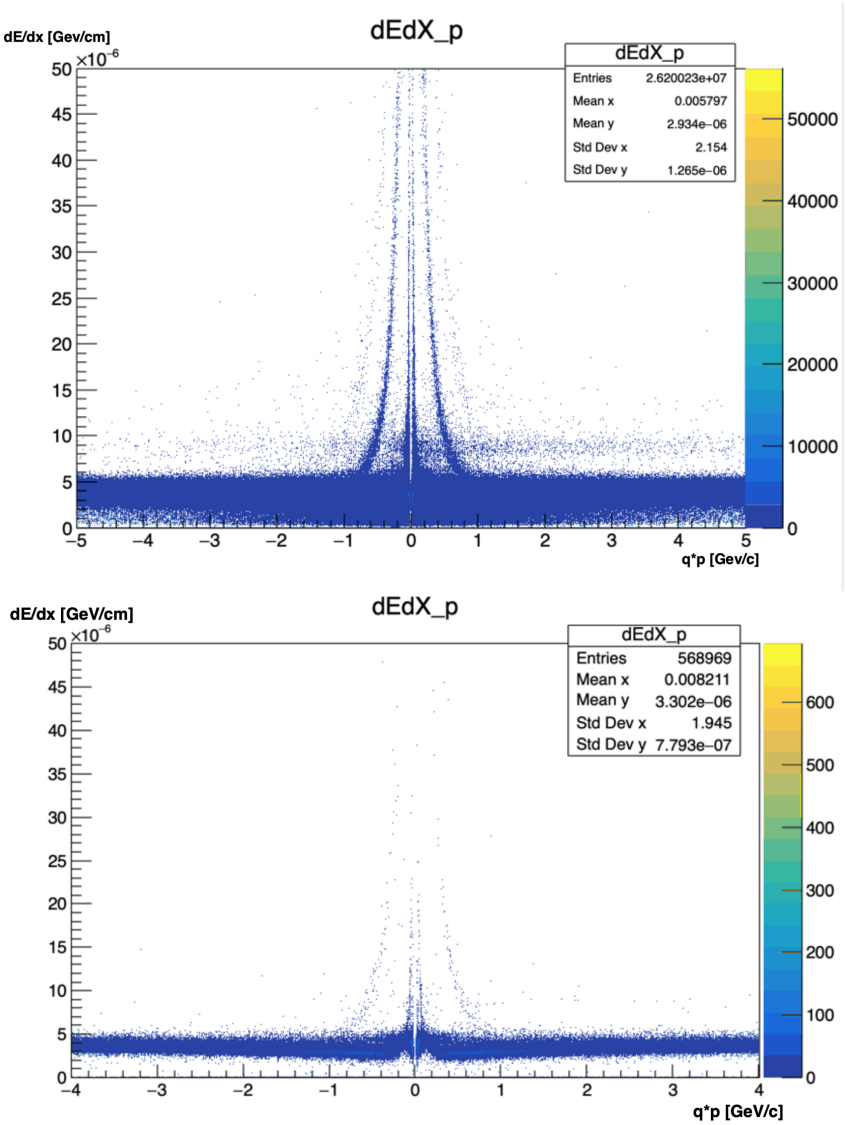

Figure 9.3 – The particle energy loss dependence on the momentum of registered particles from cosmic rays during days 20^{th} (top) and 25^{th} (bottom) during data taking in 2019. This thesis

Chapter 10

Appendix C: Rivet software development

Another additional project, I am engaged is the development of the Rivet software. My input is shortly described in this Appendix.

Rivet **R**obust **I**ndependant **V**alidation of **E**xperiment and **T**heory

A Rivet is a software dedicated to comparing the simulated with event generator, and experimental data [**Rivet-website**]. It is a simple-in-use, and standardized tool developed thanks to the contribution of the users community. Rivet consists of a set of hundreds of analysis based on the experimental published research. It gives a mutual benefit for experimentalists and theorists. The first ones have easy access to outputs of many models, which can be used for the explanation of obtained results. On the other hand, theorists developing MC models can profit from the library consisting of the significant variety of available experimental data, including different measured observables. Moreover, it is still growing as new analysis are submitted by the Rivet community users.

The first version of the Rivet software was dedicated only to the $p-p$ collision systems. The second part of the software development was mainly related to including the heavy ions in the possible collision systems. There were multiple problematic issues to be solved, like centrality definition, the introduction of cumulants, or providing the framework for HBT analysis. Secondly, as the development of the project mainly depends on the experimentalists' engagement, it had to be popularized in Collaborations performing studies of the heavy-ion collisions.

I am engaged in developing the Rivet software from both sides: experimental (STAR Collaboration) and theoretical (represent authors of EPOS model). During my thesis, I wrote the first STAR analysis, which was added to the Rivet resources and can be found at `https://rivet.hepforge.org/analyses/STAR_2016_I1414638.html`. It is the code that can be used for comparing the experimental data from [82] with any MC model providing the output in HepMC data format. In Figure 10.1, the few examples output plots

of Rivet comparison of between the STAR measurements and Pythia [186] simulations of v_3 as a function of $\Delta\eta$. In the top panels, the experimental data are illustrated with black markers, while two lines, red and blue, correspond to the event generator data, where two different methods of the centrality definitions were applied. One *IMP* is based on the impact parameter extracted from the simulated data, the *GEN* corresponds to the method using the multiplicity of the events. In the bottom panels, the ratios of MC data to experimental ones are shown. With the introduction of this analysis's code into the Rivet repository, the popularization of the Rivet in the heavy-ion STAR community was initiated.

Secondly, with my Master student Johannès JAHAN, we modified the EPOS code, adding the possibility of having the output file from simulations consistent with the Rivet software requirements.

This phase of the Rivet development was described and published in [1].

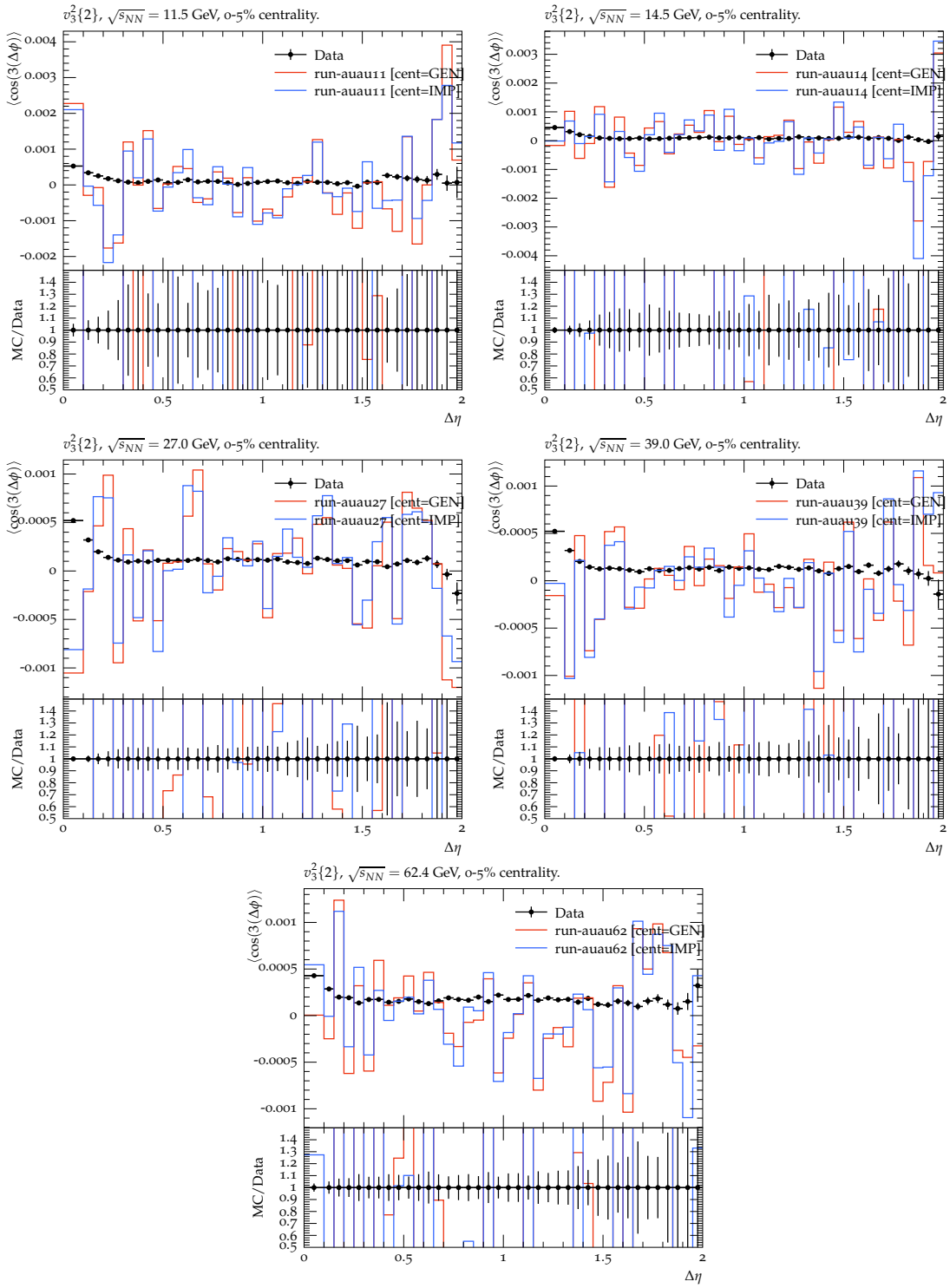

Figure 10.1 – Rivet comparison of $v_3\{2\}$ measured by STAR [82] and simulated with Pythia [186]. The most central collisions $0-5\%$ of Au+Au at $\sqrt{s_{NN}} = 11.5$, 14.5, 19.6, 27, 39, 64.4 GeV

BIBLIOGRAPHY

(1) M. Stefaniak et al., *Eur. Phys. J. C*, 2020, **80**, 485.

(2) M. Stefaniak, *Acta Phys. Polon. Supp.*, 2018, **11**, 695.

(3) M. Stefaniak and H. Zbroszczyk, *EPJ Web Conf.*, 2017, **164**, 07013.

(4) M. Stefaniak, *Phys. Part. Nucl.*, 2020, **51**, 305–308.

(5) *Pauli exclusion principle*, `https://www.britannica.com/science/Pauli-exclusion-principle`, 04/06/2020.

(6) S. Nagataki, *JPS Conf. Proc.*, 2017, **14**, ed. S. Kubono, 010003.

(7) *Standard Model*, `https://home.cern/science/physics/standard-model`, 04/06/2020.

(8) https://physics.info/standard/.

(9) A. D. Martin, *Acta Phys. Polon. B*, 2008, **39**, 2025–2062.

(10) O. Greenberg, *Phys. Rev. Lett.*, 1964, **13**, 598–602.

(11) M. Han and Y. Nambu, *Phys. Rev.*, 1965, **139**, B1006–B1010.

(12) https://www2.ph.ed.ac.uk/ playfer/PPlect8.pdf.

(13) G. Prosperi, M. Raciti and C. Simolo, *Prog. Part. Nucl. Phys.*, 2007, **58**, 387–438.

(14) W. M. Yao et al., *J. Phys. G*, 2006, **33**, 1–1232.

(15) K. G. Wilson, 1974, 45–59.

(16) G. 't Hooft, *Nucl. Phys. B*, 1978, **138**, 1–25.

(17) G. 't Hooft, *Nucl. Phys. B*, 1981, **190**, 455–478.

(18) D. J. Gross and F. Wilczek, *Phys. Rev. Lett.*, 1973, **30**, 1343–1346.

(19) D. Gross and F. Wilczek, *Phys. Rev. D*, 1973, **8**, 3633–3652.

(20) H. Politzer, *Phys. Rev. Lett.*, 1973, **30**, 1346–1349.

(21) C. Amsler et al., *Phys. Lett. B*, 2008, **667**, 1–1340.

(22) B. Andersson, 7th European Symposium on Antiproton Interactions: From LEAR to the Collider and Beyond, 1986, pp. 447–462.

(23) K. Grebieszkow, Lecture: Introduction to Heavy-Ion Physics.

(24) P. Skands, Proceedings, AEPSHEP 2014, [,63(2107)], 2013, pp. 341–420.

(25) Z. Fodor and S. D. Katz, *JHEP*, 2004, **04**, 050.

(26) S. Datta, R. V. Gavai and S. Gupta, *Nucl. Phys.*, 2013, **A904-905**, 883c–886c.

(27) G. Odyniec, *J. Phys. Conf. Ser.*, 2013, **455**, 012037.

(28) C. Allton, S. Ejiri, S. Hands, O. Kaczmarek, F. Karsch, E. Laermann, C. Schmidt and L. Scorzato, *Phys. Rev. D*, 2002, **66**, 074507.

(29) A. Bazavov, T. Bhattacharya, M. Cheng, N. H. Christ, C. DeTar, S. Ejiri, S. Gottlieb, R. Gupta, U. M. Heller, K. Huebner, C. Jung, F. Karsch, E. Laermann, L. Levkova, C. Miao, R. D. Mawhinney, P. Petreczky, C. Schmidt, R. A. Soltz, W. Soeldner, R. Sugar, D. Toussaint and P. Vranas, *Phys. Rev. D*, 2009, **80**, 014504.

(30) M. Stephanov, *PoS*, 2006, **LAT2006**, 024.

(31) R. Gavai and S. Gupta, *Phys. Rev. D*, 2008, **78**, 114503.

(32) K. Redlich, F. Karsch and A. Tawfik, *J. Phys. G*, 2004, **30**, S1271–S1274.

(33) S. Borsanyi, G. Endrodi, Z. Fodor, S. Katz, S. Krieg, C. Ratti and K. Szabo, *JHEP*, 2012, **08**, 053.

(34) J. Günther, R. Bellwied, S. Borsanyi, Z. Fodor, S. D. Katz, A. Pasztor and C. Ratti, *EPJ Web Conf.*, 2017, **137**, 07008.

(35) A. Bazavov et al., *Phys. Rev. D*, 2017, **95**, 054504.

(36) *Neutron Stars*, `https://imagine.gsfc.nasa.gov/science/objects/neutron_stars1.html`, 04/06/2020.

(37) P. Parotto, *Nucl. Phys. A*, 2019, **982**, 183–185.

(38) S. A. Voloshin, A. M. Poskanzer and R. Snellings, *Landolt-Bornstein*, 2010, **23**, 293–333.

(39) N. Demir and S. A. Bass, *Phys. Rev. Lett.*, 2009, **102**, 172302.

(40) A. El, A. Muronga, Z. Xu and C. Greiner, *Phys. Rev. C*, 2009, **79**, 044914.

(41) K. Olive et al., *Chin. Phys. C*, 2014, **38**, 090001.

(42) A. Buckley et al., *Phys. Rept.*, 2011, **504**, 145–233.

(43) R. Snellings, *New J. Phys.*, 2011, **13**, 055008.

(44) J.-Y. Ollitrault, *Phys. Rev. D*, 1992, **46**, 229–245.

(45) U. W. Heinz, *in Relativistic Heavy Ion Physics*, ed. R. Stock, 2010, vol. 23, p. 240.

(46) P. Huovinen and P. Ruuskanen, *Ann. Rev. Nucl. Part. Sci.*, 2006, **56**, 163–206.

(47) P. Christakoglou, *EPJ Web of Conferences*, 2015, **90**, 08004.

(48) M. Luzum and P. Romatschke, *Phys. Rev. C*, 2008, **78**, 034915.

(49) P. Liu and R. A. Lacey, *Phys. Rev.*, 2018, **C98**, 021902.

(50) I. Karpenko, M. Bleicher, P. Huovinen and H. Petersen, *Nucl. Phys. A*, 2016, **956**, ed. Y. Akiba, S. Esumi, K. Fukushima, H. Hamagaki, T. Hatsuda, T. Hirano and K. Shigaki, 834–837.

(51) N. Borghini, P. M. Dinh and J.-Y. Ollitrault, *Phys. Rev. C*, 2000, **62**, 034902.

(52) P. M. Dinh, N. Borghini and J.-Y. Ollitrault, *Phys. Lett. B*, 2000, **477**, 51–58.

(53) A. Bilandzic, R. Snellings and S. Voloshin, *Phys. Rev.*, 2011, **C83**, 044913.

(54) M. Stefaniak, *Beam-energy and collision-system size dependence of the anisotropic flow measurements from STAR*, `https://indico.cern.ch/event/854124/contributions/4135473/`, 2021.

(55) J.-Y. Ollitrault, A. M. Poskanzer and S. A. Voloshin, *Phys. Rev. C*, 2009, **80**, 014904.

(56) J. Brachmann, S. Soff, A. Dumitru, H. Stoecker, J. Maruhn, W. Greiner, L. Bravina and D. Rischke, *Phys. Rev. C*, 2000, **61**, 024909.

(57) B. Abelev et al., *Phys. Rev. Lett.*, 2008, **101**, 252301.

(58) G. Wang, *Nucl. Phys. A*, 2019, **982**, ed. F. Antinori, A. Dainese, P. Giubellino, V. Greco, M. P. Lombardo and E. Scomparin, 415–418.

(59) L. Adamczyk et al., *Phys. Rev. Lett.*, 2014, **112**, 162301.

(60) Y. Pandit, 2012, [J. Phys. Conf. Ser.420,012038(2013)], DOI: `10.1088/1742-6596/420/1/012038`.

(61) H. Petersen, R. La Placa and S. A. Bass, *J. Phys.*, 2012, **G39**, 055102.

(62) B. Alver and G. Roland, *Phys. Rev.*, 2010, **C81**, [Erratum: Phys. Rev.C82,039903(2010)], 054905.

(63) B. Schenke, P. Tribedy and R. Venugopalan, *Phys. Rev.*, 2014, **C89**, 064908.

(64) L. P. Csernai, J. I. Kapusta and L. D. McLerran, *Phys. Rev. Lett.*, 2006, **97**, 152303.

(65) I. A. Karpenko, P. Huovinen, H. Petersen and M. Bleicher, *Phys. Rev. C*, 2015, **91**, 064901.

(66) L. Adamczyk et al., *Phys. Rev. C*, 2012, **86**, 054908.

(67) K. Aamodt et al., *Phys. Rev. Lett.*, 2010, **105**, 252302.

(68) N. Benmoshe, M. Pinsky, A. Pokrovsky and A. Khain, *Journal of Geophysical Research: Atmospheres*, 2012, **117**, DOI: `https://doi.org/10.1029/2011JD016603`.

(69) S. Voloshin et al., *Nucl. Phys. A*, 1998, **638**, ed. T. Hatsuda, Y. Miake, K. Yagi and S. Nagamiya, 455C–458C.

(70) S. Afanasiev et al., *Phys. Rev. Lett.*, 2007, **99**, 052301.

(71) B. Abelev et al., 2009.

(72) A. Adare et al., *Phys. Rev. Lett.*, 2007, **98**, 162301.

(73) L. Adamczyk et al., *Phys. Rev.*, 2013, **C88**, 014902.

(74) S. Voloshin, *Nucl. Phys. A*, 2003, **715**, ed. H. Gutbrod, J. Aichelin and K. Werner, 379–388.

(75) B. I. Abelev et al., *Phys. Rev.*, 2007, **C75**, 054906.

(76) G. Odyniec, *PoS*, 2019, **CORFU2018**, 151.

(77) A. Taranenko, *KnE Energ. Phys.*, 2018, **3**, 178–187.

(78) X. Luo, *Nucl. Phys. A*, 2016, **956**, ed. Y. Akiba, S. Esumi, K. Fukushima, H. Hamagaki, T. Hatsuda, T. Hirano and K. Shigaki, 75–82.

(79) D. Keane, *J. Phys. Conf. Ser.*, 2017, **878**, 012015.

(80) H. Caines, *Nucl. Phys. A*, 2017, **967**, ed. U. Heinz, O. Evdokimov and P. Jacobs, 121–128.

(81) J. Auvinen and H. Petersen, *Phys. Rev. C*, 2013, **88**, 064908.

(82) L. Adamczyk et al., *Phys. Rev. Lett.*, 2016, **116**, 112302.

(83) N. Magdy, *J. Phys. Conf. Ser.*, 2017, **779**, ed. H. Z. Huang, R. Seto, J. Thäder and N. Xu, 012060.

(84) L. Adamczyk et al., *Phys. Rev. Lett.*, 2013, **110**, 142301.

(85) L. Adamczyk et al., *Phys. Rev.*, 2016, **C93**, 014907.

(86) J. C. Dunlop, M. A. Lisa and P. Sorensen, *Phys. Rev.*, 2011, **C84**, 044914.

(87) J. Steinheimer, V. Koch and M. Bleicher, *Phys. Rev.*, 2012, **C86**, 044903.

(88) Y. Burnier, D. E. Kharzeev, J. Liao and H.-U. Yee, *Phys. Rev. Lett.*, 2011, **107**, 052303.

(89) Y. Hatta, A. Monnai and B.-W. Xiao, *Phys. Rev.*, 2015, **D92**, 114010.

(90) J. Xu, T. Song, C. M. Ko and F. Li, *Phys. Rev. Lett.*, 2014, **112**, 012301.

(91) Y. Guo, F. Liu and A. Tang, *Phys. Rev. C*, 2012, **86**, 044901.

(92) B. Tu, S. Shi and F. Liu, 2018.

(93) S. A. Bass, M. Belkacem, M. Bleicher, M. Brandstetter, L. Bravina, C. Ernst, L. Gerland, M. Hofmann, S. Hofmann, J. Konopka, G. Mao and L. Neise, *Prog. Part. Nucl. Phys.*, 1998, **41**, 225–370.

(94) M. Bleicher, E. Zabrodin, C. Spieles, S. Bass, C. Ernst, S. Soff, L. Bravina, M. Belkacem, H. Weber, H.and Stocker and W. Greiner, *J. Phys.*, 1999, **G25**, 1859–1896.

(95) G. Aad et al., *Phys. Rev. Lett.*, 2016, **116**, 172301.

(96) L. Milano, *Nucl. Phys. A*, 2014, **931**, ed. P. Braun-Munzinger, B. Friman and J. Stachel, 1017–1021.

(97) M. Aaboud et al., *Phys. Rev. C*, 2017, **96**, 024908.

(98) M. A. Lisa, S. Pratt, R. Soltz and U. Wiedemann, *Ann. Rev. Nucl. Part. Sci.*, 2005, **55**, 357–402.

(99) K. Aamodt et al., *Phys. Lett.*, 2012, **B708**, 249–264.

(100) Ł. K. Graczykowski and M. A. Janik, *Nucl. Phys.*, 2014, **A926**, 205–212.

(101) V. Okorokov, *EPJ Web Conf.*, 2017, **158**, 01004.

(102) H. Satz, *Phys. Rept.*, 2004, **403-404**, 33–50.

(103) *Alternating Gradient Synchrotron*, https://www.bnl.gov/rhic/AGS.asp, [Online; accessed 20-February-2021].

(104) W. Henning, *Nucl. Phys. News*, 1990, **1**, 13–19.

(105) K. Aamodt et al., *JINST*, 2008, **3**, S08002.

(106) A. Sorin, V. Kekelidze, A. Kovalenko, R. Lednicky, I. Meshkov and G. Trubnikov, *Nucl. Phys.*, 2011, **A855**, 510–513.

(107) X. Luo, *J. Phys. Conf. Ser.*, 2015, **599**, 012023.

(108) *J-PARK*, https://j-parc.jp/c/en/, [Online; accessed 20-February-2021].

(109) *Compact Stars in the QCD Phase Diagram VI*, https://indico.jinr.ru/event/299/.

(110) *Brookhaven National Laboratory*, https://www.bnl.gov/.

(111) H. Hahn et al., *Nucl. Instrum. Meth. A*, 2003, **499**, 245–263.

(112) M. Harrison, S. G. Peggs and T. Roser, *Ann. Rev. Nucl. Part. Sci.*, 2002, **52**, 425–469.

(113) W. Fischer, *Run Overview of the Relativistic Heavy Ion Collider*, https://www.agsrhichome.bnl.gov/RHIC/Runs/.

(114) M. Anerella et al., *Nucl. Instrum. Meth. A*, 2003, **499**, 280–315.

(115) I. Alekseev et al., *Nucl. Instrum. Meth. A*, 2003, **499**, 392–414.

(116) J. A. et al., *BNL-73700-2005-IR-R1*, 2005.

(117) A. Zelenski, *PoS*, 2013, **PSTP2013**, ed. D. Crabb and M. Poelker, 048.

(118) E. Beebe, J. Alessi, S. Binello, T. Kanesue, D. McCafferty, J. Morris, M. Okamura, A. Pikin, J. Ritter and R. Schoepfer, *AIP Conf. Proc.*, 2015, **1640**, ed. A. Lapierre, S. Schwarz and T. M. Baumann, 5–11.

(119) A. Trzupek et al., *Acta Phys. Polon. B*, 1996, **27**, ed. E. Grosse, H. Machner, A. Magiera and Z. Rudy, 3103–3111.

(120) M. Adamczyk et al., *Nucl. Instrum. Meth. A*, 2003, **499**, 437–468.

(121) D. Morrison et al., *Nucl. Phys. A*, 1998, **638**, ed. T. Hatsuda, Y. Miake, K. Yagi and S. Nagamiya, 565–570.

(122) S. Campbell, *J. Phys. Conf. Ser.*, 2017, **832**, 012012.

(123) M. Connors, *J. Phys. Conf. Ser.*, 2016, **736**, 012027.

(124) K. Ackermann et al., *Nucl. Instrum. Meth. A*, 2003, **499**, 624–632.

(125) W. J. Llope et al., *Nucl. Instrum. Meth.*, 2004, **A522**, 252–273.

(126) W. Llope, *Nucl. Instrum. Meth. B*, 2005, **241**, 306–310.

(127) M. Beddo et al., *Nucl. Instrum. Meth. A*, 2003, **499**, 725–739.

(128) J. Schambach et al., 20th International Conference on Particles and Nuclei, 2014, pp. 659–664.

(129) T. Huang et al., *Nucl. Instrum. Meth. A*, 2016, **833**, 88–93.

(130) W. Llope et al., *Nucl. Instrum. Meth. A*, 2014, **759**, 23–28.

(131) C. Yang, *EPJ Web Conf.*, 2018, **182**, ed. Y. Aharonov, L. Bravina and S. Kabana, 02130.

(132) P. Shanmuganathan, *PoS*, 2018, **CPOD2017**, 066.

(133) C. e. G. STAR, *arXiv, nucl-ex, 1609.05102*, 2016.

(134) *STAR Collaboration, STAR Note 619*, `https://drupal.star.bnl.gov/STAR/starnotes/public/sn0619`.

(135) M. Anderson et al., *Nucl. Instrum. Meth.*, 2003, **A499**, 659–678.

(136) H. Bichsel, *Nucl. Instrum. Meth. A*, 2006, **562**, 154–197.

(137) W. R. Leo, *Techniques for Nuclear and Particle Physics Experiments*, [doi:10.1007/978-3-642-57920-2, ISBN 978-3-642-57920-2.

(138) *SN0439 : Comparison of Bethe-Bloch and Bichsel Functions*, `https://drupal.star.bnl.gov/STAR/starnotes/public/sn0439`.

(139) G. Nigmatkulov, *The PicoDst format documentation*, `https://drupal.star.bnl.gov/STAR/blog/gnigmat/picodst-format`, [Online; accessed 22-February-2021], 2020.

(140) G. Nigmatkulov, *Introduction to PicoDst*, `https://drupal.star.bnl.gov/STAR/system/files/Nigmatkulov_intro2pico_Krakow2019.pdf`, [Online; accessed 22-February-2021], 2019.

(141) G. Marr, *Run-17 Au+Au Review, Run-18 Zr+Zr, Ru+Ru Plans*, `https://www.rhichome.bnl.gov/RHIC/Runs/RhicRun17AuAu.pdf`, [Online; accessed 11-December-2020].

(142) *Collision Energy Dependence of pt Correlations in Au+Au Collisions at RHIC Analysis Note*, 2018.

(143) L. Adamczyk et al., *Phys. Rev.*, 2017, **C96**, 044904.

(144) H. J. Drescher, M. Hladik, S. Ostapchenko, T. Pierog and K. Werner, *Phys. Rept.*, 2001, **350**, 93–289.

(145) V. Gribov, *Sov. Phys. JETP*, 1968, **26**, 414–422.

(146) K. Werner, *Physics Reports*, 1993, **232**, 87–299.

(147) M. Froissart, *Phys. Rev.*, 1961, **123**, 1053–1057.

(148) R. P. Feynman, *Phys. Rev. Lett.*, 1969, **23**, ed. L. Brown, 1415–1417.

(149) V. N. Gribov and L. N. Lipatov, *Sov. J. Nucl. Phys.*, 1972, **15**, 438–450.

(150) S. Ferreres-Solé and T. Sjöstrand, *Eur. Phys. J. C*, 2018, **78**, 983.

(151) K. Werner, I. Karpenko, T. Pierog, M. Bleicher and K. Mikhailov, *Phys. Rev.*, 2010, **C82**, 044904.

(152) X. Artru and G. Mennessier, *Nucl. Phys. B*, 1974, **70**, 93–115.

(153) K. Werner, B. Guiot, I. Karpenko and T. Pierog, *Phys. Rev.*, 2014, **C89**, 064903.

(154) K. Werner, *Phys. Rev. Lett.*, 2007, **98**, 152301.

(155) C. Gale, S. Jeon and B. Schenke, *Int. J. Mod. Phys.*, 2013, **A28**, 1340011.

(156) S. Borsanyi, G. Endrodi, Z. Fodor, A. Jakovac, S. D. Katz, S. Krieg, C. Ratti and K. K. Szabo, *JHEP*, 2010, **11**, 077.

(157) Y. Karpenko, private communication.

(158) W. Israel, *Annals Phys.*, 1976, **100**, 310–331.

(159) W. Israel and J. Stewart, *Annals Phys.*, 1979, **118**, 341–372.

(160) M. Takamoto and S.-i. Inutsuka, *J. Comput. Phys.*, 2011, **230**, 7002–7017.

(161) F. Cooper and G. Frye, *Phys. Rev.*, 1974, **D10**, 186.

(162) S. A. Bass et al., *Prog. Part. Nucl. Phys.*, 1998, **41**, [Prog. Part. Nucl. Phys.41,225(1998)], 255–369.

(163) M. Bleicher et al., *J. Phys.*, 1999, **G25**, 1859–1896.

(164) C. Patrignani et al., *Chin. Phys. C*, 2016, **40**, 100001.

(165) J. Steinheimer, V. Vovchenko, J. Aichelin, M. Bleicher and H. Stöcker, *EPJ Web Conf.*, 2018, **171**, ed. A. Mischke and P. Kuijer, 05003.

(166) P. Parotto, *PoS*, 2018, **CPOD2017**, 036.

(167) C. Nonaka and M. Asakawa, *Phys. Rev. C*, 2005, **71**, 044904.

(168) R. Guida and J. Zinn-Justin, *Nucl. Phys. B*, 1997, **489**, 626–652.

(169) P. Schofield, J. Litster and J. T. Ho, *Phys. Rev. Lett.*, 1969, **23**, 1098–1102.

(170) M. Bluhm and B. Kampfer, *PoS*, 2006, **CPOD2006**, ed. F. Becattini, 004.

(171) K. Werner and J. Aichelin, *Phys. Rev. C*, 1995, **52**, 1584–1603.

(172) K. Werner, *Latest developments in EPOS*, `http://pyweb.swan.ac.uk/~aarts/talks-thor-lisboa/Werner_THOR_Lisboa2018.pdf`, [Online; accessed 10-October-2020], 2018.

(173) F. M. Liu, K. Werner and J. Aichelin, *Phys. Rev. C*, 2003, **68**, 024905.

(174) F. Becattini and L. Ferroni, *Eur. Phys. J. C*, 2004, **35**, 243–258.

(175) F. Becattini and L. Ferroni, *Eur. Phys. J. C*, 2004, **38**, [Erratum: Eur.Phys.J. 66, 341 (2010)], 225–246.

(176) K. Saraswat, P. Shukla and V. Singh, *J. Phys. Comm.*, 2018, **2**, 035003.

(177) A. Adare et al., *Phys. Rev. C*, 2010, **81**, 034911.

(178) *Centre de Calcul de l'IN2P3/CNRS Lyon*, `https://cc.in2p3.fr`.

(179) S. Vogel, G. Torrieri and M. Bleicher, *Phys. Rev. C*, 2010, **82**, 024908.

(180) S. Sombun, J. Steinheimer, C. Herold, A. Limphirat, Y. Yan and M. Bleicher, *J. Phys. G*, 2018, **45**, 025101.

(181) X. Luo and N. Xu, *Nucl. Sci. Tech.*, 2017, **28**, 112.

(182) C. Athanasiou, K. Rajagopal and M. Stephanov, *Phys. Rev. D*, 2010, **82**, 074008.

(183) M. Stephanov, *Phys. Rev. Lett.*, 2009, **102**, 032301.

(184) M. Stephanov, *Phys. Rev. D*, 2010, **81**, 054012.

(185) M. Aggarwal et al., *Phys. Rev. Lett.*, 2010, **105**, 022302.

(186) T. Sjöstrand, *Comput. Phys. Commun.*, 2020, **246**, 106910.

(187) J. L. Klay et al., *Phys. Rev.*, 2003, **C68**, 054905.

(188) S. Y. Panitkin et al., Proceedings, 15th Winter Workshop on Nuclear Dynamics (WWND 1999), Springer, 1999, pp. 271–279.

(189) Y. Wu, *Nucl. Phys.*, 2019, **A982**, 899–902.

(190) A. C. W. P. on the Future of Relativistic Heavy-Ion Physics in the US.

(191) L. Adamczyk et al., *Phys. Rev.*, 2018, **C98**, 014915.

(192) N. Magdy, *Universe*, 2019, **5**, 94.

(193) J. Adam et al., *Phys. Rev. Lett.*, 2019, **122**, 172301.

(194) N. Magdy, *Nucl. Phys.*, 2019, **A982**, 255–258.

(195) N. a. a. Magdy, *Phys. Rev.*, 2018, **C98**, 061902.

(196) C. Bierlich, COST Wokshop on interplay of hard and soft QCD probes for collectivity in heavy-ion collisions, February 25, 2019.

(197) J. Adam et al., *Phys. Lett.*, 2018, **B783**, 459–465.

(198) J. Thäder, *Nucl. Phys.*, 2016, **A956**, 320–323.

(199) A. Bazavov et al., *Phys. Rev.*, 2017, **D96**, 074510.

(200) V. Vovchenko, D. V. Anchishkin, M. I. Gorenstein and R. V. Poberezhnyuk, *Phys. Rev.*, 2015, **C92**, 054901.

(201) A. P. Mishra, R. K. Mohapatra, P. S. Saumia and A. M. Srivastava, *Phys. Rev.*, 2008, **C77**, 064902.

(202) V. Skokov, B. Friman, E. Nakano, K. Redlich and B. .-. Schaefer, *Phys. Rev.*, 2010, **D82**, 034029.

(203) D. T. Son and M. A. Stephanov, *Phys. Rev. Lett.*, 2001, **86**, 592–595.

(204) A. J. Mizher, M. N. Chernodub and E. S. Fraga, *Phys. Rev.*, 2010, **D82**, 105016.

(205) E. S. Fraga, L. F. Palhares and P. Sorensen, *Phys. Rev.*, 2011, **C84**, 011903.

(206) W. F. Henning, *J. Phys.*, 2007, **G34**, S551–S557.

(207) V. Koch and A. Bzdak, *Acta Phys. Polon.*, 2016, **B47**, 1867.

(208) D. K. Mishra, P. K. Netrakanti and B. Mohanty, *Phys. Rev.*, 2016, **C94**, 054906.

(209) P. Braun-Munzinger, A. Kalweit, K. Redlich and J. Stachel, *Nucl. Phys.*, 2016, **A956**, 805–808.

(210) S. Borsányi, *PoS*, 2016, **LATTICE2015**, 015.

(211) A. Bhattacharyya, S. K. Ghosh, R. Ray, K. Saha and S. Upadhaya, *EPL*, 2016, **116**, 52001.

(212) R. A. Lacey, *Phys. Rev. Lett.*, 2015, **114**, 142301.

(213) E. S. Bowman and J. I. Kapusta, *Phys. Rev.*, 2009, **C79**, 015202.

(214) M. Asakawa and K. Yazaki, *Nucl. Phys.*, 1989, **A504**, 668–684.

(215) R. D. Pisarski and F. Wilczek, *Phys. Rev.*, 1984, **D29**, 338–341.

(216) S. Ejiri, *Phys. Rev.*, 2008, **D78**, 074507.

(217) F. R. a. a. Brown, *Phys. Rev. Lett.*, 1990, **65**, 2491–2494.

(218) Y. Aoki, G. Endrodi, Z. Fodor, S. D. Katz and K. K. Szabo, *Nature*, 2006, **443**, 675–678.

(219) P. Parotto, M. Bluhm, D. Mroczek, M. Nahrgang, J. Noronha-Hostler, K. Rajagopal, C. Ratti, T. Schäfer and M. Stephanov, 2018.

(220) S. Adler et al., *Phys. Rev. Lett.*, 2003, **91**, 182301.

(221) S. Singha, *PoS*, 2018, **CPOD2017**, 004.

(222) B. B. Abelev et al., *JHEP*, 2015, **06**, 190.

(223) C. Bierlich et al., *SciPost Phys.*, 2020, **8**, 026.

(224) A. Buckley, D. Kar and K. Nordström, *SciPost Phys.*, 2020, **8**, 025.

(225) M. Stefaniak and H. Zbroszczyk, *EPJ Web of Conferences*, 2017, **164**, 07013.

(226) H. Zbroszczyk, Ph.D. Thesis, Warsaw U. of Tech., 2008.

(227) J. Adam et al., *Phys. Lett.*, 2019, **B790**, 490–497.

(228) L. Adamczyk et al., *Phys. Rev.*, 2017, **C95**, 034907.

(229) D. Kikola, L. Yi, S. Esumi, F. Wang and W. Xie, *Phys. Rev.*, 2012, **C86**, 014901.

(230) L. Adamczyk et al., *Phys. Rev. Lett.*, 2018, **120**, 062301.

(231) H. Petersen, *Phys. Rev.*, 2011, **C84**, 034912.

(232) D. Cebra, *Exploring the QCD Phase Diagram: RHIC Beam Energy Scan II*, `https://www.c-ad.bnl.gov/ardd/LEeC/Presentations/Cebra_LEReC_BESII_ver2.pdf`, [Online; accessed 12-December-2018], 2013.

(233) http://theor.jinr.ru/7Ewpcf2019/files/talks/06/4.20mstefaniak$_w pcf_v ol8.pdf$.

(234) https://indico.cern.ch/event/433345/contributions/2358275.

(235) https://indico.cern.ch/event/792436/contributions/3570051/.

(236) M. E. Peskin and D. V. Schroeder, *An Introduction to quantum field theory*, Addison-Wesley, Reading, USA, 1995.

(237) https://root.cern.ch.

(238) https://indico.gsi.de/event/5593/session/4/contribution/13/material/slides/0.pdf.

(239) `https://wigner.mta.hu/en/zimanyi-medal`.

(240) K. Werner, B. Guiot, I. Karpenko, A. G. Knospe, C. Markert, T. Pierog, G. Sophys and M. Stefaniak, *Adv. Ser. Direct. High Energy Phys.*, 2018, **29**, 391–409.

(241) K. Werner, B. Guiot, I. Karpenko, T. Pierog, G. Sophys and M. Stefaniak, *J. Phys. Conf. Ser.*, 2018, **1070**, 012007.

(242) G. Bonsignori, *Nucleus-nucleus Collisions*, World Scientific Publishing Company, 2001.

(243) J. Jia, M. Zhou and A. Trzupek, *Phys. Rev.*, 2017, **C96**, 034906.

(244) J. L. Nagle and M. P. McCumber, *Phys. Rev.*, 2011, **C83**, 044908.

(245) B. H. Alver, C. Gombeaud, M. Luzum and J.-Y. Ollitrault, *Phys. Rev.*, 2010, **C82**, 034913.

(246) H. Petersen, G.-Y. Qin, S. A. Bass and B. Muller, *Phys. Rev.*, 2010, **C82**, 041901.

(247) G.-Y. Qin, H. Petersen, S. A. Bass and B. Muller, *Phys. Rev.*, 2010, **C82**, 064903.

(248) A. P. Mishra, R. K. Mohapatra, P. S. Saumia and A. M. Srivastava, *Phys. Rev.*, 2010, **C81**, 034903.

(249) Y. Pandit, *Nucl. Phys.*, 2013, **A904-905**, 357c–360c.

(250) *RCF home page*, `www.racf.bnl.gov`, 2018.

(251) *PDSF home page*, `https://www.nersc.gov/users/computational-systems/pdsf`, 2018.

(252) *Condor home page*, `https://research.cs.wisc.edu/htcondor/`, 2018.

(253) S. A. Voloshin, *Prog. Part. Nucl. Phys.*, 2012, **67**, 541–546.

(254) P. Chaloupka, *EPJ Web Conf.*, 2017, **164**, 06001.

(255) S. A. Voloshin, 2001, [AIP Conf. Proc.610,591(2002)], 591–596.

(256) H. Petersen, J. Steinheimer, G. Burau, M. Bleicher and H. Stocker, *Phys. Rev.*, 2008, **C78**, 044901.

(257) A. Bazavov et al., *Phys. Rev.*, 2014, **D90**, 094503.

(258) K. a. a. Aamodt, *Phys. Rev. Lett.*, 2010, **105**, 252302.

(259) K. Werner, I. Karpenko, M. Bleicher, T. Pierog and S. Porteboeuf-Houssais, *Phys. Rev.*, 2012, **C85**, 064907.

(260) K. Werner, I. Karpenko, T. Pierog, M. Bleicher and K. Mikhailov, *Phys. Rev.*, 2011, **C83**, 044915.

(261) K. H. Ackermann et al., *Nucl. Instrum. Meth.*, 2003, **A499**, 713–719.

(262) L. Adamczyk et al., *Phys. Rev.*, 2013, **C88**, 014904.

(263) L. Song, *Nucl. Phys.*, 2016, **A956**, 397–400.

(264) D. Velicanu, *J. Phys.*, 2011, **G38**, 124051.

(265) M. A. Bloomer, W. A. Love and L. Waters, *Nucl. Phys.*, 1991, **A527**, 595–600.

(266) K. Filimonov et al., *Nucl. Phys.*, 1999, **A661**, 198–204.

(267) K. Meehan, *Nucl. Phys.*, 2017, **A967**, 808–811.

(268) M. L. Miller, K. Reygers, S. J. Sanders and P. Steinberg, *Ann. Rev. Nucl. Part. Sci.*, 2007, **57**, 205–243.

(269) L. Adamczyk et al., *Phys. Lett. B*, 2013, **719**, 62–69.

(270) E. Aschenauer et al., 2014.

(271) L. Kotchenda, S. Kozlov, P. Kravtsov, A. Markov, M. Strikhanov, B. Stringfellow, V. Trofimov, R. Wells and H. Wieman, *Nucl. Instrum. Meth. A*, 2003, **499**, 703–712.

(272) F. Geurts et al., *Nucl. Instrum. Meth. A*, 2004, **533**, ed. P. Dupieux, R. Santonico and E. Vercellin, 60–64.

(273) F. Bieser et al., *Nucl. Instrum. Meth. A*, 2003, **499**, 766–777.

DOCTORAT MATIERE BRETAGNE MOLECULES LOIRE ET MATERIAUX

IMT Atlantique
Bretagne-Pays de la Loire
École Mines-Télécom

POLITECHNIKA WARSZAWSKA
WARSAW UNIVERSITY OF TECHNOLOGY

Titre : Étude de la dépendance en énergie des flux elliptique et triangulaire pour les particules identifiées dans le Beam Energy Scan avec l'expérience STAR et le générateur d'événements EPOS

Mot clés : ions lourds, diagramme de phase, équation d'état, flux

Résumé : L'étude des propriétés de l'expansion collective de la matière créée dans les collisions d'ions lourds est un outil unique, permettant de mieux comprendre les aspects non-perturbatifs de la QCD, et nécessitant un travail tant sur le plan théorique que sur le plan expérimental. D'une part, des calculs d'évolution hydrodynamique prédisent, en conséquence de l'asymétrie du système dans l'état initial, une anisotropie dans la production des particules finales. D'autre part, les mesures de cette anisotropie, en fonction du système et de l'énergie considérés, permettent non seulement de valider les prédictions théoriques, mais aussi de déterminer des éléments inconnus comme les propriétés du plasma créé lors de ces collisions (e.g. son équation d'état), ou bien les processus de thermalisation mis en jeu. Améliorer nos connaissances sur ce sujet est le principal objectif de cette thèse. Les méthodes expérimentales décrites ont pour objectif de donner un aperçu de la mesure de l'anisotropie de l'expansion des particules et anti-particules, tandis que les approches théoriques ont été utilisées pour étudier l'équation d'état de la matière.

Title: Beam Energy Scan dependance of elliptic and triangular flow of identified hadrons in the STAR experiment and the EPOS model

Keywords: heavy-ions, phase diagram, equation of state, flow

Abstract: Studying the properties of the collective expansion of matter created in heavy-ion collisions provides a unique tool to understand better the nonperturbative aspect of QCD. Input from both the theoretical and the experimental side is needed. Hydrodynamic calculations predict anisotropies in particle production, as a consequence of asymmetries in the initial state of the system's evolution. Measurements of the systematics (energy-, system- dependence) of these anisotropies allow one not only to validate theoretical ideas but also to determine the unknown elements, like plasma properties (EoS), thermalization processes. The broadening of our knowledge in these topics is the main goal of the thesis. The experimental methods were used to provide insight into the investigation of the anisotropies in the expansion of the particles and antiparticles, while the theoretical approach was used for the EoS studies.